Modelling Structure Direction and Morphology Control in Zeolite Synthesis

Alan John William Lobo

Department of Chemistry, University College London (UCL)

Thesis submitted for the degree of Doctor of Engineering
2012

I, Alan John William Lobo, confirm that the work presented in this thesis is my own. Where information has been derived from other sources, I confirm that this has been indicated in the thesis.

Abstract

The role of the organic template has been at the centre of research into zeolite synthesis since its first inclusion in synthesis in the 1950s. Since then research has shown that the template plays many roles in the synthesis starting from ordering species in the prenucleation stage, right through to controlling the final crystal morphology. However, there currently exists no way of predicting what effects a particular template will have on either the zeolite topology or morphology.

The ZEBEDDE code has been expanded to automate the building and docking processes. This allows large numbers of templates to be screened as part of systematic studies. This improved code has been used to design templates for the zeolite Boggsite. Two templates have been proposed for this role through a series of building and docking calculations starting from a methane seed.

The role of the template on the morphology of zeolite crystals has been investigated. Using docking calculations, 21-crown-7 was predicted to fit well inside the cavity within zeolite L and as such may template the cancrinite columns and so promote growth in the normally frustrated *a*-direction. Experimental work confirmed that this was the case, and yielded crystals with a lower aspect ratio than had previously been made. The role of long chain amines on the crystal morphology of AlPO-11 was also investigated as when long chain surfactants are included in the synthesis, the length of the crystals is reduced. On the {001} and {010} surface the amine can be incorporated into the framework, but on the {001} this is not possible and so hinders growth giving the observed morphology.

Building on previous work, a systematic study of the effects of some small organic templates as well as two series of diquaternary ammonium cations commonly used in synthesis has been carried out. *Ab initio* molecular dynamics simulations have been carried out on the templates in the presence of water. Using a code specifically written for the task, the ring structures present in the hydration layer around the template have been analysed. These ring structures have been compared to the rings found in the zeolites which they eventually form, with some links being found.

This work has been supported by the Engineering and Physical Sciences Research Council, and by ExxonMobil Research and Engineering. Simulations in chapter five were possible due to computer time on the national super computer HeCTOR, provided by the Materials Chemistry Consortium.

Acknowledgements

I would first like to thank my supervisor Dr. Dewi Lewis for his advice and support throughout the project. I am also grateful to Dr. David Willock for his assistance with the ZEBEDDE code and Dr. Ben Slater for fruitful discussions and guidance. I am especially grateful to my industrial supervisor Dr. Simon Weston for organising my visits to ExxonMobil Research and Engineering and making the transition to US culture that little bit easier. Thank you also to the members of the zeolite discovery group at ExxonMobil Research and Engineering for their input to the project.

There have been a huge number of people both within in department and the university as a whole that have helped with my research and made the last four years that bit more enjoyable. I'd like to thank in particular, Adam, Jenna, Liz, Isaac, Jay, Kim, Martijn, Tony, and Sheena. A special thank you goes to Dr. Jamieson Christie and Dr. Keith Butler for proof reading parts of this thesis. I'd also like to thank my friends Meghan, Natalie, Gerardina, Jon, Dan, Tom, Lucy, Robin, Holly and Mike, as well as my housemates over the last few years Paul, Neil, Jasmine, Ben and Joe, especially over the past few months when I've spoken of little else but this thesis.

Finally, I'd like to thank my parents and sister for their support throughout my time as a graduate student and indeed throughout my time at UCL over the last eight years.

List of Publications

Work in this thesis has been published in the following papers:

R. Brent, A. J. W. Lobo, D. W. Lewis, M. W. Anderson, "Modifying the Crystal Habit of Zeolite L by Addition of an Organic Space Filler", *J. Phys. Chem. C*, **2010** 114, 42, 18240-18246.

A. M. Beale, M. G. O'Brien, M Kasunic, A. Golobic, M. Sanchez-Sanchez, A. J. W. Lobo, D. W. Lewis, D. S. Wragg, S. Nikitenko, W. Bras, B. M. Weckhuysen, "Probing ZnAPO-34 Self-Assembly Using Simultaneous Multiple in Situ Techniques", *J. Phys. Chem. C*, **2011**, 115, 14 , 6331-6340

Key to figures

Figures have the following colours for elements, unless otherwise indicated.

 Hydrogen

 Carbon

 Oxygen

 Silicon

 Phosphorus

 Nitrogen

Contents

List of Figures

List of Tables

CHAPTER 1

Introduction

1.1 Zeolites

The first zeolite was discovered in 1756 by the Swedish mineralogist Cronstedt [1] as a minor constituent in vugs or cavities in basaltic and volcanic rock. He observed that when heated, the mineral appeared to boil as it released large amounts of steam, which we now know was the water escaping from the cavities and pores of the zeolite. He named these materials "zeolites" which is derived from the ancient Greek words "zeo" meaning "to boil" and "lithos" meaning "a stone", so literally translated as "boiling stone". For roughly the next 200 years zeolite science was restricted to zeolites that were found naturally in rock. It was not until the pioneering work of Barrer in the mid 1930s on adsorption and synthesis that the field of zeolite science truly started. Over the following 70 years, the field has grown massively, with zeolites being used on a multi-tonne scale in industry and new zeolite structures are being discovered each year. However, the chemical processes which occur to yield a zeolite are still not fully understood and the aim of zeolite science is to understand the nucleation of these materials so that we can design and synthesise zeolites which meet our requirements.

This thesis focuses on the role of the organic template molecule in synthesis in an attempt to relate its structure to the zeolite that eventually forms. The template and its role will be discussed in greater detail in the following chapter, with this chapter serving to introduce the nature of zeolites and some of the basic properties they possess. Each chapter contains further details as to the methods utilised and

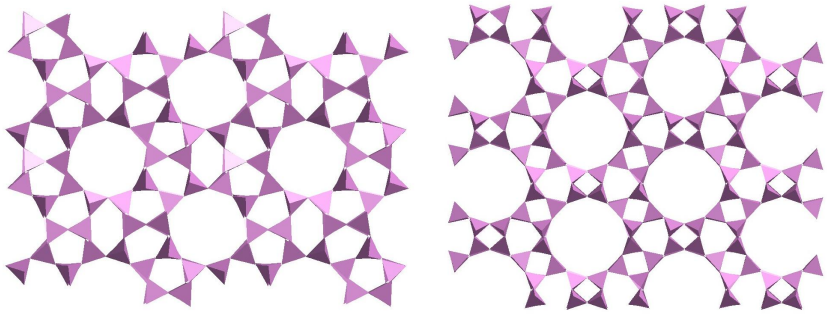

Figure 1.1: Examples of zeolite topologies: ZSM-5 (left) and Boggsite (right), each SiO_4 is represented by a tetrahedron.

the fundamental technicalities of the questions which it aims to answer.

1.2 Structure and Composition of Zeolites

Zeolites are microporous crystalline materials made of corner-sharing tetrahedra with pore dimensions typically ranging from 5-15 Å[2]. The fundamental building units of a zeolite are $[SiO_4]^{4-}$ and $[AlO_4]^{5-}$ tetrahedra. Although the chemical composition is limited to silicon, aluminium and oxygen, there are numerous ways that these fundamental units can be linked together giving a wide variety of topologies (see Figure 1.1 for examples) and properties. There are also a large number of materials isomorphic to zeolites such as aluminophosphates (ALPOs) and silicoaluminophosphates (SAPOs). Although not technically zeolites other elements such as Ti, Fe, V, Ge, Cr and Mn have also been incorporated into the framework in order to alter chemical properties [3].

1.2.1 Framework Types and Fundamental Building Units

The fundamental building units can be linked together in a huge number of ways which yield zeolites with different structural properties. It is these unique structural properties which give zeolites their industrial applications, and the variety of structures which are theoretically possible make the desire to find new topologies particularly appealing. Zeolite frameworks are classified by a three letter code which is assigned by the International Zeolite Association (IZA) [4] for each unique framework topology. This three letter code only refers to the framework type and not to a specific material. For example, Linde Type A [5], ZK-5 [6] and ITQ-29 [7] all have framework code LTA but have different chemical compositions. Currently there are 201 different frameworks listed on the IZA website [4] and this number has been

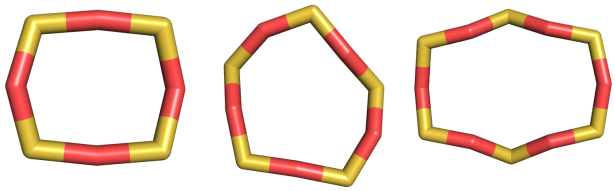

Figure 1.2: Examples of ring units found in zeolites. Left to right: 4 ring, 5 ring, 6 ring.

steadily increasing.

1.2.2 Composite Building Units

The fundamental tetrahedral building units can be linked together to form composite building units. The simplest composite building units are rings which are constructed from n fundamental tetrahedral units. Most commonly in zeolites $n =$ 4, 5, 6, 8, 10 and 12, but rings of up to $n = 30$ have been found [8]. It is rare to find zeolites containing 3, 9 and 11 ring structures [9]. Some common ring structures can be seen in Figure 1.2.

Rings can be combined together to form larger composite units, examples of which can be seen in Figure 1.3. Cage composite building units are usually considered to have rings (usually 6 ring) which are small enough to restrict the passage of all molecules larger than water. These cages can be described by the following notation $[n^m]$ where n is the order of the ring and m is the frequency with which that ring occurs. For example a SOD cage is referred to as a $[4^6 6^8]$ polyhedron, because it has 6 4-rings and 8 6-rings (Figure **??**).

Larger composite building units can also be made. Chains are one dimensional, for example, made of 4 rings (Figure **??**). Even larger are cavities which are similar to cages but contain rings which are large enough to allow the passage of molecules bigger than water such as long chain hydrocarbons. Like cages, cavities can also be described by the $[n^m]$ notation, for example the LTA cavity is referred to as a $[4^{12} 6^8 8^6]$ polyhedron. These units contain 8 rings and so allow the diffusion of molecules such as carbon dioxide.

Lastly when we link composite building units together a larger channel may form. A channel is a pore which runs indefinitely in one dimension, and is described by the smallest ring of T-atoms (where T is a vertex atom, Si or Al) within the structure. For example zeolite L (LTL) has a 12 ring channel despite the channel being undulating and therefore wider at certain points. Most commonly channels

Figure 1.3: Figure Removed.

Figure 1.4: Figure Removed.

are 8, 10 or 12 ring but recently zeolites with channels much larger than this have been synthesised and these will be discussed in greater detail in Chapter 2. It is often the case that channels intersect to give two or three dimensional pores, and frequently it is these structures which have the more interesting properties.

1.2.3 Secondary Building Units

The last type of building unit is the secondary building unit. It is these types of unit which are most commonly used to describe a zeolite and it dates back to the work of Meier in 1967 [10]. These units have been proposed to be important species in the growth of zeolites, and are the smallest entities from which zeolites may be built. The current list of secondary building units can be seen in Figure 1.4.

1.3 Naturally Occurring Zeolites

As mentioned in Section 1.1 the early history of zeolite science was founded on naturally occurring zeolites that had been discovered in cavities and vugs of basalts. In the 19th century zeolites were discovered in sedimentary rocks and this led to further geological explorations which culminated in the proposal of zeolite formation [10]:

- Crystals resulting from hydrothermal or hot spring activity, involving reactions between solutions and basaltic lava flows.
- Deposits formed from volcanic sediments in closed alkaline and saline lake-systems.
- Similar formations from open fresh-water and ground-water systems acting on volcanic sediments.
- Deposits formed from volcanic minerals in alkaline soils.
- Deposits formed from hydrothermal or low-temperature alterations of marine sediments.
- Formations as the result of low-grade burial metamorphism.

It was these observations that zeolites form in sedimentary rock that led to the theory that zeolites do not require high temperatures and pressures to form as was previously thought. This forms the basis of hydrothermal synthesis which will be discussed in greater detail in Chapter 2.

To date, geological exploration has led to the discovery of over 40 types of naturally occurring zeolites, although only 30 of these have had their structures solved [11]. Although this thesis focuses on synthetic zeolites, naturally occurring zeolites have their place within industry. This is usually where purity and uniformity in pore size is not an issue as some naturally occurring zeolites have the advantage of being available in large quantities. Due to the fact they are found relatively near the Earth's surface in sedimentary rock the cost of extraction is not prohibitively high. This has led to their use in water treatment, water softening, and the drying and separation of gases [1].

1.4 Applications of Zeolites

The applications of zeolites are wide ranging and some are used on a multi-tonne scale. The three main uses are catalysts, ion exchangers and molecular sieves. The reason zeolites have these broad applications is the properties of the zeolite are tunable by modifying the chemical composition and by changing the framework topology.

The fact that in a zeolite some of the silicon has been exchanged with aluminium means that there is an overall negative charge on the framework. In order to balance this charge, the framework incorporates small inorganic cations such as sodium, potassium and lithium. These are often loosely bound and as such can be exchanged. It is this property that makes zeolites useful as materials for nuclear waste cleanup after incidents such as Three Mile Island, Chernobyl and more recently the Fukushima disaster in Japan. However, the first large scale use of zeolites as an ion exchanger was in washing powder. The loosely bound sodium in zeolite A exchanges with the calcium in water thereby softening it. This had huge environmental impacts as previously the removal had been achieved using phosphates which are known to cause eutrophication. Zeolites also have a high affinity for water which has made them useful in the drying of gas streams whether in small scale columns or in large industrial reactors. Furthermore, they have been used to separate molecules by size, which has led to zeolites being referred to as molecular sieves. A particularly important use is the separation of more valuable branched hydrocarbons from linear hydrocarbons in hydro-isomerisation reactions [1].

The growth in the use of zeolites as catalysts, especially in the petrochemical industry occurred around 30 years ago with the discovery of ZSM-5 [12]. ZSM-5 is widely used for a variety of applications such as fluid catalytic cracking (FCC) [13], conversion of methanol to gasoline [14, 15], and isomerisation of xylenes [16]. The location of the Brønsted acid sites within the zeolite, drive the formation of particular products through size selectivity, whether it be selective on the reactant, product or transition state. Very recently zeolites have found applications in medicine for controlled drug release and as membranes for gas sensors [17].

1.5 Computational Methods

The computational methods used in this thesis are discussed in Chapter 3, however, it seems sensible to provide a brief introduction to the field as some of the methods are discussed in Chapter 2. Broadly there are two different methods by which the energy of a system can be calculated. The first is using molecular mechanics where a potential function is fitted to a molecular interaction. Using a set of potentials we can model a chemical system and derive properties from the simulations. The second method is known as *ab initio* or electronic structure calculations. Here we assume nothing about the atom and calculate the energy based on quantum mechanics. In order to carry out these calculations several approximations must be made which are discussed in detail in Section 3.3.

1.6 Aims of This Study

This study aims firstly to improve the ZEBEDDE code by developing the template building routines to have more chemical "sense" and also to automate many of the processes to speed up the generation of templates. This improved code will be used to design templates for use in zeolite synthesis. As well as designing new templates, modelling techniques will be used to gain an understanding of the role of the template on a molecular level. That is, how the template affects the initial synthesis gel in order to direct a particular zeolite structure. Furthermore, the role of the template on the overall morphology of the zeolite will be investigated. By combining these roles it is hoped that templates can be designed to yield selectively a particular zeolite morphology and topology.

CHAPTER 2

Zeolite Synthesis

2.1 Introduction

This chapter introduces the common methods used to synthesise zeolites and the current understanding of the processes involved.

2.2 Hydrothermal Synthesis

The first hydrothermal synthesis of a zeolite was carried out by Barrer at Imperial College London the late 1940s [18], although it had been claimed many years previously [19]. At the time the structure was unknown but it was later identified by Kerr [6, 20] as ZK-5 (KFI). A typical hydrothermal synthesis at the time was carried out at high temperature (170°C – 270°C) in strong salt solutions. Subsequently many other zeolites were synthesised, and during the early 1950s a limited number of new zeolites were discovered with no natural analogue including, Zeolites A [21], B, C and X [22]. Arguably the biggest leap in zeolite synthesis came in 1961 when Barrer and Denny [23] replaced the inorganic cations with small organic ammonium cations and synthesised zeolite A. This discovery led to the synthesis of many new zeolites.

What was becoming clear was that the final zeolite structure obtained is highly dependent on the initial synthesis conditions such as Si/Al ratio, temperature, synthesis duration and cations. Since zeolites are metastable with respect to α-quartz and α-Al_2O_3 the zeolite obtained is the kinetic rather than the thermodynamic product. Increasingly, attempts at synthesising new zeolites since these initial discoveries

have focused on a trial and error approach, lately using high-throughput techniques to scan a range of synthesis conditions in the hope of discovering a new structure.

The processes that occur in zeolite synthesis have been widely studied with the first work being carried out by Barrer *et al* [24]. It is now generally accepted that there are three stages in a zeolite synthesis [25]. The first is where the solution reaches supersaturation as the concentration of dissolved aluminosilicate species increases and the first nuclei appear. This stage is followed by nucleation of the species present. Initially the solids formed are amorphous but slowly become ordered as the synthesis proceeds. The third stage is crystal growth when the nuclei have reached a critical size and the species from solution add to the zeolite crystal surface. Each of the stages will be discussed in greater detail in the following sections.

2.3 Structure Directing Agents

Templates, or more accurately structure directing agents (SDAs), have been at the centre of zeolite synthesis since their discovery [23]. In this section their uses, development and role will be discussed.

2.3.1 Early Templates

The simplest, and first, template used in zeolite synthesis was the singly charged tetramethylammonium (TMA) [23]. Since then a number of zeolites have been made using this template such as Gismondine (GIS) and Sodalite (SOD) [26, 27]. In a review by Lok, Cannan and Messina in 1983 they state that there are 17 different structures made using TMA [28]. However, this is where some ambiguity is introduced into the assignment of structures and the definition of a zeolite material. This point was highlighted by Meier [29] in a comment relating to a review by Lok *et al.* where zeolites should be described by their topology rather than by the specific material e.g. zeolite N which has framework type EDI (Edingtonite). To avoid this confusion, the zeolites discussed herein will also be described by their framework code as assigned by the IZA [4].

After TMA, the next logical step was to use larger tetraalkylammonium (TAA) cations in the synthesis. Those used have included tetraethylammonium (TEA), tetrapropylammonium (TPA) and tetrabutylammonium (TBA) along with mixed variations on these such a dimethyldiethylammonium [28]. A number of new topologies were discovered, including one of the most widely studied and industrially used zeolites, ZSM-5(MFI) [30, 31, 32], which was synthesised using TPA. As well as giving a number of new topologies, the inclusion of the template gave zeolites with

Organic SDA	Zeolite
Me_6-diquat-3	NON, ZSM-48, FER
Me_6-diquat-4	ZSM-12, FER
Me_6-diquat-5	EU-1, ZSM-12, ZSM-48, Mordenite, MCM-22
Me_6-diquat-6	EU-1, Mordenite, Analcime, ZSM-48
Me_6-diquat-7	EU-1, ZSM-23
Me_6-diquat-8	ZSM-5, ZSM-48
Me_6-diquat-9	ZSM-5, ZSM-48
Me_6-diquat-10	ZSM-48, Mordenite

Table 2.1: List of zeolites made using Me_6-diquat-n series with $n = 3 - 10$ [39].

much higher silicon to aluminium ratios. The first high silica zeolite was zeolite beta (*BEA) [33] synthesised using TEA, closely followed by ZSM-11 (MEL) [34] using TPA and ZSM-5. Indeed, both ZSM-5 and ZSM-11 have since been synthesised in purely siliceous forms, silicalite-1 (MFI) [35] and silicalite-2 (MEL) [36].

2.3.2 Diquaternary Ammonium Cations

The discussion so far has been related to singly charged organic cations. Doubly charged, or diquaternary cations, were first used in the mid-80s, with EU-1 (EUO) [37] formed with hexamethonium ($(CH_3)_3N^+(CH_2)_6N^+(CH_3)_3$) as the template. After this initial discovery, a number of new zeolites were discovered using relatively simple diquaternary ammonium cations. NU-87 (NES) was synthesised using decamethonium ($(CH_3)_3N^+(CH_2)_{10}N^+(CH_3)_3$) as the template and was the first new multidimensional high-silica zeolite to be made for nearly 20 years [38]. Following on from this work a number of systematic studies were carried out on diquaternary ammonium cations. Lee *et al.* studied the methyl series $(CH_3)_3N^+(CH_2)_nN^+(CH_3)_3$ (abbreviated here to Me_6-diquat-n) with $n = 3-10$ [39]. The results from this work highlight how complex the synthesis is.

From Table 2.1 we can see that a large number of different zeolites are made by each template. However, there are some which occur more often. It also seems that Me_6-diquat-5 is 'special' in some way as five different zeolites are made with this template.

The ethyl diquaternary ammonium cation series, abbreviated here to Et_6-diquat-n, $(CH_3CH_2)_3N^+(CH_2)_nN^+(CH_3CH_2)_3$ with $n = 3 - 10$ was also studied by the same group [40]. They once again find that there is a wide range of zeolite products formed, with $n = 5$ yielding five structures (ZSM-57 (MFS), P1 (GIS), SSZ-16 (AFX), SUZ-4 (SZR) and Mordenite (MOR)). Of particular interest in this series is

Organic SDA	Zeolite
Et_6-diquat-3	ZSM-5, Mordenite
Et_6-diquat-4	Mordenite, ZSM-5, Analcime
Et_6-diquat-5	ZSM-57, P1, SSZ-16, Mordenite, SUZ-4
Et_6-diquat-6	Mordenite, ZSM-5
Et_6-diquat-7	ZSM-5, Mordenite
Et_6-diquat-8	ZSM-5, Mordenite
Et_6-diquat-9	ZSM-5, Mordenite
Et_6-diquat-10	ZSM-5, Mordenite

Table 2.2: List of zeolites made using Et_6-diquat-n series with $n = 3 - 10$ [40].

ZSM-57 (MFS) as currently Et_6-diquat-5 is the only known template for this zeolite. As well as requiring this template, there is also a narrow range of conditions which give this zeolite, a SiO_2/Al_2O_3 ratio of 60 and a $NaOH/SiO_2$ ratio of 0.60. Varying these even slightly gave a different zeolite, as did changing the inorganic cation. ZSM-57 forms best, in terms of purity and yield, with sodium, although it was found as a minor product when lithium was used. As well as carrying out X-ray diffraction (XRD) in order to determine the crystal structures of the products, further spectroscopic techniques were used in order to gain an understanding of where the template (if at all) was incorporated in the zeolite. The TGA/DTA (thermogravimetric analysis/differential thermal analysis) show that Et_6-diquat-5 is incorporated into the framework. Raman and $^1H-^{13}C$ CP MAS NMR (cross polarised magic angle spinning nuclear magnetic resonance) show very different chemical environments from the solution spectrum. This suggests the template is in a very different conformation in the zeolite than in solution.

A few years before the work of Lee *et al.* another study of the conformations adopted by Et_6-diquat-5, this time in zeolite P1, ZSM-57 and SUZ-4 was carried out using NMR [41]. This work proposed a strong link between the conformation of Et_6-diquat-5 and the eventual zeolite formed. In the case of SUZ-4 there are two signals for the methyl groups, and it was proposed that like TPA in ZSM-5 [42] these are due to four ethyl groups lying down the 8 MR (member ring) channel, and two along the 10 MR channel. However, in ZSM-57 there is no splitting of the methyl signals and it is inferred that this is because the intersection in ZSM-57 is larger than that of SUZ-4. In the case of P1 the Et_6-diquat-5 is so tightly bound inside the framework that the methyl groups in the chain, and those on the ethyl groups are indistinguishable so a broad signal is observed in the NMR spectrum. ZSM-57 gives just one methyl signal which is almost the same as that for solution phase Et_6-diquat-5.

2.3.3 Large Pore Zeolites

As well as the relatively flexible diquaternary ammonium cations discussed in detail so far, a number of rigid molecules have also been trialled. Corma, ExxonMobil and Chevron amongst others use high-throughput [43] techniques to study a wide range of compositions, thus increasing the chances of a particular template making a new zeolite. The aim has been to make zeolites containing "large" pores, defined as containing channels with greater than 12 MR using templates formed of a number of fused rings. The first of these[1] was UTD-1 (DON) which is a one-dimensional zeolite with a 14 MR channel [46]. UTD-1 was synthesised with the organometallic bis−(pentamethyl−cyclopentadienyl)−cobalt(III)hydroxide, which is a relatively unusual template [47]. Soon after UTD-1 followed CIT-5 (CFI) [48], which is also a one-dimensional zeolite with a 14 MR channel. However, this was synthesised with N–methylsparteinium, a more conventional quaternary ammonium compound. Over the next few years several other large pore zeolites were discovered: SSZ-53(SFH), SSZ-59(SFN) [49], OSB-1(OSO) [50] and the 18 MR channel zeolite ECR-34(ETR) [51], however, they are all one-dimensional zeolites.

The first multidimensional large pore zeolite was synthesised by Corma *et al.* in 2006. ITQ-15(UTL) has intersecting 14 MR and 12 MR channels, and is synthesised using 1,3,3-trimethyl-6-azonium-tricyclo-[3.2.1.46,6]dodecane hydroxide, a large rigid multi-ring organic compound [52]. However, this zeolite can only be formed with germanium, which is required to form the D4Rs. Recently, the size of the channel has been expanded by Corma *et al.* in the three-dimensional zeolite ITQ-33 which has intersecting 10 MR and 18 MR channels [53]. Interestingly this zeolite is made with the relatively small template Me_6-diquat-6 which was discussed in section 2.3.2. In 2009 Corma *et al.* synthesised the silicogermanate ITQ-37 (ITV) which has 30 MR channels [8]. Although ITQ-37 has the largest channels of any currently known zeolite, it is not the least dense framework. A year later Corma *et al.* synthesised ITQ-40 which has a three-dimensional 16 x 15 x 15 MR channel network. Although these channels are not larger than those found in ITQ-37, ITQ-40 (OSO) has a lower framework density at 10.1 T/1000 Å^3 (compared to 10.3 T/1,000 Å^3 for ITQ-37) [54]. Both ITQ-37 and ITQ-40 were the first observed structures to contain 3 MR, but since ITQ-40 is a germanosilicate it is not technically a zeolite which is also the case with ITQ-37. The drive now is to synthesise these materials as aluminosilicates.

[1]This relates to the first large pore aluminosilicate. Large pore aluminophosphates had been synthesised a few years previously. See references [44, 45] for examples.

2.3.4 Other Template Types

So far the discussion has focused on ammonium cation templates which are the most common. However, a wide variety of organic molecules have also been tested with varying success. A number are now highlighted.

2.3.4.1 Phosphorus Based Templates

In the last few years tetraalkylphosphonium (TAP) cations have been used in zeolite synthesis. TAP cations have the advantage of not being susceptible (as with ammonium cations) to degradation via a Hoffman mechanism and being more thermally stable. Thus more severe crystallisation conditions are accessible when using TAP cations [55]. ITQ-27 was the first new zeolite to be synthesised using a TAP cation [55], which is a two-dimensional zeolite with intersecting 12 MR channels, but the channels are connected by 14 MR windows. ITQ-27 has also been synthesised as an aluminosilicate. TAP cations have lead to a number of new zeolite structures in the last few years, ITQ-26(IWS) [56], ITQ-34 (ITR) [57], and recently a phosphazene based template was used in the first synthesis of the naturally occurring zeolite Boggsite (BOG) [58]. Clearly, this is a growing area of zeolite synthesis and is sure to produce further new zeolites in the future.

2.3.4.2 Macrocycles

Until relatively recently macrocycles have not been used much in zeolite synthesis. However, they do possess some of the useful properties which make an effective template [59]. The first macrocycles to be used in zeolite synthesis were crown ethers. A crown ether is a heterocyclic compound containing repeating alkoxide units. The most common is ethylene oxide $-CH_2CH_2O-$ which forms compounds such as 18-crown-6. In 1990 Delprato *et al.* used a variety of crown ethers as the template in the synthesis of zeolite Y. They were able to improve the crystallinity and increase the Si/Al ratio from about 3 to 5. When using 15-crown-5 as the template, the cubic polymorph of zeolite Y (FAU) is formed whilst 18-crown-6 gives the hexagonal polymorph (EMT) [60]. It is thought that the crown ethers complex with the sodium cations, and then these are incorporated into the framework. EMT has slightly larger pores and so this is why the larger 18-crown-6 templates this structure. The increase in Si/Al ratio is thought to occur due to the sodium crown ether complex reducing the dissolution of alumina [61].

18-crown-6 has also been used to prepare high-silica versions of zeolite Rho(RHO) [62] and ZK-5(KFI) [63]. Whilst both these zeolites can be prepared without the

use of a template, when 18-crown-6 is used the Si/Al ratio increases from 3 to 4.9 in the case of RHO and from 3 to 4 in the case of KFI. As well as increasing the Si/Al ratio the presence of the crown ethers appear to stabilise the zeolite. RHO synthesised in the absence of crown ether undergoes a reverseable phase transition when heated: not the case for RHO synthesised with crown ether. As with zeolite Y, the crystallinity of the zeolite is also improved when using crown ethers, suggesting it is assisting either at the crystal growth stage, or in stabilising the final structure.

MCM-61(MSO) is a novel zeolite that was synthesised using 18-crown-6 as the template [64]. Although the pore volume is inaccessible, this zeolite contains some unusual structural features, comprising solely of 4 MR and 6 MR. These join together to form a large cage which is a similar size and shape to 18-crown-6, suggesting that the crown ether has a strong templating role.

As well as crown ethers, other macrocycles have been used in zeolite syntheses. Replacing some of the oxygens in crown ethers give oxa-aza macrocycles such as kryptofix 22 (1,7,10,16-tetraoxa-4,13-diazacyclooctadecane). Alternatively, all the oxygens can be replaced giving aza macrocycles which are similar to amine-based templates which have already been discussed in great detail in sections 2.3.1, 2.3.2 and 2.3.3. Aza macrocycles have lead to some new frameworks which are STA-6 (SAS) [65] and STA-7 (SAV) [66] both of which are metal aluminophosphates, where the metal is a divalent cation such as cobalt, zinc or magnesium. Generally, macrocycles have had limited success in templating novel zeolite frameworks, but as with phosphonium cations, there has been relatively little synthetic work carried out.

2.3.5 Seed Assisted and Template Free Synthesis

Ideally zeolites would be synthesised without templates. The template is often the most expensive component in the synthesis and once the zeolite has formed the template must be removed for it to be useful. This is achieved by a process called calcination, where the zeolite is heated in an oxygen flow, leading essentially to combustion of the template. Of course, the first synthetic zeolites were made without templates but these were low silica and so not selective catalysts. For these reasons there is a drive to remove the template from synthesis, thus making zeolites which have shown good catalytic activity, but currently require expensive templates, commercially feasible. An alternative to using a template is to include seeds in the synthesis. A seed is a small amount of the target zeolite which is added to the initial gel, with the aim of encouraging (in some ways analogous to the role of the template) the formation of that zeolite. Since only small amounts of the seed are

required, these can be synthesised using the expensive template.

ZSM-5 was the first zeolite that, although initially discovered via a templated synthesis, was then made in a template-free synthesis [67]; although much of the work was published in the patent literature [68]. From work published by Shiralkar and Clearfield [67], making ZSM-5 in the absence of an organic template is relatively straightforward. As ZSM-5 is like any other sodium zeolite (zeolite A or zeolite X [2]) it just requires the correct sodium-to-silica ratio.

More recently, Song *et al.* have synthesised ECR-1 (EON) in the absence of a template [69]. They note that ECR-1 is similar to Mordenite, and that it had previously been made as a gallosilicate (TNU-7) [70] without a template. In forming the gallosilicate there appears to be a strong link between the Na_2O/SiO_2 ratio suggesting that this plays an important role in the synthesis of ECR-1 [69]. Over the following few years a number of industrially important zeolites were synthesised in the absence of an organic template, such as ZSM-34 [71, 72] an intergrowth of offretite and erionite, RUB-13 (RTH) [73] and ZSM-12 (MTW) [74].

Kamimura *et al.* studied seed assisted zeolite beta synthesis. By including zeolite beta seeds they were able to synthesise zeolite beta over a wide range of compositions [75]. Analysis of the amorphous aluminosilicate by ^{23}Na and ^{27}Al MAS NMR and XRD showed that the seeds induced no change in the amorphous structure. When the beta seeds are added part way through the synthesis new beta crystals are seen to crystallise around existing beta crystals, and so the seeds are providing a surface for nucleation. They also note that when seeds are not included, mordenite is the zeolite obtained and so to understand this they analysed these zeolites to find common structural features. These two zeolites, along with ferrierite which is also obtained from the same composition [76], have 5 MR and 12 MR in common. These structural features are also common to the building units in the frameworks and so it is hoped that this will allow the synthesis of other pentasil zeolites [77].

2.3.6 Role of the Organic Template

Discussion so far has focused on the types of template which are used to synthesise zeolites. Some broad links have been discussed, for example the case of Et_6-diquat-5, but so far what exactly happens on the molecular level in the synthesis is not well understood. This is an area in which computational methods have seen great success as it is possible to follow species on the molecular level which for the most part is not possible with experimental techniques.

The most successful monocationic templates have C/N ratios of between 10 and 14 [78]. In order for a template to be used in synthesis purely from a practical

point of view, it must not degrade at high temperatures and pressures as found in an autoclave. It must also not degrade via Hofmann elimination reactions that are favoured by the highly alkaline conditions used in synthesis [79]. Along with practical considerations, the template should also have strong non-bonded interactions with the framework. These will of course be a function of how tight the fit is within the framework and have been studied extensively by computational methods which will be discussed later in this section and in section 2.4.3.1. Gies and Marler [80] established a series of conditions that an organic molecule should satisfy in order to be a successful template for clathrasils:

1. The molecule must be stable under synthesis conditions.
2. The molecule should fit in the desired cage.
3. The molecule should form as many van der Waals contacts as possible with the inner surface.
4. The molecule should only have weak a tendency to form complexes with the solvent.
5. The molecule should be rigid as they will tend to form clathrasils more easily than flexible molecules.
6. The tendency to form a clathrasil will increase with the increase in basicity or polarisability.

Gies and Marler use the terms 'host' and 'guest' to describe the framework and template respectively. Clearly, some of these conclusions could be considered as intuitive such as the fact the molecule must be stable under synthesis conditions. However, others are far harder to measure, for example the relationship between the ability to form a clathrasil and the template's flexibility.

One of the easiest of these criteria to study is location and template fit, using X-ray diffraction methods to determine the location of the template within the zeolite framework. The first of these studies by Price *et al.* determined from XRD that the TPA in ZSM-5 sits at the tetrahedral channel intersection, but also noted that the separation between the one propyl limb and the next limb from the TPA in the neighbouring intersection is only $\sim$3 Å and so it is not possible to accommodate TBA [81, 82]. A combined TGA and mass spectrometry (MS) study by Parker *et al.* showed that there are two unique TPA sites in ZSM-5 [83]. One is associated with an acid site, balancing the charge from Al, and the other is not associated to an acid site. These sites were differentiated by the greater thermal stability of

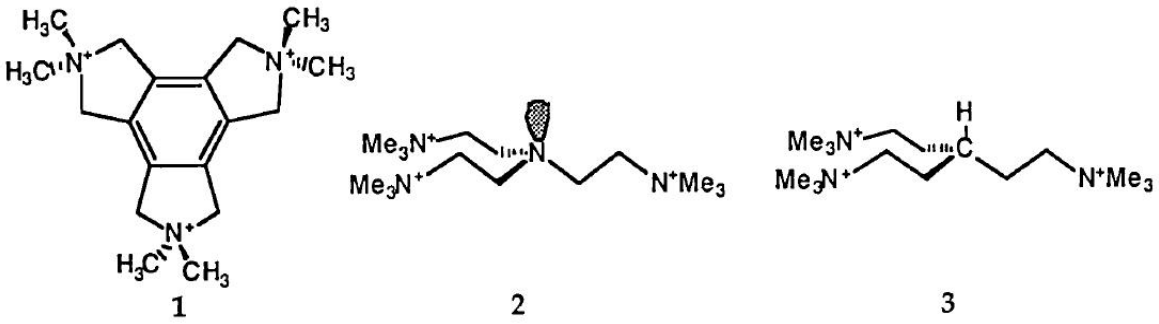

Figure 2.1: **1**: The original ZSM-18 template. **2** and **3**: Templates designed by modelling studies. Reprinted from reference [86], Copyright (1994), with permission from Elsevier.

TPA confined in the acid site which therefore decomposes at a higher temperature. They also note that the number of TPA occluded within the framework varies with alumina content.

Since these early studies, more detailed work has been carried out, for example the XRD study by van Koningsveld [84] and this has given theoretical chemists experimental data which can be used to validate their models. Some of the earliest theoretical work related to TMA occluded in the sodalite β-cage [85]. Here interatomic potentials were used to study the fit of TMA within the β-cage. It was found that there is considerable mobility of TMA within the cage. As well as using theoretical methods, the results were compared to NMR data, which also show similar results. It is this agreement between spectroscopic and computational results that showed that this kind of method can provide useful insights. The ability of the TMA to move rapidly within the cage means that it may not stabilise the zeolite as much as previously thought. The authors note that it this raises questions over the classic "hand in glove" idea of a template which fits tightly inside a pore.

The idea that if a template fits within the pore space then it will be a good structure director was tested by Schmitt and Kennedy with the synthesis of ZSM-18 (MEI) [86]. ZSM-18 had previously only been prepared with a triquaternary ammonium compound 2,3,4,5,6,7,8,9-octahydro-2,2,5,5,8,8-hexamethyl-lH-benzo[1,2-c:3,4-c':5,6-c"]tripyrrolium. Using molecular modelling they were able to narrow down twenty templates to just two (shown in Figure 2.1) based on van der Waals interactions with the framework. When templates **2** and **3** were used in synthesis, template **2** produced ZSM-18, but template **3** only yielded ZSM-18 when seeded. The modelling to a certain extent predicted this as template **3** was found to have a poorer fit than the original template due to the central carbon being tetrahedral and so making the molecule less flat.

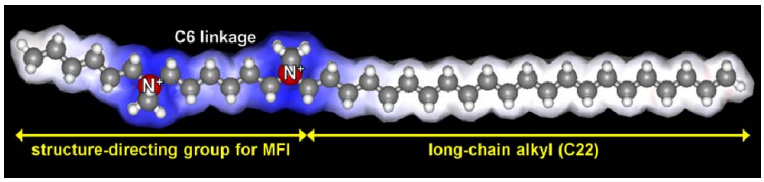

Figure 2.2: Surfactant molecule used to make MFI thin films. Reprinted by permission from Macmillan Publishers Ltd: Nature (reference [87]), copyright (2009).

Perhaps one of the best examples of an organic template molecule performing a templating role has been the work of Ryoo *et al.* making monolayers of zeolite [87]. Here Ryoo *et al.* use functionalised surfactant molecules to synthesise monolayers of MFI. The theory being that the head portion of the molecule directs the formation of MFI (see Figure 2.2), whilst the tail separates the layers. This led to 2 nm thick layers of MFI i.e. one unit cell thick, separated by a surfactant micelle layer 2.8 nm thick. The template portion of the molecule resides in the straight channel, with one ammonium group at the intersection, and the other at the channel entrance. Along with being interesting structures, the catalytic activity of these zeolite monolayers material has been measured and shown to be dramatically better than its conventional counterpart.

Another way to think about the role of the template is to consider the phase space of the synthesis. In theory if each variable is optimised, i.e. concentrations of reactants, temperature, duration etc, then it should be possible to synthesise the zeolite without a template, as is the case with ZSM-5. But including the template we expand the phase space where a particular zeolite will form, as is illustrated in Figure 2.3. In this case we plot concentration of SiO_2 against concentration of NaOH, (we could of course consider any variable) and by altering the concentrations of both we expand the range of points where the zeolite forms.

2.3.6.1 Role of Fluoride

The first use of fluoride in zeolite synthesis was reported by Flanigen and Patton in 1978 [88]. However, it was not until some years later in the work of Camblor *et al.* that it was shown how useful including fluoride in synthesis can be [89]. Camblor and co-workers used gels with F^- anions to synthesise zeolite beta with a wide range of Si/Al ratios. Fluoride has been shown to act as a structure director for D4Rs [90]. This has been supported by theoretical calculations by George and Catlow where they show that although the fluoride is not essential to form the D4R, it does stabilise the structure [91].

As well as a structure directing role, fluoride also has been shown to stabilise

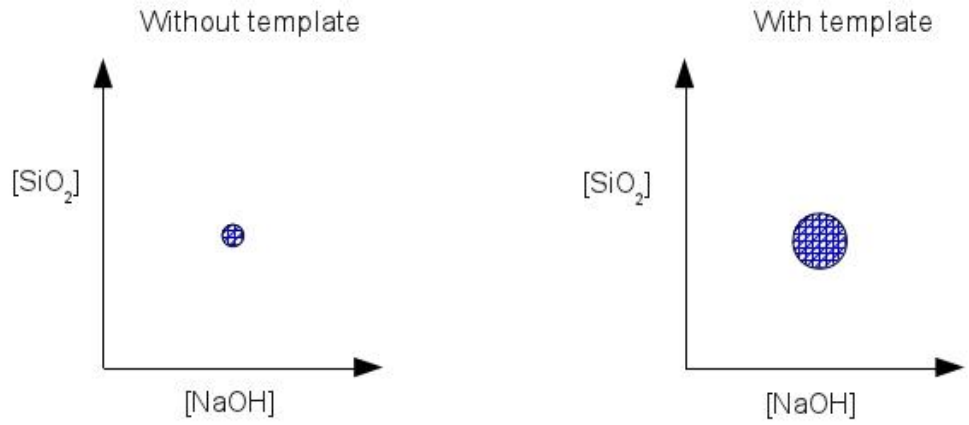

Figure 2.3: We can think of the template expanding the phase space where a zeolite (hatched circle) will form. Without a template the reaction conditions must be exactly correct. With a template, the phase space where a particular zeolite forms is expanded making it easier to form that zeolite. Although here the concentrations of NaOH and SiO_2 are plotted, we could of course consider any variable.

other building units via electron density transfer into Si atoms. This occurs through a pentacoordinated complex [92], and is stabilised by coordination to the positively charged template. Of course there are drawbacks to using fluoride in synthesis, mostly due to handling HF, which is highly toxic.

2.3.6.2 Role of Germanium

New-large pore silicates tend to be germanosilicates, for example the recent ITQ-40 [54] and usually contain D4Rs. This also became apparent in germanates such as those synthesised by Li *et al.* [93], and Conradsson *et al.* [94]. In a siliceous structure the Si−O−Si bond angle is around 148°. When in a silica D4R, the angle is much smaller due to the Si−Si−Si needing to be 90°. On average Ge−O−Ge and Si−O−Ge angles are smaller and so germanium is more easily incorporated into a D4R.

Computational work by Blasco *et al.* showed that including germanium into the D4R stabilises the structure [95, 96]. This is reflected in the faster synthesis of ITQ-7 (ISV) which is an all-silica zeolite containing D4Rs. When including germanium in the synthesis the reaction time drops from seven days to just one [97]. It is for this reason that including germanium in zeolite synthesis has led to less dense structures as it is more easily able to form 3R and 4R which are required for low density frameworks. However, from a commercial point of view, germanium is undesirable as it is significantly more expensive than silica or alumina. Moreover, germanium

containing zeolites tend to be less thermally stable, although only at Si/Ge ratios below 20. At ratios above 20, it is possible to recover the germanium via post-synthesis treatments [98].

2.3.7 Hypothetical Frameworks

Early work on structure prediction was carried out by Breck [99]. He predicted the existence of a polytype of the FAU framework which he named "Breck structure 6" [99]. This structure was later synthesised by Delprato *et al.* and is known as EMT [60].

More recently, there has been much progress in the prediction of hypothetical zeolite frameworks. This has largely been due to the use of computational methods and a number of groups have generated millions of hypothetical structures. Deem and Earl used a simulated annealing method to search through the 230 crystal space groups and generate hypothetical structures by adding Si atoms to an empty unit cell. A number of factors were explored such as unit cell dimensions, density of T-atoms, and number of unique T-sites [100]. Using this, they were able to generate 3.3 million hypothetical frameworks [101]. Once generated the structures were optimised using interatomic potentials and their stability compared relative to quartz. This yielded 1,120 structures that were lower or within +30 kJ mol^{-1} Si in energy of quartz, and a overall database size 2.2 million structures. The authors note that when using a different set of interatomic potentials, the figure drops from 1,120 to just 81, but they do believe that these are not artefacts (some structures had overlapping shells causing the energy to be lower than expected) and are viable synthetic targets. The database contains 2.2 million structures overall. When comparing the number of known topologies [4] to even just the number with energies less than quartz (1,120) only a fraction of what is theoretically possible have been made synthetically.

Another database of hypothetical frameworks has been designed by Klinowski *et al.*, this time using a tiling method [102]. This has the advantage that it is systematic rather than random as is the case with the Monte Carlo method of Deem and Earl. As with the hypothetical frameworks of Deem and Earl, Klinowski *et al.* also compare the energies of their frameworks to quartz [103, 104], and arrive at a similar number of frameworks that are chemically feasible. Later these frameworks were tested for potential use as catalysts using a feasibility factor. The feasibility factor was first determined by plotting the framework energy of the known zeolites (176 at the time) against framework density. The feasibility factor is then just the distance the hypothetical framework falls from the line of best fit through the data

points of these known frameworks [105].

Other groups have also generated databases of hypothetical frameworks. Treacy *et al.* have developed an online database [106] with over 5 million structures. However, many are high in energy, or contain 3 MR. Treacy uses a symmetry constrained bond searching method to generate the structures [107, 108]. Treacy also proposed a flexibility criteria for zeolites and postulate that an ideal zeolite should be "stress free" [109]. Another database of hypothetical frameworks by Li *et al.* where they define a forbidden zone where framework atoms are not allowed to exist, and so are able to generate frameworks with specific pore geometries [110].

We can see there has been a great deal of research carried out on hypothetical frameworks, and millions have been identified. Currently the databases of hypothetical structures only provide information to aid structure determination of newly synthesised zeolites as unit cell dimensions, and powder patterns can be generated from the theoretical data. However, the aim is to be able to generate a structure and then be able to synthesise it.

2.4 Zeolite Nucleation

2.4.1 Introduction

This section focuses how zeolites form on a chemical level. Starting from sources of silica and alumina and reacting to form networks and eventually zeolite frameworks. There has been much controversy over the exact processes which occur and a number of theories have been proposed.

2.4.2 Prenucleation

During the prenucleation stage, the synthesis gel moves towards supersaturation, as larger solution species form. This stage continues until nucleation when crystalline products are detected. The silica and alumina sources are dissolved and Si-O and Al-O bonds are broken. Condensation reactions then occur to form small silicate species known as zeolite precursors:

$$(OH)_3Si{-}O{-}H + H{-}O{-}Si(OH)_3 \rightleftharpoons (OH)_3Si{-}O{-}Si(OH)_3 + H_2O$$

and with alumina:

$$[(OH)_3Al{-}O{-}H]^- + H{-}O{-}Si(OH)_3 \rightleftharpoons [(OH)_3Al{-}O{-}Si(OH)_3]^- + H_2O.$$

In a typical zeolite synthesis there is a high concentration of OH^- from mineralisers such as NaOH or KOH and so it would be expected that the reaction mechanism would be ionic:

$$(OH)_3Si{-}O^- + H{-}O{-}Si(OH)_3 \rightleftharpoons (OH)_3Si{-}O{-}Si(OH)_2O^- + H_2O$$

and with alumina

$$(OH)_3Si{-}O^- + [(OH)_3Al{-}O{-}H]^- \rightleftharpoons [(OH)_3Al{-}O{-}Si(OH)_2O^-]^- + H_2O.$$

Although the condensation reactions are straightforward, there is much controversy over the species present in the synthesis mixture. There are both kinetic and thermodynamic factors which affect the precursor species that are present. These factors will in turn depend on the synthesis conditions and these may not be the same throughout the synthesis. An understanding of the precursor species will, however, give an insight into zeolite growth mechanisms. There now follows a discussion of some of the early work carried out in order to understand the prenucleation stage.

Barrer *et al* [24] proposed that the growth of zeolites was solution mediated. Barrer suggested that secondary building units in the form of small tetrahedra or polyhedra link together to form the zeolite crystal. From this two different mechanisms were proposed. Firstly, that the zeolite grew by the condensation of these small precursor species from solution and second that an amorphous solid formed first which then becomes more ordered through dissolution and transport processes. The second of these processes is now generally accepted to be the mechanism of growth.

Building on the early work of Barrer, Breck and Flanigen used X-ray diffraction (XRD) to study the crystallisation of zeolite A [25]. They concluded that initially there is extensive heterogeneous nucleation to form a highly supersaturated gel. The nuclei that are formed are not all zeolite-like, but instead are like those described by Barrer [24]. These nuclei then develop until reaching a critical size where there is rapid formation of small uniformly sized crystals. This occurs before crystal growth which proceeds through polymerisation and depolymerisation processes catalysed by OH^-. This mechanism involves both the solid and liquid phases.

In 1966, Kerr [111] carried out an experiment where sodium hydroxide was circulated round an apparatus containing two filters (see Figure 2.4), one with amorphous aluminosilicate and the other with crystalline zeolite A. Once the experiment was complete, the mass of zeolite A crystal had doubled and nearly all the amorphous aluminosilicate had been dissolved. This led to the conclusion that the process occurs via the amorphous material dissolving to form active species which then

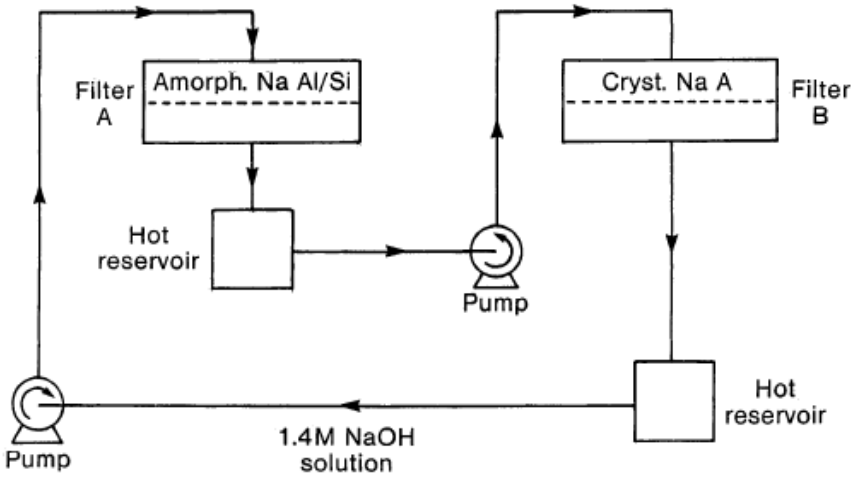

Figure 2.4: Schematic diagram of the apparatus used by Kerr. Reprinted with permission from ([2]). Copyright (2003) American Chemical Society.

nucleated on the zeolite A crystal, essentially providing evidence for the first mechanism described above. Some years later, Kerr stressed that this may not be the only mechanism involved in the formation of zeolites [112].

The discussion so far has focused on using simple experiments to infer what may be happening in the solution. In recent years multiple characterisation techniques have been used to analyse the sample. Ideally these are carried out *in situ* to follow the reaction as it proceeds. The most common technique is ^{29}Si NMR spectroscopy which can be used to obtain structural information by measuring the chemical shift. The chemical shift varies due to changes in the nuclear magnetic resonance frequency caused by the local geometry of nuclear spins. Much of the work has focused on the silicalite-1(MFI) system which is synthesised from dilute solutions containing TPA. The first of these experiments was by Harris *et al.* [113] who used ^{29}Si NMR to analyse the structure of precursors present in solution. They were able to assign signals to species containing up to 6 silicon atoms. This is a complex process especially if the silicon is not enriched with ^{29}Si. Subsequent extensive work by Kinrade and Knight [114, 115, 116, 117] which culminated in the identification of 48 distinct silicate oligomers (see Figure 2.5) present in solution. From this it was determined that the most likely silicate precursors to zeolites are D3Rs and D4Rs. The work of Kinrade and Knight also contradicted some previous results by Kirschhock *et al.* in which they proposed the existence of 'nanoslabs' in solution which have the MFI structure and aggregate to form the zeolite [118].

As well as NMR spectroscopy, ESI-MS (Electron Spray Ionisation-Mass Spectrometry) has also proved a useful tool to elucidate precursor species. This technique

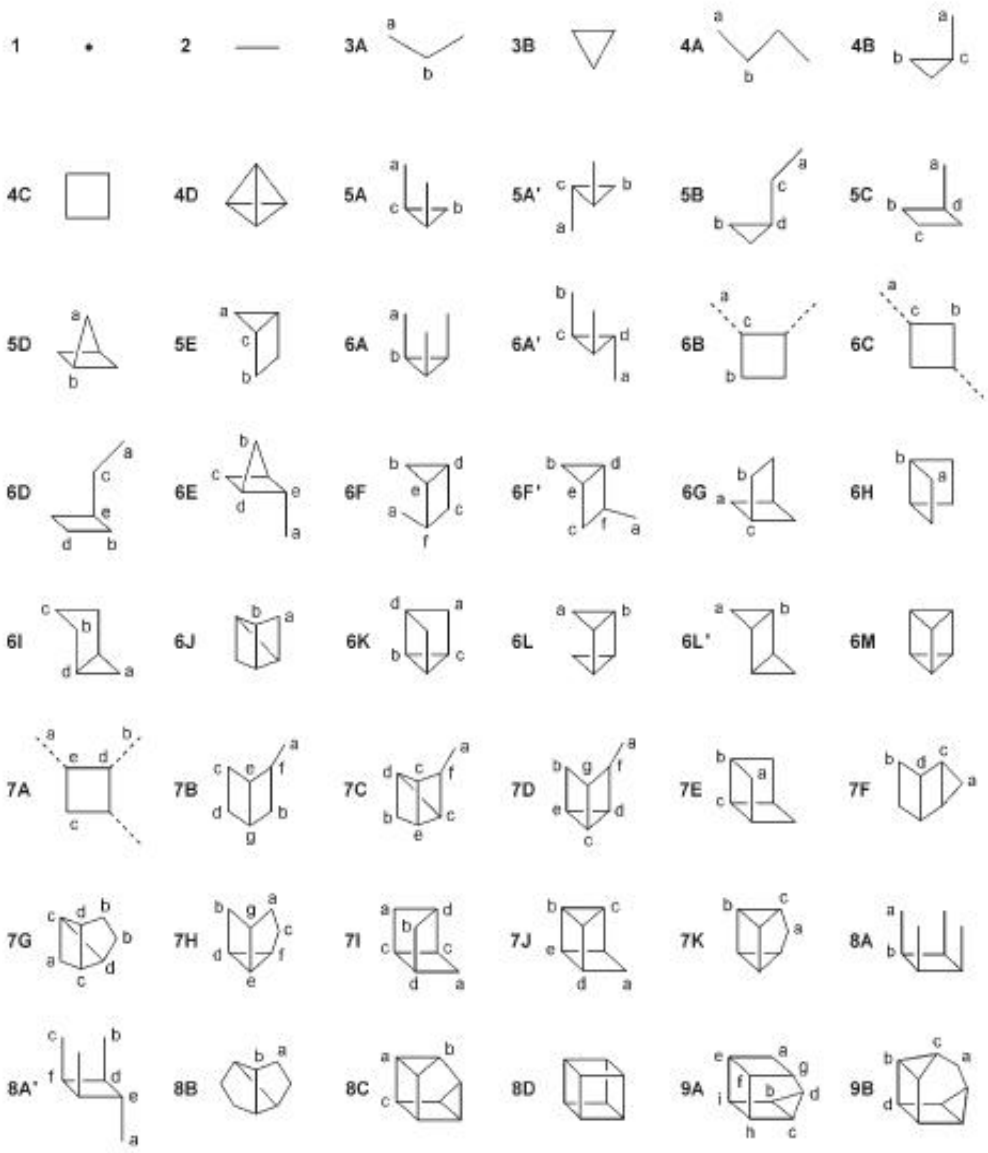

Figure 2.5: Aqueous silicate structures identified by Kinrade and Knight by ^{29}Si COSY NMR spectroscopy. Each solid line represents a Si−O−Si link and dashed lines represent $OHSi(OH)_3$ units. Reprinted with permission from ([117]). Copyright (2007) John Wiley and Sons.

works by first ionising the precursors before passing them through a charged field to calculate the mass to charge ratio (m/z). The main drawback of ESI-MS over NMR spectroscopy is that it provides less structural information. However, it is possible to study the time evolution of species. ESI-MS has been used with great success by the group of Schüth [119, 120, 121, 122, 123, 124]. Initially, the species present are monomers, dimers and D3Rs. With time, these grow to form larger species, and by the end the solution contains almost exclusively D4Rs. Although larger species were detected, none were in the range proposed by Kirschhock *et al.* , and the results of Schüth *et al.* are in good agreement with those of Kinrade and Knight. By isotopic labelling of silicates a mechanism for the interconversion of D3Rs and D4Rs was found. The study showed that rather than happening by a single substitution mechanism, it was in fact concerted between two units, realising two single rings. As well as studying pure silicate systems, Schüth *et al.* also studied a germanosilicate system [125, 126, 127], namely ITQ-21 [128]. By combining ESI-MS with MS/MS it was possible to determine the structure of the germanosilicate species. It was found that the oligomers present in the solution have zeolite-like structural characteristics, for example, a D4R connected by a bridge to a S4R. So far these techniques have not solved the problem of zeolite nucleation, but they are providing important clues to the mechanisms and building units that exist in solution which will go on to form the zeolite crystal. The idea of building units has been far more successful in aluminophosphate chemistry [129] where there appears to be a more distinct path, starting from precursor nucleation building units (PNUBUs) which then go on to form the SBUs and finally link together to form the framework [130]. As already discussed, however, the picture for (alumino)silicates seems to be far more complex.

2.4.3 Nucleation

The second stage in a zeolite synthesis is nucleation. Similar to the prenucleation stage, the actual mechanism is still a matter of controversy. At this stage the synthesis gel will contain amorphous silica along with a solution phase. There is continuous hydrolysis of the Si−O−Si bonds and the amorphous phase slowly becomes more ordered. Once these nanocrystals are large enough to self-propagate [2], the crystal will grow into a zeolite structure. As with prenucleation, the silicalite/TPA system is the test case for most work. de Moor *et al.* conducted a series of SAXS (small angle X-ray scattering) experiments, which uses X-rays at low angles (typically 0.1°-10°), allowing particles on the scale of nanometres to be detected. The work of de Moor *et al.* show the presence of particles ranging in size from 2.8 nm to 10 nm [131]. It is believed that the smaller 2.8 nm particles are primary units of silica around TPA,

while the 10 nm particles are simply aggregates of these smaller particles.

The template has already been discussed in great detail in previous sections, but as with the precursor species present in solution, the exact action of the template is still a point of much controversy. As with the silicate species, the study of the template and its interactions in the early stages of synthesis have proved challenging. As in the NMR and ESI-MS work, the silicalite/TPA system is the one of choice. Some of the earliest work was by Chang and Bell [132] which concluded that the nucleation of silicalite occurs in three steps:

1. the formation of clathrate-like water structure around the template,
2. isomorphic substitution of silicate for water in these cages which resemble ZSM-5 channel intersections,
3. progressive ordering of these structures into the final crystal structure.

These steps are in agreement with the mechanism proposed by Breck and Flanigen [133]. But Chang and Bell also noted that the structure around the hydration layer will be affected by other factors such as temperature, pH, inorganic cations etc. Building on this work, Burkett and Davis published possibly one of the most significant papers in the field where they use $^{1}H-^{29}Si$ CP MAS NMR spectroscopy on the same silicalite/TPA system to probe the relationship between the inorganic and organic components (see Figure 2.6) [134]. From these experiments, it was found there was a greater degree of cross-polarisation when TPA is used as the template rather than TMA. This suggests that there is a difference between the strength of interactions and proximity of the templates to the silicate species. In addition to the proton-silicon NMR spectroscopy, $^{1}H-^{13}C$ CP MAS NMR was used to gain information on the conformation of the TPA molecules. Although there is some ambiguity in the assignment of the spectra, it is thought that the TPA in solution adopts a similar conformation to that occluded in the framework. The differences between TPA and TMA were attributed to the greater hydrophobicity of TPA and so would interact more strongly with the hydrophobic silica. Burkett and Davis also proposed a modified version of the growth mechanism proposed by Chang and Bell [132] where there is diffusion of the growth species to the surface of a growing crystal. This accounts for observed intergrowths e.g. ZSM-5/ZSM-11, which must occur by a layer-by-layer growth mechanism.

Fourier transform infrared (FT-IR) spectroscopy has also been used as a tool to study the species present in solution. Jacobs *et al.* carried out FTIR spectroscopy on a number of high silica zeolites that all contain different arrangements of 5 rings [135]. Based on previous work by Flanigen *et al.* [136] they were able to assign some bands

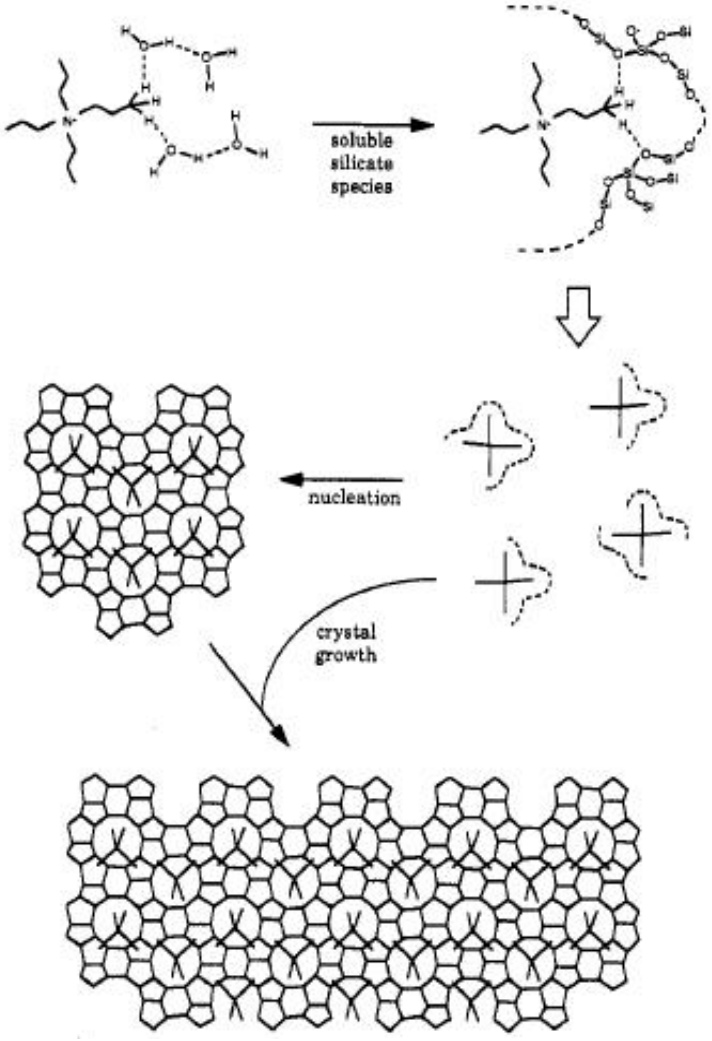

Figure 2.6: Schematic of the mechanism of structure direction proposed by Burkett and Davis. TPA silica interactions are in the upper portion of the diagram. Reprinted with permission from ([134]). Copyright (1994) American Chemical Society.

to the vibrations of internal tetrahedra, and then they noted that the remaining bands vary in intensity and this can be related to the external environment. For example, a peak at 1225 cm^{-1} can be attributed to a Si−O symmetric stretch that is unique to a zeolite containing chains of 5 member rings. With further study of the spectra obtained it was determined that a peak at 540 - 550 cm^{-1} is characteristic to D5R in MFI-type zeolites [135, 137, 138] and so this allows structures present in solutions to be identified from FT-IR. It is noted by the authors however that this peak is very similar to that found in ZSM-11 [135].

2.4.3.1 Computational Studies

Clearly, studying prenucleation and nucleation stages by experimental methods is challenging. Computational methods are ideal for these kinds of systems, and with experimental data to validate the models it is possible to expand to the systems studied. Most computational work on the prenucleation stage has focused on barriers to reactions, and on calculating exact geometries of precursors. The reader is directed to an excellent review on the subject by Catlow *et al.* [139]. Some of the earliest work used forcefield methods, Feuston and Garofalini [140] derived a new interatomic potential for silicate/water interactions that was then used to study small silicates. A few years later Hill and Sauer also derived a potential for the same interactions and used it to study larger silicate clusters [141]. However, it quickly became clear that because of the complexity of the potential energy surface due to conformational flexibility of silicates, and because these clusters are strongly affected by hydrogen bonding, that *ab initio* calculations would be a better choice for obtaining accurate conformations and properties.

In recent years, there has been increased interest in the prenucleation stages and a large amount of research has been carried out. Initial work by Trinh *et al.* focused on the mechanism of the silica oligomerisation reaction [142]. Using DFT (density functional theory) they studied both the anionic and neutral mechanisms (see Figures 2.7 and 2.8). They included solvation using the conductor-like screening model (COSMO) and studied the condensation reactions which led to the dimer, trimer, tetramer, 3MR and 4MR. The reaction mechanism for the neutral species is studied as a single step process with a concerted mechanism releasing water. The anionic mechanism on the other hand is a two step process, first forming a penta-coordinated silicon, followed by loss of water by removal of a proton by the leaving OH^- group. This is the same mechanism as proposed by Xiao *et al.* [143].

Further work by Trinh *et al.* , this time including explicit water, was done to understand the role of water in the oligomerisation reaction [144]. Using a different

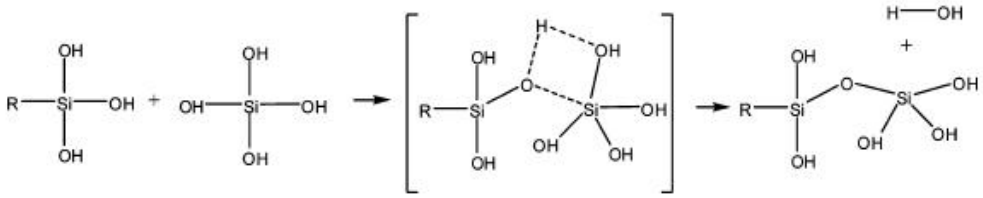

Figure 2.7: Schematic of the neutral reaction mechanism. Reprinted with permission from ([142]). Copyright (2006) American Chemical Society.

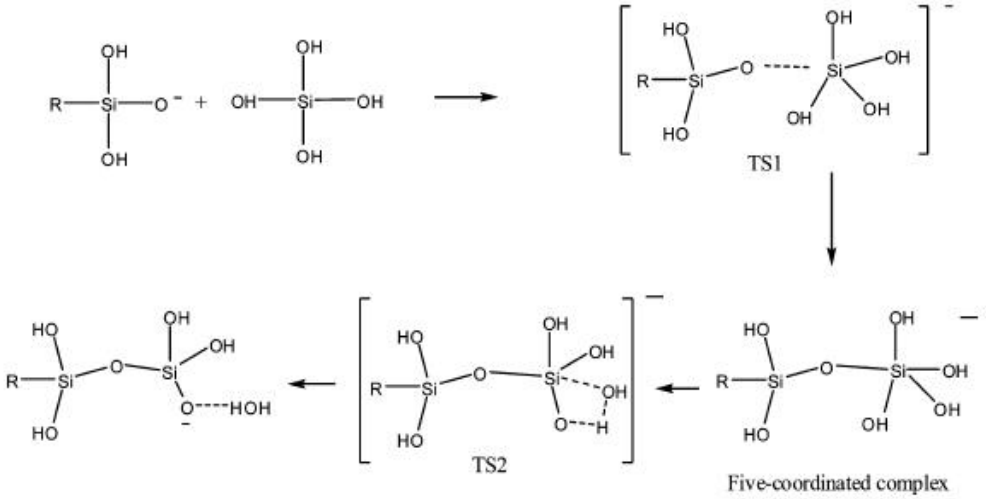

Figure 2.8: Schematic of the anionic reaction mechanism. Reprinted with permission from ([142]). Copyright (2006) American Chemical Society.

function with the Car-Parrinello [145] method of molecular dynamics, the formation of the dimer, trimer, tetramer, 3MR and 4MR was investigated but only via the preferred anionic pathway. Trinh *et al.* concluded that it is essential to include explicit water molecules in the simulation as this captures chemical properties of silica in solution better.

Mora-Fonz *et al.* studied anionic species which are the more likely species in the high pH conditions of a zeolite synthesis [146, 147] and found the 3MR is highly favourable. This then raises the question as to why these rings, until very recently, have not been seen in zeolites. However, the authors note that it is more favourable to form the tetramer from the trimer than to close the ring. When they move to a more complex system, include explicit solvation and sodium to balance the charge from the anionic silicate, they find that there is very little change in the geometry. A similar study by Schaffer and Thomson [148] examine, the neutral, anionic and acidic mechanism, finding the same pathways as previous work. They also confirmed that the barriers to the formation of small oligomers are greater, than to form larger oligomers.

2.5 Crystal Growth

Crystal growth is the final stage of a zeolite synthesis. By now there are small crystalline nuclei [79] of zeolite and there is rapid growth of the crystalline zeolite. As with the other stages of crystal growth there is still controversy over the exact growth units. It is possible that any of the units discussed so far, monomer, dimers and other primary building units right through to larger silicate oligomers may be present. We do know that the growth is typically a layer-by-layer mechanism, and is thought to be controlled by the kinetics of the reactions involved rather than by diffusion of silicate species to the surface [149].

The experimental study of crystal growth has been focused around atomic force microscopy (AFM) and more recently high resolution transmission electron microscopy (HRTEM). AFM is a relatively new technique [150] that uses a probe with a tip of atomic dimension to scan over the surface. The probe interacts with the surface and this deflects the tip. This deflection can be measured, usually by an optical technique and then the force derived form this. These techniques provide information about the surface of the zeolite crystal often to an atomic level, but they cannot provide insight into the microscopic processes occurring. The first studies on crystal growth used XRD to monitor the growth of the zeolite crystal. Kacirek *et al.* [151, 152] followed the growth of Na zeolite X and Y, and concluded

that the rate of zeolite growth is related to the degree of supersaturation. As the degree of supersaturation increases, the rate of growth increases, as there is a greater concentration of nutrients available to the growing crystal.

Since monitoring growth is difficult, much of the work has focused on monitoring dissolution as it is inferred that this can be considered as the reverse of growth. In this case the surface is first imaged via AFM, HRTEM etc., followed by a controlled dissolution of the crystal, and then re-imaging of the crystal. Although dissolution can be thought of as growth in reverse there is no firm evidence for the processes being identical. By running AFM in constant force mode, that is the force on the tip is kept constant, which is achieved by moving the tip up and down relative to the surface [153], surface features can be imaged. The first use of AFM to image a zeolite was reported by Weisenhorn *et al.* in 1990 [154] who imaged the surface of clinoptilolite and were also able to 'etch' an X into the surface by applying a force to the surface via the tip. Around the same time Gratz *et al.* studied quartz using AFM [155]. Their aim was to study the dissolution of the crystals in KOH and gain an understanding of the kinetics of the process.

Building on these early experiments, Anderson *et al.* carried out AFM experiments on zeolite Y and zeolite A [156, 157], with similar experiments by Yamamoto *et al.* on Heulandite published simultaneously [158]. These experiments confirmed by AFM the layer-by-layer growth previously proposed by Vaughan [159], and supported HRTEM experiments a few years previous by Terasaki and Alfredsson *et al.* [160, 161]. In these HRTEM experiments, on intergrowth in zeolite Y, the surface of the zeolite showed steps with heights of around 14.2 Å with this step height corresponding to the height of a complete faujasite cage, and as no other steps were found it can be inferred that the zeolite grows by forming complete faujasite layers. AFM studies by Anderson *et al.* on zeolite A also showed the same features with the steps on the surface consisting of complete sodalite cages [157]. Although these experiments confirmed the layer-by-layer growth mechanism, they still did not give information on which units are condensing onto the surface. It is quite possible that complete faujasite or sodalite cages attach to the surface, or more likely that smaller units condense to form an intermediate which then rapidly grows to the complete cage structure. Since these experiments are carried out *ex situ* only the final structures are observed, and there may be many different processes occurring throughout the crystal growth which may even change as the reaction proceeds.

The first *in situ* AFM experiments were carried out by Anderson *et al.* in 2007 [162] of the dissolution of zeolite A. They found that the dissolution first occurs with removal of the S4R capping the β-cage, in an uncorrelated manner, which precedes

the removal of the β-cages in a correlated manner by terrace retreat.

A technique which has recently been been employed to study zeolite crystal morphology is high resolution scanning electron microscopy (HRSEM). Although not a new technique, until the last few years it was not possible to achieve the highest resolution due to charge effects on the sample [163]. Recent development have allowed the use of low current and voltages to give nanometre resolution. With this kind of resolution it is possible to image the surface structure as shown by the work of Che *et al.* on SBA-15 [164], where the surface terminations on SBA-15 (a mesoporous ordered material) were determined. Recent work by Cubillas *et al.* combined AFM and HRSEM to study the growth of zeolite A [165]. They were able to follow the growth by AFM of the crystals, and subsequent HRSEM of the same crystal proved that zeolite A crystals form at the surface of the amorphous gel and that observed intergrowths occur when the crystals aggregate in the early stages of crystal growth.

2.5.1 Templates in Zeolite Crystal Growth

As well as having an effect in the early stages of the synthesis in controlling the topology, the template can also impact the final crystal morphology. This occurs due to the template altering the growth rates of some crystal surfaces and so a particular surface may grow more rapidly, hence altering the crystal morphology. Early work by Charnell on zeolite A and zeolite X showed that triethanolamine increased the crystal size of both zeolites [166]. Once again, the TPA/silicalite-1 system is often chosen for the study of the effect of templates on crystal morphology [167]. It is not just the inclusion of a template which can affect the growth, but also the concentration of the template. Romannikov *et al.* studied the effect of the concentration of TPA on the crystal size of ZSM-5 [168]. They find that increasing the concentration of TPA gives larger crystals of silicalite-1, which they propose is due to the TPA forming clathrates in the solution phase. The TPAs role in forming these clathrates both speeds up the rate of crystallisation and increases the size of the crystals. A few years later Cundy *et al.* carried out a similar study on silicalite-1 and found similar trends with respect to the concentration of TPA [169].

A landmark paper in 1993 by de Vos Burchart *et al.* included a diquat of TPA (di-TPA) in their synthesis of silicalite-1 [170]. They found this decreased the aspect ratio of the crystals. Using molecular modelling, they proposed that the di-TPA lies preferentially on the straight 10MR channel. Consequently de Vos Burchart *et al.* proposed that the effect of the template on crystal morphology can be separated as follows:

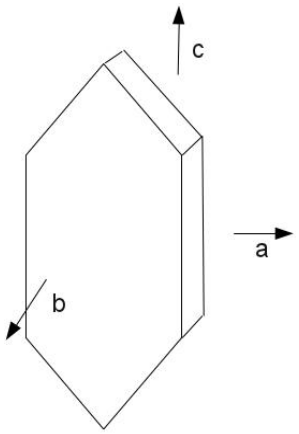

Figure 2.9: Schematic of an MFI crystal indicating the lattice directions of a standard coffin shaped MFI crystal. Reprinted with permission from ([171]). Copyright (2004) American Chemical Society.

Location effect: The template may prefer a particular location on the zeolite such as one of the surfaces.

Growth direction effect: Once the location has been chosen it may influence the crystal growth direction.

Using these two template effects they propose that there are two possible location effects. The di-TPA initially locates with one propyl group into a channel. The propyl groups on the other end can then locate in either the straight channel, or the sinusoidal channel. It was proposed that although locating the propyl groups is not a rate limiting step, when it is inside the sinusioidal channel it is less favoured and hence there is a greater rate of growth in the **b** direction (see Figure 2.9).

Building on the work of de Vos Burchart *et al.* , Bonilla *et al.* studied the effect of a number of other diquats on the crystal morphology of silicalite. They were able to make a variety of different crystal morphologies, by using templates to control growth rates along any of the axes (unlike the crystals previously seen) [171]. More recent work by Chen *et al.* has used microwave assisted synthesis (where the solvent acts as the template) and they show that it is possible to tune the aspect ratio of the crystals [172].

The discussion so far has focused on organic templates. However, it has been shown that inorganic cations also affect zeolite crystal morphology. Warzywoda and Thompson [173] carried out experiments on sodium zeolite A where a percentage of potassium was added. Initially larger crystals of zeolite A formed but once the concentration of potassium reached 20% zeolite K-F began to contaminate the product. Beyond 80% potassium zeolite A no longer formed. Clearly this indicates

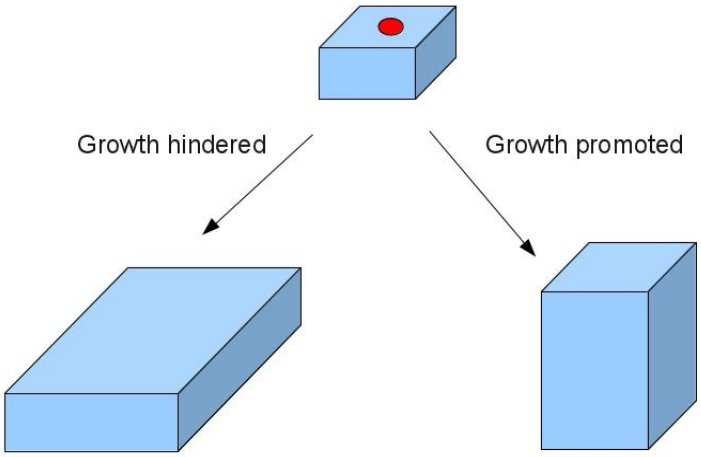

Figure 2.10: Schematic which shows the effect a template (red circle) could have on the growth of the crystal when adsorbed on the top surface.

that sodium is required for zeolite A nucleation. However, it is interesting that low concentrations of potassium changed the crystal morphology. At the same time a similar study by Camblor and Perez-Pariente, again on the role of potassium in zeolite beta, showed that crystal size increased as the concentration of potassium was increased [174].

We can summarise these findings and say that once a template has adsorbed on the surface it can either promote growth on that surface by assisting condensation, or slow its growth by sterically hindering the surface to silicate condensation (see Figure 2.10). The reader is referred to recent reviews and references within for more on the subject of template effects on crystal growth [175].

2.5.2 Computational Studies on Crystal Growth

As with other areas of zeolite growth, computer modelling provides an excellent method to gain an understanding into the crystallisation processes. The first reported atomistic calculations on zeolite surfaces were by Loades *et al.* which reproduced the crystal morphology of zeolite A [176]. Baram and Parker built upon this work by including the energetics of water dissociation to hydroxylate the surface which gave more accurate surface energies than those derived by Loades *et al.* , and matched better with experimentally derived energies [177]. More recent work by Slater *et al.* also focuses on calculating accurate surface energies [178, 179]. They studied zeolite A and zeolite β-C and were able to reproduce the surfaces observed in HRTEM. However, as with the work of Baram and Parker [177], the inclusion of a solvent is essential when calculating the surface energies.

In a combined *in situ* AFM and modelling study on Zeolite A, Anderson *et al.* found that a D4R terminated surface is most stable in hydrated conditions and so most resistant to dissolution [180]. Chiu *et al.* went deeper into the mechanisms of zeolite growth at the surface by studying the relative energies of adding different sized silicate species in dissolution simulations. It was determined that the most stable surfaces are those with the least number of dangling OH bonds [181], and it is the growth of this surface that is the rate determining step for the growth. For zeolite β-C the growth of this step is closing the 12MR channel that runs parallel to the surface. A similar study by Agger *et al.* on analcime also came to similar conclusions to the growth mechanisms of zeolites [182]. Very recent work by Gren *et al.* extensively characterises zeolite A surfaces. As well as determining surface structures, they also study the effect of water on the surface by including explicit water. They find that the structure of the water is strongly influenced by the surface terminations. For example when D4Rs are parallel to the {100} surface there is strong ordering of the water, but when they are perpendicular there is almost no ordering of the water.

CHAPTER 3

Theoretical Methods

3.1 Introduction

The vast increase in processor speed over the last few years along with the emergence of national supercomputers such as HECToR [183] has allowed the expansion of the computational sciences. Combined with the increase in computational power there are also an increasing number of programs available which allow the modelling of chemical systems and the field of computational chemistry has expanded rapidly. The aim of computational chemistry is to calculate the energy of a system as a function of its coordinates. From this a number of properties can be derived. Broadly speaking, the energy of the system can be calculated by two different methods. Molecular mechanics which ignores all electronic structure of the atoms and uses a potential function which is fitted to a particular molecular interaction and electronic structure methods which are based on quantum mechanical principles. Each method has a subset of methods some of which combine these two fundamental methods. The advantages and disadvantages of each will be discussed in this chapter.

3.2 Molecular Mechanics

As already mentioned force field or Molecular Mechanics (MM) methods ignore the motion of the electrons around an atom and instead treat the atom as a classical particle [184]. This application of the Born-Oppenheimer approximation [185] where the motion of the nuclei can be considered slow compared to the motion of

the electrons and as such only the positions of the nucleus need be considered as the motion of the electrons adapt instantly to nuclear movement. By making this approximation systems of many thousands or even millions of atoms can be considered. In MM a forcefield is utilised to model the interactions of the atoms in the system. The forcefield is broken down into intramolecular components such as bond stretches and bending and intermolecular interactions such as van der Waals (vdW) forces. A typical forcefield has the form:

$$E_{sys} = E_{elec} + E_{vdW} + E_{bond} + E_{angle} + E_{torsion} \tag{3.1}$$

where E_{sys} is the total system energy, E_{elec} is the energy contribution from electrostatic interactions, E_{vdW} is the energy contribution from vdW interactions. The final three terms are intramolecular contributions for the bond stretch (E_{bond}), angle deformation (E_{angle}) and bond torsion ($E_{torsion}$). These energies are calculated from a potential which is fitted either to experimental data or to *ab initio* models. The functional forms of the intra- and intermolecular interactions will now be discussed in greater detail.

3.2.1 Intramolecular Interactions

Intramolecular interactions are concerned with keeping the molecule in a chemically accurate structure. Generally this is achieved by applying energy penalties to deviations away from standard or equilibrium values.

The simplest method of describing the potential energy curve of a bond is Hooke's law where the energy varies with the square of the displacement from the the reference bond length.

$$E_{bond} = \frac{k}{2}(l_{ij} - l_0)^2 \tag{3.2}$$

where l_0 is the equilibrium bond length and k is the force constant for the particular bond. Generally Hooke's law is sufficient for describing bonds in chemical systems as it is unusual for them to deviate far from equilibrium. However, on occasion it is necessary to use a more complex functional form. The Morse potential is able to describe a wide range of behaviour from equilibrium to dissociation. The Morse potential has the form:

$$E_{bond}(morse) = D_e\{(1 - \exp[-a(l_{ij} - l_0)])\}^2 \tag{3.3}$$

where D_e is the the depth of the potential energy minimum and $a = \omega\sqrt{\frac{\mu}{2D_e}}$, where

μ is the reduced mass and ω is the frequency of the bond vibration. ω is related to the stretching frequency of the bond k by $\omega = \sqrt{\frac{k}{\mu}}$. Clearly this can describe the bond more accurately than the harmonic function but the extra term in the Morse potential adds computational expense.

Angle deviations from their equilibrium can also be described using Hooke's law:

$$E_{angle} = \frac{k}{2}(\theta_{ijk} - \theta_0)^2 \tag{3.4}$$

where θ_0 is the equilibrium bond angle and k is the force constant. Since less energy is required to deform an angle, than is required to stretch a bond, the force constants associated with angle deformations are far smaller.

The final type of deformation that will be discussed are the torsional terms. Not all forcefields use torsional terms (although those used within this thesis do) as often it is possible to rely on nonbonded interactions with atoms at the end of each torsion i.e. at the 1,4 positions to describe the energy profile. A common form of torsional potential is the harmonic potential:

$$E_{torsion} = \frac{k}{2}(\phi_{ijkl} - \phi_0)^2 \tag{3.5}$$

where ϕ_0 is the equilibrium dihedral angle and k is force constant for the deformation.

3.2.2 Intermolecular Interactions

Intermolecular or nonbonded interactions do not depend on a specific bonded relationship between atoms and act throughout. As already mentioned these, are broken down into two types. Electrostatic interactions are calculated using Coulomb's law:

$$V = \sum_{i=1}^{N_A} \sum_{j=1}^{N_B} \frac{q_i q_j}{4\pi\epsilon_0 r_{ij}} \tag{3.6}$$

where N_A and N_B are the numbers of point charges in each molecule, q_i and q_j are the values of the point charges, r_{ij} is the separation between the point charges and ϵ_0 is the permittivity of free space. An issue arises when using Coulomb's law in periodic systems as it may not converge. A method of overcoming this is to use the Ewald summation [186] where the charges are considered in real and reciprocal space (see Section 3.2.4).

Finally there are van der Waals (vdW) interactions. vdW forces include the

long range dispersive forces and short range repulsive forces. The long range forces result from instantaneous dipoles forming on particles which then induce a dipole in a neighbouring particle. This results in an attraction between the particles. Short range repulsive forces arise due to the Pauli exclusion principle where two electrons in a system are not allowed to have the same quantum number. This results in the electrons of two nearby nuclei dispersing and hence reducing the density of electrons in the internuclear region. This leads to a repulsion between the now less shielded nuclei. The most common form of potential used to represent vdW forces is the Lennard-Jones 12-6 potential:

$$V(r) = 4\epsilon\Big[\Big(\frac{\sigma}{r}\Big)^{12} - \Big(\frac{\sigma}{r}\Big)^{6}\Big] \tag{3.7}$$

where σ is the collision diameter, the point at which the vdW energy is zero and ϵ is the well depth. The Lennard-Jones 12-6 potential is characterised by a r^{-6} attractive part and a r^{-12} repulsive part. The r^{-6} variation is the same power-law relationship that is found in the leading term for theoretical dispersive models such as the Drude model. On the other hand the r^{-12} has no theoretical basis especially as quantum mechanical calculations suggest an exponential term. In terms of computational expense the Lennard-Jones 12-6 potential is useful for large systems as r^{-12} can be calculated by squaring r^{-6}. Alternatively a slightly modified version of the Lennard-Jones potential can be used:

$$V(r) = k\epsilon\Big[\Big(\frac{\sigma}{r}\Big)^{n} - \Big(\frac{\sigma}{r}\Big)^{m}\Big]; \qquad k = \frac{n}{n-m}\Big(\frac{n}{m}\Big)^{m/(n-m)} \tag{3.8}$$

This of course returns to the Lennard-Jones 12-6 potential when $n = 12$ and $m = 6$. A value of n of 9 or 10 gives a less steep repulsive curve. A further improvement to equation 3.8 is the Buckingham potential:

$$V(r) = \epsilon\Big[\frac{6}{\alpha - 6}\exp[-\alpha(r/r_m - 1] - \frac{\alpha}{\alpha - 6}\Big(\frac{r_m}{r}\Big)^{6}\Big] \tag{3.9}$$

This replaces the repulsive r^{-12} term with an exponential term which better represents the repulsions at short range. However, care must be taken when running simulations as at very short separations the potential becomes strongly attractive which can result in fused nuclei. It is therefore common in simulations to employ a cutoff below which the Buckingham potential does not apply.

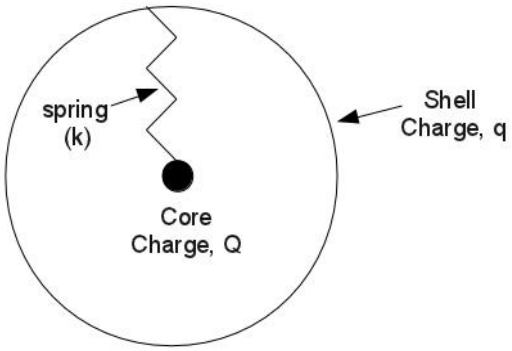

Figure 3.1: Shell Model: The core and shell are held together by a harmonic spring.

3.2.2.1 Shell Model

It was previously stated that electrons are essentially ignored in MM. However, in some systems the polarisation of atoms, oxygen being an excellent example, is very important to the structure and hence derived properties. The shell model of Dick and Overhauser [187] models polarisation by representing the ion as a core containing the mass connected to a massless shell (see Figure 3.1) representing the electrons by a harmonic spring. Both the shell and the core have a charge the sum of which is the total charge on the ion.

$$V_{spring} = \frac{k_{spring}}{2}(l - l_0)^2 \tag{3.10}$$

where l_0 is the equilibrium spring distance, and k_{spring} is the force constant for the spring. Modelling the polarisation of oxygen ions is extremely important in zeolites as this is necessary to give the correct T-O-T angle [188].

3.2.3 Periodic Boundary Conditions

Periodic Boundary Conditions (PBC) allow simulations of bulk solids to be performed where they would otherwise require a large number of atoms. The simulation cell is surrounded by an infinite number of images of itself. If a particle leaves the simulation cell an image of this particle appears on the opposite side (see Figure 3.2) keeping the number of particles constant. Since this means we have an infinite number of non-bonded interactions a cutoff is applied: generally we apply the *minimum image convention* where each particle only interacts with each other particle once, whether it be in the actual simulation cell or one of the images.

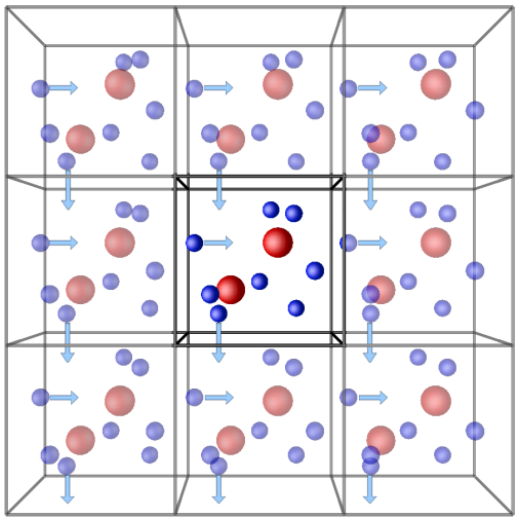

Figure 3.2: Image to illustrate periodic boundary conditions. Figure reproduced with kind permission from Dr. Sébastien Le Roux from reference [189].

3.2.4 Ewald Summation

The $1/r$ dependence of long range electrostatic forces means a cutoff can not simply be used to terminate the forces as this would mean the magnitude of the electrostatic force would depend on the cutoff distance. As mentioned previously, the Ewald summation method overcomes this [186]. The Ewald summation works by converting the sum into two series which converge more rapidly: one in real space and one in reciprocal space. Although this method means that the electrostatic energy can now be computed, the method is still computationally expensive and as such calculating electrostatic forces will be the most time consuming part.

3.2.5 Summary

The molecular interactions described in this section are by no means an exhaustive list, but are the most commonly used functional forms, and are the ones used in this thesis. An interesting point to note, is that sometimes a chemical interaction which we would consider to be covalent, for example a Si−O bond in a zeolite, will actually be described by a long range Buckingham potential combined with a Coulomb potential.

3.3 Electronic Structure Methods

Electronic structure methods are sometimes referred to as *ab initio* which is a Latin term meaning "from the beginning". These calculations are derived from theoretical principles, and not from experimental data as is most often the case with molecular

mechanics. The drawback of these methods is they are far more computationally expensive than classical molecular mechanics methods. To illustrate this, classical methods scale roughly to $O(N^2)$, that is as we increase the number of particles the time for the calculation will scale roughly square. However, for *ab initio* methods the scaling factor is somewhere between two and eight depending on the level of theory. It is clear therefore that once we get to systems containing more than a few hundred particles, the simulation time can be prohibitively long.

However, there are significant advantages of using *ab initio* methods. Molecular mechanics uses a potential which is fitted to a set of data, be it experimental or calculated using *ab initio* methods. If the potentials are used to simulate systems far from those in which they were derived e.g. high pressure, they may not perform well and yield inaccurate results. Similarly, potentials are unable to model chemical reactions (bond breaking, electron transfer), although recent methods have sought to overcome this disadvantage [190].

Electronic structure methods assume nothing about the system in question and solve the electronic state of the system in order to calculate the desired properties. This is achieved by applying the laws of quantum mechanics, the basis of which is the Schrödinger equation [191]:

$$\left\{ -\frac{\hbar^2}{2m}\left(\frac{\partial^2}{\partial x^2}+\frac{\partial^2}{\partial y^2}+\frac{\partial^2}{\partial z^2}\right)+\mathcal{V}\right\}\Psi(\mathbf{r},t)=i\hbar\frac{\partial}{\partial t}\Psi(\mathbf{r},t) \tag{3.11}$$

where Ψ is the wavefunction, $\mathcal{V}$ is the external potential, and the first section in braces is the Hamiltonian operator, often abbreviated to $\hat{H}$. When the external potential is time independent we can rewrite the Schrödinger equation in its more common time-independent form:

$$\hat{H}\Psi = E\Psi \tag{3.12}$$

where E is the energy of the particle. It is only possible to solve the Schrödinger equation exactly for a few simple problems such as the particle in a box.

Although it is not possible to solve the Schrödinger equation exactly for many-body systems, we can make a series of approximations in order to derive a solution. One of these is the Hartree-Fock method. This method calculates the N-electron wavefunction by assuming that it is the sum of the individual one electron wavefunctions in the form of a single Slater determinant in order to obey the Pauli principle. However, the disadvantage of the method is electron correlation is completely ignored. That is, a particular electron is assumed to be moving in an average

potential of all the other electrons, which of course is not the case as electronic motion is correlated and electrons will tend to avoid each other. This causes the energy calculated using Hartree-Fock methods to be higher than the actual value. Methods have been derived for correcting for electron correlations, but they are extremely computationally demanding and so only feasible for the smallest of systems.

3.3.1 Density Functional Theory

Density Functional Theory (DFT) gained popularity in the late 1980s [184] and as computational power has increased so has the use of DFT. In contrast to Hartree-Fock methods where the the full N-electron wavefunctions are calculated, DFT only calculates the total electronic energy and overall electronic density distribution. This is based on the idea that there is a relationship between the total electronic energy and the overall electronic density. Hohenberg and Kohn [192] showed in a *reductio ad absurdum* proof that the ground-state energy and other properties are defined by the electron density and there is a 1:1 correspondence between the wavefunction and the density. The Hohenberg and Kohn theorem also states that the functional delivers the ground state if the input density is the true ground state i.e. the variational principle. The DFT energy functional is written as follows:

$$E[\rho(\mathbf{r})] = \int V_{ext}(\mathbf{r})\rho(\mathbf{r})dr + F[\rho(\mathbf{r})] \tag{3.13}$$

where $\rho(\mathbf{r})$ is the electronic density, V_{ext} is an external potential which arises due to the electrons interacting with the nuclei. The $F[\rho(\mathbf{r})]$ term is the sum of the kinetic energy of the electrons and interelectronic interactions. Kohn and Sham [193] showed that $F[\rho(\mathbf{r})]$ should be approximated to the sum of three terms:

$$F[\rho(\mathbf{r})] = E_{KE}[\rho(\mathbf{r})] + E_H[\rho(\mathbf{r})] + E_{XC}[\rho(\mathbf{r})] \tag{3.14}$$

where $E_{KE}[\rho(\mathbf{r})]$ is the kinetic energy, $E_H[\rho(\mathbf{r})]$ is the electron-electron Coulombic energy, and $E_{XC}[\rho(\mathbf{r})]$ is the contribution from exchange and correlation. Of these three terms, the Coulombic (or Hartree electrostatic) energy can be calculated using the equation:

$$E_H[\rho(\mathbf{r})] = \frac{1}{2}\int\int \frac{\rho(\mathbf{r}_1)\rho(\mathbf{r}_2)}{|r_1 - r_2|}d\mathbf{r}_1 d\mathbf{r}_2 \tag{3.15}$$

The other two terms are not as easily calculated and approximations must be made. The kinetic energy term is written in terms of the one-electron Kohn-Sham orbitals,

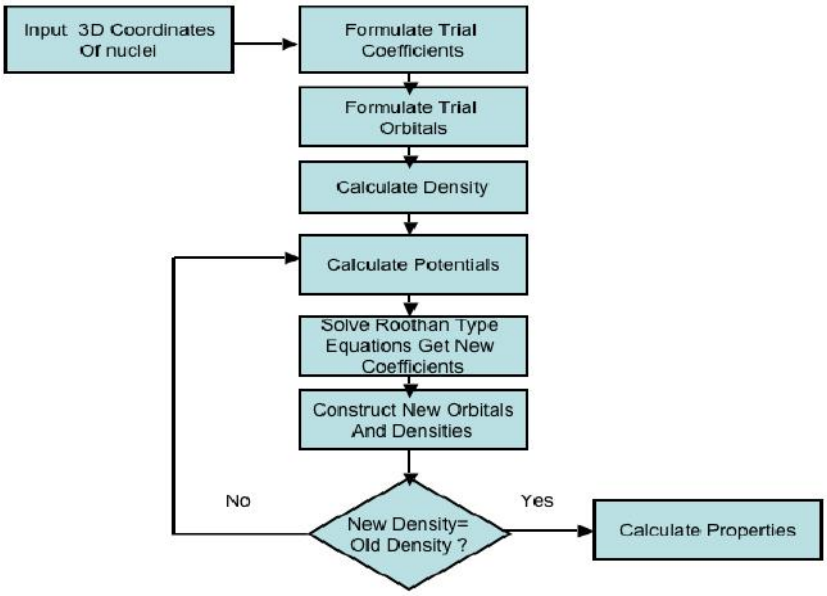

Figure 3.3: Schematic of the SCF process in density function theory.

$\psi_i(\mathbf{r})$:

$$E_{KE}[\rho(\mathbf{r})] = \sum_{i=1}^{N} \int \psi_i(\mathbf{r}) \Big(-\frac{\nabla^2}{2} \Big) \psi_i(\mathbf{r}) d\mathbf{r} \tag{3.16}$$

This equation for the kinetic energy is for a system of non-interacting particles and the difference between this and the real kinetic energy is incorporated into the exchange-correlation energy functional $E_{XC}[(\mathbf{r})]$. Combining the above equations yields the final form of the Kohn-Sham expression for the energy of the N-electron system:

$$E[\rho(\mathbf{r})] = \sum_{i=1}^{N} \int \psi_i(\mathbf{r}) \Big(-\frac{\nabla^2}{2} \Big) \psi_i(\mathbf{r}) d\mathbf{r} + E_H[\rho(\mathbf{r})] + \frac{1}{2} \int \int \frac{\rho(\mathbf{r}_1)\rho(\mathbf{r}_2)}{|r_1 - r_2|} d\mathbf{r}_1 d\mathbf{r}_2 + E_{XC}[(\mathbf{r})] - \sum_{A=1}^{M} \int \frac{Z_A}{|\mathbf{r} - \mathbf{R}_A|} \tag{3.17}$$

where the final term is the electron-nuclear interaction term. This equation is in theory exact, if we knew the exact form the exchange-correlation functional. However, as mentioned before, this is impossible so approximations must be made. Many forms of the exchange-correlation functional exist and these are discussed in the next section.

In order to solve the above equations, an iterative procedure is carried out as

illustrated in Figure 3.3. Guesses are made at the Kohn-Sham orbitals and from these the electron density is then calculated. This density is in turn used to calculate the Kohn-Sham potential and finally building a new set of orbitals from which a new density can be calculated. This process is iterated until the Kohn-Sham density and electron densities are self-consistent.

3.3.1.1 Exchange-Correlation Functional

The most important part of a DFT calculation is the choice of exchange-correlation functional. This functional contains the exchange energy, correlation energy and the difference between the non-interacting and interacting kinetic energies. The exact functional form is known only for a homogeneous electron gas [194] so approximations must be made in order to solve more complex systems. The first approximation was called the local density approximation (LDA) and was used by Kohn and Sham in their original paper [193].

A point in the inhomogeneous electron distribution is considered locally homogeneous and the exchange-correlation functional of a homogeneous electron gas can be used as it is known exactly. Generally LDA is good for systems such as metals where the electron density is relatively uniform. It has been shown to result in overbinding, shortening of bonds, and to poorly represent hydrogen bonds [195].

An improvement to the local density approximation is the generalised gradient approximation (GGA). Here, we consider the gradient and higher derivatives of the of the density rather than just the local density. There have been a number of GGA functionals developed and these usually give improved energies and geometries of the systems modelled. Typically these gradient corrected functionals are divided into separate exchange and correlation contributions. A commonly used correction to the gradient functional was proposed by Becke [196] by fitting to experimental data. This is often combined with the correlation functional of Lee, Yang and Parr (LYP) [197] and is abbreviated to BLYP.

3.3.2 Basis Sets

Basis sets are used in quantum mechanical calculations to define molecular orbitals in the form of atomic functions. There are two main types of basis sets, atom centred and plane wave. An atom centred basis set consists of a number of atomic functions which define the electron population at a given distance from the nucleus. There are a number of different functions available and the most common ones will be discussed now. The first is a Slater type orbital (STO) which has the functional

form:

$$R(r) = Nr^{n-1}e^{-\zeta r^2} \tag{3.18}$$

where r is the distance from the nucleus, n is the principle quantum number, N is a normalisation constant and ζ is the effective charge of the nucleus as there is a partial shielding of the core due to the electrons. The drawback with using STOs in molecular orbital calculations is that some of the integrals are extremely difficult to evaluate especially when the orbitals are centred on different nuclei.

A more commonly used function is one based on Gaussians. Gaussian type orbitals (GTO) have the form:

$$R(r) = x^a y^b z^c e^{-\alpha r^2} \tag{3.19}$$

where α determines the radial extent of the orbital, a, b and c determine the order and x, y and z are Cartesian variables, of the Gaussian function. A function with $a + b + c = 0$ is a zeroth order function and can be compared to a s orbital. A first order function has $a + b + c = 1$ and can be related to the p_x, p_y and p_z orbitals, and so forth up the orders.

It is unlikely that simply representing the occupied atomic orbitals in a quantum calculation will be sufficient, and it is common to include higher unoccupied orbitals in order to improve the accuracy of the calculation. The basis set can be split into two basis functions (double zeta) that correspond to the valence orbitals. Further splitting gives triple zeta, quadruple zeta etc. functions, although it is uncommon to go further than quadruple zeta. An alternative method is to double the number of functions used for the valence electrons but keep single functions for the inner shells. The logic behind this is that the properties of interest will be defined by the valence electrons as these are the ones that will interact. This method is so popular that is has been given its own notation. For example the 3-21G basis set has three Gaussian functions to describe the core electrons and the valence electrons are described by two contracted and one diffuse Gaussian.

Further improvements can be made by including a polarisation function. For example a hydrogen atom will have a spherical electron cloud when in isolation. When however, it is in a molecule there will be a perturbation of the electron cloud towards the other nuclei and give a *sp* hybrid. The solution to this problem is to introduce polarisation functions to the basis set. A polarisation function has a higher angular quantum number and so will correspond to p orbitals in our hydrogen atom example. The polarisation function is denoted by an asterisk *. A 6-31G* basis set

has polarisation functions on the heavy atoms and a 6-31G** basis set also includes polarisation functions on the light (hydrogen and helium) atoms.

The final addition that can be made to a basis set is to deal with atoms which have a significant amount of electron density far away from the nucleus. This occurs for example when an atom has a lone pair. In this case a highly diffuse function is added to the basis set and a basis set with this included is given the '+' notation. A 6-31+G basis set has a single set of diffuse functions *s*- and *p*-type Gaussian functions. In a manner analogous to the polarisation functions, a double plus (6-31++G) means that the diffuse functions are included on the light atoms as well.

3.3.2.1 Plane Wave Basis Sets

When the system being studied is periodic, as if often the case in solid state systems, the basis set of choice is a plane waves. This is the equivalent representation to a Fourier series and represents each orbital wavefunction as a linear combination of plane waves which differ by reciprocal lattice vectors.

$$\psi(r) = \sum_{G} a_G \exp(i(k+G)r) \tag{3.20}$$

3.3.2.2 Pseudopotentials

Generally speaking the properties of interest depend only on the valence electrons [198] as these are the ones involved in bonding. The core electrons are not affected much by the atomic environment and so we can make an approximation and only consider valence electrons explicitly. Pseudopotentials [194] aim to replace the core electrons by representing the way valence electrons interact with the core electrons plus nucleus. The potential function gives wavefunctions with the same shape outside the core region, but with fewer nodes inside the core region, thus reducing the number of terms required for plane wave expansion, and so reducing computational expense.

Pseudopotentials were initially derived by fitting to empirical data, however it is now more common to fit to all-electron *ab initio* calculations. The pseudopotential is fitted to the data (in a manner analogous to a classical potential) in order to accurately reproduce the behaviour and properties. Ideally pseudopotentials will be norm-conserving: that is the valence electron density within the core radius equals that for the all-electron situations.

3.4 Energy Minimisation

Unless the system we are studying is very simple, i.e. a few atoms, the potential energy surface is extremely complicated, and even for simple molecules finding the absolute minimum energy configuration is not a trivial problem. We can formally state the minimisation problem as follows:

$$\frac{\partial E}{\partial x_i} = 0; \qquad \frac{\partial^2 E}{\partial x_i^2} > 0 \tag{3.21}$$

where the function E represents the energy of the system and depends on one or more independent variables $x_1, x_2, \ldots, x_i$. The aim is to find values of those variables where E has a minimum value. In the case of chemical systems, the variables x_i will be Cartesian or internal coordinates. For an analytical function finding the minimum is relatively straightforward and can be achieved using calculus methods. For a molecular system however this is not the case and numerical methods must be used since the energy varies in a complicated way with respect to the coordinates of the atoms. A system with N atoms will have $3N - 6$ internal coordinated of $3N$ Cartesian coordinates. The numerical methods locate minima by gradually changing the coordinates until the minimum is reached.

Although initially this seems straightforward another question arises when searching for the minimum. That is, how do we know if we have found the absolute or global minimum or if we are stuck in a local minimum?

3.4.1 Minimisation Methods

The most common methods for finding the minimum on a potential energy surface use derivatives, where the first derivative of the energy, i.e. the gradient, indicates where the minimum is, and the magnitude indicates the steepness of the slope.

3.4.1.1 The Steepest Descent Method

The steepest descent method [184] is one of the simplest and moves in the direction parallel to the net force. For the $3N$ Cartesian coordinates this can be represented using a $3N$-dimensional unit vector $\mathbf{s}_k$:

$$\mathbf{s}_k = -\frac{\mathbf{g}_k}{|\mathbf{g}_k|} \tag{3.22}$$

where $\mathbf{g}_k$ is the gradient vector. Once the direction of the step has been found the next stage is to decide the size of the step. This can be an arbitrary step along the

gradient unit vector $\mathbf{s}_k$,

$$\mathbf{x}_{k+1} = \mathbf{x}_k + \lambda_k \mathbf{s} \tag{3.23}$$

where λ_k is the step size. The step size has a predetermined value and if the first iteration leads to a reduction in energy then the step size is increased by a factor for the next iteration. This continues until there is an increase in energy and then the step size is reduced by a multiplicative factor to narrow in on the minimum.

A more robust, but computationally more expensive approach, is the line search method. This method first brackets the minimum by finding three points along the search direction where the middle point is lower in energy than the two either side. The minimum must then lie between these two outer points. The procedure then iterates narrowing the minimum to a smaller region.

3.4.1.2 Conjugate Gradient Method

The major disadvantage of the steepest descent method is that it will oscillate around the minimum value if the minimum is located along a narrow valley. With the conjugate gradient methods [184] the gradients are orthogonal at each point but the directions are conjugate. The search will move in direction $\mathbf{v}_k$ from point $\mathbf{x}_k$ where $\mathbf{v}_k$ is calculated from the gradient at the previous direction vector $\mathbf{v}_{k-1}$

$$\mathbf{v}_k = -\mathbf{g}_k + \gamma_k \mathbf{v}_{k-1} \tag{3.24}$$

where γ_k is given by

$$\gamma_k = \frac{\mathbf{g}_k \cdot \mathbf{g}_k}{\mathbf{g}_{k-1} \cdot \mathbf{g}_{k-1}} \tag{3.25}$$

The directions and gradients must then satisfy the following relationships:

$$\mathbf{g}_i \cdot \mathbf{g}_j = 0 \tag{3.26}$$

$$\mathbf{v}_i \cdot V''_{ij} \cdot \mathbf{v}_j = 0 \tag{3.27}$$

$$\mathbf{g}_i \cdot \mathbf{v}_j = 0 \tag{3.28}$$

where V''_{ij} is a matrix of the second derivatives of the potential in the direction of i and j. Since the method requires a previous set of gradients to work from, this method can only be used from the second step onwards and the first step is the same as the steepest descent method.

3.4.1.3 Newton-Raphson Method

The Newton-Raphson method is a second derivative method. The second derivative of a function provides information about the curvature of the function. The advantage of using second derivative methods is that it gives more information on the potential energy surface and so will lead to the minimum more efficiently. The main disadvantage is the extra computational expense. Calculating second derivatives is both computationally demanding and requires large amount of storage space, especially for large systems.

Generally, when carrying out a minimisation two or more of these methods are combined. For example the minimisation will start with the steepest descent method, before moving to the conjugate gradients method as the system approaches the minimum.

3.5 Molecular Dynamics

In molecular dynamics (MD) the system configurations are generated by integrating Newton's laws of motion. These can be summarised as follows:

1. A body continues to move in a straight line at a constant velocity unless a force acts upon it.

2. Force equals the rate of change of momentum.

3. To every action there is an equal and opposite reaction.

The result is a trajectory of how the position and velocity of the atoms vary with time and is obtained by solving the differential equations derived from Newton's second law, $F = ma$.

$$\frac{d^2x_i}{dt^2} = \frac{F_{x_i}}{m_i} \tag{3.29}$$

where F is the force, m is the mass and a is acceleration. Equation 3.29 describes the motion of a particle of mass m_i along one coordinate, x_i, and has a force, F_{x_i} on the particle in that direction.

We can solve Newton's laws of motion for a system of interacting bodies, i.e. our chemical system of interest, and generate a trajectory which can then be analysed and the relevant chemical properties extracted. The difficulty arises because we have many bodies interacting under a continuous potential with their motion coupled together. Several methods have been derived to solve these problems, the most relevant of which will now be discussed.

3.5.1 Finite Difference Methods

Finite difference methods are used to generate trajectories with continuous potentials. The integration is broken down into many small steps, separated by a fixed time step δt. The force on each particle is calculated at time t as a vector sum of its interactions with other particles. From the forces the accelerations can be calculated and these used with the positions and velocities at time t to calculate the positions and velocities at time δt.

All of the algorithms for integrating the equations of motion using finite difference methods assume that the dynamic properties can be approximated to Taylor series expansions:

$$\mathbf{r}(t+\delta t) = \mathbf{r}(t) + \delta t\mathbf{v}(t) + \frac{1}{2}\delta t^2\mathbf{a}(t) + \frac{1}{6}\delta t^3\mathbf{b}(t) + \frac{1}{24}\delta t^4\mathbf{c}(t) + \ldots \tag{3.30}$$

$$\mathbf{v}(t+\delta t) = \mathbf{v}(t) + \delta t\mathbf{a}(t) + \frac{1}{2}\delta t^2\mathbf{b}(t) + \frac{1}{6}\delta t^3\mathbf{c}(t) + \ldots \tag{3.31}$$

$$\mathbf{a}(t+\delta t) = \mathbf{a}(t) + \delta t\mathbf{b}(t) + \frac{1}{2}\delta t^2\mathbf{c}(t) + \ldots \tag{3.32}$$

where $\mathbf{v}$ is the velocity (first derivative of the positions with respect to time, $\mathbf{a}$ is the acceleration (2nd derivative) and $\mathbf{b}$ is the third derivative etc. The Verlet algorithm [199] is one of the most popular for integrating the equations of motion. The Verlet algorithm uses the positions and accelerations at time t and the positions from the previous step $\mathbf{r}(t-\delta t)$ to calculate the positions at $t+\delta t$. This leads to the following equations:

$$\mathbf{r}(t+\delta t) = \mathbf{r}(t) + \delta t\mathbf{v}(t) + \frac{1}{2}\delta t^2\mathbf{a}(t) + \ldots \tag{3.33}$$

$$\mathbf{r}(t-\delta t) = \mathbf{r}(t) - \delta t\mathbf{v}(t) + \frac{1}{2}\delta t^2\mathbf{a}(t) + \ldots \tag{3.34}$$

These two equations can then be added to give:

$$\mathbf{r}(t+\delta t) = 2\mathbf{r}(t) - \mathbf{r}(t-\delta t) + \delta t^2\mathbf{a}(t) \tag{3.35}$$

Clearly, the velocities do not appear in the above equations, and so when using the Verlet algorithm, velocities must be calculated retrospectively:

$$\mathbf{v}(t) = [\mathbf{r}(t+\delta t) - \mathbf{r}(t-\delta t)]/2\delta t \tag{3.36}$$

The advantage of the Verlet algorithm is that it is straightforward and the memory requirements are modest. However, there are a few drawbacks to the method, particularly that position $\mathbf{r}(t+\delta t)$ is obtained by adding $\delta t^2\mathbf{a}(t)$, which is small, to the difference of two large terms, $\mathbf{r}(t+\delta t) - \mathbf{r}(t-\delta t)$, which can lead to a loss of precision.

A variation of the Verlet algorithm is the velocity Verlet method [200]. The velocity Verlet method is a three step process and is implemented as follows:

$$\mathbf{r}(t+\delta t) = \mathbf{r}(t) + \delta t\mathbf{v}(t) + \frac{1}{2}\delta t^2\mathbf{a}(t) \tag{3.37}$$

$$\mathbf{v}(t+\delta t) = \mathbf{v}(t) + \frac{1}{2}\delta t[\mathbf{a}(t) + \mathbf{a}(t+\delta t)] \tag{3.38}$$

To calculate the new velocities, the accelerations at t and $t+\delta t$ are required, and so the first step in the velocity Verlet method is to calculate the positions at $t+\delta t$ using the velocities and accelerations at time t. Velocities at time $t+\frac{1}{2}\delta t$ are found using:

$$\mathbf{v}(t+\frac{1}{2}\delta t) = \mathbf{v}(t) + \frac{1}{2}\delta t\mathbf{a}(t) \tag{3.39}$$

Forces from the current positions are calculated which in turn give the accelerations at $t+\delta t$ and finally the velocities at $t+\delta t$ can be calculated:

$$\mathbf{v}(t+\delta t) = \mathbf{v}(t+\frac{1}{2}\delta t) + \frac{1}{2}\delta t\mathbf{a}(t+\delta t) \tag{3.40}$$

The velocity Verlet method has the advantage over the standard Verlet algorithm

in that it gives positions, velocities, and accelerations at the same time without compromising precision.

3.5.2 Temperature and Pressure Control

Molecular dynamics is usually performed under the *NVE* ensemble. That is the number of particles, the volume and energy are kept constant. It is possible to transform results between different ensembles but only at the thermodynamic limit, that is, when we have an infinite number of particles. Clearly this is not achievable in a computational simulation so we perform the simulation under different ensembles depending on the properties we wish to derive. The two most commonly used ensembles are *NVT*, with a constant number of particles, constant volume and constant temperature, and *NPT*, with a constant number of particles, constant pressure, and constant temperature.

3.5.2.1 Constant Temperature

The temperature of the system is related to the time averaged kinetic energy which for an unconstrained system, is given by:

$$\langle \mathscr{K} \rangle_{NVT} = \frac{3}{2} N k_B T \tag{3.41}$$

where $\langle \mathscr{K} \rangle_{NVT}$ is the average kinetic energy, N is the number of particles, k_B is the Boltzmann constant and T is the temperature. The simplest way to change the temperature of the system is to scale the kinetic energy i.e. scale the velocities. So, if the temperature multiplied by a factor λ at time t, the temperature change associated with this can be found as follows [201]:

$$\Delta T = \frac{1}{2} \sum_{i=1}^{N} \frac{2}{3} \frac{m_i (\lambda \nu_i)^2}{N k_B} - \frac{1}{2} \sum_{i=1}^{N} \frac{2}{3} \frac{m_i \nu_i^2}{N k_B} \tag{3.42}$$

$$\Delta T = (\lambda^2 - 1) T(t) \tag{3.43}$$

$$\lambda = \sqrt{T_{new} / T(t)} \tag{3.44}$$

where $T(t)$ is the temperature at time t. Therefore, by multiplying the velocities at each time step by a factor $\lambda = \sqrt{T_{req}/T_{curr}}$, where T_{req} is the desired temperature for the system and T_{curr} is the current temperature of the system, the overall system temperature can be kept constant.

Clearly this method is not physical as it does not allow for fluctuations in system temperature. An improvement on this method was made by Berendsen *et al* [202] where the system is coupled to an external heat bath that is fixed at the desired temperature. Heat is then supplied or removed from the system by using the bath as a source of thermal energy. Velocities are scaled at each step by a factor proportional to the difference between the system temperature and the bath temperature:

$$\frac{dT(t)}{dt} = \frac{1}{\tau}(T_{bath} - T(t)) \tag{3.45}$$

This leads to the scaling factor for velocities:

$$\lambda^2 = 1 + \frac{\delta t}{\tau}\Big(\frac{T_{bath}}{T(t)} - 1\Big) \tag{3.46}$$

where τ is a coupling constant which determines how strongly the bath and system are coupled together and δt is the time step. When $\tau = \delta t$ the method is equal to the velocity scaling method discussed previously.

Although the Berendsen algorithm is an improvement over velocity scaling, neither generate canonical averages and as such are only used in the initial equilibration stages of a MD simulation. The extended system method, an alternative method which does give rigorous canonical ensembles, was developed by Nosé [203, 204] and Hoover [205]. The Nosé-Hoover method has the thermal reservoir as an integral part of the system with its own degree of freedom, s. This reservoir has potential energy:

$$V = (f + 1)k_B T \ln s \tag{3.47}$$

where f is the number of degrees of freedom in the physical system and T is the desired temperature. The kinetic energy of the system, is given by:

$$\mathscr{K} = \frac{Q}{2}\Big(\frac{ds}{dt}\Big)^2 \tag{3.48}$$

where Q is the fictitious mass of the extra degree of freedom. The size of Q determines the strength of the coupling between the reservoir and the real system. If Q is small then the flow of energy is large, and when Q approaches infinity, conventional

MD is regained, as the reservoir and real system are no longer coupled.

The extended system generated by the MD simulation corresponds to a unique state of the real system, however there is no direct relation between the velocities and time. The time step $\delta t'$ is related to the 'real time' time step δt by:

$$\delta t = s\delta t' \tag{3.49}$$

and as such the regular time intervals in extended space are related to the trajectory of the real system which is unevenly spaced.

3.5.2.2 Pressure Control

As with temperature control, it is sometimes desirable to control the pressure to study effects such as phase transitions. The methods used to control pressure are analogous to those used to control temperature, however instead of velocities we now scale the volume. Berendsen [202] also derived an algorithm to control pressure analogous to that used to control temperature. The volume of the system is scaled by a factor λ:

$$\lambda = 1 - \kappa\frac{\delta t}{\tau_p}(P - P_{bath}) \tag{3.50}$$

where τ_p is the coupling constant, P_{bath} is the pressure of the external bath, and κ is the isothermal compressibility. κ and τ_p can be combined into a single constant and this expression applied directly to the volume or by scaling the atomic coordinates:

$$\mathbf{r}_i' = \lambda^{\frac{1}{3}}\mathbf{r}_i \tag{3.51}$$

where $\mathbf{r}$ is the new coordinate. Similar to the Nosé-Hoover extended system method, Andersen [206] added an extra degree of freedom to the system that corresponds to the volume. The kinetic energy associated with this degree of freedom, which can be considered as a piston acting on the system, is given by:

$$\mathscr{K} = \frac{1}{2}Q\Big(\frac{dV}{dt}\Big)^2 \tag{3.52}$$

where Q is the mass of the piston. The potential energy of the system is given by:

$$T = PV \tag{3.53}$$

where P is the desired pressure and V is the system volume. A small value of Q (a piston with small mass) will allow the volume to vary rapidly, conversely a large Q will slow fluctuations with the system returning to normal molecular dynamics as Q approaches infinity.

3.5.3 Constrained Dynamics

MD simulations are often unfeasible when the aim is to sample a certain region of the phase space. This may be the case when searching for a transition state, or along a reaction coordinate. Potential of mean force (PMF) [207, 208] calculations can be used to find how the free energy changes as a function of a particular reaction coordinate. The reaction coordinate could be a bond angle, bond length, or torsion.

If, in a MD simulation we were able to sample the whole potential energy surface, then it is possible to calculate the free energy from the radial distribution function $g(r)$:

$$A(r) = k_B T \ln[g(r)] + C \tag{3.54}$$

where r is the reaction coordinate being studied, for example the separation between two particles, k_B is the Boltzmann constant, and $A(r)$ is the Helmholtz free energy. The constant C is chosen so that the most probable distribution corresponds to a free energy of zero. In practice, a PMF calculation is carried out by running a series of simulations at regular points on the reaction coordinate. There is a constraint applied between the two units of interest, and the average force required to keep these two units in place is the quantity of interest. If we select sufficiently small steps along the reaction coordinate then the average force can be integrated in order to obtain the free energy profile.

3.6 Monte Carlo

Monte Carlo (MC) methods generate system configurations by making random changes to the species in the system. Unlike molecular dynamics where only a small portion of the phase space is sampled, MC methods allow the whole space to be explored. In its simplest form MC methods simply accept a configuration if it is lower in energy than the previous configuration. Clearly high and low energy states will be generated with equal probability which leads to an extremely inefficient samplings. Methods such as the Metropolis algorithm [209] weight configurations based on the Boltzmann factor $\exp(-\nu(\mathbf{r})^N/k_B T)$ where ν is the potential energy. The

state is then weighted by the Boltzmann factor and so lower energy states will be favoured. This method has obvious advantages over molecular dynamics as we can sample more of the potential energy surface, and also make 'uphill' moves which is not possible in molecular dynamics.

3.6.1 Metropolis Method

The Metropolis algorithm ensures that the generated state depends only on the previous state and no other, by generating a Markov chain of states that satisfies the following conditions.

1. The outcome of each trial depends only on upon the preceding trial and not upon any previous trials.

2. Each trial belongs to a finite set of possible outcomes.

We can immediately see a difference between molecular dynamics and Monte Carlo methods as condition (1) states that the outcome of each trial depends on *only* the previous trial. In contrast to molecular dynamics where each state is connected in time. For example, if we have a particle at position x then we can generate a new position as follows:

$$x_{new} = x_{old} + (2\xi - 1)\delta r_{max} \tag{3.55}$$

A random number generator produces a number ξ which is between 0 and 1. The new position is then generated and the change in energy calculated. If the energy is lower in the new state then the move is accepted. If it is higher then another random number is generated between 0 and 1, and compared to the Boltzmann factor. If the Boltzmann factor is greater then the move is rejected. At higher temperatures, the Boltzmann factor will of course be greater so there is an increased chance an uphill move being accepted.

δr_{max} is the maximum allowed size of a displacement and is adjusted so that the probability of a step being accepted is equal to the probability of rejection. This is so that the states generated will be sufficiently different. If the value for the maximum displacement is too small the generated states will be similar and the phase space will be explored slowly. Similarly, if the value is too large, many states will be rejected. As well as moving random atoms, groups of atoms could be moved. For example, a part of a molecule could be rotated through a torsional term. This has the advantage of requiring fewer calls to the random number generator, and also allows faster exploration of the phase space.

Generally MC simulations are carried out in the NVT ensemble. However, it is possible to carry them out in the NPT ensemble where random changes to the volume are additional possible moves. Simulations can also be carried out in the μVT ensemble (grand canonical ensemble) where we can adjust the chemical potential i.e. the random addition or removal of particles is also an available move.

3.6.2 Random Number Generators

The random number generator is the centre of all Monte Carlo codes. It is used to decide if a given move should be accepted and to generate new configurations. The sequence of numbers produced by a random number generator is in fact not random and is often referred to as a 'pseudo-random' number generator. When the program is started, the random number generator is seeded, usually with the time. This generates a starting point for the sequence, and unless instances of the program start at exactly the same time, the sequence will always be different.

3.7 Solvation

Solvation is an important factor to consider when modelling systems, especially when studying small clusters in solution as the solvent can have a large effect on the stability of the molecule. There are two extremities of methods used to model solvation: *implicit*, where the effect of solvation is modelled, and *explicit* where the solvent molecules are included in the simulation. Both methods come with their own advantages and disadvantages. Implicit solvation methods are based on continuum representations of solvents and can be traced back as far as the 1920s [184]. Born placed a charge within a spherical solvent cavity [210] and calculated the free energy. This was later extended by Onsager to a dipole [211]. The Born model calculates the work done in moving a point charge from a vacuum to a spherical cavity. Whilst clearly a very simple idea, it remains a very effective method for modelling the solvation of ions. One of the most commonly used implicit solvent models is the conductor-like screening model (COSMO) [212].

Explicit solvation is a more realistic method of modelling solvation as we include the actual molecules of solvent around the solute. This is of course more computationally expensive as we have increased the number of atoms in the simulation and if the solute in question is particularly large then it may require an unfeasible number of solvent molecules. The issue then becomes how many solvent molecules is 'enough' for a realistic representation? A single layer may not be sufficient as the solvent molecules will also interact with other solvent molecules and these effects

could also be important. In order to reduce the number of solvent molecules used, it can be useful to apply periodic boundary conditions (PBC) which were discussed in Section 3.2.3. Specific issues arising from the use of implicit solvation methods in this thesis are discussed in the relevant chapters.

3.8 Surfaces

Often the most interesting chemistry occurs at the surface and by studying only bulk properties we will not gain an understanding of what is happening when the materials interfaces with others. In the case of crystal growth the surface is of course extremely important as the processes which occur here will control the eventual crystal morphology. The surface energy γ is one quantity which we can measure, and it gives us an idea of the stability of a particular surface. It is a measure of the work done in cleaving a surface and is defined as follows:

$$\gamma = \frac{E_{surface} - nE_{bulk}}{A} \tag{3.56}$$

where $E_{surface}$ is the energy of the surface which contains n bulk unit cells of energy E_{bulk}. A is the area of the slab.

3.8.1 Building surfaces

A surface is built by cleaving the bulk optimised structure at the Miller plane index of interest. After the surface has been cleaved, care must be taken in order to make sure the surface is properly terminated, so that there is no dipole running perpendicular to the surface. Tasker classified surfaces into three types.

Type 1 Non-polar surfaces that can be cleaved at any plane as each layer is charge neutral

Type 2 Consists of charged planes but arranged symmetrically so that it is possible to cleaves the surface into neutral blocks

Type 3 A series of alternately charged planes. It is not possible to cleave this type to leave a neutral surface and so it must be reconstructed.

Often when a surface is cleaved it will leave dangling bonds. This is the case in zeolites as dangling Si or O atoms will be left. In order to appropriately terminate the surface, hydroxyls are added to the dangling Si, and H added to the dangling O to form silanol groups.

3.9 Summary

This chapter has aimed to give an overview of the computational methods used in this thesis. Most of the methods discussed in this chapter will be used at some point, and the details are discussed in the relevant chapters.

CHAPTER 4

ZEBEDDE Developments and Template Design

4.1 Introduction

As already discussed one of the aims of zeolite science is to understand the role of the template. ZEBEDDE [213] (ZEolites By Evolutionary De novo DEsign) is a computer program written in the mid 1990s with the goal of designing a template that would direct to a particular zeolite topology. The aim of the ZEBEDDE code is to apply *de novo* techniques to microporous materials. ZEBEDDE "grows" an organic molecule in a given pore space by starting from a seed molecule, which is placed randomly or in a user defined location, and then adding organic fragments on to this seed until the pore space is filled. As the molecule is growing a series of actions can be carried out in order to improve the location of the template. These are rotations (either of the molecule as a whole or fragments of it), translations, and minimisation, which is carried out by the internal minimiser or can be sent to an external minimiser such as the General Utility Lattice Program (GULP) [214] or Discover [215]. If only the rotation, and translation actions are used then it is possible to use ZEBEDDE to optimise the position and orientation of a template within a zeolite pore. The ZEBEDDE building process is illustrated in Figure 4.1. In order to illustrate the use of ZEBEDDE in template design, templates for zeolite EU-1(EUO) [216]. In this work, Willock *et al.* design a number of templates for EU-1, as well as optimising the existing template for Chabazite(CHA).

The role of the template in the synthesis was covered in the introduction to this thesis and although there are examples where templates have been designed to

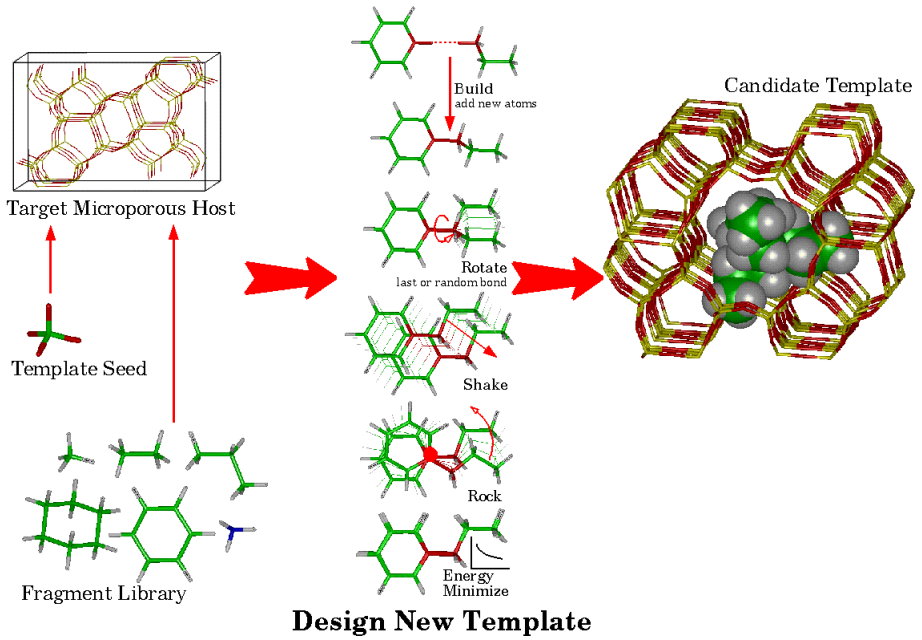

Figure 4.1: The ZEBEDDE building process [213].

direct a particular zeolite structure, with ZSM-18 being one of the best examples [86], generally they are found by a trial and error process. This is often achieved using high throughput techniques where a wide variety of compositions and templates are "screened" for new zeolites. This is both time consuming, and expensive so designing templates using codes like ZEBEDDE would be useful as this can reduce the search region which must be covered experimentally.

This chapter describes improvements to ZEBEDDE to improve its performance at carrying out the building action, most specifically the ability to form rings. This feature is desirable as many zeolites' templates contain ring structures and previous versions of ZEBEDDE did not account for this effectively. Several modifications were also made to the docking routines. This improved code has been tested by designing templates for the zeolite Boggsite.

4.2 Code Development

4.2.1 Introduction

Although over the last 15 years various alterations have been made to the ZEBEDDE code, none focused on what the code was originally designed to do which is construct templates. Therefore, in order to improve the code, a number of functions within the code were selected for improvement. These were:

- Ring building routine
- Docking routines
- Integration with external minimisers
- Integration with supercomputers

4.2.2 Ring Builder

Many templates that are used in zeolite synthesis contain ring structures, and more recently fused ring structures in order to maintain the molecule's rigidity. The previous ring making routine was limited to six member rings and would often fail because it randomly selected a pair of atoms from anywhere within the growing template. These two issues have been addressed to allow the formation of any size ring and allow the user to control which size rings are allowed in the template.

The ring making routine first generates a list of all atoms within a cutoff (user definable) that could be connected. The next check is to confirm they are able to be bonded. This implies the pair of atoms should have free hydrogen atoms, and not be in the excluded connections list. If these criteria are fulfilled, then the order of the two atoms is checked. Order refers to the number of connections separating the two atoms. This is achieved by working through the neighbour lists and counting the number of links required. This serves two purposes; the first is to ensure that the two atoms are in fact connected, and the second is so that the ring size can be controlled. By restricting only atoms to be connected if they are 5th order neighbours i.e. could form a six ring, we can control the ring structures present in the final generated template. This process is given schematically in Figure 4.2 and an example of ZEBEDDE forming a five ring is shown in Figure 4.3.

4.2.3 Docking Routines

The docking routines in ZEBEDDE have been central to this thesis. It is therefore appropriate to describe the improvements made to automate and streamline such calculations. The existing process merely places the template within the framework which results in a high chance that all or part of the template molecule will be overlapping with the framework requiring extensive optimisation. Monte Carlo docking in comparison is significantly less computationally expensive. In order to speed this up, another keyword command was added which allows the user to define a maximum interaction energy after the initial docking. If the interaction energy of the template with the framework is above this cutoff value, the docked structure

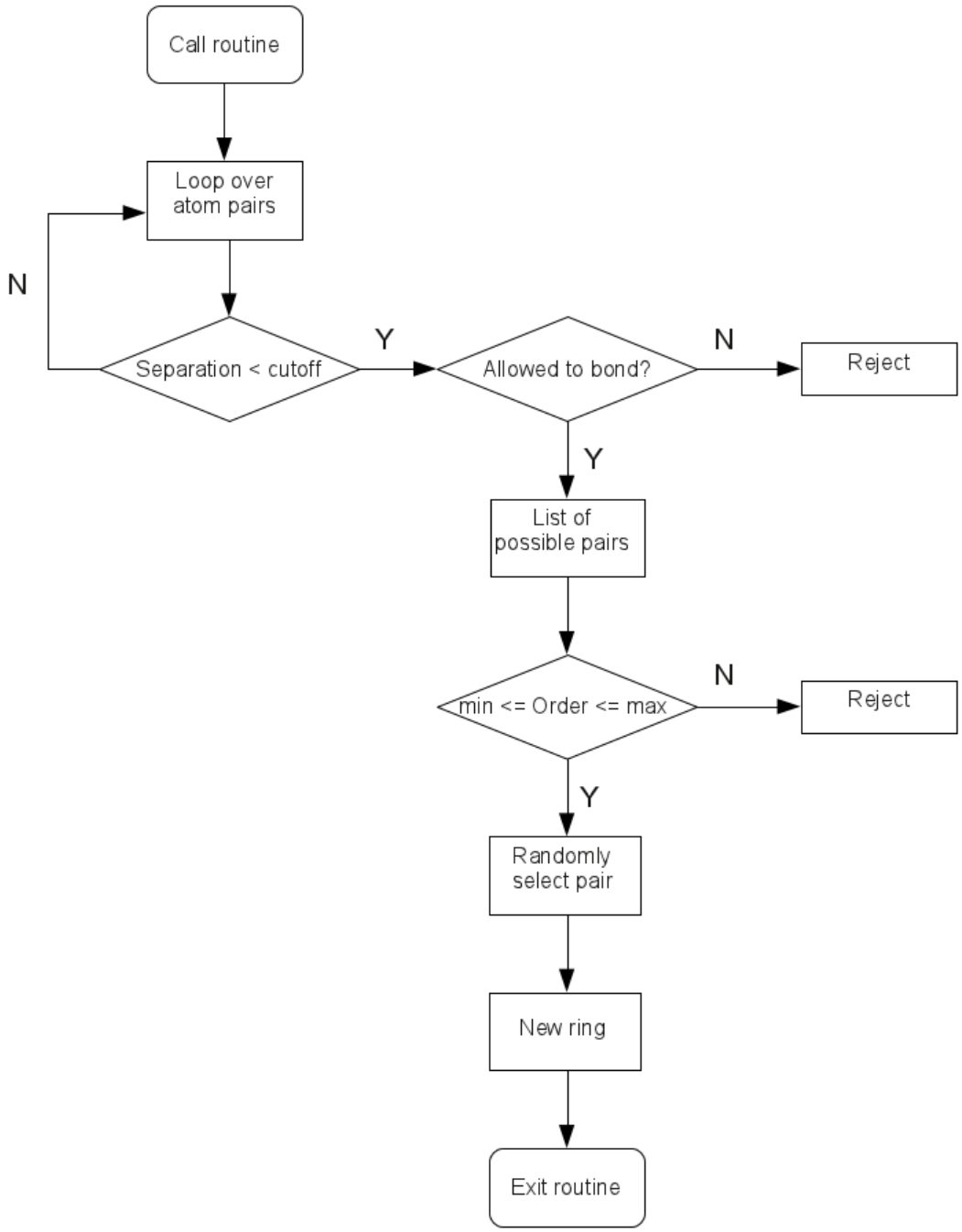

Figure 4.2: Flow diagram of the ring making process. Order refers to the number of bonded atoms between the two atoms in question.

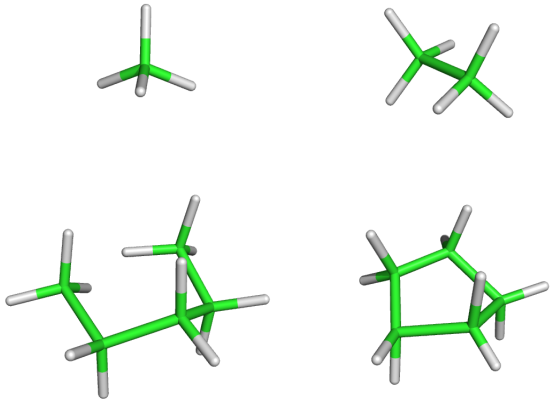

Figure 4.3: ZEBEDDE forming a five ring starting from a methane seed.

is rejected immediately and the template re-docked. If it is below this threshold, the template is then optimised by performing random rotations and translations. Once completed, this structure is the output and optionally submitted to an external minimiser such as Discover or GULP, or to a molecular dynamics code for a simulated annealing though this is extremely computationally expensive and rarely used. Figure 4.4 shows this process schematically.

4.2.4 Integration with External Minimisers and Supercomputers

Although ZEBEDDE was written to utilise external minimisers, these routines were out of date and so were unable to output files for use in modern codes. The main minimiser used for docking optimisations is Discover and so the routines to generate input files for this code were written. The biggest challenge was outputting a suitable MDF (molecular data file) which Discover uses to control the connectivity of the molecule. ZEBEDDE already had some routines to run GULP and these were streamlined. ZEBEDDE is now able to generate input files for both Discover and GULP minimisers.

When running docking calculations a large number of single processor calculations are required. If these were run sequentially the docking process would be inefficient and time consuming. Therefore we chose to incorporate routines to allow ZEBEDDE to be run on both supercomputers and a Condor pool [217] automatically with minimal input from the user. As the Monte Carlo docking is running, each time it finds a structure below the user defined threshold discussed in section 4.2.3, instead of just outputting this structure for later optimisation, it can be sub-

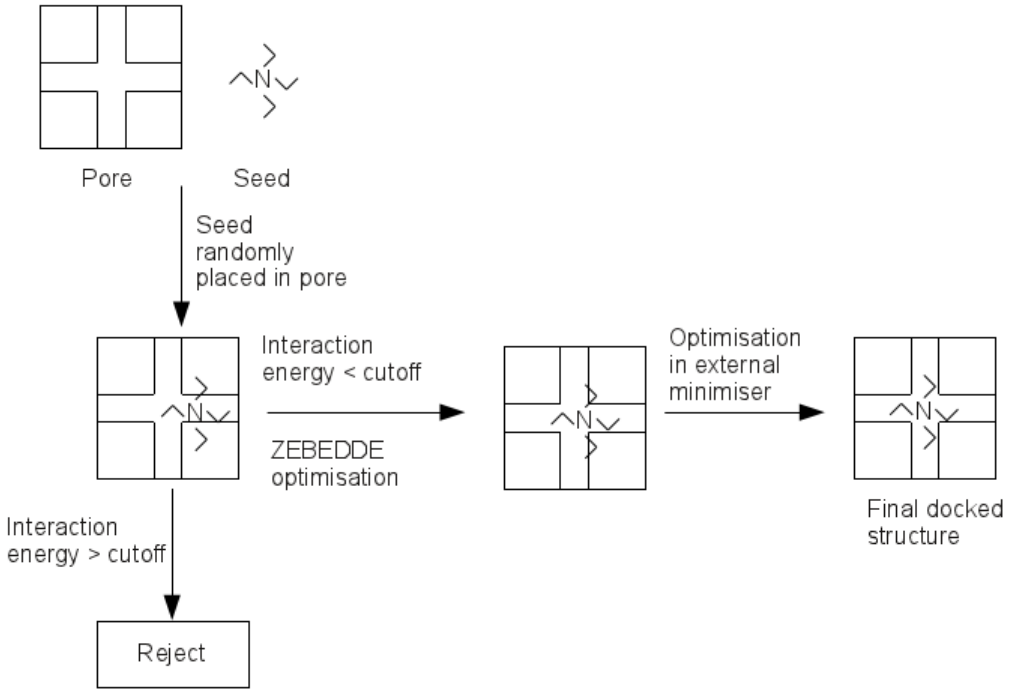

Figure 4.4: Diagram of the docking process in ZEBEDDE. The seed is the template and the pore is the framework. Typically the external minimiser used is Discover, but it is also possible to skip this step and take the docked structure straight from ZEBEDDE.

mitted to another computer resource where it can run whilst the initial job searches for further structures. Once the ZEBEDDE optimisation is complete the required files for submission to an external minimiser are generated automatically and again execute on either a supercomputer or Condor pool. By automating this docking process it is possible to scan a large number of templates for fit within a particular framework efficiently with minimal input from the user.

4.3 Boggsite Template Design

4.3.1 Introduction

Boggsite is a naturally occurring two dimensional zeolite with intersecting 12 and 10 member channels, which create a large cage. Boggsite was first discovered in Goble, Columbia-county, Oregon, USA [218, 219] and later in Antarctica [220]. However, it was only found in very small quantities and so its catalytic abilities could not be properly evaluated. When the work presented in this chapter was carried out, Boggsite had not been made synthetically, but in a recent paper by Simancas *et al.* the first synthesis of this zeolite was proposed using a novel phosphazene template [221].

4.3.2 Computational Methods

The improved ZEBEDDE code has been used for the majority of the calculations presented here. Molecular interactions are modelled using the PCFF forcefield [222]. The Boggsite structure used in this work is that of Pluth and Smith [218], where a siliceous framework was first optimised using the potentials of Sanders, Catlow and Leslie [188] in the GULP code [214]. A 2x2x3 supercell was created which was then kept fixed and used for all building, and docking calculations. When carrying out the building of new templates it is possible to weight certain actions over others meaning there is a higher chance of particular actions being selected. The building process started from a methane seed and the only fragments which were added were methane and ethane which were weighted equally. A number of different building regimes were used and these are summarised in Table 4.1. The weighting factors were heavily in favour of ring formation (with ring sizes limited to five and larger) so that more clustered organics were grown rather than long chain hydrocarbons.

Regime	Rotation	Translation	Build	Ring formation	Actions
A	20	20	1	40	5000
B	30	30	1	40	5500
C	50	50	1	100	10000
D	50	50	1	100	12000

Table 4.1: Docking regimes used for the Boggsite template building calculations.

For each regime 20 templates were generated. The generated templates were examined by inspection for common structural 'motifs'. A motif might be a recurring ring structure for example two fused six rings, or two larger groups connected by a

carbon chain. These motifs are taken and docked back into the target framework. Since we are only considering space filling, the templates are constructed purely from carbon (and hydrogen). The position of the nitrogen(s) can be considered at a later stage, as we can imagine that the space occupied, and the geometry of groups around a 4 coordinated nitrogen atom will be similar to a four coordinated carbon. The interaction energies for the templates were also normalised by dividing by the number of carbon atoms in the molecule. This is to try and separate significant changes in interaction energy, that is interaction energy is more favourable because that molecule fits better within the cavity, from changes purely because the molecule is larger.

4.3.3 Results

Eighty templates were made using the four regimes described in Section 4.3.2. Generally, the templates comprised of bulky groups which resided in the channel intersections connected by long chains in the channels. From the eighty templates, nine were selected based on common recurring structural features, as starting motifs for the subsequent docking calculations[1]. The majority of these templates contain some kind of ring structure, either five or six, along with a chain. The templates made by ZEBEDDE were optimised and then docked into Boggsite to gain an understanding of which template structures work well within the framework. These templates can be seen in Figure 4.5.

Some of these structures, *Organic 2* and *Organic 3* for example, are flexible alkyl molecules with a small cross-section which are unlikely to have any structure directing effect. Nevertheless, they were included as a comparison to the more complex organics that were built by ZEBEDDE. *Organic 7* is a relatively complex structure in that it has a multiply substituted ring, but of course it is therefore likely to be difficult to synthesise. Table 4.2 contains the interaction energies of the nine templates made by ZEBEDDE within the Boggsite framework. In an attempt to normalise the results as to more easily compare templates with one another, the average interaction energy per carbon atom is also presented. Ideally, a template should interact strongly with the framework [223], and have a high average interaction energy per carbon. All the templates interact favourably with the framework and as expected the simple alkyl molecules are the worst (but still favourable) along with the bridged six member ring molecule *Organic 1*. *Organic 5* has the strongest interaction energy with the Boggsite framework, although on average per carbon it is the weakest. *Organic 8* shows promise as it has a high

[1]For clarity two dimensional structures are provided in Appendix C

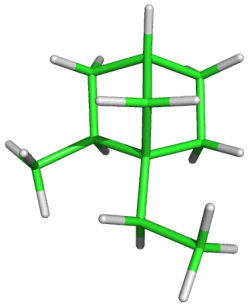

(i) *Organic 1*

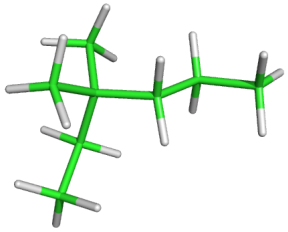

(ii) *Organic 2*

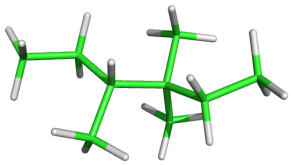

(iii) *Organic 3*

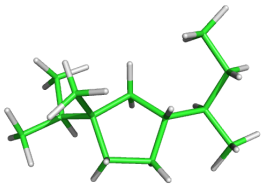

(iv) *Organic 4*

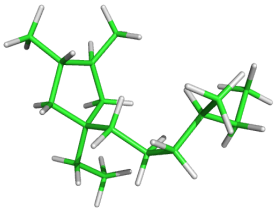

(v) *Organic 5*

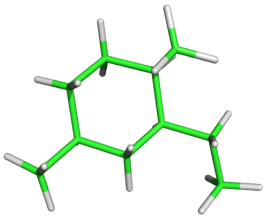

(vi) *Organic 6*

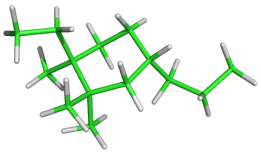

(vii) *Organic 7*

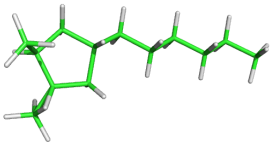

(viii) *Organic 8*

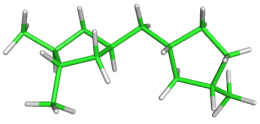

(ix) *Organic 9*

Figure 4.5: The nine starting motifs made by ZEBEDDE.

Template	Interaction energy	Number of Carbons	I.E per carbon
Organic 1	-59	10	-5.9
Organic 2	-55	8	-6.9
Organic 3	-61	9	-6.8
Organic 4	-79	13	-6.1
Organic 5	-92	16	-5.7
Organic 6	-62	10	-6.2
Organic 7	-83	14	-6.0
Organic 8	-89	13	-6.8
Organic 9	-81	14	-5.8

Table 4.2: Interaction energies for the nine motifs made by ZEBEDDE. All energies in kJ mol^{-1}.

Template	Interaction energy	Number of Carbons	I.E per carbon
Organic 10	-81	12	-6.8
Organic 11	-95	15	-6.4
Organic 12	-98	16	-6.0

Table 4.3: Interaction energies for the organic molecules derived from *Organic 8*. All energies in kJ mol^{-1}.

interaction energy and is the second highest on average per carbon. Currently this stage must be carried out manually, but the aim for the future should be to automate this using a comparison algorithm (see Chapter 7).

From the nine starting motifs, it was clear that there was a strong tendency towards five member ring structures, presumably because there is a greater probability of forming a five member ring. *Organic 8* was then taken as a starting point and some alkyl groups removed, one methyl group was left on the five ring which was in turn connected to an alkyl chain comprised of six carbon atoms. This template was named *Organic 10* was first optimised, then docked into Boggsite using ZEBEDDE. Given that organic templates are often quaternary ammonium compounds three more methyl groups were added to the end of the chain to form an isopropyl group (*Organic 11*). This forms a fully substituted carbon where a nitrogen can be inserted to give a quaternary ammonium compound. Along with this, a second methyl was added to the same carbon on the five ring (*Organic 12*) as to give a diquaternary ammonium compound. These new organic molecules were optimised before docking into Boggsite. The interaction energies calculated from the ZEBEDDE docking calculations, and structures and be found in Table 4.3 and Figure 4.6.

We can see that removing one of the methyl groups from the five ring causes a favourable drop in interaction energy of about 8 kJ mol^{-1}, but adding the isopropyl

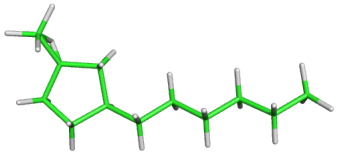

(i) *Organic 10*

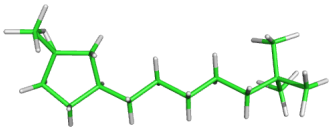

(ii) *Organic 11*

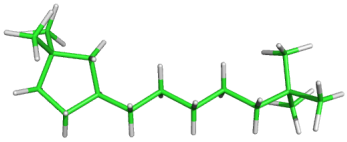

(iii) *Organic 12*

Figure 4.6: Organic templates derived from the *Organic 8* template.

group to the end significantly improved the interaction energy. *Organic 12* now has the strongest overall interaction energy. The location of the template within the Boggsite framework is almost exclusively in the 12-MR channel, with the "head" groups in the intersection with the 10-MR channel. It is therefore not surprising that increasing the size of these head groups improves the interaction energy.

The next series of molecules aims to look at the effect of chain length on the interaction energy. *Organic 11* was taken and the methyl group on the five ring removed to give *Organic 13* which has (not counting the isopropyl head group) a carbon chain length of five. *Organic 14* has a chain length of four, *Organic 15* has a chain length of six and *Organic 16* a chain length of 7. Figure 4.7 shows the structure of these templates and Table 4.4 contains the interaction energies for these templates with the Boggsite framework. From the interaction energies it is clear that the chain length of six is the most stable within the framework followed by five then four. Although *Organic 16* has an interaction energy very slightly more favourable than *Organic 15*, the energy per carbon is also lower. This implies the optimum is a chain length of six.

Organic 1 has a bridged six ring structure which previously had an interaction energy of -59 kJ mol^{-1}. This was taken and connected to an isopropyl group to give *Organic 17*. *Organics 18*, *19*, *20* and *21* are once again investigating the effect of

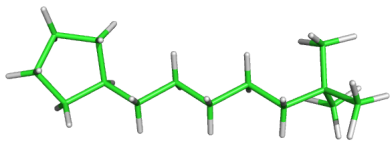

(i) *Organic 13*

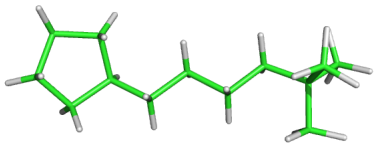

(ii) *Organic 14*

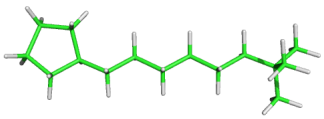

(iii) *Organic 15*

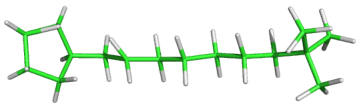

(iv) *Organic 16*

Figure 4.7: Organic templates derived from the *Organic 11* template to investigate the effect of chain length.

Template	Interaction energy	Number of Carbons	I.E per carbon
Organic 13	-87	14	-6.2
Organic 14	-80	13	-6.2
Organic 15	-99	15	-6.6
Organic 16	-101	16	-6.3

Table 4.4: Interaction energies for the organic molecules derived from *Organic 11* to investigate chain length. All energies in kJ mol^{-1}.

Template	Interaction energy	Number of Carbons	I.E per carbon
Organic 17	-70	12	-5.9
Organic 18	-89	15	-5.9
Organic 19	-98	16	-6.1
Organic 20	-103	17	-6.1
Organic 21	-107	18	-5.9

Table 4.5: Interaction energies for the organic molecules derived from *Organic 17* to investigate chain length. All energies in kJ mol^{-1}

Template	Interaction energy	Number of Carbons	I.E per carbon
Organic 22	-91	15	-6.1
Organic 23	-98	16	-6.2
Organic 24	-108	17	-6.3
Organic 25	-111	18	-6.2

Table 4.6: Interaction energies for the organic molecules derived from *Organic 12* to investigate chain length. All energies in kJ mol^{-1}.

chain length on the interaction energies with Boggsite. These can be seen in Figure 4.8 and the interaction energies in Table 4.5. *Organic 21* has the most favourable interaction energy at -107 kJ mol^{-1}, approximately 4 kJ mol^{-1} better than *Organic 20* which has a chain length of six. However, if we look at the average energy per carbon we can see that this peaks at *Organic 19*, with *Organic 20* having an identical per carbon energy. Unlike the series of organics derived from *Organic 11*, there is not as clear a peak in the average interaction energy per carbon, because the larger bridged six ring filling more space within the channel intersections.

The final set of four templates trialled (*Organics 22-25*) were derived from *Organic 12* and can be see in Figure 4.9. Once again, the chain length was altered to find the optimum length. If we look only at the interaction energies in Table 4.6, we notice the interaction energy becomes steadily more favourable as the chain is made longer. We also notice that overall the energies are more favourable than for the those obtained from the series derived from *Organic 17*. This is due to the five ring head group being smaller than the bridged six ring in the previous series, and so fitting better within the channels of Boggsite. As with the previous set of organics, the chain length of six is most favourable.

4.3.3.1 Existing Templates

As well as the templates designed here, some existing templates were docked into the Boggsite framework as a comparison. These were the templates that are used

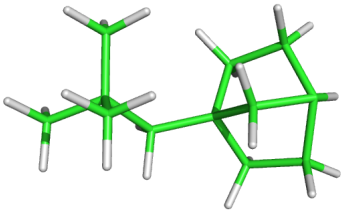

(i) *Organic 17*

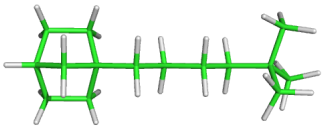

(ii) *Organic 18*

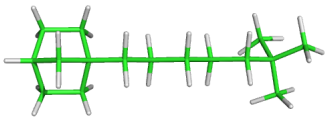

(iii) *Organic 19*

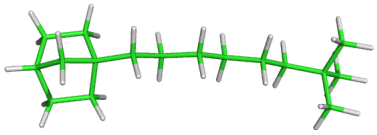

(iv) *Organic 20*

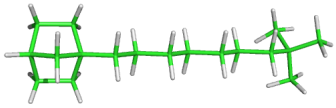

(v) *Organic 21*

Figure 4.8: Organic templates derived from the *Organic 17* template to investigate the effect of chain length.

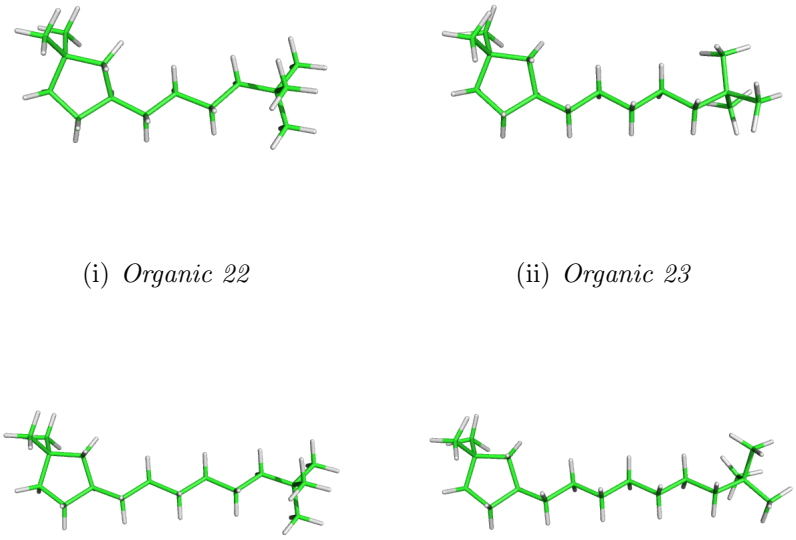

(i) *Organic 22* (ii) *Organic 23*

(iii) *Organic 24* (iv) *Organic 25*

Figure 4.9: Organic templates derived from the *Organic 12* template to investigate the effect of chain length.

to synthesise the pentasil zeolite SSZ-56 (SFS) and CIT-1 (CON). Both of these structures, like Boggsite, have 12-10 MR intersecting channels and so if these templates have an interaction energy less favourable than those designed for Boggsite, we can be more certain that the templates designed with ZEBEDDE will direct Boggsite. As well as these two templates, the template recently found by Corma *et al.* to make Boggsite was also tested [58]. These templates are shown in Figure 4.10 with the interaction energies given in Table 4.7. We can see that *Organic 26* which is used to make SSZ-56 has a strong interaction energy but still less than the templates designed here. Interestingly the template which has been shown to make Boggsite also has a weaker interaction energy (although still favourable) than the templates designed here. When looking at the synthesis conditions used by Corma it is interesting to note that germanium, known to assist in the formation of four member rings, was used in the synthesis, whereas the natural Boggsite is found as an aluminosilicate [220] with no germanium. Although it does appear that this template is less favourable than those generated here we must also consider limitations in the method. We have considered the central phosphorus atom in the Corma template as a carbon and there may be framework-template interactions which are not adequately represented by the forcefield. Similarly, the molecule was optimised

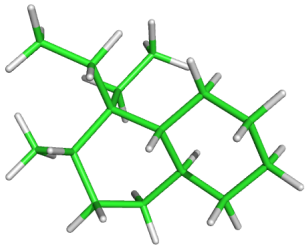

(i) *Organic 26*

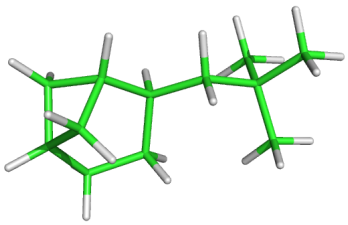

(ii) *Organic 27*

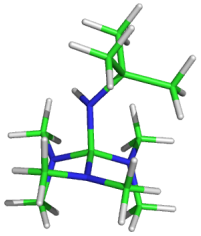

(iii) *Organic 28*

Figure 4.10: These templates are known to make 10-12 MR channel zeolites. *Organic 26* makes SSZ-56 and *Organic 27* makes CIT-1. *Organic 28* is the template used by Corma *et al.* to synthesise Boggsite. Note that the templates have been simplified in order to make the results comparable. The nitrogen groups in SSZ-56 and CIT-1 have been converted to carbons, and the central carbon in *Organic 28* have been converted from phosphorus.

with a carbon not a phosphorus and therefore bond lengths may be different.

4.3.4 Conclusions

The ZEBEDDE code has been used to design two organic templates that may direct the zeolite Boggsite. These templates were designed by first building many structures using ZEBEDDE. These were then analysed by inspection for "motifs" which are common structural features. Taking these motifs as initial starting points, templates were designed, using chemical intuition, around these using features which ze-

Template	Interaction energy	Number of Carbons	I.E per carbon
Organic 26	-83	15	-5.5
Organic 27	-69	12	-5.7
Organic 28	-84	15	-5.6

Table 4.7: Organic templates used to make other pentasil zeolites, and the template (*Organic 28*) used by Corma *et al.* to make Boggsite. All energies in kJ mol^{-1}.

olite organic templates usually posses such as quaternary sites which can be changed to nitrogen ammonium cations. By docking these back into the Boggsite framework and analysing the interaction energies the template was improved upon. This led to two asymmetrical templates that could be made as diquaternary ammonium compounds which are shown in Figure 4.11 within the Boggsite structure. It is also interesting to note that the template which has been shown to make Boggsite has a lower interaction energy than some of the templates tested here, both overall, and per carbon. This could either be because the simplification of the template, or because of flaws in the method. Here we are treating the template as purely space filling, meaning we will lose any electrostatic effects caused by the charged phosphorus atom in the centre.

Although templates have been designed which may direct Boggsite, there are of course many other synthesis parameters that can be adjusted. As was discussed in the introduction to this thesis, the template expands the phase space (i.e. ratios of SiO_2/Al_2O_3, SiO_2/NaOH etc.) where a particular zeolite can be found. This still means careful selection of synthesis conditions are required, or more likely, a search using high throughput techniques.

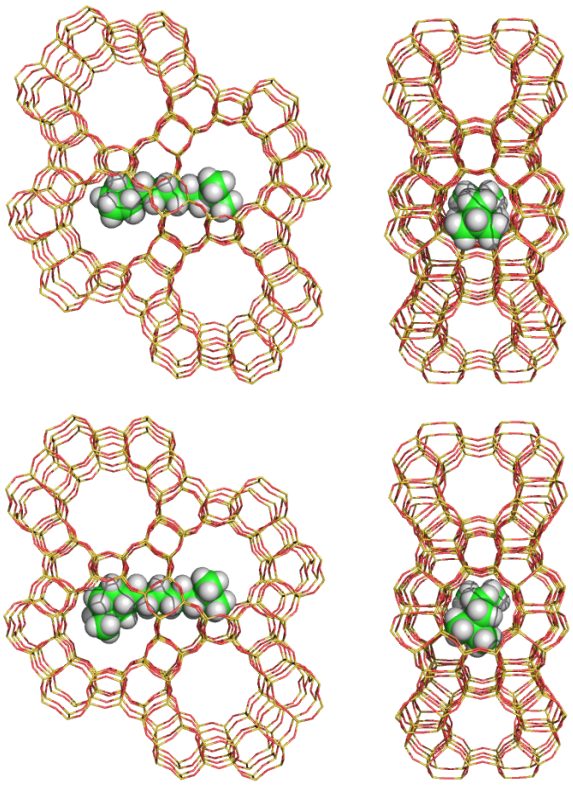

Figure 4.11: Possible organic templates for the direction of the zeolite Boggsite within the framework. Organic 20 (1-(7,7-dimethyloctyl)-bicyclo[2.2.1]heptane) (top) and Organic 24 (3-(7,7-dimethyloctyl)-dimethylpentane) (bottom), viewed down the 12 MR channel (left) and 10 MR channel (right).

4.4 MCM-68

4.4.1 Introduction

MCM-68 (MSE) was discovered in 1997 at Mobil by Weston and Dhingra with the patent being released a few years later, [224, 225, 226, 227], MCM-68 was the focus of much research over the next few years, owing to its catalytic properties [228, 229]. MCM-68 is a three dimensional zeolite, with a straight 12-ring channel and two orthogonal tortuous 10-ring channels, see Figure 4.12. The 10-ring channels intersect with each other forming an 18 x 12-ring cage with four 10-ring windows into the 12-ring straight channels. MCM-68 was originally synthesised from a hydrogel containing N,N,N',N'-tetraethylbicyclo[2.2.2]-oct-7-ene-2R,3S:5R,6S-dipyrrolidinium diiodide, Bicyclo-NEt_4-Diquat, (denoted SDA#1 here) as the template with a SiO_2/Al_2O_3 ratio of 18. Increasing the SiO_2/Al_2O_3 ratio leads to the formation of ZSM-12 (MTW) whilst decreasing the SiO_2/Al_2O_3 ratio leads to Beta (BEA). Interest in this particular zeolite has recently been renewed with the discovery of new template 1,1-dialkyl-4-cyclohexylpiperazin-1-ium (SDA#2) which directs MCM-68 [230] but also expanded the compositional space where the zeolite could be formed. Two new templates have recently been identified as directing MCM-68, 3-hydroxy-1-(5-(1-methylpiperidin-1-ium-1-yl)pentyl)quinuclidin-1-ium (SDA#3) and 3-hydroxy-1-[2-(1-methylpiperidinium-1-yl)butyl]-1-azoniabicyclo[2.2.2]octane (SDA#4) [231]. During the course of this work, 1,1'-pentane-1,2-diylbis(1-methylpiperidinium) (SDA#8) was also identified.

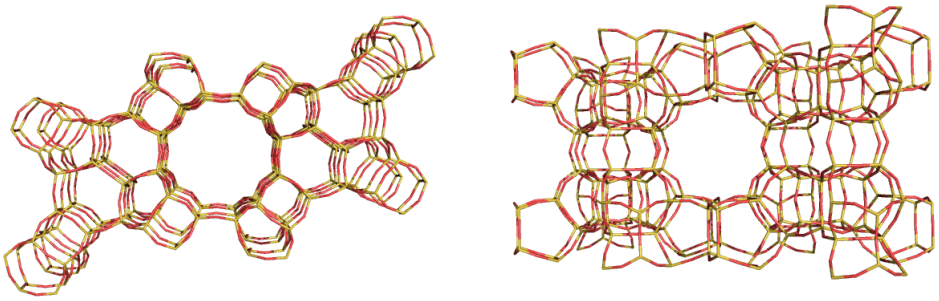

Figure 4.12: View along the 12 MR channel of MCM-68 (left) and along the tortuous 10 MR channel (right) into the cage at the intersection.

4.4.2 This Study

The aim of this study is to compliment synthetic work being carried out at Exxon-Mobil Research and Engineering on the zeolite MCM-68. Due to the excellent catalytic activity of MCM-68, there is a drive to synthesise this zeolite with different templates in order to make the material commercially viable. Computational methods will be used to carry out docking calculations on organic templates which have recently been found to direct the synthesis of MCM-68 [230]. It is hoped that these simulations will provide insight into the reasons why these templates lead to the formation of this zeolite. Moreover, it will serve as a guide as to whether some templates which have already been screened but did not form MCM-68 should be evaluated further. When carrying out screening of templates via high throughput techniques some zeolites, such as Mordenite and ZSM-12, form more frequently than others. Therefore in this study we also test how well a template fits within these other frameworks as we can imagine that if the template has a stronger interaction energy in ZSM-12 than in MCM-68 it is more likely that ZSM-12 will form. As well as ZSM-12, Offretite (OFF) and Erionite (ERI) are also observed as competing phases in synthesis from potassium containing gels with SiO_2/Al_2O_3 ratios of 10-40 and so the templates were also docked into these frameworks.

4.4.3 Computational Methods

The following calculations were carried out on the high performance computing cluster at ExxonMobil Research and Engineering . The coordinates for the frameworks were taken from the IZA website [4] and optimised using the Discover module that is part of the Accelrys Materials Studio package [215] with the energy contributions being calculated using the PCFF forcefield [222]. Once optimised, the frameworks were kept fixed for all subsequent calculations. The templates for the study were built using the visualiser in Materials Studio, and optimised in the same way as the frameworks. See Figure 4.13 for the template structures. The docking calculations were carried out using the improved ZEBEDDE code discussed in section 4.2.3. Twenty five docked structures were generated for each framework/template combination. The average energy interaction energy for each combination was then calculated. Note all energies were calculated with electrostatics turned off.

4.4.4 Results

The interaction energy per guest template molecule has been calculated for each of the framework/template (host/guest) combinations and are shown in Table 4.9. For

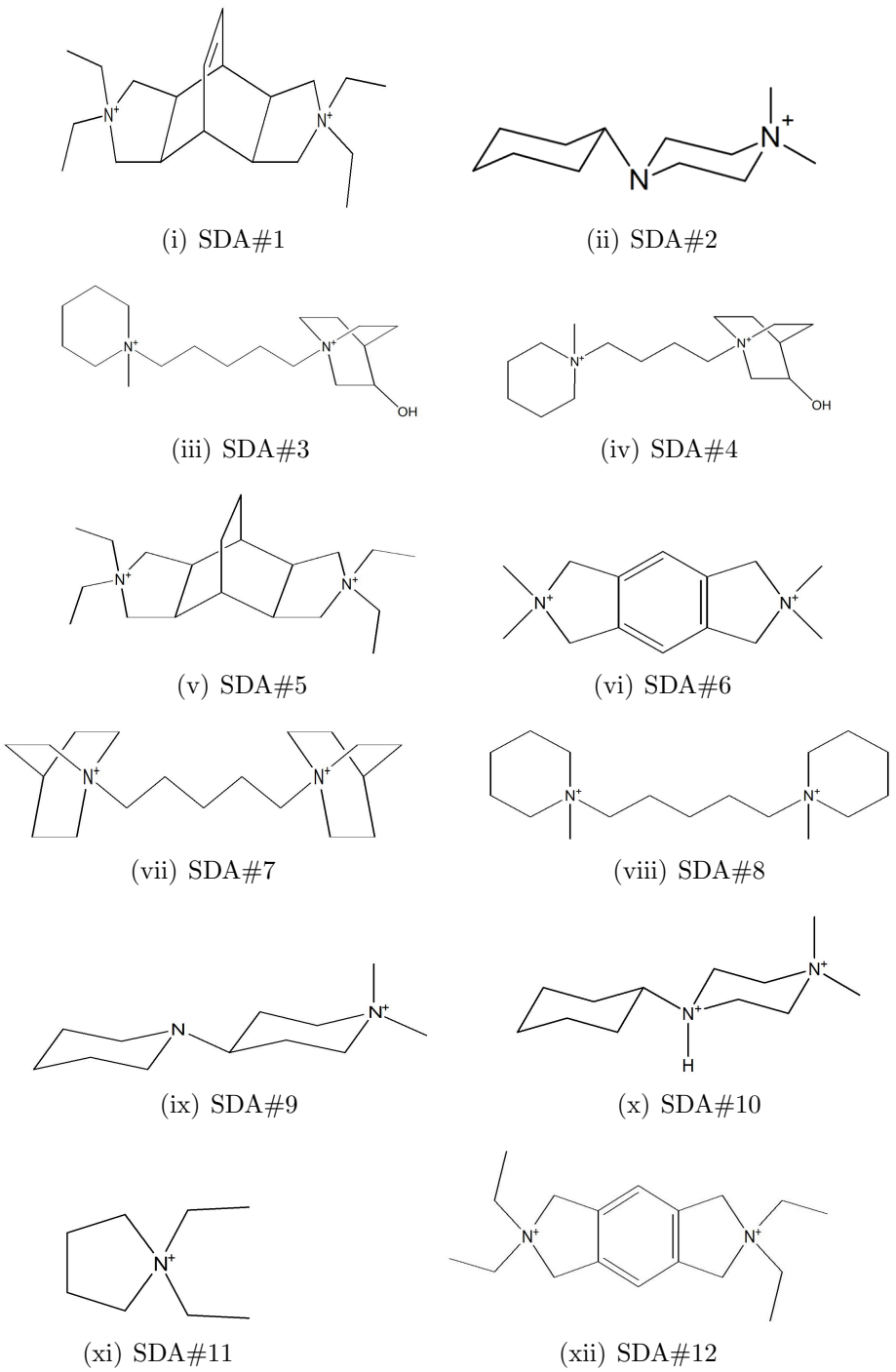

Figure 4.13: Templates used in the study. SDA#1 is the original template used to synthesise MCM-68. SDA#2 is the template recently reported make MCM-68 [230]. SDA#3, #4 and #8 are also also known to make MCM-68 [231].

the one-dimensional frameworks only one position for the template is observed and the energies of the 25 structures were averaged. However, some of the two- and three-dimensional structures have multiple potential template locations and therefore each structure was viewed and the interaction energies for the different template locations were averaged separately. This is particularly clear for the locations in MSE. The frequency a particular template docked into the three positions is presented in Table 4.8 and the average interaction energies are presented in Table 4.9. Each template is discussed in turn, highlighting unusual, or significant features which may be related to why a particular template does, or does not direct the formation of MCM-68.

Template	Channel	Cage	Intersection
SDA#1	20	2	3
SDA#2	9	4	12
SDA#3	19	1	5
SDA#4	10	0	15
SDA#5	20	1	4
SDA#6	8	4	13
SDA#7	14	1	10
SDA#8	13	0	12
SDA#9	13	2	10
SDA#10	13	1	11
SDA#11	21	4	0
SDA#12	18	2	5

Table 4.8: Frequencies of the template in the three positions in MSE.

	Framework								
Template	MSE channel	MSE cage	MSE int	BEA	MTW	MOR	ERI	OFF	MFI
SDA#1	-186.2	-174.4	-43.5	-154.2	-150.7	-173.3	-47.3	-157.0	-68.2
SDA#2	-123.8	-132.8	-113.1	-118.7	-128.3	-126.2	-143.7	-131.0	-76.1
SDA#3	-167.2	-137.9	-96.1	-221.5	-108.7	-158.8	-83.6	-121.2	-179.7
SDA#4	-195.4	-178.2	-161.9	-173.6	-183.6	-192.0	-59.9	-199.6	-160.9
SDA#5	-185.6	-182.4	-80.2	-138.5	-154.1	-181.1	-9.0	-156.8	-50.1
SDA#6	-131.4	-131.9	-78.3	-124.8	-138.2	-134.0	-125.9	-138.9	-75.3
SDA#7	-173.2	-124.1	-130.0	-148.2	-168.1	-170.1	-50.5	-182.4	-154.1
SDA#8	-188.7	-175.1	-156.9	-174.3	-193.6	-197.7	-33.6	-194.8	-174.8
SDA#9	-122.9	-135.1	-96.6	-119.0	-128.8	-127.2	-135.6	-131.0	-75.6
SDA#10	-127.2	-141.7	-75.9	-120.8	-132.1	-133.4	-147.9	-135.2	-78.8
SDA#11	-75.8	-31.8	0.0	-73.4	-80.6	-79.0	-74.2	-76.4	-74.9
SDA#12	-156.1	-152.2	-57.0	-144.5	-150.3	-154.5	-97.0	-150.9	-100.6
Largest ring size	12	12	10	12	12	12	8 (12 cage)	12	10

Table 4.9: Average interaction energies for the twelve templates in the study with the frameworks. Note that the energy for SDA#4 in MSE cage drops to -146 kJ mol^{-1} after simulated annealing. All energies are in kJ mol^{-1}.

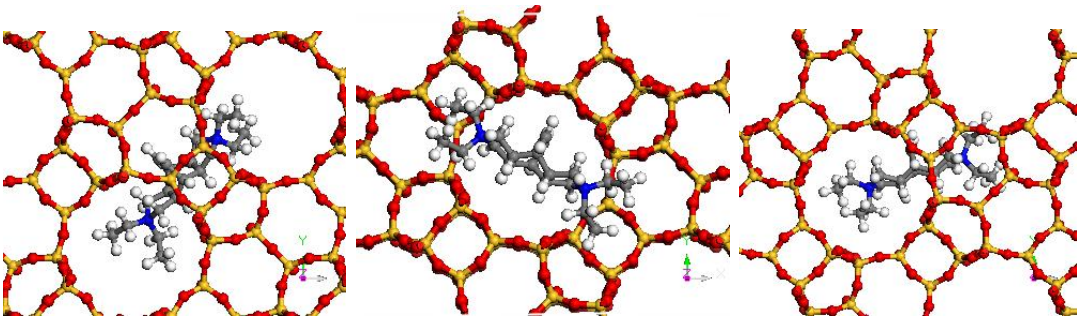

Figure 4.14: Three different positions of SDA#1 at the cage-channel intersection.

4.4.4.1 SDA#1

In a previous study by Weston SDA#1 in MSE [232] was seen to occupy two locations. In this study a third location was found. This third location has SDA#1 sitting in the 10-ring channel intersection with the 12-ring cage. Three variations of this are seen (Figure 4.14) where the template sits in the 10-ring channel;

1. It spans one 12-ring channel through the 18-ring cage into an adjacent 12-ring channels.

2. It spans one 12-ring channel.

3. It sits half in the 18-ring cage and half in the 12-ring channel.

An interesting point which came from running multiple calculations was that we could get an idea of how likely a guest would dock in a particular position. For example the number of times a guest ends up in the intersection position in MSE appears to be related to how flexible the organic molecule is. SDA#1 only docked into the intersection 4 times out of 25, whereas SDA#8 which has a flexible chain docked into the intersection 12 times out of 25. This is not a particularly surprising result as clearly a more flexible molecule will be able to bend through the 10-ring window. Figure 4.15 compares the cage, the 12-ring channel and the more stable 4b 10-ring channel. If we look at SDA#1, which is the original MSE template, the interaction energy at the channel site is much lower than in all other frameworks. The cage has a similar energy to MOR, however, MOR is not seen in the synthesis, possibly due to other conditions preventing its formation. It is likely that MOR is not formed because of the lack of sodium and thus potassium inhibits the formation of MOR. The intersection position in MSE is far less favourable.

MFI and BEA also have multiple locations for SDA#1. In MFI it can sit along the straight 10-ring channel, or in the sinusoidal channel. There is a great deal of

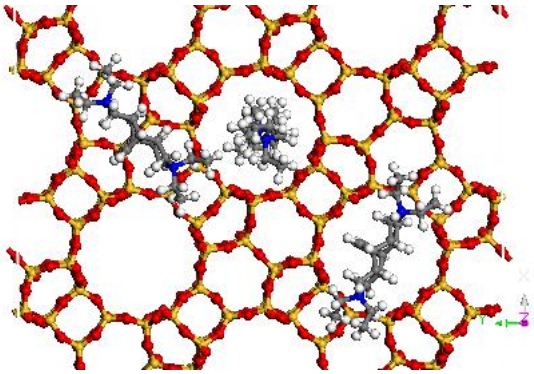

Figure 4.15: Three docked positions of SDA#1 in MSE. Left - cage. Middle - channel. Right - intersection.

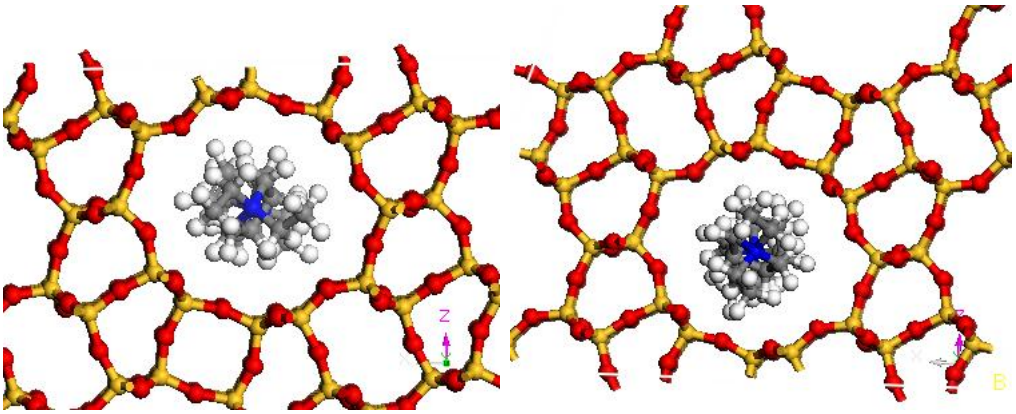

Figure 4.16: The two orientations of SDA#1 in MTW. The position on the right is more stable.

variation between these two positions with minimal difference in interaction energy, and so an average over all 25 was still taken. In BEA SDA#1 can sit in the cage, or bridge two cages, but the energies for each site are almost identical, so again these were averaged over all 25. Although MTW has a uniform channel (there are no cavities/channels leading off it), the cross section is actually oval. Hence rotating the guest within the channel can actually give significantly different energies. This occurs because the template is relatively planar and so the vdW interactions are strongest when the template is orientated such that the greatest surface is presented to the channel wall, see Figure 4.16.

4.4.4.2 SDA#2

The second template experimentally found for MCM-68 is SDA#2. It is only possible to make MCM-68 using this template if the synthesis is seeded with MCM-68 made using SDA#1. The same template locations are observed with SDA#2 as with

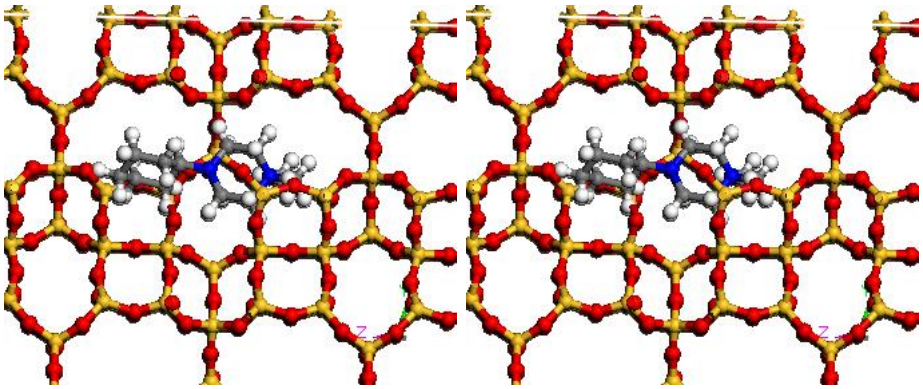

Figure 4.17: SDA#2 in ERI. The template only just fits inside the cage of ERI.

SDA#1. However, due to the smaller size of SDA#2 more intersection locations are seen. The interaction energies for all the other frameworks are nearly identical to MSE with the exception of ERI. Figure 4.17 shows the location of SDA#2 in ERI. The template sits in the 12-ring cage. These cages are relatively short hence the larger molecules do not fit well within them. Given that it is only possible to make MCM-68 with SDA#2 when seeds are incorporated into the synthesis it appears that it is a non-specific template and is acting as a space filler rather than a structure director.

4.4.4.3 SDA#3 and SDA#4

SDA#3 and SDA#4 are asymmetric diquaternary ammonium cations with quinuclidinol at one end and methyl piperidine at the other and both have been observed to make MCM-68 [231]. SDA#3 has a chain length of 5 and SDA#4 has a chain length of 4. SDA#4 gave favourable binding energies for MSE with the interaction energies being slightly more negative (stronger interaction) than for SDA#1. SDA#4 on the other hand is now approximately 41 kJ mol^{-1} less favourable in MSE than SDA#3. This could be due to the longer chain positioning the head groups in less favourable locations at the intersections.

There are a couple of interesting differences between the two templates. The interaction energy of SDA#3 in OFF is far better than with SDA#4. This is due to the longer chain length forcing the molecule into the channel where it is more stable, and excluding it from the cavity, see Figure 4.18. By removing the cavity docked structures of SDA#4 from the analysis the average interaction energy in OFF becomes comparable to that of SDA#3 (which has no cavity docked structures because it is too long).

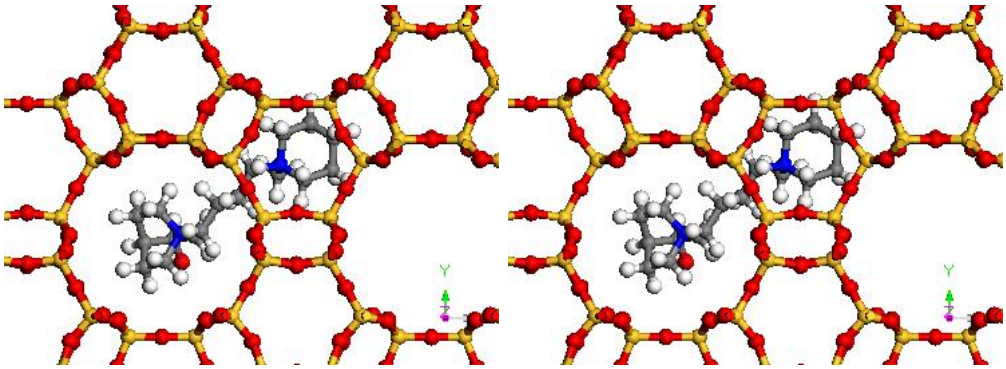

Figure 4.18: SDA#4 in OFF. The template only just fits inside the cage of OFF.

Framework/location	SDA#1	SDA#5	SDA#1 → SDA#5
MSE channel	-186.2	-185.6	-186.2
MSE pore	-174.4	-182.4	-174.4
MOR	-173.3	-181.1	-173.3

Table 4.10: The interaction energies from the initial docking run and the conversion from SDA#1 to SDA#5

4.4.4.4 SDA#5

SDA#5 is the hydrogenated version of the original template (SDA#1). Based on its good interaction with MSE it looks promising with only MOR near in energy. It is therefore surprising that attempts to synthesize MSE with this template have failed with only poorly crystalline ZSM-12 being observed [232], although only a few experiments were carried out. These results suggest that SDA#5 should make MSE. The interaction energies are very slightly lower than for SDA#1 (8 kJ mol^{-1}) which is only a few degrees of temperature in a synthesis. The difference between these two molecules is very small, with just two extra hydrogen atoms on the bridge. This does not significantly change the conformation, nor does it increase the volume, and with the energy calculated with purely vdW interactions, it is therefore not surprising that the energies are similar. As a test, the structures from SDA#1 were hydrogenated and re-minimized. The interaction energies of these altered SDA#1s are identical energies to the initial run with SDA#5 (see Table 4.10) and so we know that the bridge does play a role as the interaction energy changes when the bridge is hydrogenated.

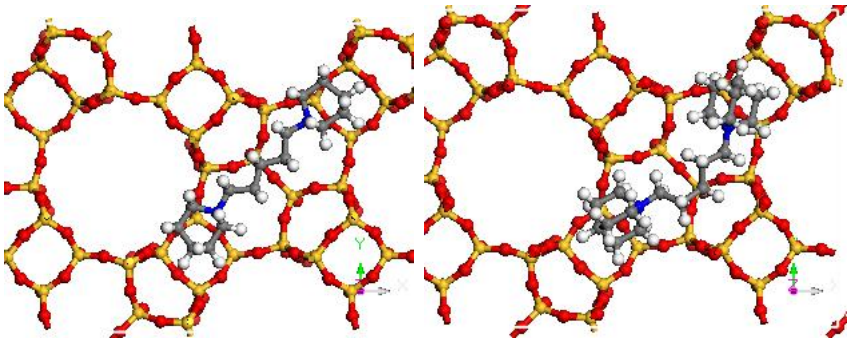

Figure 4.19: Pre (left) and post (right) simulated annealing of SDA#7. Note the buckled chain conformation in the image on the right.

4.4.4.5 SDA#6, SDA#7 and SDA#8

SDA#6 has near identical binding energies for most of the frameworks. This would mean that this template is unlikely to make MSE selectively over another material. SDA#6 was not found to have the largest interaction energy with MSE contrary to the previous computational study. SDAs #7 and #8 are symmetrical versions of SDA#3. The most obvious difference is the cage energy observed in SDA#7 which is less stable than that for SDA#3 and SDA#8. Interestingly the asymmetric diquaternary cation energies fall between the two energies for the symmetric cations. This suggests that the larger quinuclidine group makes the molecule slightly too large for the cage. A simulated annealing of this structure with the framework fixed shows that the methylene chain in SDA#7 buckles to relieve the unfavourable interactions at the end groups. The interaction energy also drops from -124 to -146 kJ mol^{-1} which brings it in line with SDA#3, see Figure 4.19. Although in this case running a simulated annealing was useful, many of the templates studied here are rigid and so running these templates would not be useful. While these calculations were being carried out experiments were in progress with SDA#8 and these yielded MCM-68 agreeing with the observed highly favourable interaction energy (better than SDA#1).

4.4.4.6 SDA#9 and SDA#10

SDAs #9 and #10 were run to compare to SDA#2. SDA#9 has the second N in a different position and SDA#10 is a protonated SDA#2. SDA#2 and #9 have similar energies, but when we protonate SDA#2, as we would expect it to exist in solution, to give SDA#10 we see the interaction energy for all frameworks improve, and spread slightly further apart. This could be because the change in the conformation of the molecule which is caused by the protonated nitrogen. In SDA#10 the two rings are in

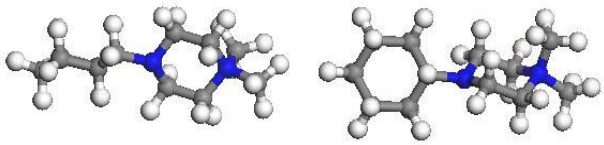

Figure 4.20: Two pictures to show the orthogonal ring conformation of SDA#2.

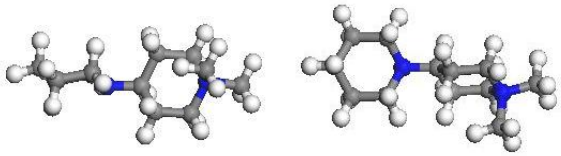

Figure 4.21: Two pictures to show the orthogonal ring conformation of SDA#9.

the same plane where as SDA#2 and #9 have very similar *spiro*-conformations, see Figures 4.20, 4.21 and 4.22. The image on the right is a 90° rotation of the left image. This drastic change arising from conformation changes mean that it is important to treat amine groups carefully and possibly always consider the protonated version.

4.4.4.7 SDA#11 and SDA#12

SDA#11 was chosen since it is a subunit that appears in the original template, as well as others trialled. The interaction energies for this organic are less favourable than the others. This is probably due to its smaller size, and so the interactions with the framework will be lower. If we consider SDA#11 to have roughly half the number of atoms as the other templates and multiply the interaction energy by two we do get interaction energies on a par with the other templates. This could be an ideal cation to use as a space filler.

SDA#12 is identical to SDA#6 except that the methyl groups are replaced with ethyl groups. The interaction energies for SDA#12 are generally better than SDA#6. The interaction energies for SDA#12 are again clumped together suggest-

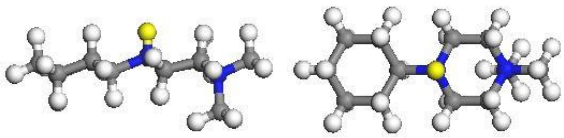

Figure 4.22: Two pictures to show the conformation of SDA#10 with the two rings in the same plane. Note the proton on the middle nitrogen which is highlighted yellow.

ing that this template would not selectively give MSE over another framework.

4.4.5 Discussion

The above calculations were also tried with the electrostatic interactions turned on for the Discover minimisations (ZEBEDDE still works on purely vdW interactions). When the host-guest interaction energies were calculated the values were very high, approximately -650 kJ mol^{-1}, and the ordering of the guests differed from the experimental evidence. On comparison to the previous work, it was thought that this could be due to the use of PCFF forcefield instead of cff91_czeo forcefield.

Tests were carried out on a selected number of docked structures. Each was re-minimized using cff91_czeo, and then the interaction energies calculated. The absolute value of the energy changed slightly, which is expected with the use of a different forcefield, but the ordering of the interaction energies remained the same and so the choice of forcefield is unimportant.

The reason the energies are higher is due to the electrostatic interactions being strong, and hence we are trying to get a small interaction energy number by subtracting two large numbers introducing a large error. What is more surprising is that the ordering of the templates has changed. It would be expected that just the absolute values would change on inclusion of the electrostatics but the ordering would remain the same. The ordering difference is most likely due to how the overall positive charge was being neutralized by Discover. It applies a homogeneous background negative charge to the cell. This is of course nothing like an actual zeolite where the positive charge of the template is balanced by localised aluminium atom in the framework, or extra framework anions.

4.4.5.1 Advantages and Disadvantages to the Approach

The advantage of using a Monte Carlo process to perform docking calculations over manually docking templates is there is no bias toward any particular position. Had each of these been docked manually by eye, the intersection position in MSE would not have been found. The automation of the docking procedure has allowed large numbers of calculations to be run, quickly. However, improvements need to be made in the analysis process. Currently the analysis is carried out manually. Each docked structure is opened, the bonds "fixed" and the energy calculated and copied into a spreadsheet. For this study, 12 organics were docked into 7 frameworks producing 25 docked structures each, giving a theoretical total of 2,100 docked structures.

Although some frameworks, such as ERI, did not produce the full number of

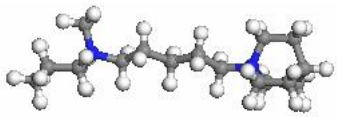

Figure 4.23: SDA#3 showing the slight curve of the main chain.

structures for each organic since the pores are small and therefore hard to dock into, there was still a large number to analyse.

For the framework/template combinations below, ZEBEDDE produced no docked structures even after 500,000 attempts:

- MSE cage for SDA#4 and #8
- MOR for SDA#3 and #8
- SDA#5 in ERI.

However, SDA#11 failing to dock in the intersection of MSE is probably due to its small size, and so if it did dock there it would be quickly moved into the channel, or into the cage by ZEBEDDE. For the MSE and MOR SDAs which failed to dock, the template was inserted manually into the framework and a simulated annealing run. Simulated annealing calculation was used instead of minimization because only one structure was made for each framework/template combination and so an average can not be taken. Interestingly, SDA#3, SDA#4 and #8 all dock favourably into MSE and MOR, it is therefore surprising that these did not dock in the initial ZEBEDDE run. It could be that the chain is slightly curved and so would not fall below the threshold energy, see Figure 4.23.

A similar procedure was carried out for ERI and SDA#5, and this gave a very poor interaction energy. This is a case where hydrogenating the double bond in SDA#1 makes a significant difference to the energy. In the case of ERI and SDA#5 the extra hydrogens must make it slightly too large for the cage. SDA#1 in ERI = -46 kJ mol^{-1}, SDA#5 in ERI = -8 kJ mol^{-1}. This highlights that sometimes ZEBEDDE is correct and sometimes not. Results obtained from ZEBEDDE are not foolproof and must be interpreted with care.

4.4.6 Summary

It is surprising that MOR is not seen in the synthesis of MSE, as the interaction energy is often as good as, and on occasion better than MSE, or MTW. We must therefore assume it is because Mordenite is normally found in a sodium system

and MSE is made in a potassium system. However, the data clearly shows why MTW is often formed during attempts to make MSE. SDA#5, the hydrogenated version of the original template (SDA#5) is also a surprising case as this one appears to interact with the framework better than the original template, and the other frameworks observed are far worse.

4.5 Tetraethylammonium in ZnAPO-34

4.5.1 Introduction

ZnAPO-34 (CHA) is a cage based zeolite, with 8 MR pore openings which connect the cages in three dimensions. The zeolite Chabazite which is the type material is a naturally occurring zeolite found in basaltic rocks, the structure first being solved in 1958 by Dent and Smith [233]. Chabazite has been synthesised with a wide variety of compositions, including pure silica [234], silicoaluminophosphate [235], and more recently a pure aluminophosphate [236]. A wide variety of transition metals have also been incorporated in the structure. The work in this chapter focuses on the zincoaluminophosphate version of Chabazite which was first synthesised in 1995 by Tulsar *et al.* [237]. This work is in collaboration with an experimental group at Utrecht University with the aim of gaining a deeper understanding of the effects of the conformation of TEA on the assembly of ZnAPO-34.

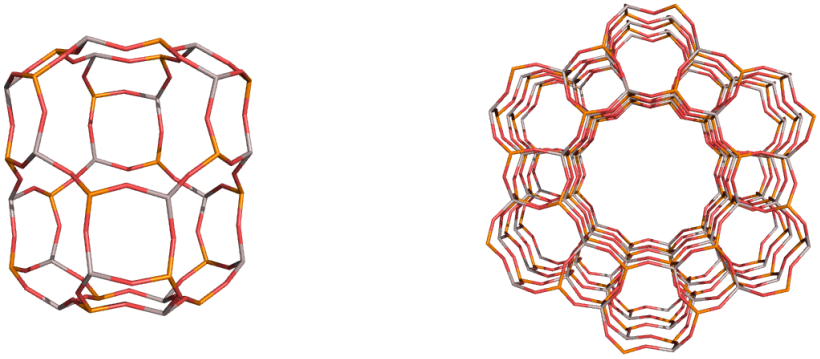

Figure 4.24: The Chabazite cage (left) and AFI channel (right).

AlPO-5 (AFI) is a one dimensional aluminophosphate containing a straight 12 MR channel. It was first characterised in 1983 by Bennett *et al.* [238]. It is also made using TEA as the organic template and so has been used as a comparison to the values calculated for Chabazite. The calculations in this section were carried out to explain observed experimental results where a particular conformation of TEA appears to be key in the formation of ZnAPO-34 [239].

4.5.2 Experimental Results

ZnAPO-34 is made using tetraethylammonium (TEA) as the organic template. The structure of TEA in solution has been studied in great detail in a combined theoretical and experimental study by Brand *et al.* Here they show TEA has four equilibrium conformations [240]. The two most stable, the D_{2d} (tt.tt) and the S_4 (tg.tg)

are shown in Figure 4.25. Using these results an experimental study by O'Brien *et al.* have shown there is an intimate link between the template conformation and the Zn^{2+} substituted into the Al^{3+} [239]. *In situ* Raman spectroscopy shows that the TEA preferentially locates in the tg.tg conformation near a Zn^{2+} substitution. It was hypothesised that the Zn^{2+} interacts with the TEA stabilising the tg.tg conformation, in contrast to the solution phase tt.tt, and this is the driving force behind the formation of ZnAPO-34. This is supported by the fact that when no zinc is included in the synthesis, AlPO-5 is the final aluminophosphate structure formed which contains most TEA in the tt.tt conformation.

As mentioned in the Section 4.5.1 , this was a combined theoretical and experimental study [241] which aims to understand further the growth of metal substituted aluminophosphates (MeAPOs). A variety of experimental techniques were used to study the crystallisation of ZnAPO-34. A number of different spectroscopic techniques were used to characterise the initial gel and follow the crystallisation, along with post-synthesis characterisation by NMR and Raman spectroscopy. It was established from these experiments that crystallisation begins from a highly heterogeneous gel which becomes increasing homogeneous as the synthesis proceeds. The *in situ* Raman measurements show an increase in concentration of TEA in the tg.tg conformation in the presence of Zn^{2+}. Furthermore, this is linked via WAXS data to an increase in the amount of crystalline ZnAPO-34 present in the mixture. Both these results imply the tg.tg conformation of TEA being essential to the formation of ZnAPO-34. *Ex situ* Raman measurements made a few years previous [239] further support this with tg.tg TEA being the dominant conformation present in the ZnAPO-34 crystals.

4.5.3 Computational Methods

The improved ZEBEDDE code discussed in Section 4.2.3 was used for the docking of TEA into the CHA framework, as well as into AFI (AlPO-5). The frameworks for both CHA and AFI were optimised using GULP [214] with the Gale and Henson potentials [242]. Once optimised the framework was kept fixed for all further calculations. The TEA was constructed in both the tt.tt and tg.tg conformations, optimised using GULP, then also kept fixed for subsequent calculations. One molecule of TEA was docked into the framework and the interaction energy calculated based on the PCFF forcefield [222]. A total of 50 structures were generated for each framework/TEA conformation combination and the interaction energy averaged. The second TEA was added manually by taking the best i.e. most negative, structure from the singly docked calculations and positioning a second molecule in the

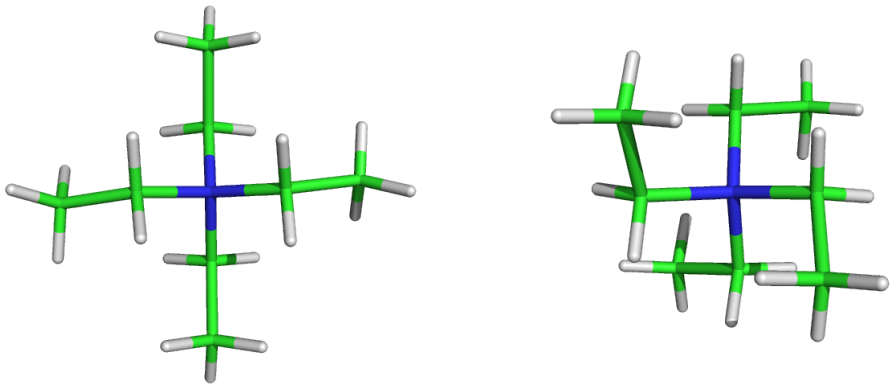

Figure 4.25: The D_{2d}(tt.tt) conformation of TEA (left) and the S_4 (tg.tg) conformation (right).

nearest possible position to the first. A simulated annealing calculation was then carried out to optimise the location of the TEA molecules, starting from 300 K and cooling in steps of 50 K to 0 K. Five annealed structures were generated for each framework/TEA conformation combination and the interaction energy averaged.

4.5.4 Results

The interaction energies for TEA in the Chabazite cage are given in Table 4.11. When we have one template in the Chabazite cage we see that the interaction energy of the TEA with the framework is favourable, with the tt.tt conformation being 4 kJ mol^{-1} more favourable showing a small preference for this conformation. However, if we compare this to the gas phase energies (Table 4.12) we see that here we have a difference in energy between the two conformations is 14 kJ mol^{-1} implying that by including it in the Chabazite framework we have brought the tg.tg conformation closer in energy by 10 kJ mol^{-1} to the tt.tt. When two templates are present in the Chabazite cage, the interaction energies are highly unfavourable. The tt.tt/tt.tt pair fits best, but when a tg.tg conformation is present the interaction energy increases by nearly 1000 kJ mol^{-1}. This result could suggest why it is not possible to prepare highly substituted ZnAPO-34 (using TEA) with a concentration of Zn greater than 30 % [241], equating to one per cage.

Table 4.13 contains the interaction energies for TEA within the AFI structure. Overall, these are less negative i.e. less favourable than in Chabazite. This is due to the pore volume in Chabazite being formed of small cages rather than a large channel as in AFI. As such, when one molecule of TEA is present in the Chabazite cage it can interact more strongly with the framework (see Figure 4.26) as it sits in the centre of the cage. Clearly, given that the pore in AFI is a channel, the TEA can only interact with the channel walls (see Figure 4.27) and this leads to a slightly lower

Conformer Configuration	Number of Templates	Interaction Energy
tt.tt	1	-102
tg.tg	1	-98
tt.tt/tt.tt	2	+632
tg.tg/tt.tt	2	+1596
tg.tg/tg.tg	2	+1587

Table 4.11: Interaction energies for TEA template within the cages of the CHA structure. All energies are in kJ mol^{-1} and per TEA molecule.

Conformer Configuration	Energy
tt.tt	-6.1
tg.tg	8.1

Table 4.12: Gas phase energies of the two TEA conformations. All energies are in kJ mol^{-1} and per TEA molecule.

interaction energy. However, it does mean that more template molecules can be accommodated within the AFI framework as can be seen in the interaction energies when multiple templates are included. There is an increase in the interaction energy by 4 kJ mol^{-1} per template when a second template is included suggesting there are favourable interactions between the two template molecules. It is also interesting to note that the favoured conformation in Chabazite is the tt.tt but in AFI it is the tg.tg. There are a number of simplifications in the calculations presented here, we are comparing gas phase TEA with solution phase. We have also omitted the zinc from the framework thereby removing potentially significant electrostatic interactions which could explain why these calculations suggest a preference for the tt.tt conformation in contrast to the experimentally observed tg.tg.

These results can be compared to the work of Lewis *et al.* on the same zeolite frameworks although this time cobalt as the transition metal and triethylammonium (TrEA) as the template [243]. In contrast to this work, where it is clear that only one TEA can be accommodated in the CHA cage, it is possible to fit two TrEA molecules due to their smaller cross section. This result was later backed up by diffraction experiments by Sankar *et al.* where they observe two triethylamine molecules in the cage of Chabazite [244]. The authors also propose a correlation between the concentration of template and cobalt with the formation of Chabazite [243] where there must be sufficient cobalt present in the gel to balance the charge of the template i.e. one per template.

Conformer Configuration	Number of Templates	Interaction Energy
tt.tt	1	-77
tg.tg	1	-81
tt.tt/tt.tt	2	-85
tg.tg/tt.tt	2	-85
tg.tg/tg.tg	2	-85

Table 4.13: Interaction energies for TEA template within the cages of the AFI structure. All energies are in kJ mol^{-1} and per TEA molecule.

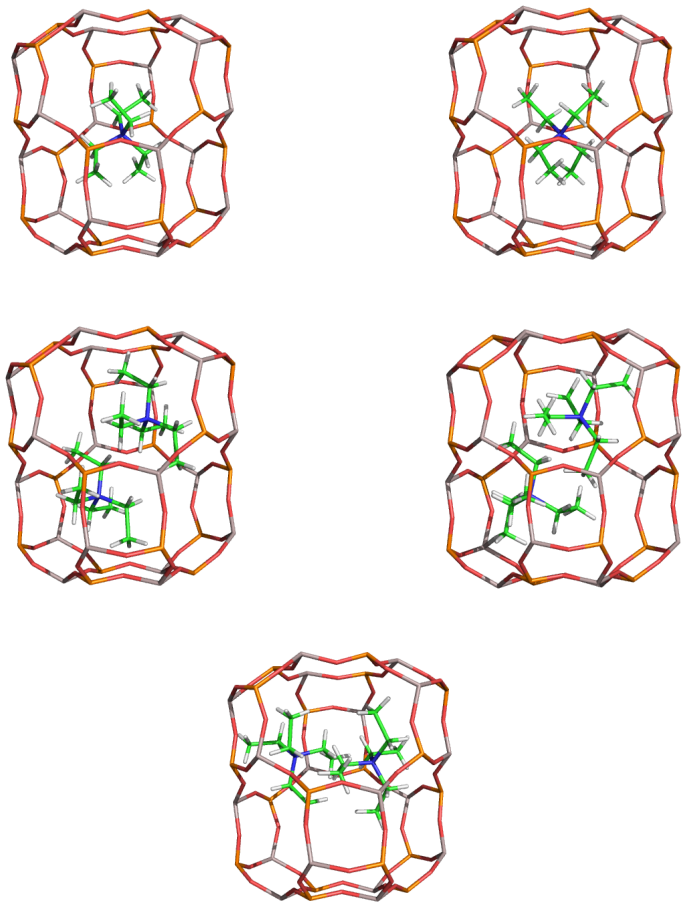

Figure 4.26: Images showing the location of TEA in CHA.

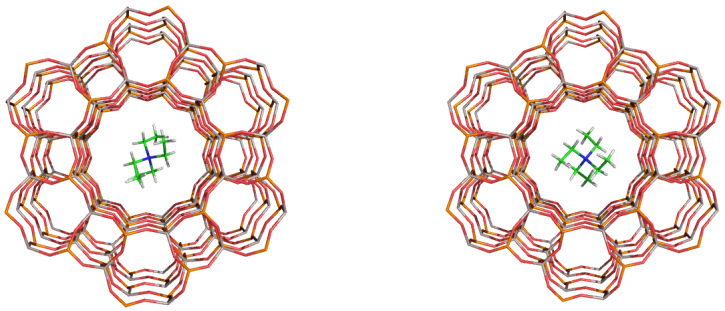

Figure 4.27: Images showing the location of TEA in AFI.

4.5.5 Conclusions

The ZEBEDDE code has successfully been used to dock TEA in two conformations into the cavities of both Chabazite and AlPO-5. The results suggest that only one TEA molecule will fit into the CHA cage. The calculations presented here do not agree with the experimental evidence. This is probably because of simplifications in the model used. Zinc has been omitted from the framework and there will be strong interactions between the template and the framework due to the negative charge introduced. It could be that these are stronger when the template is in the tg.tg conformation and this is why it is observed experimentally. Since it seems specific conformations of TEA are required to make ZnAPO-34 we can say that it must have more than a space filling role, but it is also difficult to say it had a strong structure directing role as MeAPO-34 can also be synthesised in the presence of other templates [245, 243]. What is clear, is that there is a strong interaction between the template and the presence of the metal ion, and this leads to the formation of MeAPO-34. However, that these calculated results do suggest the template-framework combination would favour the conversion of solution tg.tg TEA to the tt.tt form most favoured in the framework. Moreover, it is easy to rationalise the experimental maximum in Zn content based on these (and previous) docking calculations. However, the interactions between the template and metal cations are not trivial, and are something not considered in the calculations presented here and future work should focus on gaining insight into this.

4.6 Conclusions

The ZEBEDDE code has been improved by rewriting the ring making routine. The new routine allows rings to be formed more readily within the growing template molecule producing more yielding more complex organic molecules. Along with this the docking routines have been updated in order to automate the processes allowing more systems to be analysed with less input from the user. In order to further take advantage of these improved routines, ZEBEDDE can now be used on a supercomputers allowing task farming. Using this enhanced code, and combining it with high throughput techniques it could be possible to screen templates efficiently.

Using the improved ZEBEDDE code two candidate templates for the formation of Boggsite have been proposed. These are *Organic 20* (1-(7,7-dimethyloctyl)-bicyclo[2.2.1]heptane) and *Organic 24* (3-(7,7-dimethyloctyl)-dimethylpentane). These templates have been selected because they have favourable interactions within the Boggsite framework, compared to other templates which were tested. Although some aspects of the building process have been improved, it is still relatively time consuming and requires input from the user. Future modifications to the code to allow comparison of the growing template to know organic molecules would speed the process as well as forming more chemically sensible structures. Something not considered here is how well these organics fit within commonly formed synthetic zeolites such as ZSM-5 or Mordenite. If the interaction energies are more favourable in structures such as these then we can expect them to direct these over Boggsite.

The most successful use of the code relates to the work on MCM-68. The calculations explained the 'fit' of SDAs #1,#2,#3 and #4 and supported the experimental hypothesis that SDA#8 and similar molecules could template MCM-68. During the course of this work SDA#8 and two other similar organics were found to make MCM-68. An interesting outcome from these results is how close the interaction energies are when the same template is docked in different zeolites. This suggests that in some cases it may be difficult to force a particular zeolite structure over another, although the role of the other components in the synthesis are not considered here. The work on MCM-68 also provided an opportunity to investigate the inclusion of electrostatic interactions when calculating the interaction energy. It was concluded that inclusion of electrostatics is not necessary, at least for the initial screening of molecules, partly due to extra computational expense, but mostly due to the fact we are trying to fill a pore space and therefore van der Waals interactions are sufficient. The accuracy of the simulations could be improved by including electrostatics but we would need to know details such as aluminium location. If the location of the aluminium atom is unknown, the negative charge caused by the aluminium must be

balanced by smearing over the framework. This is of course unrealistic as it would, in reality, be balanced by either the template or an extra framework cation.

The work on ZnAPO-34 highlights the way calculation can complement experiment. Here, the calculations have confirmed that only one TEA molecule can fit in the Chabazite cage and hence why ZnAPO-34 cannot be prepared with concentrations of zinc greater than 30 %. The experimental work suggests that the tg.tg is the more stable conformation and this is not confirmed by these calculations. However, this is likely due to simplifications in the model used and by including the zinc in the framework the ordering could easily be reversed.

CHAPTER 5

Morphology Control

5.1 Introduction

In this chapter the influence of the template on zeolite morphology is investigated. The first section considers attempts to form crystals of zeolite L with high aspect ratio. A variety of common templates were tested for fit within the framework using the ZEBEDDE [213] code. Once suitable templates had been found, experimental work[1] was then carried out to confirm the computational findings.

The second section investigates the role of surfactant molecules on morphology of the aluminophosphate AlPO-11. Experimentally, it had been determined that including long chain (molecules with carbon chains 10-16 atoms long) amine surfactants can affect the crystal morphology of AlPO-11. Simulations have been carried out on the role of the surfactant on the surface of AlPO-11, and how this may alter the growth mechanisms.

5.1.1 Zeolite L

Zeolite L (LTL) was first characterised by Barrer and Villiger in 1969 [247] (the synthesis was a few years previous [248]) and is a one-dimensional aluminosilicate with a 12 member ring channel. The usual morphology for a zeolite L crystal is a hexagonal (see Figure 5.1) with the 12 MR channel running along the long axis of the crystal. In applications as a catalyst it is more desirable to form crystals with a

[1] All experimental work was carried out by Dr. Rhea Brent at the University of Manchester, and has been published in reference [246] along with the computational results presented here.

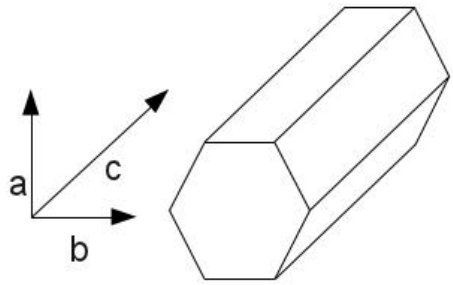

Figure 5.1: Diagram showing the usual crystal morphology of a zeolite L crystal. The channel runs along the *c*-axis.

low aspect ratio (length/diameter) i.e. short wide crystals, as this will increase the number of channel entrances and a shorter path will also reduce the diffusion time of reactants and products in the zeolite [249].

Zeolite L is typically synthesised using potassium as the only templating species and so its formation is not dependent on organic templates. Previous work has shown that varying the proportions of alumina, silica, potassium hydroxide and water [250, 251] can alter the crystal morphology of zeolite L. Specifically, Larlus *et al.* [250] showed that having a higher potassium content in the synthesis yields crystals with a smaller aspect ratio, whilst increasing water content has the opposite effect.

5.1.1.1 Growth of Zeolite L

Zeolite L is constructed of columns of cancrinite cages which are linked together by double six rings (D6R). These columns are connected by the four member rings present in the cancrinite cages to form the 12 MR channel. We have already discussed that altering the composition of the starting mixture causes crystal morphology changes, but what happens on a molecular level to cause these changes?

Brent and Anderson carried out an elegant AFM study in order to try and understand the growth of zeolite L [252]. They made three different batches of zeolite L by varying only the water content to give crystals with three different aspect ratios. In the AFM images (see Figure 5.2) they observed sharp narrow terraces on low aspect ratio crystals. However, at high aspect ratio they found that the surfaces were more spread out. By studying these terraces in more detail it was found that the narrow terraces had a height of 1.2 nm which corresponds to a single cancrinite cage on the surface, whereas the larger terraces had heights of 1.6

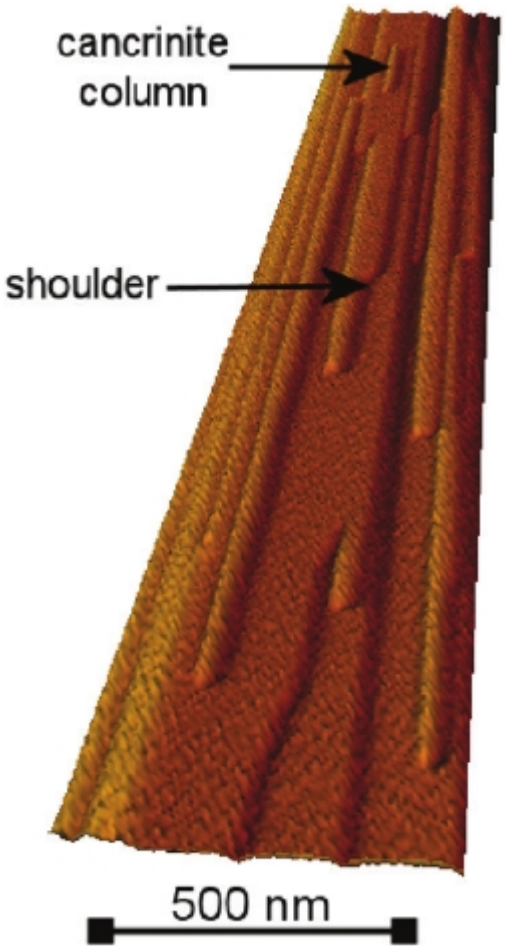

Figure 5.2: AFM of the zeolite L surface showing the terraces of cancrinite cages. Reprinted with permission from ([246]). Copyright (2010) American Chemical Society.

nm corresponding to a stacking of three cancrinite columns (see Figure 5.3). For the crystal to grow laterally, a cancrinite cage must be added to bridge the two columns on the surface and complete the 12 MR channel. Given that when on low aspect ratio crystals we observe narrow terraces, i.e. more terraces made of a single column on cancrinite cages, growth in the lateral direction is severely frustrated. In contrast, when we have crystals with a higher aspect ratio this growth becomes less frustrated.

5.2 Modifying Zeolite L Crystal Morphology

In the introduction it was noted that the growth in the lateral direction (along the a-direction) of a zeolite L crystal is frustrated. It was proposed that using an organic additive as a space-filling molecule would enable the bridging of adjacent cancrinite columns, which in turn would facilitate growth in the a-direction and create crys-

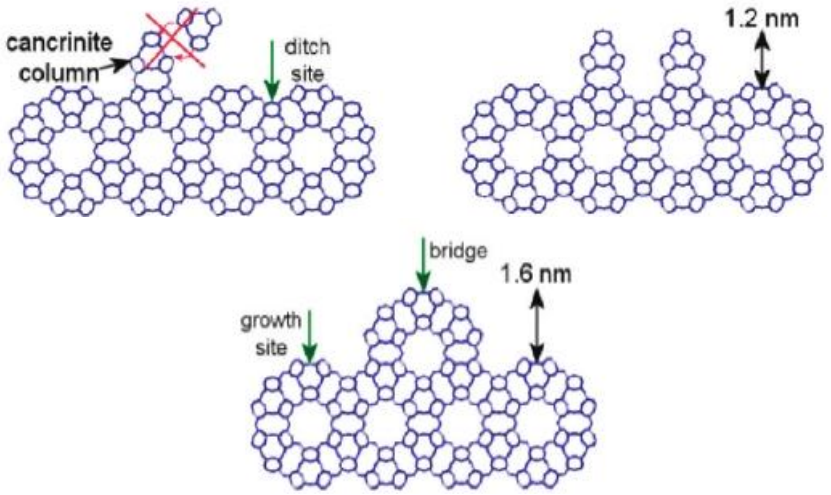

Figure 5.3: Diagrams showing the growth mechanism on the zeolite L surface by cancrinite cages. Growth is not possible when adding a cancrinite cage over a ditch site as show in the diagram in the top left. Viewed along the c-axis. Reprinted with permission from ([246]). Copyright (2010) American Chemical Society.

tals with a larger diameter. A number of organic templates were tested. Firstly, a series of crown ethers, 18-crown-6, 21-crown-7 and 24-crown-8, was considered as it was hoped these would fill the void within the channel. We also considered a series of tetraalkylammonium zeolite templates, tetraethylammonium (TEA), tetrapropylammonium (TPA) and tetrabutylammonium (TBA) along with a large cyclodextrin molecule. The structure of α-cyclodextrin is "bung" like and it was hoped that this would hinder growth in the c-direction. Growth modifications with both the crown ether and α-cyclodextrin theoretically have the same outcome as shown in Figure 5.4.

The crown ether templates were selected as they are of a similar size to the undulating channel in zeolite L which has a maximum diameter of 11 Å. Docking calculations were carried out for all the templates mentioned above. Ideally the template should interact strongly with the framework without being distorted from its equilibrium conformation and so maximising the interaction of the molecule with the framework. Thus calculation of interaction energy from docking calculations can be used as a guide for the efficacy of the molecules as a crystal modifier.

5.2.1 Computational Details

Each template was built using Materials Studio 4.3 and optimised using the Discover minimiser engine and the PCFF forcefield [222]. The template structures and approximate dimensions can be found in Figure 5.5. The Zeolite L structure is

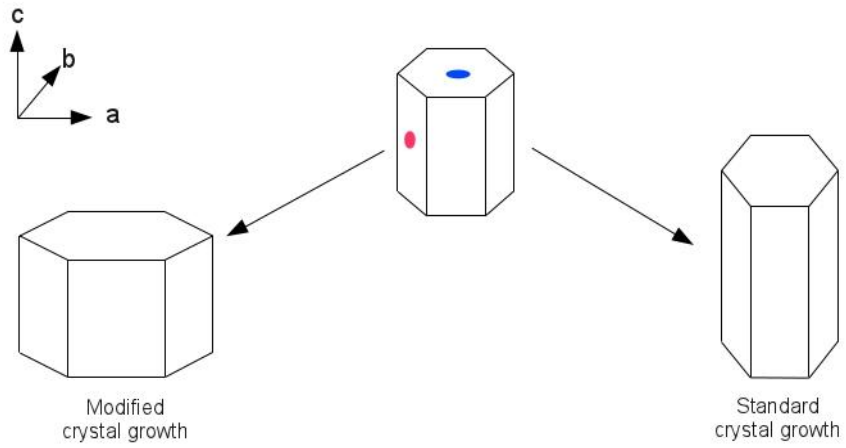

Figure 5.4: The standard growth of a zeolite L crystal (right) and the modified growth (left). The blue spot is the α-cyclodextrin which it is hoped will hinder growth in the c-direction, and the red spot is the crown ethers which it is hoped will promote growth in the a-direction.

that of Barrer and Villiger [247] with the initial coordinates being taken from the IZA website [4]. For computational ease the structure was converted to an entirely siliceous form and then optimised using the GULP code [214] and the SiO_2 potentials of Sanders, Catlow and Leslie [188]. The framework was then kept fixed for all subsequent calculations. The docking calculations were carried out using the modified ZEBEDDE code [213] with the interactions being described by the PCFF forcefield [222].

Each template was inserted into the optimised framework 10,000 times, with the interaction energy of the template with the framework calculated as follows:

$$E_{interaction} = E_{zeolite+template} - (E_{template} + E_{zeolite}) \tag{5.1}$$

where $E_{interaction}$ is the interaction energy of the template with the framework, $E_{zeolite+template}$ is the total energy of the framework and template, $E_{template}$ is the energy of the template in the gas phase and $E_{zeolite}$ is the energy of the optimised framework. If this interaction energy falls below a pre-defined threshold (+2000 kJ mol^{-1}) this structure is then further optimised using a combination of Monte Carlo steps, and finally energy minimisation using the Discover module.

The surfaces were generated using the visualisation program GDIS [253] starting from the optimised bulk structure. The surface was cleaved, in the desired Miller plane, so as to reduce the number of dangling oxygens atoms which were then hydrogenated. The opposite surface was then hydroxylated to remove any dangling silicon atoms. Both surfaces were then optimised using the potentials of Sanders,

Catlow and Leslie [188] for the bulk zeolite along with the silanol potentials of Schröder [254] using the GULP code [214]. Once the surface has been optimised ZEBEDDEs Monte Carlo simulated annealing (MCSA) routine was used to dock the template onto the surface. The MCSA calculation was started at a temperature of 300 K which was reduced in steps of 50 K to 0 K. At each temperature step, 20,000 actions were carried out in order to optimise the location of the template. The template was started at a location approximately 30 Å above the surface of the zeolite.

Here we are interested in the location effect of the template, and hoping that this will induce changes in the crystal growth. Generally speaking we can expect most templates to have favourable interactions, i.e. negative interaction energies, and we therefore are interested in differences in interaction energy between templates. For example a difference in interaction energy between two templates of a few kJ mol^{-1} is unlikely to be significant as small modifications to the templates location, or conformation can remove this. However, 10 kJ mol^{-1} or more is considered significant as it would be difficult to overcome this purely by adjusting the position or conformation. Similarly, in this case we are attempting to bridge the cancrinite columns so if the template frequently docks elsewhere (unlikely given the channel structure in zeolite L) in the framework this would again mean the template may not be an effective morphology modifier.

5.2.2 Results

5.2.2.1 Crown Ethers

The first set of templates are the crown ethers. From the structures (Figure 5.5) it might be expected that these templates are relatively planar. However, it became apparent from the Discover gas phase optimisations that this was not the case. Whilst 18-crown-6 is almost planar, both 21-crown-7 and 24-crown-8 have considerable flexibility and adopt a curved structure as can be seen in Figure 5.6. On docking the crown ethers, it was noted that the ether can site in a number of configurations with respect to the {0001} face. Either in the horizontal, vertical or diagonal position as shown in Figure 5.7. These three positions were also observed for 18-crown-6.

We can see from the interaction energies (in Table 5.1) the diagonal and vertical positions are unfavourable, with the vertical position being least likely to occur. Clearly the horizontal position is preferred, and by far the most stable is 18-crown-6 with an interaction energy of -135 kJ mol^{-1}. 21-crown-7 has a slightly weaker

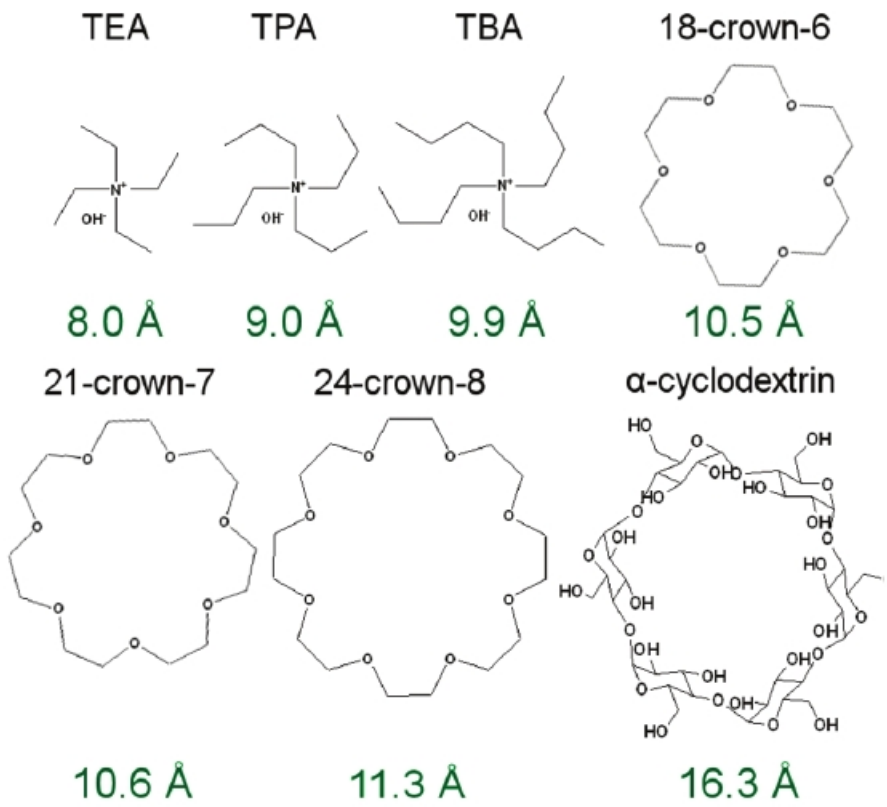

Figure 5.5: Templates tested in this study as a space filler in zeolite L. Dimensions give approximate outer diameter.

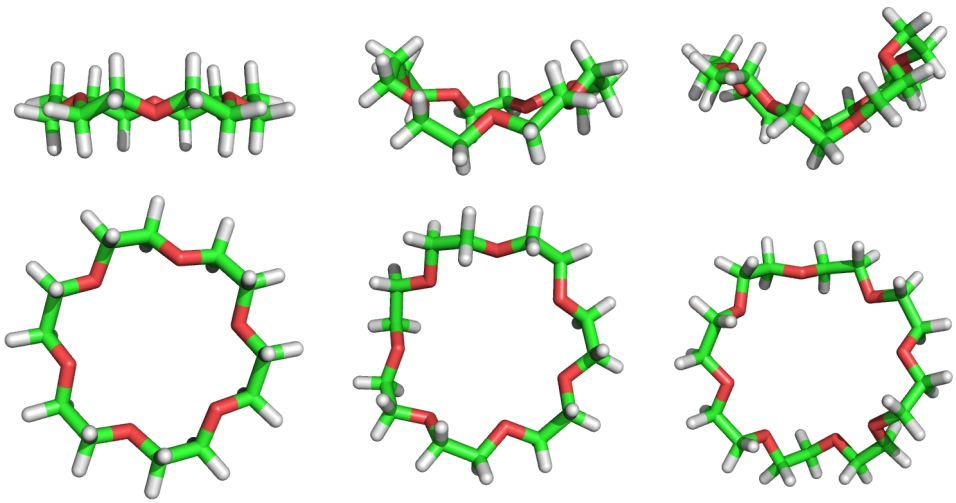

Figure 5.6: Pictures of the optimised crown ethers in the gas phase taken from "above" (top) and an orthogonal view Bottom. Left to right: 18-crown-6, 21-crown-7, 24-crown-8.

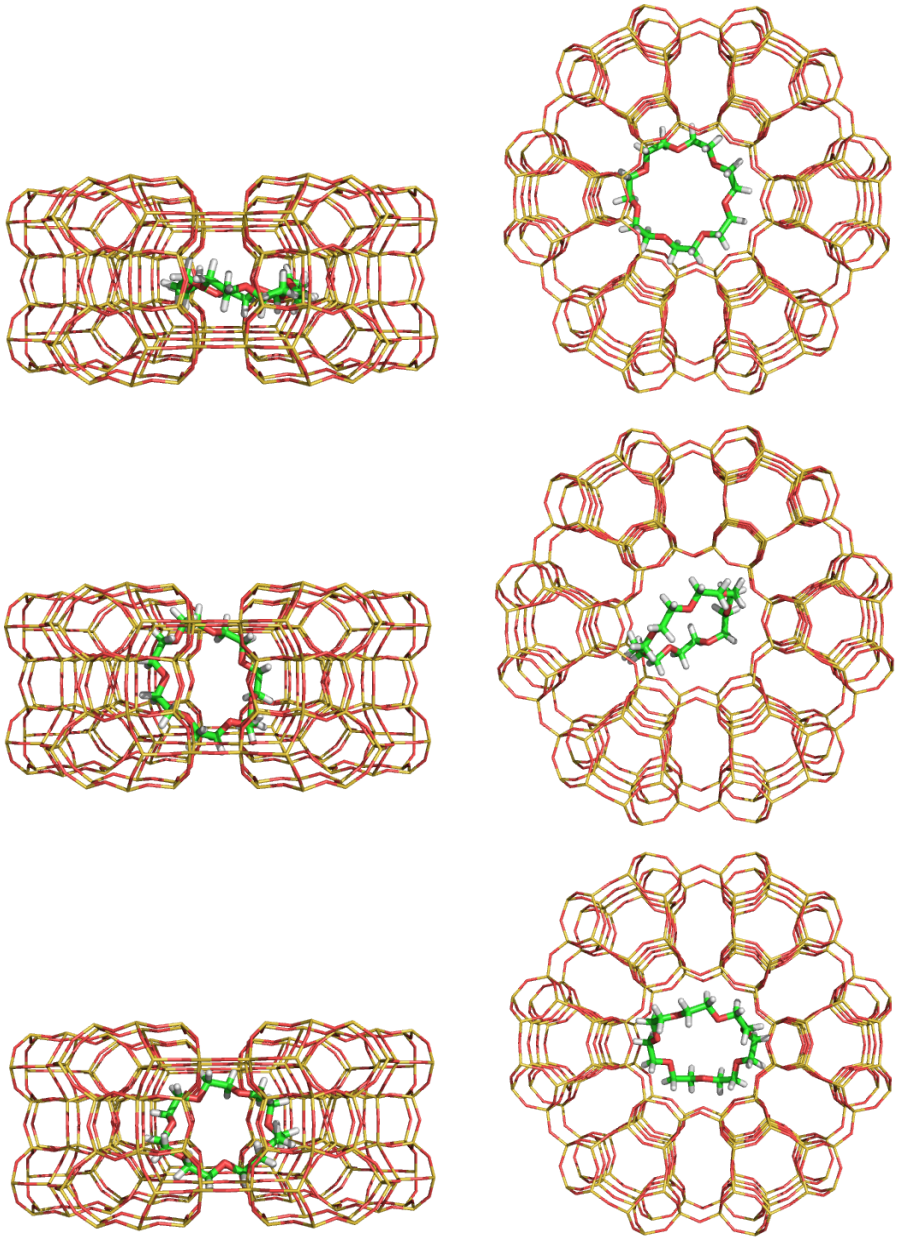

Figure 5.7: The three different positions for 21-crown-7 in zeolite L. Top: The horizontal position; middle the vertical position; bottom the diagonal position.

Template	Position	Interaction Energy
18-crown-6	horizontal	-135
	vertical	+108
	diagonal	+41
21-crown-7	horizontal	-122
	vertical	+161
	diagonal	+118
24-crown-8		+674

Table 5.1: Interaction energies with zeolite L for the crown ethers. All energies are in kJ mol^{-1}.

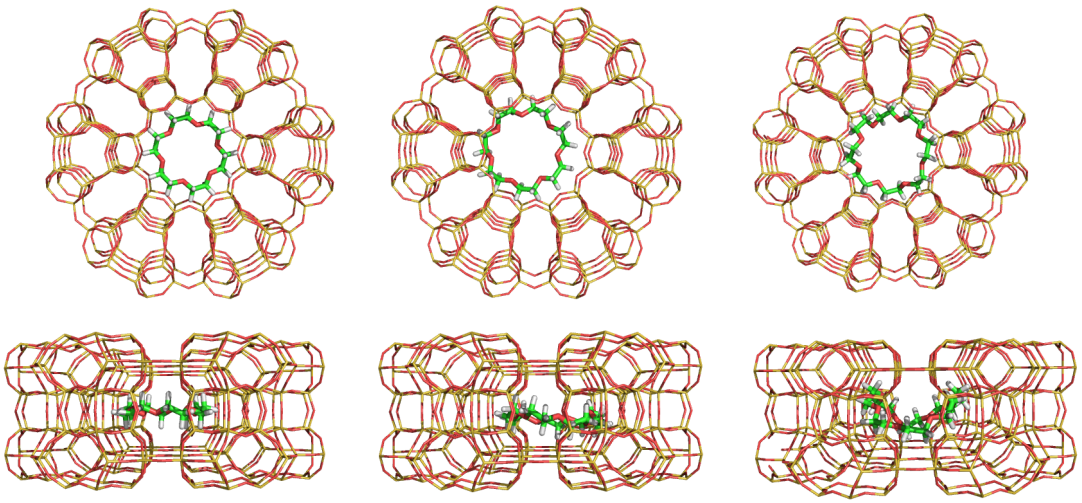

Figure 5.8: The most stable docked positions for the three crown ethers. Top row looking onto the {0001} and bottom row an orthogonal view. Left to right 18-crown-6, 21-crown-7 and 24-crown-8.

interaction energy of -122 kJ mol^{-1}. However, 24-crown-8 has a highly unfavourable interaction energy, and this shows the molecule is too large to reside in the cavity in the zeolite L channel. This suggests that 24-crown 8 will not have an affect on the crystal morphology, it will simply not interact with the growing crystal. Figure 5.8 shows the locations of the ethers within the zeolite L cavity.

5.2.2.2 Tetraalkylammonium Cations

As a comparison, a series of tetraalkylammonium (TAA) compounds were also tested for fit within the zeolite L cavity. The same docking procedure was carried out using TEA, TPA, and TBA. The interaction energies for this series are in Table 5.2. Two different positions were found for the TAA series which have been named "cavity" and "intersection". These two positions arise because of the undulating nature of the channel in zeolite L. The cavity position is where the channel is at its widest,

Template	Position	Interaction Energy
TEA	cavity	-50
	intersection	-37
TPA	cavity	-71
	intersection	-61
TBA	cavity	-36
	intersection	-89

Table 5.2: Interaction energies with zeolite L for the tetraalkylammonium cations. All energies are in kJ mol^{-1}.

and the intersection where two cavities join. The crown ethers are too large to dock at the intersection, and only the cavity position is observed. However, the smaller size and greater flexibility of the TAAs allows a greater variety of docked positions as illustrated in Figure 5.9 . Given the small size of TEA (∼8.0 Å) compared to the cavity of zeolite L (∼11 Å) we can expect there to be a large number of locations in which the template can dock, and this is indeed the case. The two positions shown in Figure 5.9 are the extremes, and as we can see from the interaction energies neither is unfavourable. However, the case where the template is located wholly within the cavity is 13 kJ mol^{-1} more favourable than when it sits at the intersection of two cavities in the channel.

For TPA there is very little difference in energy between the template locations, but the orientation of the template with respect to the *c*-axis does change. In the "cavity" position, three of the propyl chains sit perpendicular to the *c*-axis within the cavity, whereas in the "intersection" position two are aligned with the *c*-axis and two are contained within the cavity. This leads to an energy difference of 10 kJ mol^{-1} with the cavity position being more favourable. TBA is the largest TAA studied here. Once again there are two locations in which the TBA docks within the zeolite L channel. However, the cavity position is now considerably less favourable than the intersection position with an interaction energy of -36 kJ mol^{-1} compared to -89 kJ mol^{-1} for the intersection position, although neither position is unfavourable. This is due to it being relatively difficult to accommodate the large butyl groups within the cavity and so in order to overcome this, the molecule spreads over two cavities. In all cases the template remains in the same conformation, only template location and orientation with respect to the channel axis change.

5.2.2.3 Cyclodextrin

The final molecule studied as a possible morphology modifier is α-cyclodextrin, which is part of a family of cyclic oligosaccharides, and is made up of six glucose

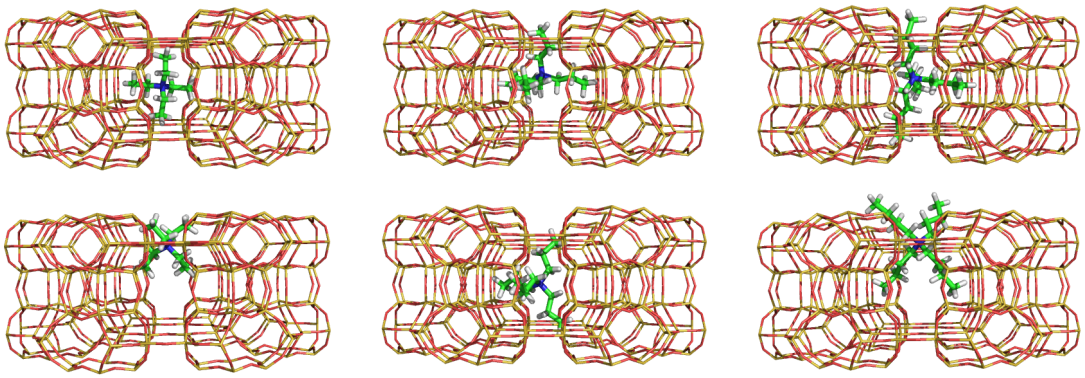

Figure 5.9: The docked locations of the tetraalkylammonium cations within zeolite L. Top row: In the cavity, bottom row: intersection. Left to right: TEA, TPA, TBA.

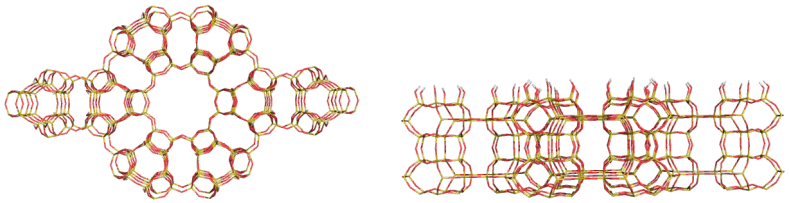

Figure 5.10: The optimised {0001} surface of zeolite L used for the ZEBEDDE MCSA calculations with α-cyclodextrin.

molecules. It was postulated that this molecule would bind to the {0001} surface and hinder growth in the c-direction. Using the method described previously, the {0001} was generated and can be seen in Figure 5.10 along with α-cyclodextrin in Figure 5.11. With a diameter of 16.3 Å α-cyclodextrin is clearly too large to fit within the zeolite and so no bulk docking calculations were carried out for this template.

The interaction energy was calculated as +2000 kJ mol^{-1} which is clearly highly unfavourable. The α-cyclodextrin does bind in the desired location, but not in the

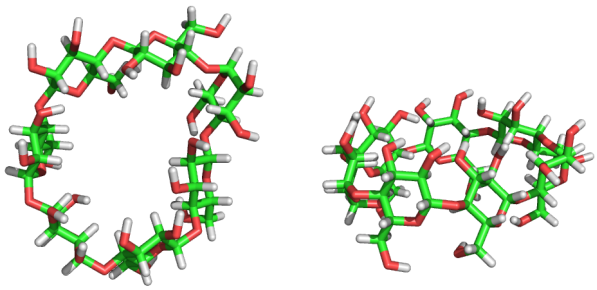

Figure 5.11: The optimised α-cyclodextrin molecule.

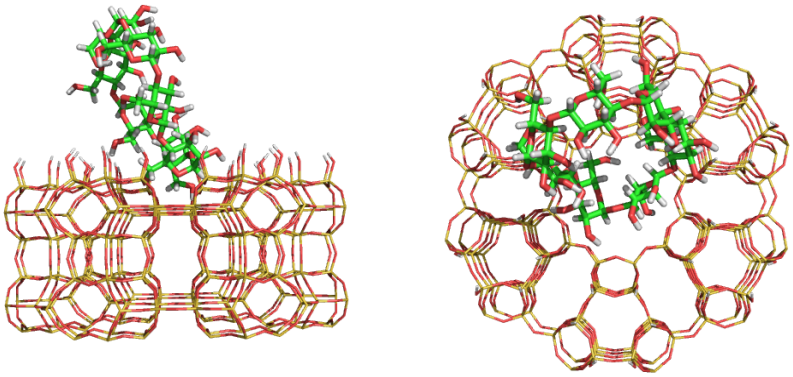

Figure 5.12: Docked locations of α-cyclodextrin on the {0001} surface of zeolite L.

expected orientation as it lands at an angle to the {0001} surface as can been seen in Figure 5.12.

5.2.2.4 Discussion

We are equating the strength of the interaction energy to the "fit" of the template within the zeolite. A more negative interaction energy should imply a better fit, and so that template is more likely to have an affect on the crystal morphology of zeolite L. Based on this we can expect the crown ethers, specifically 18-crown-6 and 21-crown-7, are most likely to affect the growth of zeolite L. 24-crown-8 has an unfavourable interaction energy and so we would not expect this template to affect the growing crystal. Although the TAAs studied have favourable interaction energies, they are not as favourable as the crown ethers. If we consider their size (especially TEA and TPA) with respect to the diameter of the zeolite L channel we can also expect them to diffuse and so also be poor crystal modifiers. By far the worst template is α-cyclodextrin which has a highly unfavourable interaction energy with the surface of zeolite L and again would have no affect on crystal morphology.

5.2.3 Experimental Results

As was mentioned in the introduction to this chapter, this was a combined computational and experimental study. The full experimental details and discussion can be found in reference [246] and only the final results are presented here in order to compare to the computational results. Based on the calculations, 18-crown-6 and 21-crown-7 were selected as possible crystal morphology modifiers. When 1 mole equivalent (see equation 5.2 for starting gel composition, where x is the mole equivalents of template) of 18-crown-6 was included in the synthesis, no zeolite L formed.

Amount of Crown Wther/ Mole Equivalents	Crystal Length/ μm	Crystal Diameter/ μm	Aspect Ratio	Si/Al (average)	K/Si (average)
0	3.8	1.5	2.5	3.47	0.35
1	2.0	1.6	1.3	3.50	0.35
2	1.8	1.5	1.2	3.49	0.34
4	1.8	2.3	0.8	3.50	0.33
1+ Cs	3.0	1.2	2.5	3.40	0.20

Table 5.3: Experimental results for zeolite L synthesis using 21-crown-7. Taken from reference [246].

However, when using 21-crown-7 in the synthesis zeolite L was formed, and altering the quantities included in the synthesis did induce a morphology change. These results are presented in Table 5.3 along with SEM images of the crystals in Figure 5.13.

$$10.2K_2O : 1Al_2O_3 : 20SiO_2 : 1030H_2O : x - template \tag{5.2}$$

From the table we can see there is a decrease in the aspect ratio as the amount of 21-crown-7 used in the synthesis is increased. The SEM images also confirm this. Thermogravimetric analysis confirmed the presence of 21-crown-7 in the synthesised zeolite, correlating well with the amount in the gel.

5.2.3.1 Further Calculations

This work successfully identified 21-crown-7 as a morphology modifier for zeolite L, initially by calculations then and by experiment. We now consider the exact mechanism by which this occurs. Previous simulations only included one crown ether so a packing study was carried out in order to determine whether addition of more 21-crown-7 was favourable, or what the expected level of uptake of 21-crown-7 would be for the as synthesised material. Figure 5.14 shows the levels of packing tested. Although not an exhaustive list of the combinations it should provide some idea of the degree to which filling the framework with 21-crown-7 affects the interaction energy. Note that in Figure 5.14 only one molecule is shown per layer, there were actually four present in each layer. Interaction energies were calculated per molecule.

We can see from Table 5.4 that there is a slight advantage to filling the structure. If we compare the two half filled results we can see that there is a preference for the template to locate next each other. From these calculations we would expect

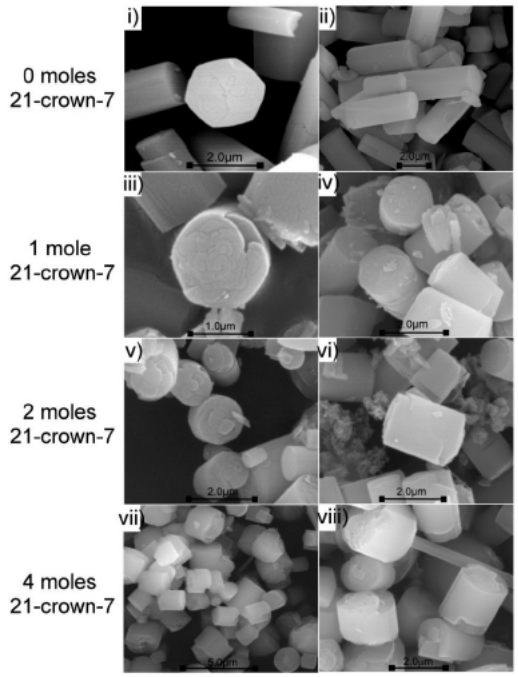

Figure 5.13: SEM image of the as synthesised zeolite L crystals. Reprinted with permission from ([246]). Copyright (2010) American Chemical Society.

Packing Level	Interaction Energy (per molecule)	Change
quarter	-122.59	-0.29
half (alternating)	-122.88	-1.02
half (together)	-123.61	-1.97
three quarters	-124.56	-2.87
full	-125.69	-4.01

Table 5.4: Interaction energies from the packing study with zeolite L and 21-crown-7. All energies are in kJ mol^{-1} per 21-crown-7 molecule. Change is the difference in energy from the single molecule calculated previously and these results presented here.

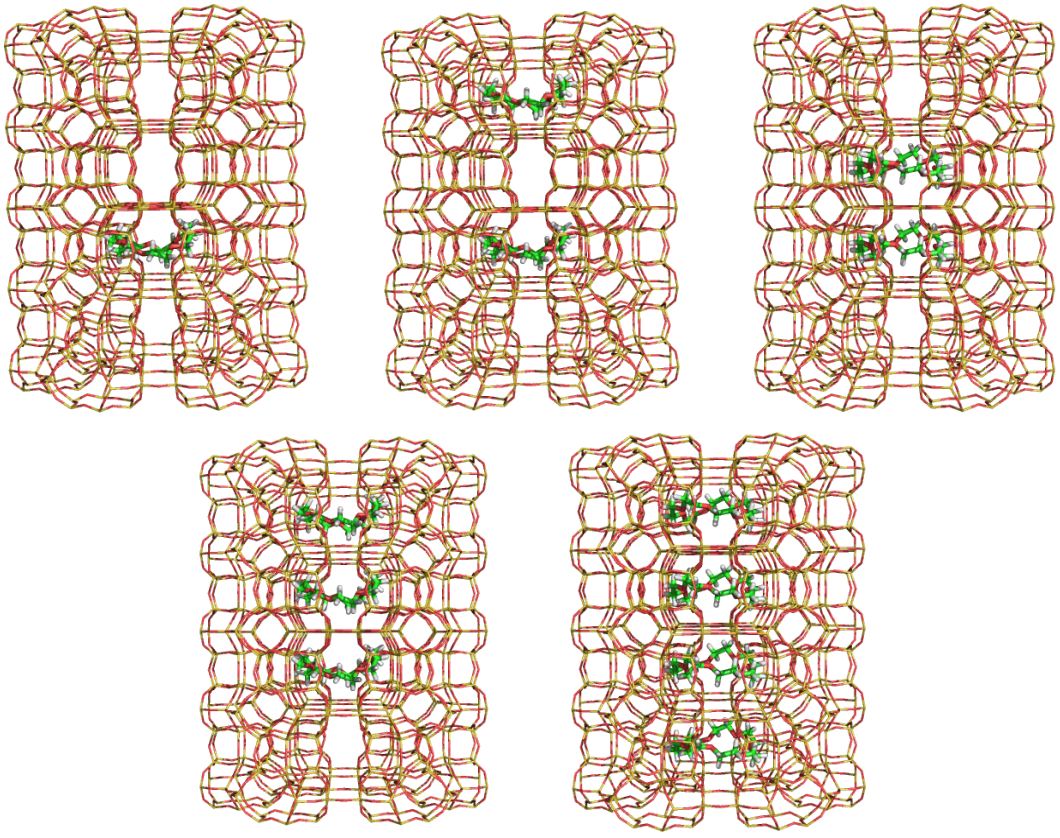

Figure 5.14: Images of the levels of packing. Left to right; Top: quarter packed, half alternating packed, half packed together. Bottom: three quarters packed, fully packed. Note only one molecule per layer is show in the pictures for clarity. In the actual simulation there were four molecules per layer.

the zeolite L to be packed full of crown ether giving a theoretical mass loss of 9.9% upon calculation. Experimental mass loss was found to be equivalent to three-quarters filled [246]. This discrepancy could be because the crown ether is bound to a potassium ion it would lead to less favourable interaction if two more molecules were placed close together and also the crown ether conformation would be more planar.

5.2.4 Conclusions

The calculations presented here were carried out to complement experimental work where the aim was to alter the crystal morphology of zeolite L. Calculations found that 21-crown-7, and 18-crown-6 fit well into the cavity in the zeolite L channel. 24-crown-8 is too large to fit inside this cavity and so was deemed unlikely to alter the crystal morphology. Other common zeolite templates, in this case small alkylammonium cations were tested as well. Although these did interact favourably with the framework, because of the their small size, they are likely to be able to diffuse through the channel and so once again are unlikely to alter the morphology of the crystal. Once experimental work had been carried out and it was determined that 21-crown-7 did alter the crystal morphology further calculations were carried out in order to better understand this effect.

There are two possible explanations that could lead to the observed morphology change in zeolite L. The first is that the crown-ether is having the desired effect and stabilising the bridging of the cancrinite columns and poisoning growth in the *c*-direction. The second is that the crown ether is in some way affecting the synthesis gel, and so it indirectly caused the change in morphology. It is suggested that the effect is actually a combination of the two [246]. The crown ether binds the potassium and this complex positions itself in the predicted location in the cavity in the zeolite L channel. Once here, it templates the cancrinite columns and so the crystal grows in the normally frustrated *a*-direction.

5.3 Morphology Control of AlPO-11

This section aims to understand why when a surfactant amine molecule is added to the synthesis of AlPO-11 the crystal morphology is altered. It is hoped that by studying the locations and interaction energies of the amine surfactant with the AlPO-11 surface it will be come evident that the amine has an effect on one or more of the surfaces and so alters the growth mechanism.

5.3.1 Introduction

AlPO-11 (AEL) is a one dimensional aluminophosphate with a straight 10 member ring channel (see Figure 5.15) whose structure was partially solved in 1987 [255] with the complete refinement being achieved a year later [256]. Initially it was made as a silicon substituted aluminophosphate (SAPO) [257] but has subsequently been synthesised as a pure aluminophosphate [255] and more recently as a germanium substituted aluminophosphate [258] Although not strictly a zeolite, the synthesis methods are nearly identical and the mechanisms of formation are thought to be similar.

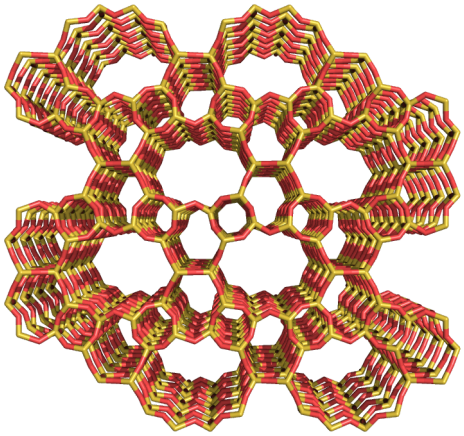

Figure 5.15: View of the {001} face of the AEL structure showing the 10 MR channels.

AlPO-11 is synthesised using N,N-dipropylamine as the template and is used as a catalyst for the transformation of linear alkanes into monobranched alkanes [258]. In a patent published in 2003, Strohmaier and Vaughan have shown that adding long chain surfactant amines, with carbon chains of length 10 to 18 alter the crystal morphology [259]. Standard crystals of AlPO-11 have their longest dimension in the direction on the channel and addition of the surfactant reduces this dimension.

5.3.2 Computational Details

The AlPO-11 structure used for these simulations is that of Richardson *et al.* and it was converted to the entirely siliceous form for computational simplicity [256] and as such subsequently is referred to by its three letter code AEL. This structure was optimised using the GULP code [214] with the Sanders, Catlow, Leslie SiO_2 potentials [188]. The optimised structure was then cleaved along the desired Miller plane using the GDIS visualiser [253]. The surfaces were cleaved in order to expose the minimum number of dangling bonds. Once cleaved, any dangling oxygen atoms were hydrogenated, and dangling silicon atoms were converted to silanols. These structures were then optimised again in GULP using the Sanders, Catlow, Leslie SiO_2 potentials [188] for the bulk and the silanol potentials of Schröder [254]. The unit cell was extended by 100 Å as to create a vacuum gap between the two surfaces in a three dimensional periodic structure. For computational simplicity the framework was kept fixed for all subsequent calculations.

The surface docking calculations were carried out using ZEBEDDE's Monte Carlo simulated annealing (MCSA) routines with the interactions being described by the PCFF forcefield [222]. The initial temperature of the system was set to 300 K and was reduced in steps of 50 K carrying out 20,000 actions at each temperature step until the temperature reached 0 K. This process was repeated fifty times and then plotted as a histogram of adsorption energies. The surfactant molecule, hexadecylamine, was built using Accelrys Materials Studio 4.3 and optimised using the Discover module and the PCFF forcefield [222]. For each of the AEL surfaces, the surfactant was initially positioned approximately 30 Å above the surface.

Molecular dynamics (MD) calculations were carried out using the DL_POLY4 code [260]. The Oie potentials [261] were used for the intramolecular template interactions along with the Kiselev [262] potentials for the intermolecular and zeolite-template interactions. The bulk zeolite uses the potentials of Sanders, Catlow and Leslie [188] and the surface silanols are modelled using the potentials of Butler [263]. The water potentials are those of deLeeuw and Parker [264]. These potentials have successfully been used in similar simulations of zeolite surfaces. In order to stop the amine surfactant diffusing down the channel the "tail" carbon was fixed, with the remainder of the molecule being free to move. For the simulation with water, the cell was filled with water using one of the utilities that comes with the DL_POLY4 code written by W. Smith [260]. The timestep for the simulation was 0.2 fs and the potential cutoff was set to 8 Å. The MD cell was first equilibrated by running under NPT ensemble for 100 ps using the Berendsen barostat and thermostats with relaxations constants of 0.2 fs and 1 fs, and then for a further 100 ps under the NVT

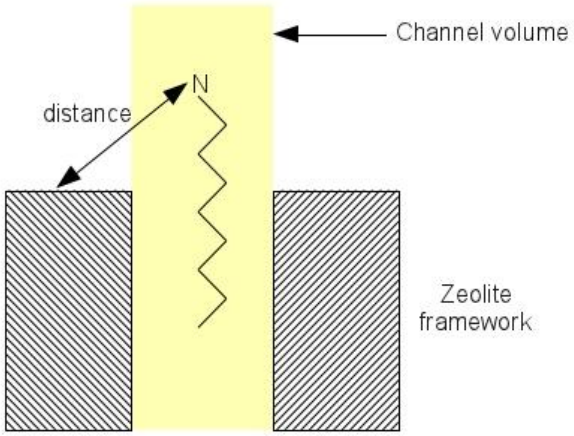

Figure 5.16: Diagram showing the measurements made by the code written to analyse the MD trajectories. It measures the "distance" between the nitrogen group and the surface, and the number of atoms outside the channel volume (shaded yellow).

ensemble. The production run was carried out using the Hoover thermostat with a relaxation constant of 0.5 fs under the NVT ensemble for 120 ps.

A bespoke code was written to analyse the MD trajectories which extracted the distance of the "head" nitrogen from the nearest surface hydrogen of a silanol. As well as calculating this distance, it also calculates the number of carbon or nitrogen atoms which are outside the channel volume (see Figure 5.16). Both these measures should give an indication of how much the amine interferes with the surface of the zeolite, and as such, how much it will affect growth.

5.3.3 Results

5.3.3.1 Surface MCSA Calculations

The results from the surface MCSA calculations are presented in Figure 5.17 as a histogram of adsorption energies. The first point to note is that there is a general distribution of energies for each of the surfaces suggesting there is no real preference for a particular face. The stronger interactions on the {001} surface at -110 kJ mol^{-1} can be attributed to the template entering into the bulk via the channel entrances (see Figure 5.18) and so these can be discounted. The distribution of energies on the {010} surface are at slightly higher values meaning the average adsorption energy would be higher on this face, than the {100} where we can see the distribution peaks at approximately -50 kJ mol^{-1}. However, the most stable position on each face has an almost identical energy at just below -100 kJ mol^{-1}.

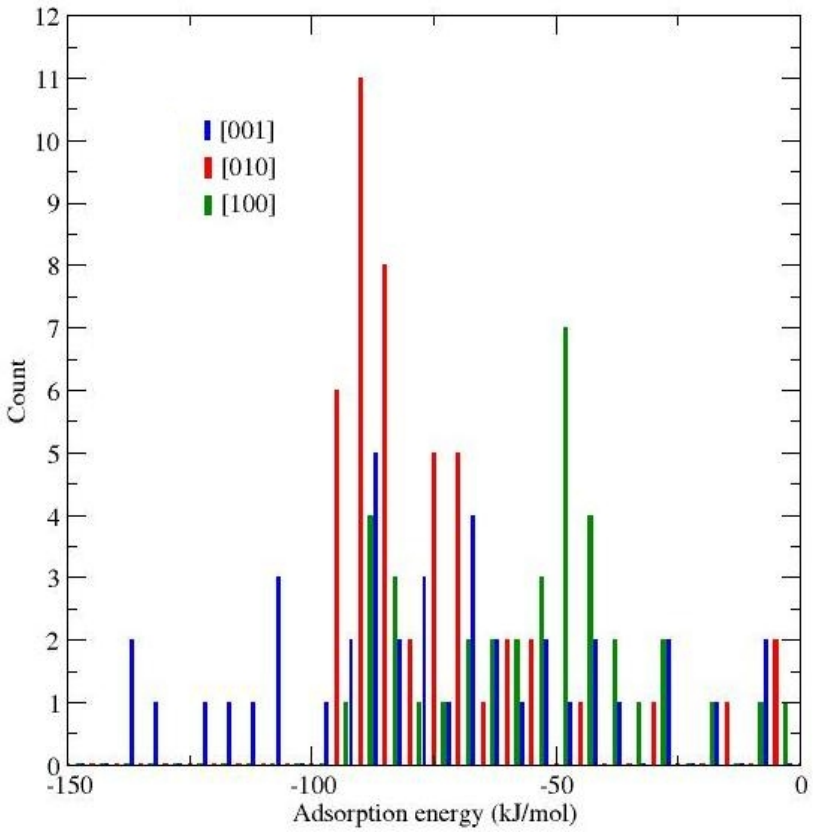

Figure 5.17: Histogram of the adsorption energies of the amine surfactant hexadecylamine on the three AEL surfaces. We can see there is no real preference for a particular location in that there is a wide distribution of energies over all the surfaces . The {010} does have a higher proportion at higher energy than the other two faces. There are some peaks for the {001} face at approximately -110 kJ mol^{-1} which can be attributed to the template entering the bulk.

Since there is no particular preference for a face the change in morphology may be due to the location of the amine on the surface, preventing or enhancing growth on the surface. By inspection of the docked locations it comes apparent that there are locations on the surface which are preferred by the template. Figure 5.19 shows the most favourable locations on the {100} surface. We can see there are two possible locations for the template. The first is in what will become a 6 MR. Clearly, in this position, the template will not be easily incorporated into the framework. However, we can imagine that the energy barrier which must be overcome in order for it to "roll" into the second position will be relatively small. This second position is the precursor to the 10 MR, and here the template can be easily incorporated into the framework.

Figure 5.20 shows the most stable position on the {010} surface. As we can see, the surface already has in place six of the ten silicon atoms which will form the 10 MR channel. The creates a trough in the surface into which the template can dock. It is for this reason we see in the histogram of adsorption energies the {001} surface has a higher average docking energy, because we have fewer possible template locations (as compared to the other two surfaces). Whilst it is possible on this surface to cleave in two different locations and create a surface with the same number of silanol groups, it is expected however that the final location of the template would be the same.

The {001} surface is the most complex. We have the situation where the hexadecylamine enters into the channel which has already been discussed. On the surface itself we have two possible locations. One completely on the surface as can be seen in Figure 5.21 and one where the template has partially entered the channel as shown in Figure 5.22. The difference in energy between the two is relatively small (4-5 kJ mol^{-1}). In both cases we can expect that the growth on the surface will be hindered by the presence of the template. In the first case the template blocks growth on the {001} surface as it cannot be incorporated into the structure. In the second case we can expect the motion of the "tail" of the hexadecylamine to interfere with the surface region around the template as it diffuses into the channel. The next section explores how much the amine will hinder the surface of the growing crystal when it is partially docked in the channel.

5.3.3.2 Molecular Dynamics Simulations

MD simulations were carried out in order to gain an understanding of how much time the hexadecylamine would spend hindering the surface as it enters the channel. The "tail" carbon has been fixed in the channel such that half of the molecule is within

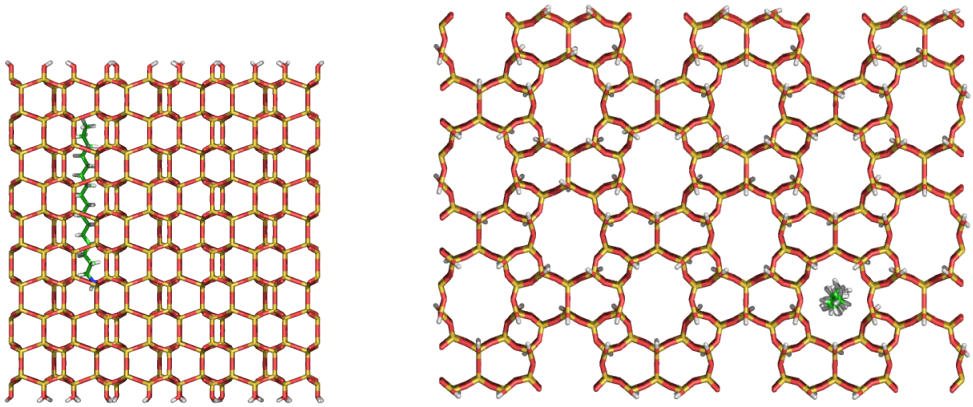

Figure 5.18: Bulk docked position with the amine in the 10 MR channel.

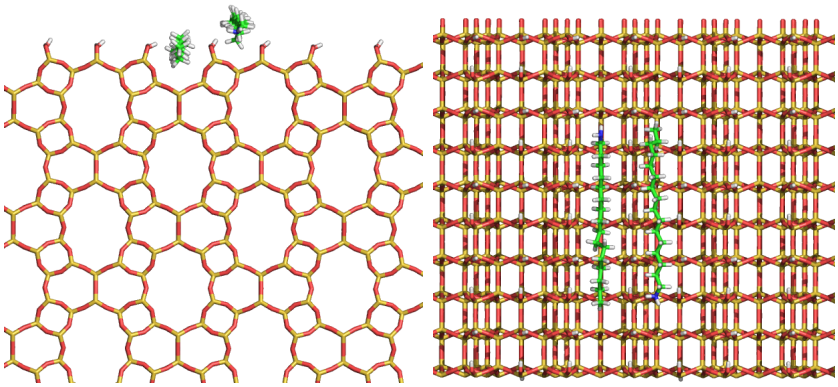

Figure 5.19: The two locations on the {100} surface which the hexadecylamine chooses to sit. The position in what will become the 10 MR channel (left) is most stable.

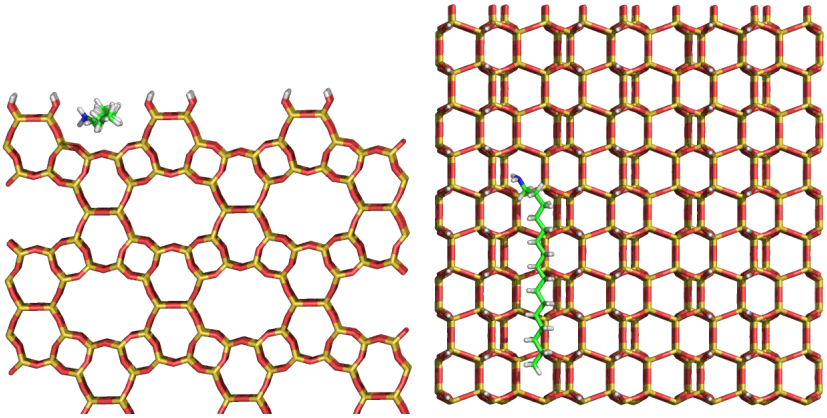

Figure 5.20: The location on the {010} surface which the hexadecylamine chooses to sit. The location is in what will become the the 10 MR channel.

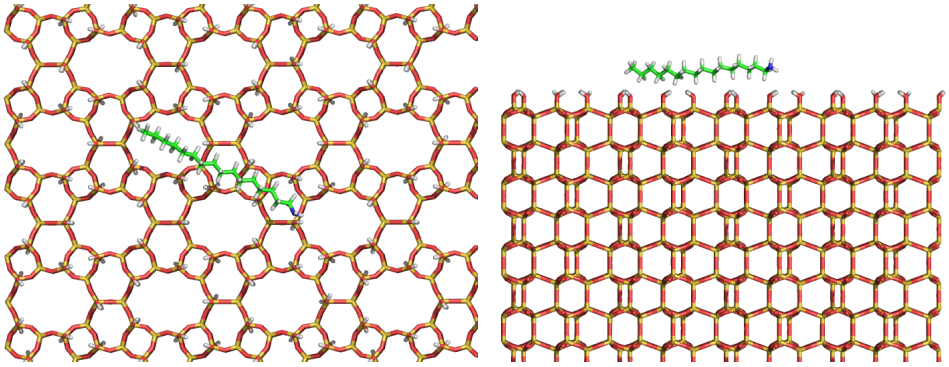

Figure 5.21: Adsorption sites on the {001} surface. Here the template completely obstructs the surface, preventing growth.

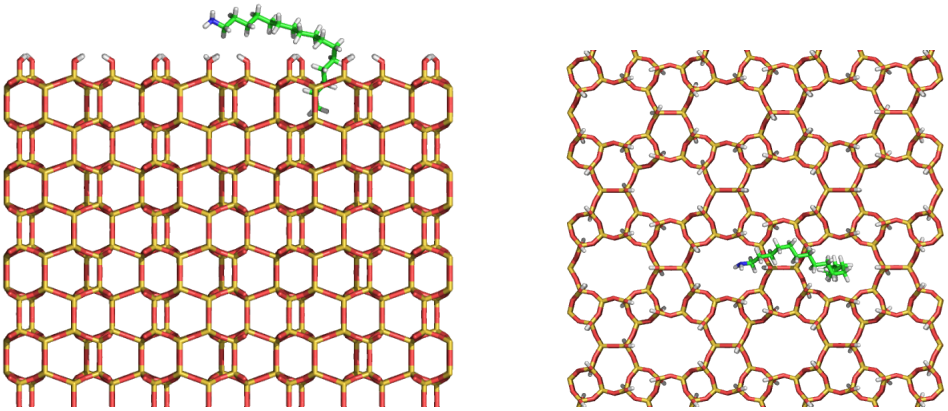

Figure 5.22: The location on the {001} surface where the template partially enters the channel. Once again the surface is partially obstructed preventing growth.

the channel, and half exposed, and orientated such that the chain is parallel to the channel. Initially the calculations were run without any water present. However, it was immediately obvious that this unrealistic as the template immediately moved to the surface and remained in the same position for the duration of the simulation. On reflection, this is not a surprising result as we would expect water on the surface, and the lack of water means the only possible outcome is for the amine to bind to the surface.

For the subsequent calculation the cell was generated from the ZEBEDDE annealed structure as shown in Figure 5.22 and the vacuum gap of the cell reduced from 100 Å to 50 Å in order to reduce the number of water molecules required. This cell was then filled with water molecules (totalling 5,450 molecules) before being optimised as discussed in Section 5.3.2. The MD trajectory was analysed for the number of carbon atoms which are outside the channel volume and the distance the "head" nitrogen is from the surface for the length of the simulation. These results are presented in figures 5.23 and 5.24. If we look at the distance of the nitrogen from the surface in Figure 5.23 we can see that the nitrogen starts at approximately 10 Å from the AEL surface. At this distance the template is orientated almost completely parallel to the channel i.e. perpendicular to the surface. It moves toward the surface over the next ∼30 ps and remains on the surface[2] for the next ∼50 ps. It leaves the surface briefly at ∼70 ps before returning. If we consider the number of carbon atoms outside the channel volume, this mirrors the nitrogen-surface distance. At the start of the simulation we have zero atoms outside and this increases to six before settling between four and five. It stays at this level until 75 ps into the simulation when it decreases to zero which implies that the template is contained within the pore volume again.

Both these measures show that for a large part of the simulation (approximately 80 ps) the template would be in a location which would hinder any building units attempting to react with the surface and so hinder growth in this direction. These results give an indication as to why long chain amines have this effect on the growth of AlPO-11 crystals. On the {100} and {010} surfaces the amine can be incorporated easily into the growing crystal and may even be assisting in the growth. However, on the {001} surface there are two mechanisms which block growth. The first is when the amine binds to the surface preventing growth, and the second is where the rotations of the molecule as it enters the channel cause hindering of the surface.

[2]The distance cannot be 0 Å because we are measuring from the nitrogen and therefore have the hydrogen that is attached to the nitrogen in between the nitrogen and the surface.

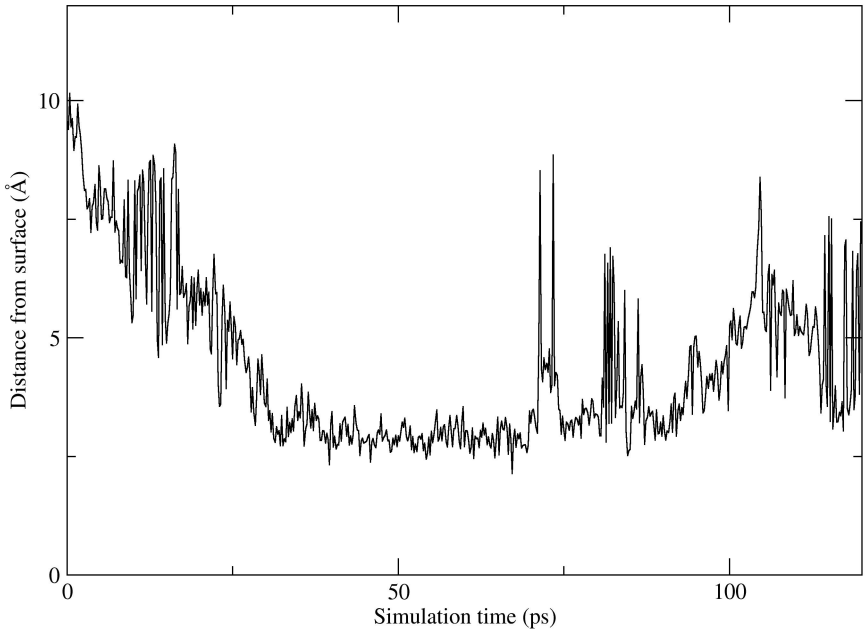

Figure 5.23: Distance between the nitrogen atom in hexadecylamine and the surface of AEL.

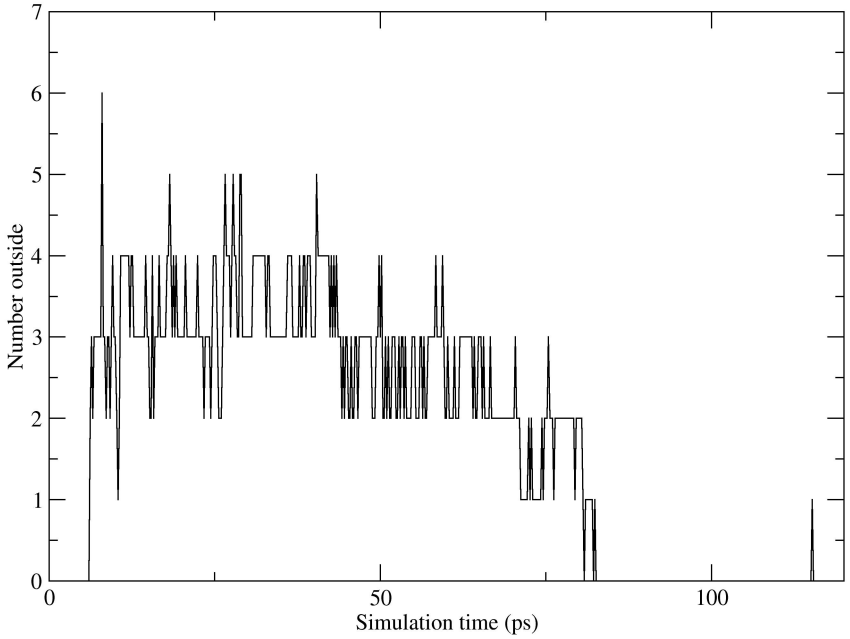

Figure 5.24: Number of carbon atoms outside the channel volume.

5.3.3.3 Conclusions

Experimentally it was known that surfactant molecules such as hexadecylamine had an effect on the crystal morphology [259] and so the work presented here was carried out in order to understand why this type of molecule has this effect. Simple Monte Carlo simulated annealing calculations show that there is no energetic preference for a particular face of the crystal and so we can expect the amine to bind to all faces equally. However, if we consider the templates location on the surface then we can see from that on both the {100} and {010} the template can easily be incorporated into the growing crystal inside the channel. On the other hand, when on the {001} face this is not the case. Constrained molecular dynamics simulations of the template on the {001} surface also show that any molecules partially incorporated on the surface will hinder growth as well.

5.4 Conclusions

In this chapter we consider how organic additives can be used to modify crystal morphology. The ZEBEDDE code has been used to screen molecules that would alter the morphology of zeolite L. Although the experimental result that when prebinding the 21-crown-7 ether molecule with caesium, there was no effect on the morphology mean that the crown ether itself did not directly affect morphology, it is clear from experimental work that the molecule was incorporated into the framework, and in the predicted location. Combined with the fact that a typical zeolite L synthesis requires only potassium as the templating species we can infer that it is a combination of the potassium binding to the crown-ether and the template docking in the location predicted by simulations that causes the morphology change. This combination provided more cations in the pore cavity and hence a template which the cancrinite columns can incorporate in the normally frustrated a-direction and this resulted in the desired lowering of the aspect ratio of the final crystals. Very recently Gomez *et al.* also achieved a similar result using small chain alcohols as a co-solvent although they did not propose a mechanism for the change in morphology of the zeolite L crystals [265].

The case of AlPO-11 is more straightforward than that of zeolite L where we simply have the large hexadecylamine surfactant hindering the AlPO-11 {001} surface. On the other two surfaces this molecule is easily incorporated into the growing crystal and so does not affect growth on this face, and indeed could be promoting growth in this direction. Although it is difficult to say for certain that growth promotion is occurring in the other two directions.

These results do show that simulations can provide insight into the mechanisms that cause templates to alter crystal morphology. The zeolite L work is an example where simulations were able to predict which templates may influence crystal morphology. This was achieved first through careful AFM studies on the growth mechanisms [252]. Once this was understood considered how it could be affected. Using the interaction energies calculated from docking simulations we were successfully able to predict which organic molecules were likely to influence the growth, as was proved by the experimental work [246]. This result in itself is very encouraging as one of the goals set out in the introduction to this thesis, and indeed for zeolite science as a whole, is to predict the synthetic outcomes. This would enable zeolites to be designed for specific purposes.

CHAPTER 6

Templates and Water

6.1 Introduction

In Section 2.4 the mechanism for nucleation was considered. It was discussed that the formation of water clathrate structures around the template which are then substituted for silica. This idea stems from work by Mootz and Siedel where they observed that clathrates isomorphic with Sodalite form around tetramethylammonium (TMA) [266, 267]. However, it is difficult to observe these structures experimentally in the liquid phase under zeolite synthesis conditions which are considerably higher in both temperature and pressure than the experiments of Mootz and Siedel, as well as synthesis vessels being impenetrable to spectroscopic techniques such as infra-red.

This chapter builds on previous work where the hydration layers of some common small organic templates were studied [263]. The water structures around some larger templates, specifically diquaternary ammonium compounds, are studied and analysed for the clathrate-like structures. It is hoped that this will explain the experimental observations, that altering the chain length, changes the zeolite structure formed. The analysis code used previously [263] has been completely rewritten in order to analyse non-spherical templates. The reasons behind this will be discussed later.

6.1.1 Water Structure

The structure of water has been widely studied, and it is known to be a highly structured liquid [268]. But problems arise when this order is required to be quantified. Most commonly, X-ray and neutron diffraction are used to determine water structure. From the total diffraction data we can derive structure factors and pair correlation functions (PCF) by Fourier transform [268]. However, this analysis of the total diffraction data leads to a structure of liquid water that resembles non-structured liquids such as liquid argon [269]. Therefore it is necessary to quantify the ordering of water using more than just the radial dependence. It was proposed by Bennetto and Caldin [270] that the general "order", and later by Marcus [271] that factors such as the "stiffness" and "openness" would serve as better measures. Here, "stiffness" relates to the work necessary to create a cavity within the water, "openness" is the difference between bulk molar and intrinsic molar volumes. "Order" is the deficit in molar entropy with respect to the gas phase. Breaking the pair correlation functions into partial functions, i.e. those between oxygen and hydrogen, as opposed to just the total PCF, has also been shown to yield more information [272].

Order in water is of course governed by hydrogen bonding. Therefore the network of hydrogen bonds provides a useful measure of the effects of a solute on the water structure because we can measure the disruption (or lack thereof) caused to the network. The hydrogen bond network of pure water has been studied experimentally using X-ray absorption spectroscopy (XAS) and X-ray Raman scattering spectroscopy (XRS). Nilsson *et al.* take the view that most of the water forms two strong hydrogen bonds with water, with a minority (20%) in an ice-like tetrahedral form [273, 274]. However, Saykally and co-workers interpret the results of similar experiments differently, finding that most of the water is in the tetrahedral ice-like form with a minority in the other form [275, 276].

Extensive neutron diffraction studies by Turner *et al.* of TMA in water show little change in the PCFs between water hydrogens, the water hydrogens and other atoms, and between other atom types [277]. They concluded that TMA has no effect on the structure of the water compared to bulk solution, and the TMA also did not sharpen the H-H peak as may be expected. However, the authors do note this could be due to the TMA not being as hydrophobic as larger tetraalkylammonium cations. A later study from the same group, this time on tetrapropylammonium (TPA) and tetrabutylammonium (TBA), does conclude that there is a small, but probably significant increase in the structuring of the water in the hydration layers compared to bulk water. This is highlighted by the increase in height and change in position

of the second H-H peak, i.e. the first intermolecular peak, which suggests there is an increase in the number of ideal hydrogen bonds. The first O-H intermolecular peak was also sharpened, suggesting there is a decrease in the number of possible conformations for the water. Turner *et al.* also conclude the average number of hydrogen bonds remains constant, supporting the hypothesis where the solute is in a cage maintaining the bulk water structure around it.

NMR studies of TMA, TPA and TBA in water by Bradl and Lang [278] show there is reduced mobility of the water around the alkyl chains for all solutes except TMA. This is the same for most experimental findings where TMA disrupts water networks, and larger more hydrophobic molecules enhance the water network structure.

6.1.1.1 Computational Studies

Computer simulations clearly have an advantage over spectroscopic techniques in that the exact positions of the particles are known. However, ambiguity still exists, in the exact definition of a hydrogen bond. Geometrically it is generally accepted that the distance between oxygen and hydrogen, i.e. $O \cdots H{-}O$ and the angle of this bond are used to define a hydrogen bond in a liquid [279]. Using this criteria, Xenides *et al.* conclude from *ab initio* simulations on pure water that there are on average 2.8 hydrogen bonds per water molecule [280]. A molecular dynamics study by Madan and Sharp on TMA in water, utilising the TIP4P model of water, shows the H-H and O-O RDF first peak-to-trough ratio increases. An increase in the peak-to-trough ratio implies that the water is becoming more ordered [281]. Madan and Sharp also state that the changes induced in the water structure are similar to a temperature drop of 20°C in pure water, again implying that there is an increase in the water structuring. By comparison with neutron diffraction data they find their results compare well for the pure water simulations, but when comparing to experiments including TMA, they note that although there are water structure altering effects apparent in the experiments, they are not as large as in the simulations. These suggest that there is a masking of these effects by bulk water, or by water coordinating to other cations which are of course indistinguishable in the experiments.

Recently, work by Szyja *et al.* have investigated the stability of tetraalkylammonium-silicate species [282, 283]. Stemming from previous experimental work in which Kirchhock *et al.* propose a Si_{11} oligomer that is essential to the formation of zeolites MFI and MEL [284]. Depending on orientation these Si_{11} units can be combined to form the Si_{33} MFI/MEL precursor. Szyja *et al.* build

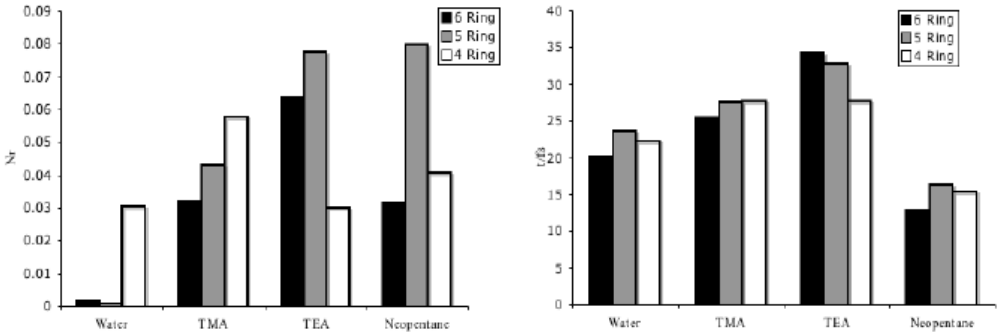

Figure 6.1: Ring statistics (left) and ring lifetimes (right) for water, TMA, TEA and neopentane. Reproduced from reference [263].

upon this by taking the Si_{22} precursor which is the smallest oligomer to have a cavity and study the relative stabilities of this structure in the presence of TPA and TBA [283]. The results suggest that TPA stabilises the MFI precursor cage, and TBA the MEL precursor cage which corresponds to the experimental results by Kirschhock *et al.* [284]. However, the most interesting the result for comparison to this work is that TPA stabilises a silica five ring and TBA the four ring.

Previous calculations by Butler investigated the affects of a number of template features on the ring structures in water within the first hydration layer of the organic molecule [263]. TMA was compared to tetraethylammonium (TEA) to study the affect of hydrophobicity, and TMA with neopentane (replacing the N^+ in TMA with carbon creates neopentane which has the same space filling properties but uncharged) to study the effect of charge. These results (see Figure 6.1) show a dramatic increase in the number of five and six rings (in pure water we observe only three and four rings) in the first hydration layer around the template. Charge appears to stabilise four member rings whilst more hydrophobic surfaces promote five rings. As well as investigating the frequency a particular ring structure appears, the lifetime of the rings was also studied. The lifetimes of the rings in the first hydration layer also increase compared to bulk water with the charge appearing to play an important role in this. We already see therefore a correlation between the effect of the templates on the structure of water and their effect on stabilising specific zeolite precursors [282, 283, 284].

6.2 Methods

6.2.1 Radial Distribution Functions

In order to analyse fully the water structure, radial distribution functions (RDF) were calculated. From the discussion of previous work in Section 6.1.1 it is clear that this provides an excellent measure of the extent with which the solutes are affecting the water network. Radial distribution functions were calculated between a pair of species from the molecular dynamics trajectories. The bins for the collection of the histogram data were set to 0.03 Å. We calculate a radial distribution function for two atom types, A and B using the following:

$$g_{ab}(r) = n_{ab}(r)/V(r)\rho_b = \rho_{ab}/\rho_b \tag{6.1}$$

where $n_{ab}(r)$ is the frequency of finding atom type B at a distance between r and $r + \delta r$ from atom type A. ρ_b is the bulk density of atom type B, ρ_{ab} is the local density at a distance r from A. $V(r)$ is the volume of the spherical shell around A between r and $r + \delta r$. In the case of a simulation involving a homogeneous solvent this is simply:

$$V(r) = 4\pi r^2 \delta r \tag{6.2}$$

We have to correct the volume of the annulus as we have a solute in the solvent. This means that a significant portion of any annulus which we are calculating may pass through the volume occupied by the solute and thus represents a volume in which it is impossible to find solvent molecules. This will lead to the pair correlation density being lower for no intrinsic reason. Therefore when calculating the radial distribution function we must take this effect, which is known as the excluded volume effect (see Figure 6.2), into account [285]. The effect is of course smaller for small solutes, but increases for larger solutes, or at high solute concentration as is the case with the calculations presented here.

Experimentally the excluded volume is taken into account by assuming the solute occupies a spherical cavity in the solvent. The RDF for A and B is then multiplied by the Fourier transform of the calculated scattering function for the spherical cavity. In a computational simulation it is much easier to account for the effect given we know the exact positions of the molecules. If we again assume the solute molecule occupies a spherical cavity then we can calculate any given volume (V_s) of an annulus

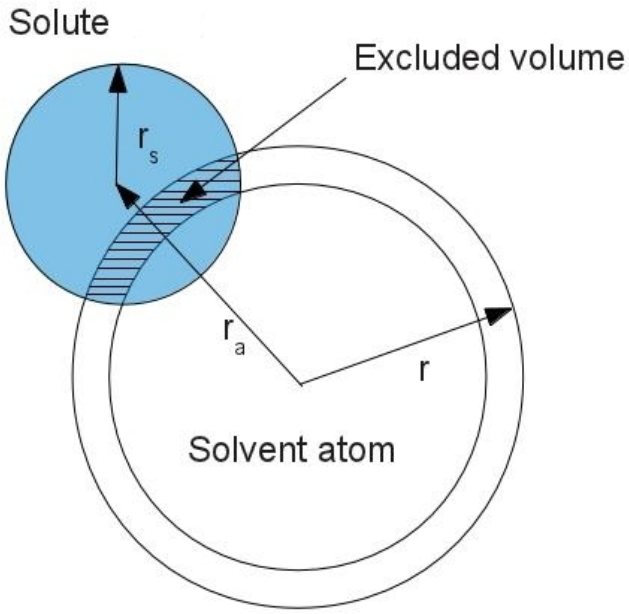

Figure 6.2: Diagram showing the excluded volume when a solute is present. The shaded region represents the excluded volume.

that falls within the solute as follows:

$$\begin{aligned} V_s &= 2\pi r\delta r(r-(r^2-r_s^2+r_a^2)/2r_a) \quad \text{for} \quad |r_s-r|<r_a<(r_s+r) \\ &= 0 \quad \text{for} \quad r_a>(r_s+r) \quad \text{or} \quad r_a>|r_s-r|; r>r_s \end{aligned} \tag{6.3}$$

where r is the radius of the annulus, r_s is the solute radius, r_a is the distance from atom A to the centre of the solute. Once V_s has been calculated the density of atoms of type B within the annulus is weighted by the ratio of the total volume outside the solute to the total annulus volume $(V-V_s)/V$.

We can see that calculating the excluded volume for a spherical solute is relatively trivial. However, for many solutes in this work, the solute can not be approximated to a sphere (see Figure 6.3). In this case it is far more complex to obtain the excluded volume and in order to overcome this a Monte Carlo method was used. Each atom in the solute is modelled as a sphere with radius equal to the van der Waals atomic radius. A random point is then placed within the annulus and the point is checked against all the spheres. The volume of the annulus V is then weighted by the ratio of the number of points that fall within the spheres to the total number of points n_i/N) in order to give the excluded volume V_s.

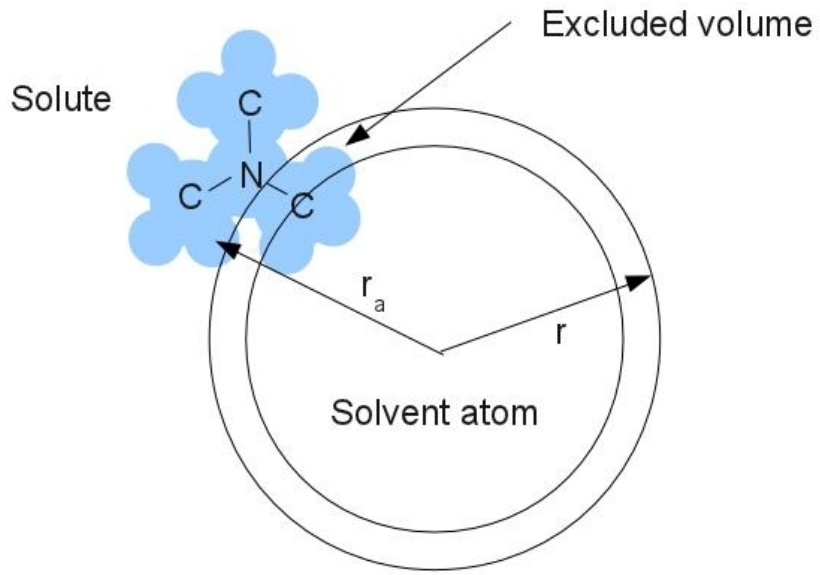

Figure 6.3: Diagram showing the correction to the RDF for solute excluded volume when the solute is not spherical.

6.2.2 Ring Searching

In order to analyse the structuring of the water a code was written to analyse the molecular dynamics, searching for rings within the first hydration layer. In this case we define a "ring" as the shortest path back to the original water molecule W_0. The code assigns each water molecule (in practice the water molecule is defined by its oxygen) a unique index and using these builds a neighbour list by searching for water molecules that are "connected" to it. That is they fall within the first oxygen-oxygen peak of the water radial distribution function.

Once the neighbour list is constructed the code then searches for paths back to the origin by moving outwards. First the code selects the first neighbour in the list of the neighbours of W_0 which will be W_1 followed by the first neighbour of W_1 which will be W_2. W_3 is then the first neighbour of W_2 and this is then checked against W_0. If W_0 has the same index as W_3 (i.e. W_3 is W_0) then we have found a three ring and the unique indices of the atoms are stored. If W_3 is not the same molecule as W_0 then the first neighbour of W_3 is selected which will be W_4. Once again if W_4 is the same molecule as W_0 then we have a four ring and the unique indices are stored. This process continues to W_6 which will equal a six ring. If no rings are found then we drop back to W_5 and select the second neighbour and repeat for all neighbours of this new W_5. Once exhausted we fall back further and select the second neighbour of W_4 and repeat the process. This continues until we have exhausted all neighbours

of W_0. Each water is assigned as W_0 in turn and the process repeats.

Once all the rings have been identified the ring lists are checked for any rings which have been double counted. At the same time, the code checks that there is not a shorter ring within the larger ring, in which case the larger ring is rejected. This set of unique rings are stored along with a counter which is initially set to zero, and the same analysis is carried out on the next step in the molecular dynamics trajectory. The unique set of rings from this set are then compared to the previous step. If a ring already appears then the counter is incremented. If it does not, it is added to the list and the analysis continues until all steps in the simulation have been analysed. The final output from the code is the number of three, four, five, and six member rings, along with the average lifetime of each ring type.

6.2.3 Hydration Layers

As already mentioned we no longer consider our solute (the templates) to be reasonably approximated as spherical which had implications when it came to calculating the excluded volume. We must also consider the solute shape when calculating the hydration layers, as we can no longer just take the centre of mass of the solute and simply calculate the water molecules that fall within the hydration layer radius. As the diquaternary ammonium compounds have a mirror plane (or centre of inversion) in the centre it seems reasonable to break the hydration layer down into two components. The first as two hemispheres around the nitrogen head groups and the second a cylinder along the chain. This allows each section to be analysed separately.

6.3 This Study

This study builds on previous work by Butler [263] by extending the calculations into more complex and flexible templates. Using *ab initio* molecular dynamics the effect of chain length, and head group on the water structure is investigated for a series of diquaternary ammonium compounds. As well as this series of templates, these results are compared back the the previous computational work, and also to the secondary building units of the zeolites which the template forms. We also consider the docking of each template into the zeolite it forms as this can provide useful information as to why some templates form specific structures.

As well as the analysis of the hydration layers, the energetic barriers to a template, specifically TMA, approaching a silica monomer are investigated using a potential of mean force (PMF) calculation in order to gain an understanding of entropic effects and what barriers (if any) exist to a monomer approaching an organic

template. If the barriers to this are high then we would expect the substitution mechanism proposed by Burkett and Davis [134] not to occur.

6.4 Computational Methods

The hydration layer calculations were carried out using the Quickstep module that is part of the CP2K code [286]. GTH pseudopotentials [287, 288, 289] were used with a DZVP basis set and an energy cutoff of 280 Ry. These have previously been shown to reproduce water adequately [290, 144]. The templates were hydrated by cutting a cavity just large enough for the template in a pre-equilibrated box of water. These systems were then run in a *NPT* ensemble for 5 ps to equilibrate the volume in the case of the methyl systems and 3.5 ps in the case of the ethyl systems for a chain length of four and up. The systems were then run for a further 1 ps under the *NVT* ensemble using the Hoover thermostat to make sure the temperature was equilibrated. During the *NPT* temperature was initially controlled using a temperature re-scaling thermostat set to 350 K. A timestep of 1 fs was used for all simulations and the positive charge on the framework was neutralised with a background negative change. The production run was executed under *NVE* for 15 ps, and only the trajectories obtained from this portion were used to calculate the RDFs and for the ring analysis. The final compositions used for the collection runs can be found in Table 6.1. Figures 6.5 and 6.6 contain plots of the simulation volumes for the *NPT* run. Figures 6.4, 6.7 and 6.8 contain the simulation temperatures for the production runs. The pure water simulation consisted of 32 water molecules with the a cell parameter set to 9.852 Å in order to maintain the water density at 0.96 g dm^{-3}.

These simulations were run predominantly on the national supercomputer HeCTOR, as well as UCLs' supercomputer Legion. A 15 ps run took approximately 200 hours to complete running on 384 cores.

Solute	Volume Å^3	Number of waters
TPA	3711	104
TBA	4812	127
Pyrrolidinium	1824	61
Piperidinium	2135	62
Me_6-diquat-3	2464	75
Me_6-diquat-4	2869	89
Me_6-diquat-5	3325	94
Me_6-diquat-6	3420	100
Me_6-diquat-7	4380	123
Et_6-diquat-3	3985	111
Et_6-diquat-4	4073	115
Et_6-diquat-5	4307	122
Et_6-diquat-6	4768	133

Table 6.1: Cell compositions after the *NPT* run.

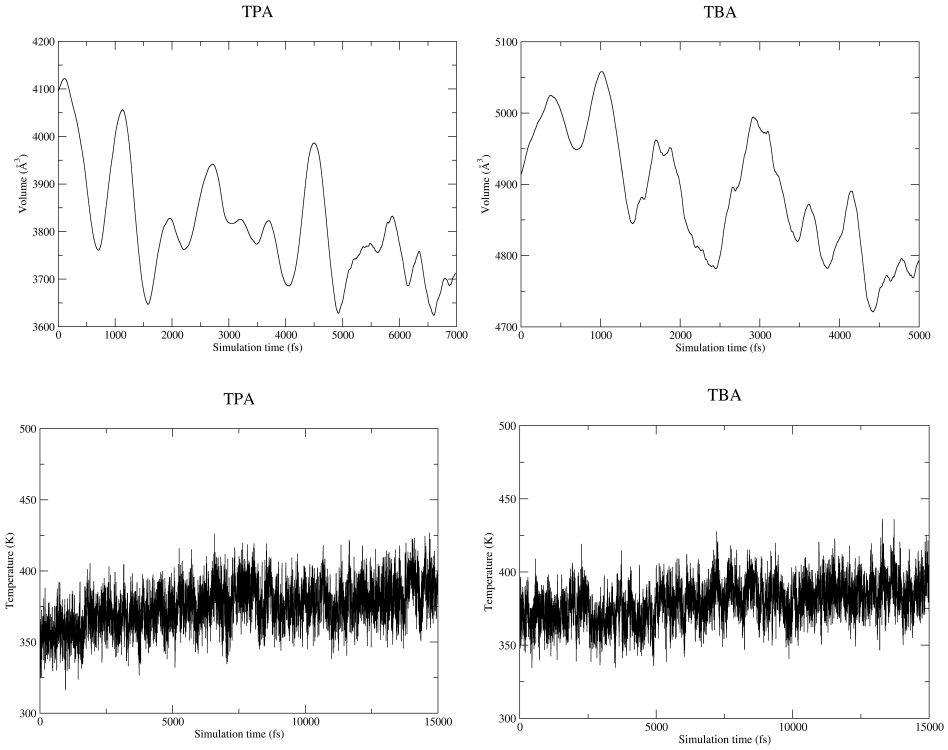

Figure 6.4: Volume (top)/temperature (bottom) vs simulation time for TPA and TBA.

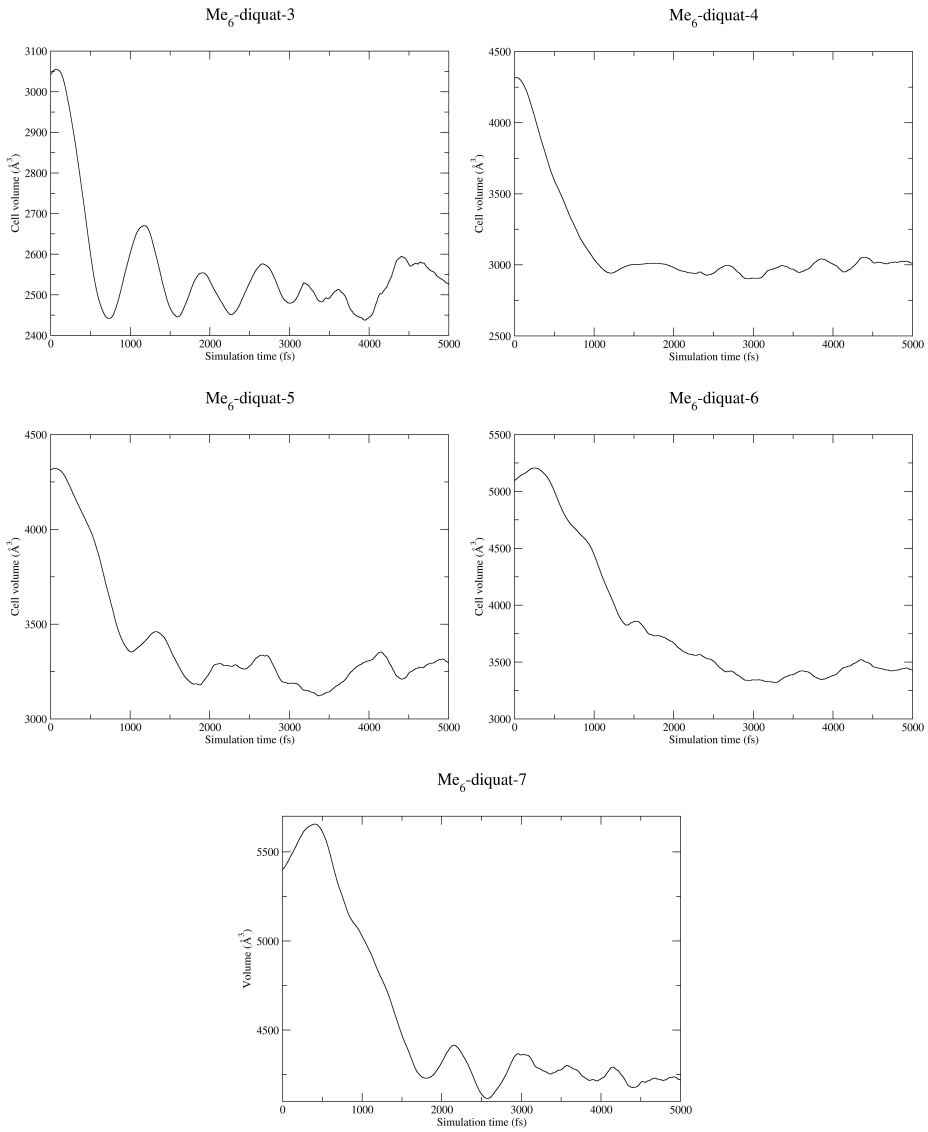

Figure 6.5: Volume vs simulation time for the methyl diquaternary ammonium cation series.

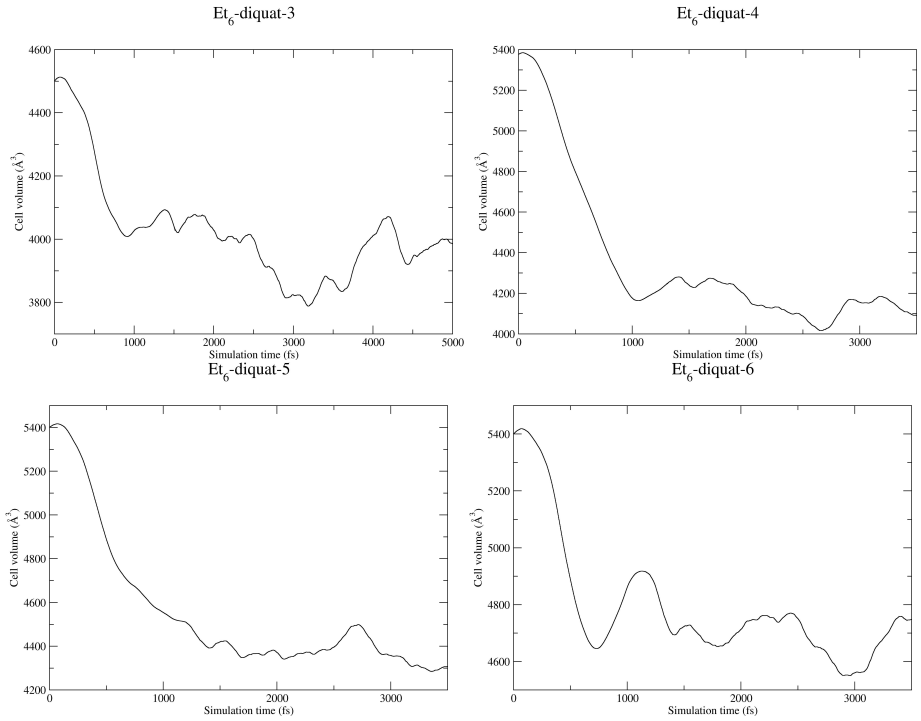

Figure 6.6: Volume vs simulation time for the ethyl diquaternary ammonium cation series.

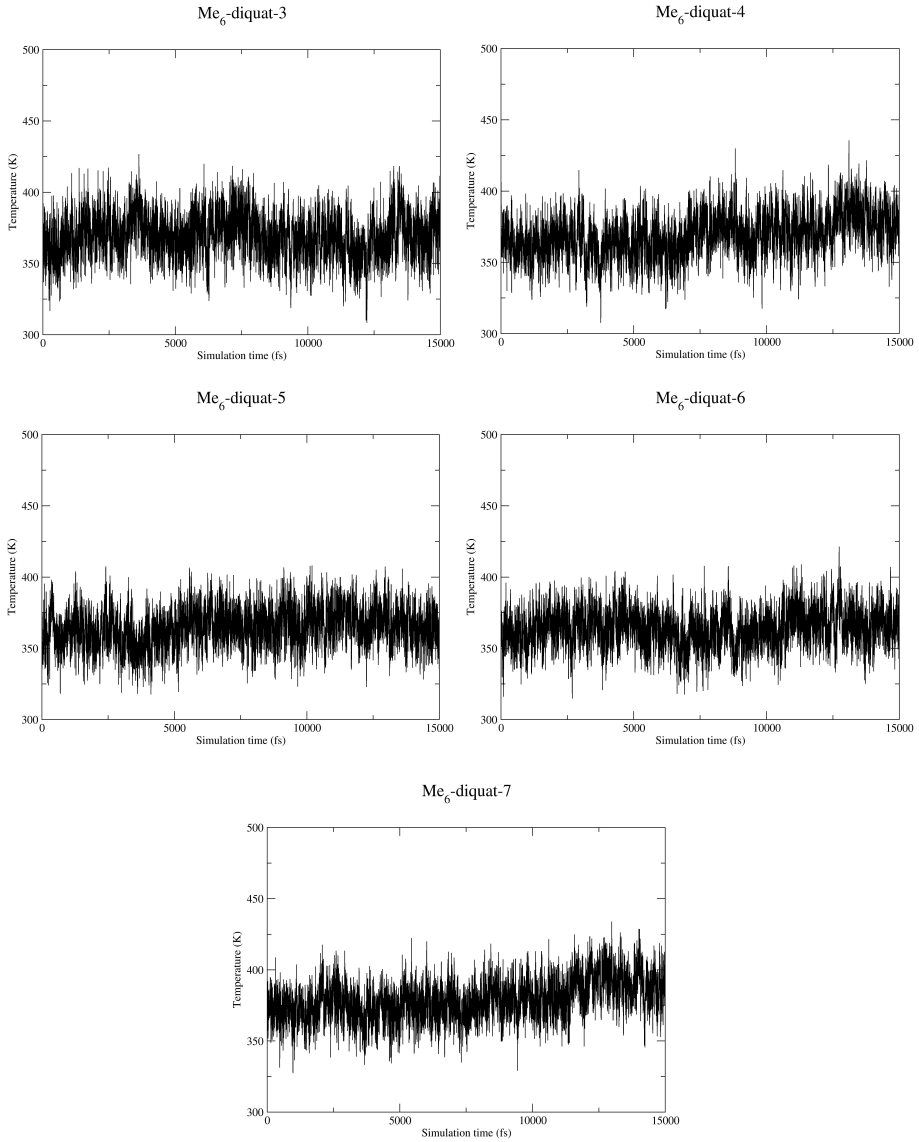

Figure 6.7: Temperature vs simulation time for the methyl diquaternary ammonium cation series *NVE* runs.

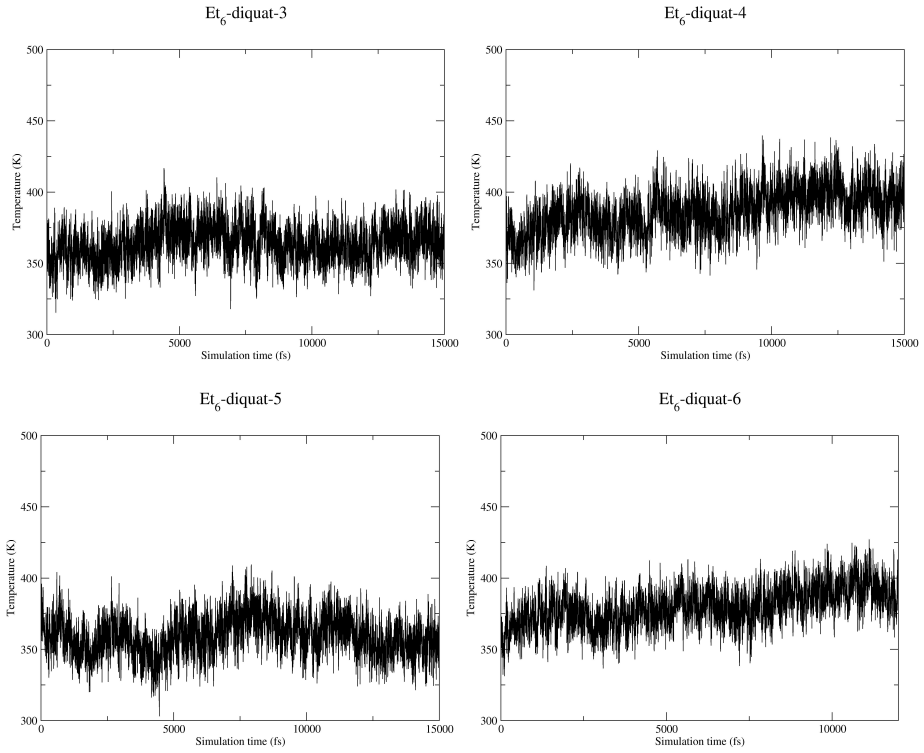

Figure 6.8: Temperature vs simulation time for the ethyl diquaternary ammonium cation series *NVE* runs.

6.4.1 Radial Distribution Functions

The theory behind measuring and calculating RDFs was discussed in section 6.2.1 and the correction for the solute excluded volume has been applied to all calculated RDFs. The hydrogen-hydrogen (H-H), oxygen-oxygen(O-O) and the oxygen-hydrogen(O-H) RDFs have been calculated for all the organic molecules studied here and compared to bulk water. Using the RDFs it is possible to determine structural features by comparing the degree of structuring of a peak, that is the peak height ratio and the peak width. In order to determine the peak height ratio the first non-zero minimum is used along with the first maximum. The peak-to-trough ratio R_c can be a very useful measurement. This is a measure of peak sharpness and this indicates the number of conformations the hydrogens in water may adopt. The O-O RDF is a measure less commonly seen experimentally as all that can be determined from neutron scattering experiments are D-X correlations, where D is deuterium and X is all other atoms. Therefore, when calculating an O-O RDF we will actually be taking into account other correlations from atoms present in the solution. Note that for the H-H and O-H RDFs the intra-molecular peak has been suppressed for clarity.

Along with the RDF, the corresponding coordination numbers have also been calculated. Coordination number is calculated by integrating the relevant peak, then weighting the result by the number density of the solution, followed by multiplication by the number concentration of the atom in question:

$$N_{ab}(r) = 4\pi C_b \rho \int_{r_1}^{r_2} r^2 g_{ab}(r) dr \tag{6.4}$$

where N_{ab} is the coordination number of atom B to atom A, C_b is the number concentration of atom B, ρ is the number density and g_{ab} is the radial distribution function at r. Note that the peak was integrated by calculating the area under half the peak then multiplying by two.

6.4.2 Ring Analysis

The ring statistics have been calculated using the code discussed in Section 6.2.2. In the case of the diquaternary ammonium cations the hydration layer has been broken down into separate components (see Figure 6.9) which we can relate back to

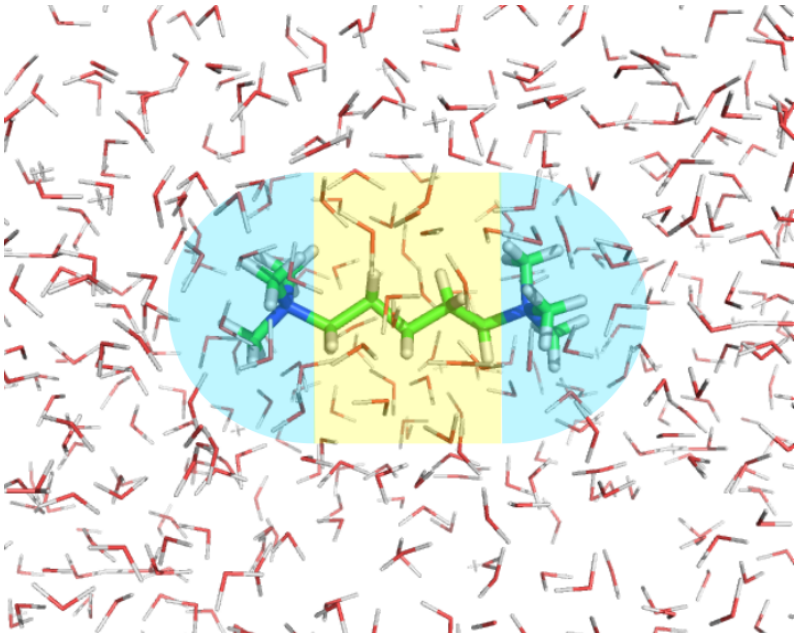

Figure 6.9: Diagram showing the two parts of the hydration layer. The nitrogen head groups in blue and the chain in yellow.

the zeolite which they form. The y-axis has been normalised as follows:

$$N_r = \frac{N}{sN_w} \tag{6.5}$$

where N_r is the normalised number of rings, N is the total number of rings found during the course of the simulation, s is the number of steps and N_w is the average number of water molecules in the hydration layer for that template. By normalising the number of rings in this manner it ensures that there is no skew of results simply because the template has a larger hydration layer.

	Zeolite							
Template	NON	MRE	FER	ZSM-12	EUO	MOR	MWW	ANA
Me_6-diquat-3	-87	-51	+49	-77	-84	-153	-71	-
Me_6-diquat-4	802	-81	-27	-82	-98	-170	-91	-
Me_6-diquat-5	-	-108	-12	-90	-99	-193	-106	-
Me_6-diquat-6	-	-101	+80	-97	-98	-196	-82	-
Me_6-diquat-7	-	-87	+7.4	-97	-101	-215	-92	-

Table 6.2: Methyl series interaction energies with the frameworks they template. The (-) indicates no docked structures were obtained. Energies in kJ mol^{-1}.

	Zeolite					
Template	MFI	MOR	MFS	GIS	AFX	SZR
Et_6-diquat-3	-87	-51	-174	-77	-84	+15
Et_6-diquat-4	+802	-81	-147	-82	-98	+196
Et_6-diquat-5	+726	-108	-171	-90	-99	+216
Et_6-diquat-6	+721	-101	288	-97	-98	+674

Table 6.3: Ethyl series interaction energies with the frameworks they template. Energies in kJ mol^{-1}.

6.5 Results

6.5.1 Docking Calculations

The docking calculations presented here were carried out using the modified ZEBEDDE code. The framework structures were taken from the IZA website [4] and converted (where necessary) to their entirely siliceous forms before being optimised using the GULP code [214] with the SiO_2 potentials of Sanders, Leslie and Catlow [188]. The docking procedure which has been discussed previously (see section 4.2.3) was then used to generate fifty docked structures. The best i.e. most negative, energy was then extracted from these and is presented in Table 6.2 for the methyl series and Table 6.3 for ethyl.

From Tables 6.2 and 6.3 it is immediately clear that zeolites with straight channels (MTW, MOR) generally have favourable interaction energies and the interaction energy increases as a function of chain length. Indeed most results fit well with the experiments of Lee *et al.* [291, 40]. MFI is only found for $n = 3, 7-10$ in significant quantities and as minor products at $n = 4, 5, 6$, we can see that only Et_6-diquat-3 has a favourable interaction energy. However, there are some surprising results. For example, that SUZ-4 (SZR) is obtained at all when using Et_6-diquat-5 templates since the interaction energy is very high, although this in in contrast to previous studies which found Et_6-diquat-5 docked with an interaction energy of -85 kJ mol^{-1}

[41]. This discrepancy occurs as the chain of Et_6-diquat-5 must contort to allow the head nitrogen groups to sit in the channel intersection which is clearly due to flaws in the calculation methodology as Monte Carlo simulation do not allow for these kind of actions. It is worth noting here that that all the Et_6-diquat-n templates, with the exception of Et_6-diquat-6 fit exceptionally well within ZSM-57(MFS). It is therefore surprising that Et_6-diquat-5 is the sole template currently known to direct the synthesis of this particular framework.

6.5.2 Large Tetraalkylammonium Compounds

6.5.2.1 RDFs

In previous work [263], solutions with TMA and tetraethylammonium (TEA) were compared to simulations of bulk water. To continue this, the next two members of the series, TPA and TBA, (see Figure 6.10) have been studied. Presented in Table 6.4 are the important peaks from the RDFs with the full graphs in Figure 6.11.

Focusing on the H-H RDF we notice that this peak has been shifted further out by 0.06 Å compared to pure water. We can see from the ratios that there is a sharpening of this peak when TPA is present but when TBA is present there is a slight reduction in the ratio. The first peak in the O-O RDF is in the same position for all species. However, both TPA and TBA have increased peak to trough ratios suggesting the water is more tightly held. The O-H RDF on the other hand, suggests that although the first peak is in almost the same place, the difference in peak to trough ratio implies that TBA is disrupting the hydrogen bond network, where as TPA is promoting it compared to pure water. If we consider the coordination numbers, we notice that compared to pure water there is a decrease in structuring on inclusion of the template. The O-O coordination number has decreased from 4.13 in pure water, suggesting ideal tetrahedral coordination, to 2.85 and 3.13 in TPA and TBA respectively. This is in line with previous work [272, 263] where disruption of the water network is observed. Furthermore, we can see from the decrease in O-H coordination number that the hydrogen bond network is also being disrupted.

6.5.2.2 Ring Analysis

The ring statistics for TPA and TBA compared to pure water are presented in Figure 6.12. As was observed with TMA and TEA in previous work [263] and with the organic ring molecules studied in this work we can immediately see there is a dramatic increase in the numbers of all types of rings, with five and six rings having the largest increase. Comparing these to the results for TMA and TEA we see the

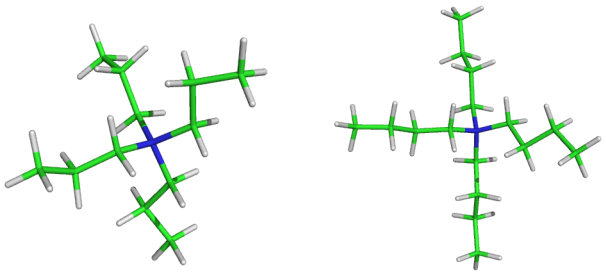

Figure 6.10: Structure of TPA and TBA.

Species	RDF	Peak	M_s	M_f	R_c	N_x
Water	HH	2.31	1.77	2.85	2.16	4.95
	OO	2.76	2.46	2.22	3.81	4.13
	OH	1.77	1.41	2.40	8.35	1.85
TPA	HH	2.37	1.80	2.97	2.29	4.18
	OO	2.76	2.40	3.36	4.65	2.85
	OH	1.80	1.38	2.46	9.27	1.44
TBA	HH	2.37	1.89	2.88	2.12	4.30
	OO	2.76	2.40	3.42	4.44	3.13
	OH	1.77	1.47	2.46	6.48	1.20

Table 6.4: Important peaks from the radial distribution functions for TPA and TBA compared to water. Peak is the position of the first peak. M_s is the start of the peak, M_f is the end, R_c is the ratio of the peak maximum to trough and N_x is the coordination number.

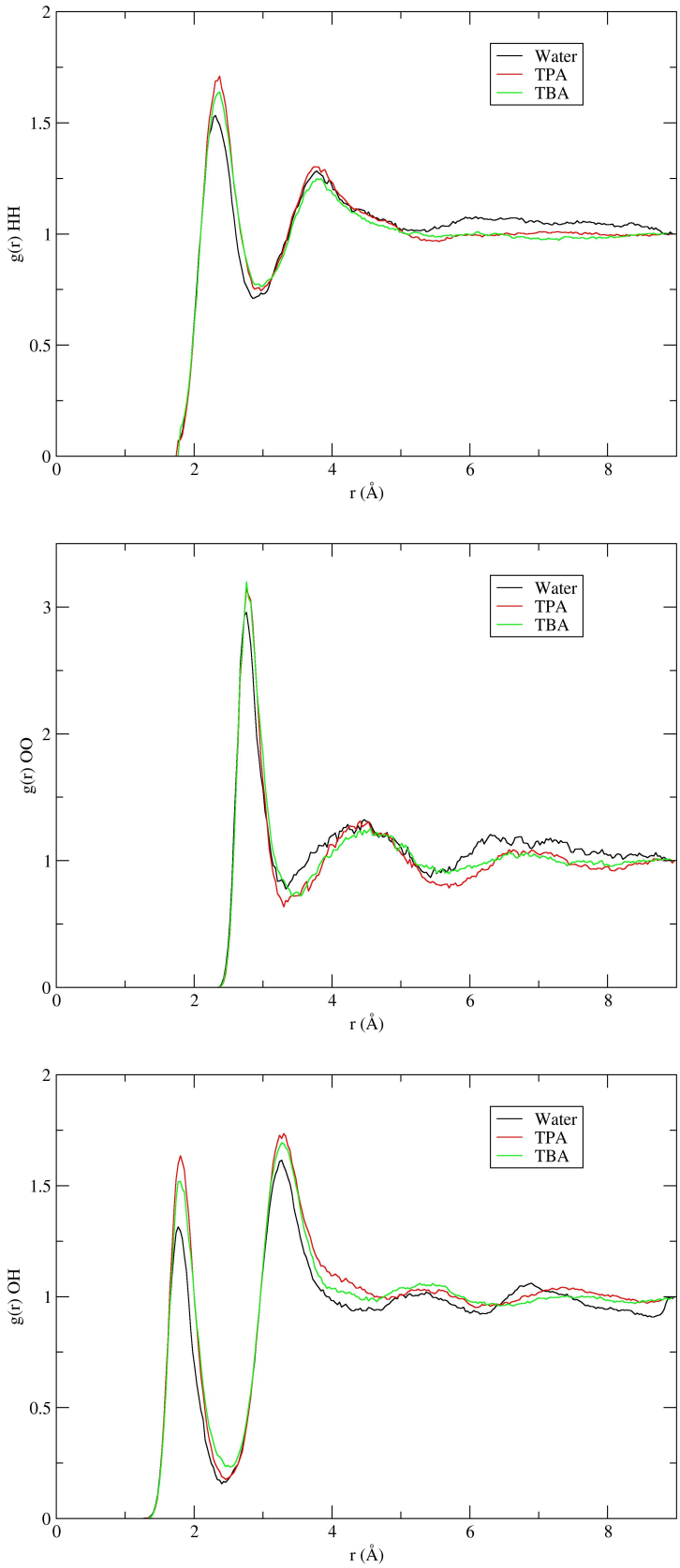

Figure 6.11: The radial distribution functions for pure water, TPA and TBA.

four ring is more prominent than for TEA but as was seen before we have an increase in the number of five rings as we make a more hydrophobic molecule.

The lifetimes of the rings around TPA/TBA are very low compared to water and relative to TMA/TEA. In fact, these are the lowest lifetimes observed for any of the rings with each type of ring only living for on average around 3.5 fs. This could be due to the flexibility of both TPA and TBA which are more flexible than TMA and TEA. This does link back to the lifetime drop observed in the rings around neopentane [263] and so this could also be a function of hydrophobicity. An alternative explanation is that lifetime is linked to charge density. Increasing the chain length screens the charge and so the larger TPA and TBA are unable to hold the water as firmly. This hypothesis also ties in with the results obtained for neopentane.

6.5.3 Cyclic Amines

6.5.3.1 RDFs

Studying the RDFs for pyrrolidinium and piperidinium (see Figure 6.13) compared to pure water (see Table 6.5 and Figure 6.14) we see that the ring structures induce ordering within the water. The first peak for pyrrolidinium in the H-H RDF has been shifted slightly from 2.31 Å in water to 2.25 Å, although the peak ratio remains the same. Piperidinium shifts the first peak further away and also causes a decrease in the ratio suggesting this molecule does not hold the water as rigidly. A similar pattern emerges for the O-O RDF, where the first peak for pyrrolidinium is shifted by -0.06 Å compared to water. This same peak for piperidinium is in the same position as for pure water. However, if we compare the peak ratio we see a dramatic increase from 3.81 to 4.65 and 4.45 for pyrrolidinium and piperidinium respectively, suggesting more rigidly held water. The O-H RDF shows similar effects, and although the peak position is almost identical both organics have an increased peak to trough ratio, piperidinium showing a slight increase of 0.31 and pyrrolidinium a much larger increase of 0.92. Like TPA/TBA the coordination numbers for the cyclic amines studied here also show a decrease in water structure, although it is less pronounced. Unusually, the hydrogen bond network in pyrrolidinium appears to be almost the same as water, but the water has been disrupted out of the tetrahedral conformation as is shown by the decrease in the O-O coordination number. We would expect large errors in calculating the coordination numbers from RDFs as there is ambiguity in assigning the peak minima and maxima and so this low O-O coordination number could be due to this.

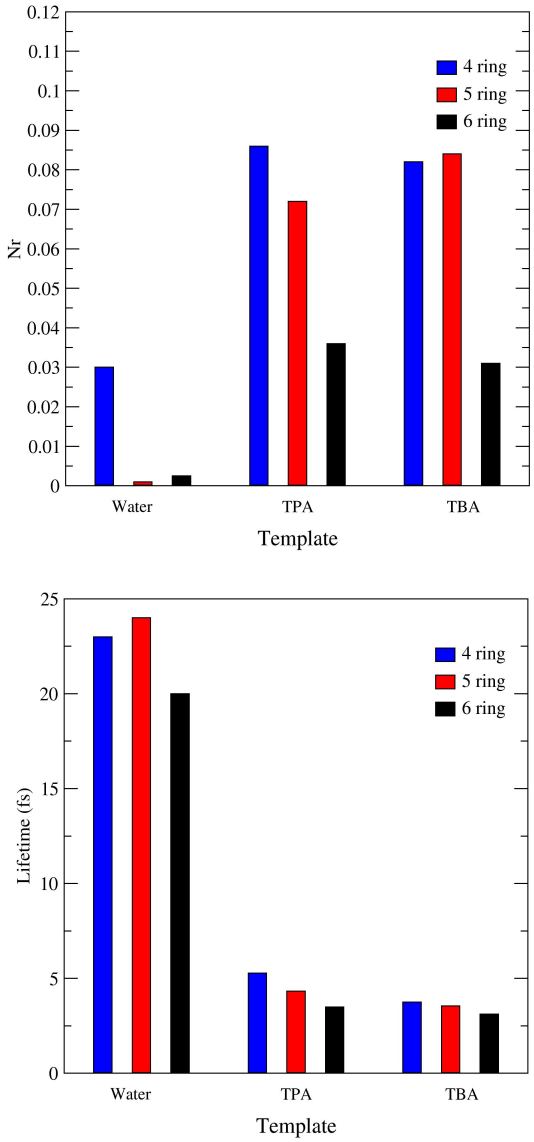

Figure 6.12: Numbers and lifetimes of rings present in the hydration layer of TPA and TBA compared to pure water.

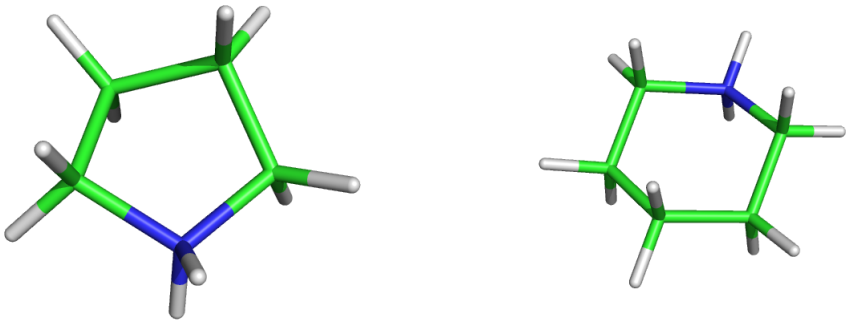

Figure 6.13: The two ring organics used in this study. Pyrrolidinium (left) and piperidinium (right).

Species	RDF	Peak	M_s	M_f	R_c	N_x
Water	HH	2.31	1.77	2.85	2.16	4.95
	OO	2.76	2.46	2.22	3.81	4.13
	OH	1.77	1.41	2.40	8.35	1.85
Pyrrolidinium	HH	2.25	1.80	2.82	2.16	3.41
	OO	2.70	2.43	3.30	4.65	2.51
	OH	1.80	1.38	2.46	9.27	1.89
Piperidinium	HH	2.37	1.89	2.91	1.91	4.83
	OO	2.76	2.40	3.42	4.45	3.31
	OH	1.77	1.47	2.46	8.66	1.40

Table 6.5: Important peaks from the radial distribution functions for TPA and TBA compared to water. Peak is the position of the first peak. M_s is the start of the peak, M_f is the end, R_c is the ratio of the peak maximum to trough and N_x is the coordination number.

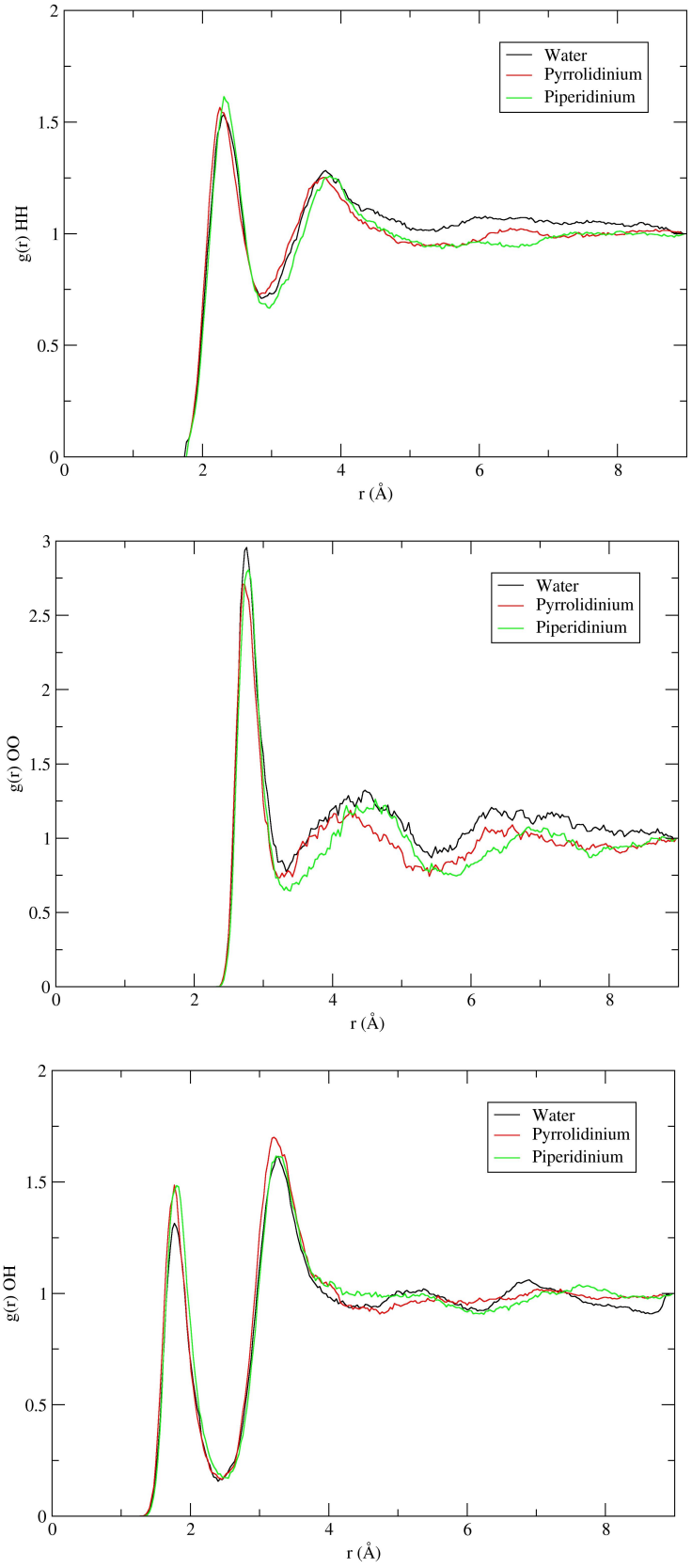

Figure 6.14: The radial distribution functions for pure water, pyrrolidinium and piperidinium.

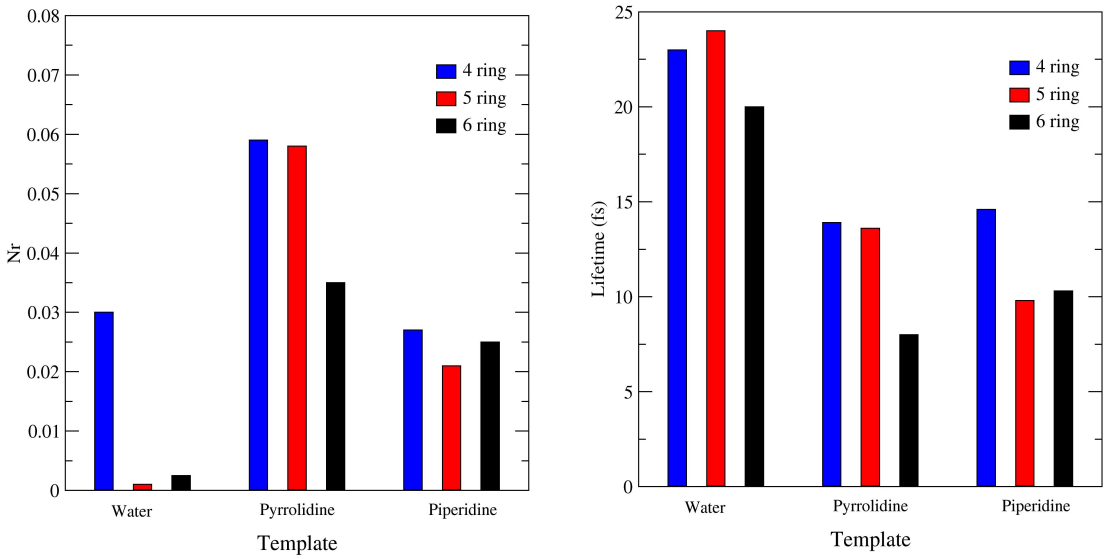

Figure 6.15: Number and lifetimes of the rings present in the hydration layer of small cyclic organics compared to pure water.

6.5.3.2 Ring Analysis

We have seen from the RDFs that there in an increase in the ordering of the water and this is reflected in the ring statistics. Figure 6.15 has the ring analysis for the two organic ring molecules studied here. For pyrrolidinium there are approximately twice as many four rings than in pure water. However, the most significant increases are in the number of five and six rings which are almost non-existent in pure water. Looking at pyrrolidinium, we still see an increase in the number of five and six rings but the number of four rings remains almost the same. This also corresponds to the RDFs where although we observe an increase in the ordering of the water, it is not as strong as in pyrrolidinium.

When comparing the lifetimes of the rings with water, we can see there is a decrease in the lifetimes of each type of ring by approximately a third. The lifetime of four rings is almost identical for both organic species. However, there is some variation in the lifetime of five rings which are longer lived in the hydration layer of pyrrolidinium. Six rings on the other hand are longer lived around piperidinium. Given that the charge on both species is the same, and just as exposed we can infer that this stabilises the four ring (as was seen in previous work [263]) and the extra carbon in the ring only disrupts ring formation, but it is interesting to note that the five member ring organic supports five rings and the six member ring supports six rings, although overall the stabilising effects are weaker.

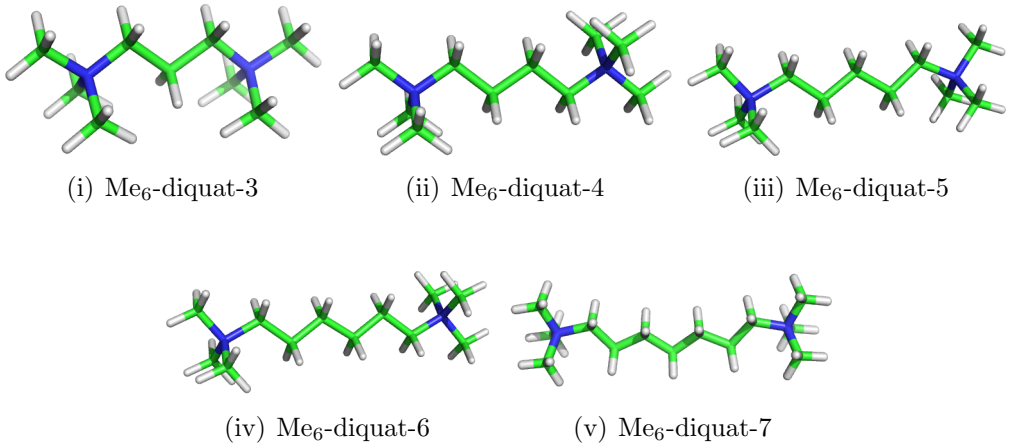

(i) Me_6-diquat-3 (ii) Me_6-diquat-4 (iii) Me_6-diquat-5

(iv) Me_6-diquat-6 (v) Me_6-diquat-7

Figure 6.16: The methyl diquaternary ammonium compounds studied.

6.5.4 Methyl Diquaternary Ammonium Series

6.5.4.1 RDFs

The first series of diquaternary ammonium compounds studied were the methyl series, (see Figure 6.16) Me_6-diquat-n, with $n = 3 - 7$. Table 6.6 contains the important measurements taken from the calculated RDFs. The H-H, O-O, and O-H RDFs of Me_6-diquat-3 are first compared to pure water (see Figure 6.17) before comparing to the whole diquaternary ammonium series in Figures 6.18, 6.19 and 6.20.

First comparing the RDFs of Me_6-diquat-3 to those of pure water, we can see that the overall shape is similar with the exception of the O-H RDF where we lose some of the intermediate range order. Focusing on the H-H RDF we see that the first inter-molecular peak is shifted slightly (0.06 Å) when in the presence of Me_6-diquat-3. We see almost no change (0.01) in this ratio suggesting that the degree of structure is almost identical. In the O-O RDF for Me_6-diquat-3 and pure water we see no change in the first inter-molecular peak. However, there is an increase in the peak ratio from 3.81 in pure water to 3.98 in Me_6-diquat-3. This suggests that although the water is not closer in to the Me_6-diquat-3 it is more restricted.

Finally, we consider the O-H RDF, which provides information on the hydrogen bond structure. The peak for both water and Me_6-diquat-3 falls at 1.77 Å which is slightly lower than the ideal hydrogen bond length observed experimentally of about 1.9 Å[292]. However, there is once again an increase in the peak-to-trough ratio from 8.35 for pure water to 8.70 in Me_6-diquat-3. Once again this suggests a slightly more restricted mobility within the hydration layer of Me_6-diquat-3. Overall this suggests that the structure of the water network around Me_6-diquat-3 is not

Species	RDF	Peak	M_s	M_f	R_c	N_x
Water	HH	2.31	1.77	2.85	2.16	4.95
	OO	2.76	2.46	3.15	3.81	4.13
	OH	1.77	1.41	2.40	8.35	1.85
Me_6-diquat-3	HH	2.37	1.80	3.00	2.15	4.76
	OO	2.76	2.37	3.36	3.98	3.25
	OH	1.77	1.41	2.43	8.70	1.41
Me_6-diquat-4	HH	2.28	1.80	2.91	2.11	3.56
	OO	2.79	2.40	3.27	3.83	4.00
	OH	1.77	1.47	2.43	7.83	1.43
Me_6-diquat-5	HH	2.31	1.80	2.94	2.60	3.62
	OO	2.79	2.46	3.42	6.28	3.61
	OH	1.80	1.47	2.46	11.14	1.60
Me_6-diquat-6	HH	2.31	1.80	2.97	2.43	3.63
	OO	2.79	2.46	3.39	4.71	3.69
	OH	1.80	1.47	2.52	9.54	1.61
Me_6-diquat-7	HH	2.31	1.80	2.97	2.25	3.23
	OO	2.79	2.46	3.33	4.59	3.43
	OH	1.80	1.47	2.55	7.88	1.40

Table 6.6: Important peaks from the radial distribution functions for Me_6-diquat-n with $n = 3 - 7$. Peak is the position of the first peak. M_s is the start of the peak, M_f is the end, R_c is the ratio of the peak maximum to trough and N_x is the coordination number.

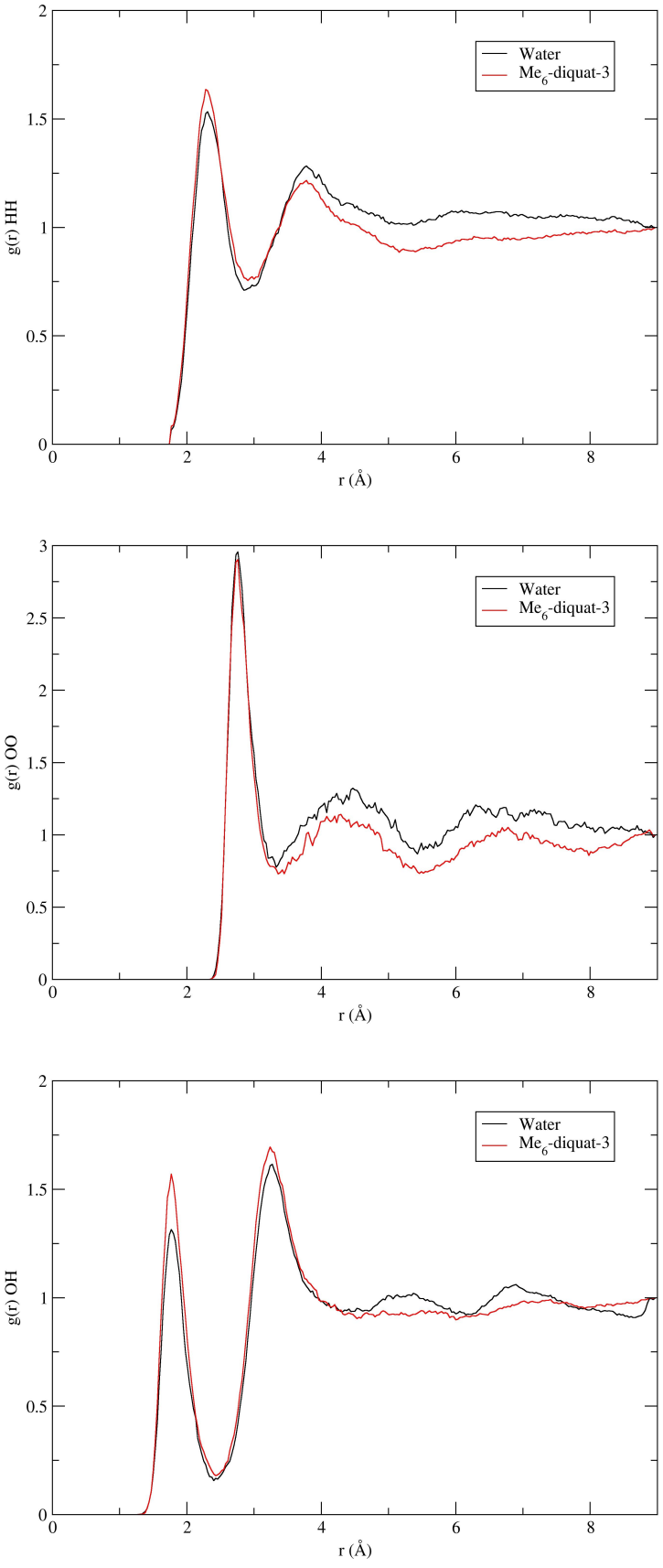

Figure 6.17: The radial distribution functions for pure water and Me_6-diquat-3.

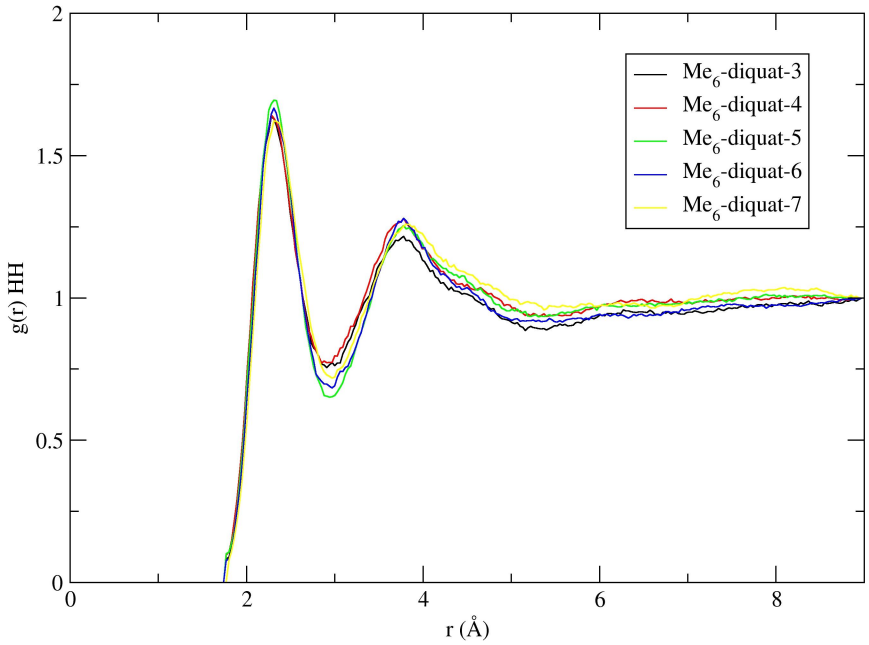

Figure 6.18: The H-H radial distribution function for Me_6-diquat-n with $n = 3 - 7$.

very different to that of bulk water, but what we can say is that the motion of the water is more restricted.

The results for the remaining methyl diquaternary ammonium cations are now compared to Me_6-diquat-3. On visual inspection we can see that the RDFs look remarkably similar. However, on closer inspection we observe some important differences. First, in the H-H RDF (Figure 6.18), there is small shift (-0.09 Å) in the first peak between Me_6-diquat-3 and Me_6-diquat-4. However, for Me_6-diquat-5, Me_6-diquat-6 and Me_6-diquat-7 the first peak shifts slightly further out to 2.31 Å. These results suggest that the chain length of four holds the water slightly closer. Comparing the ratios we see that there is a slight drop of 0.04 between Me_6-diquat-3 and Me_6-diquat-4, but this is followed by a dramatic increase (+0.49) to Me_6-diquat-5. There is then a drop in the ratio by 0.17 between Me_6-diquat-5 and Me_6-diquat-6 and finally to 2.25 for Me_6-diquat-7. These results suggest the structure of water around Me_6-diquat-5 is unique, having less flexibility than the water around the other templates considered.

In the O-O RDFs (Figure 6.19) we see almost no change in the position of the first peak. There is a slight change (0.03 Å) when moving from Me_6-diquat-3 to Me_6-diquat-4 but this remains constant at 2.79 Å for the remaining chain lengths. For the ratios we see a similar trend to the H-H RDF where there is a maximum for Me_6-diquat-5, and a minimum at Me_6-diquat-4. These same trends are also seen in the

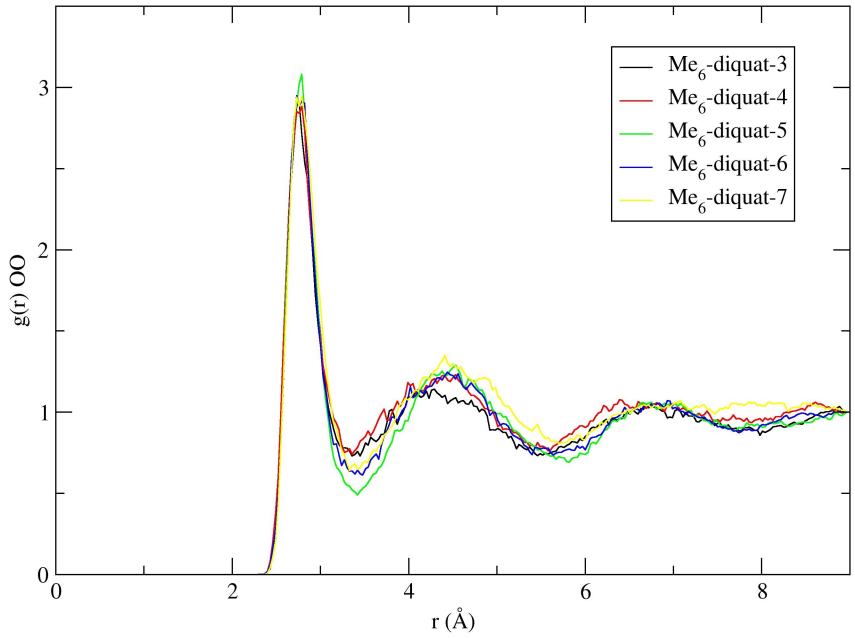

Figure 6.19: The O-O radial distribution function for Me_6-diquat-n with $n = 3-7$.

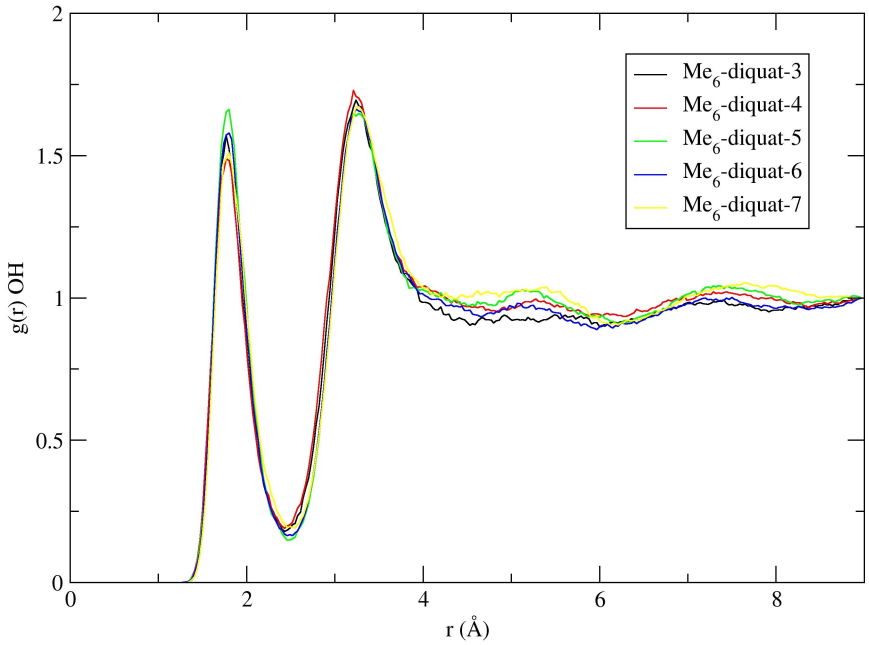

Figure 6.20: The O-H radial distribution function for Me_6-diquat-n with $n = 3-7$.

O-H RDF (Figure 6.20) where once again the highest ratio is seen for Me_6-diquat-5 at 11.14, and the lowest for Me_6-diquat-4 at 7.83, although Me_6-diquat-7 has almost the same value. Thus, regardless of RDF considered Me_6-diquat-5 appears to behave differently to the remainder of the series.

Comparing the coordination numbers we notice Me_6-diquat-5 and Me_6-diquat-6 have the greatest number of hydrogen bonds. However, given the reduced O-O coordination number, the water has been distorted from the tetrahedral configuration. Interestingly, the O-O coordination number is exactly 4.0 for Me_6-diquat-4 suggesting that the water is tetrahedral, but the O-H coordination number is low (1.43) which indicates there is a lot of movement in the hydration layer. The coordination numbers for Me_6-diquat-3 and Me_6-diquat-7 show the weakest ordering with low numbers of hydrogen bonds, and water shifted out of the bulk tetrahedral coordination.

6.5.4.2 Ring Analysis

The ring statistics for the methyl series of diquaternary ammonium compounds can be found in Figure 6.21. As with the previously studied templates [263] there is a significant increase in the number of five and six rings compared to pure water. The number of five rings in the total hydration layer remains relatively constant for all values of n, with only a slight decrease at $n = 4$ and 5, with the same trend observed for the six rings. However the number of four rings fluctuates as the chain length is made longer. This appears to follow a pattern and possibly linked to the conformation of the template, since when the number of carbons is odd the methyls on the nitrogen are on the same "side".

When we partition the water, it is interesting to note that the Me_6-diquat-3 is almost identical to TMA where four rings are most stable followed by five, then six. As we move though the series, there is a steep decline in the number of four rings present, and five rings become more dominant. The number of five rings appears to peak at a chain length of five. The six rings again follow the same trend as four rings. Around the chain, there are almost no five and six rings in the hydration layer of Me_6-diquat-3. This is due to the hydration layer being too small and so there are simply too few water molecules present to form any large rings. Moving to Me_6-diquat-4 there is a dramatic increase in the number of five rings. However there are still almost no six rings until we reach a chain length of five carbons. Once again there is an alternation in the number of four rings which ties into the orientation of the nitrogen head groups although this appears to break down one we reach Me_6-diquat-7.

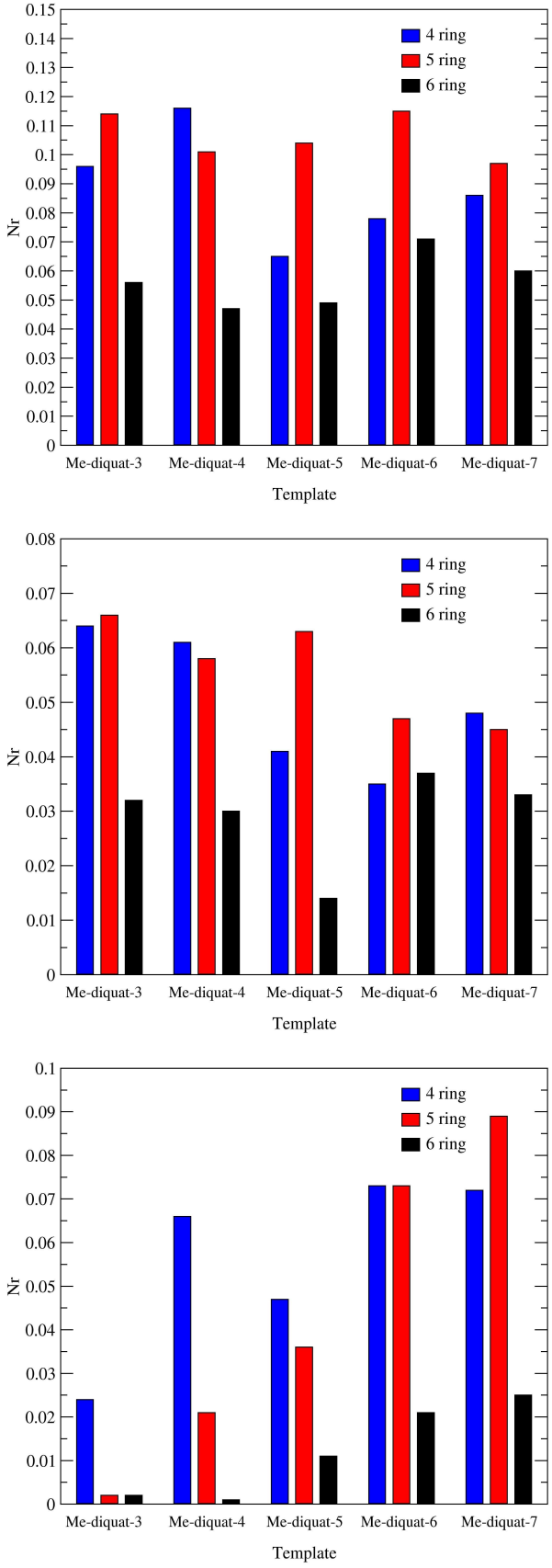

Figure 6.21: Average number of rings in the whole hydration layer (top), around the end nitrogen groups (middle) and around the chain (bottom) for Me_6-diquat-n series.

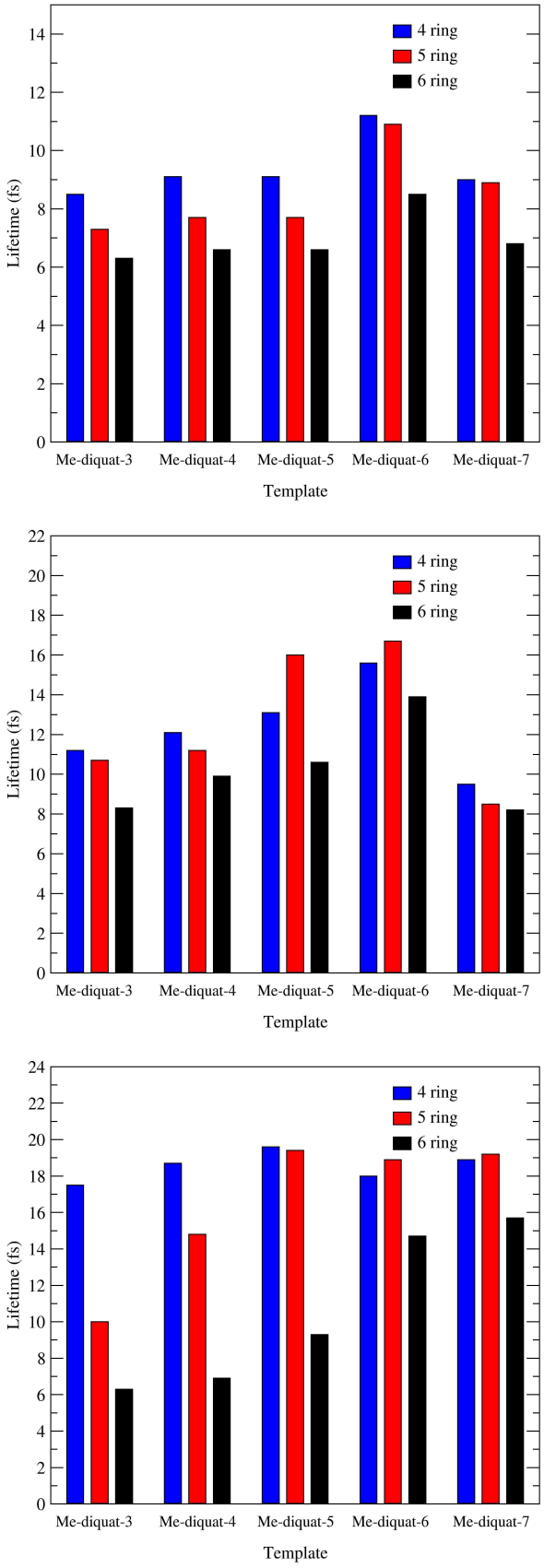

Figure 6.22: Average lifetime of rings in the whole solvation layer (top), around the end nitrogen groups (middle) and around the chain (bottom) for Me_6-diquat series.

The average lifetimes for the rings are in Figure 6.22. Starting with the total solvation layer we can see that the trend is the same for each template where the four ring is longest lived, followed by five then six. An interesting feature is the general increase in lifetimes as we increase the chain length which suggests that the chain that the hydrophobic nature of the chain has a stabilising effect on the hydration layer. Focusing on the lifetimes of the rings which form around the nitrogen head groups, we again see a general increase in the lifetimes. However, unlike for the total hydration layer, the five ring becomes dominant once the chain length reaches five.

Interestingly, around the chain of Me_6-diquat-3 despite the number of five and six rings present being extremely low, the rings that do exist are relatively long lived. The lifetime of the four ring stays relatively constant, but the lifetime of the five and six rings increases as the chain length increases.

6.5.5 Ethyl Diquaternary Ammonium Series

6.5.5.1 RDFs

A similar analysis has been carried out for the ethyl series (see Figure 6.23), Et_6-diquat-n with $n = 3 - 6$. Once again the excluded volume has been applied when calculating the RDFs and the intra-molecular peak has been removed for clarity. Figure 6.24 compares the RDF of pure water to Et_6-diquat-3, with the important peaks from all RDFs listed in Table 6.7. From a visual inspection we can immediately see there is a much greater ordering of the water around the templates than in pure water, and indeed more than with the methyl diquaternary compounds: all the peaks are more defined.

If we look first in detail at the H-H RDF for pure water and Et_6-diquat-3 we see that although the first intermolecular peak is in the same position the peak to trough ratio has increased by 0.51 which implies the water has far less freedom. We see similar results with the O-O RDF. The first peak in the Et_6-diquat-3 O-O RDF is shifted very slightly (-0.03) nearer suggesting that the water is slightly closer together but once again there is a more dramatic change (+2.25) in the peak to trough ratio. The O-H RDF is also well defined, and again the first peak is in the same position but has a greater ratio suggesting the hydrogen bond network is more stable.

Figures 6.25, 6.26 and 6.27 compare the RDFs for the full ethyl series studied. By inspection we can clearly see that Et_6-diquat-3 orders the water most. The first peak on the H-H RDF remains in the same place, with the exception of Et_6-diquat-5 where it is shifted very slightly (+0.03). The ratio R_c is considerably larger for

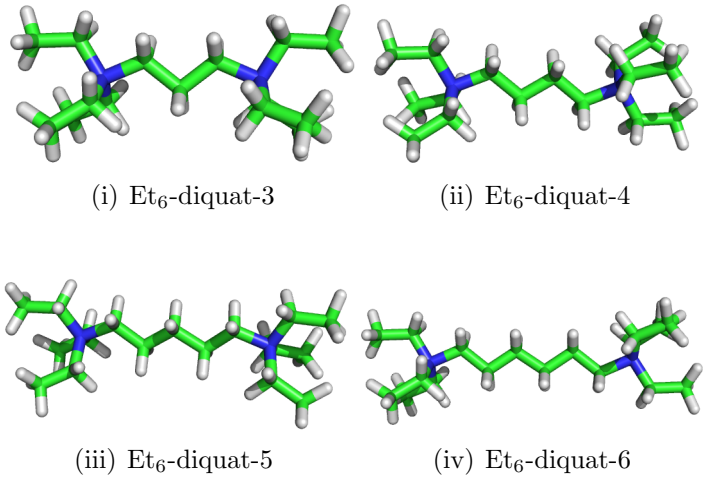

(i) Et_6-diquat-3 (ii) Et_6-diquat-4

(iii) Et_6-diquat-5 (iv) Et_6-diquat-6

Figure 6.23: The ethyl diquaternary ammonium compounds studied.

Species	RDF	Peak	M_s	M_f	R_c	N_x
Water	HH	2.31	1.77	2.85	2.16	4.95
	OO	2.76	2.46	2.22	3.81	4.13
	OH	1.77	1.41	2.40	8.35	1.85
Et_6-diquat-3	HH	2.31	1.80	2.94	2.67	3.96
	OO	2.73	2.46	3.39	6.06	2.81
	OH	1.77	1.44	2.49	12.32	1.48
Et_6-diquat-4	HH	2.31	1.80	2.94	2.07	3.69
	OO	2.73	2.37	3.36	3.75	2.49
	OH	1.80	1.47	2.46	6.56	1.50
Et_6-diquat-5	HH	2.34	1.77	2.97	2.24	4.15
	OO	2.76	2.40	3.39	4.29	3.31
	OH	1.80	1.47	2.49	8.32	1.60
Et_6-diquat-6	HH	2.31	1.77	2.97	2.15	3.71
	OO	2.79	2.46	3.39	4.40	3.74
	OH	1.80	1.47	2.46	7.52	1.56

Table 6.7: Important peaks from the radial distribution functions for Me_6-diquat-n with $n = 3-6$. Peak is the position of the first peak. M_s is the start of the peak, M_f is the end, R_c is the ratio of the peak maximum to trough and N_x is the coordination number.

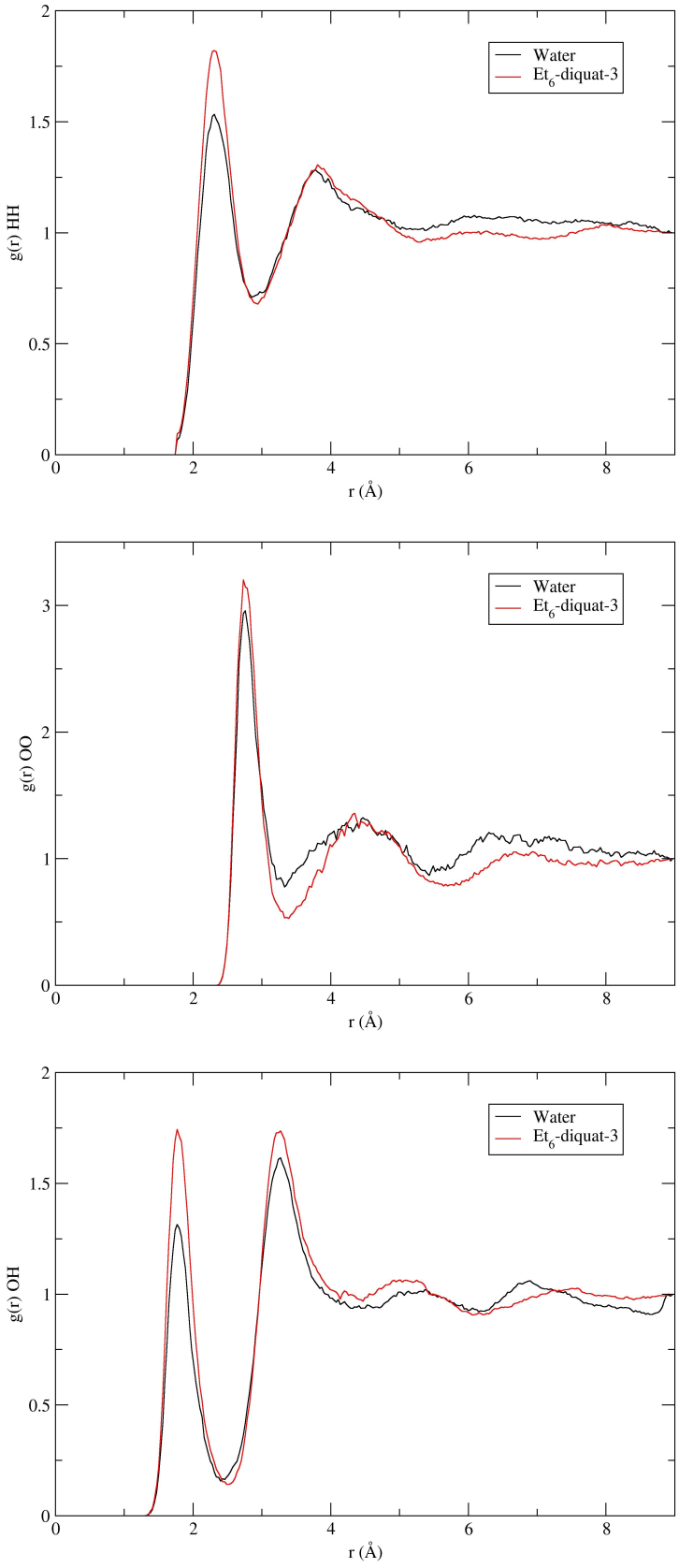

Figure 6.24: The radial distribution functions for pure water and Et_6-diquat-3.

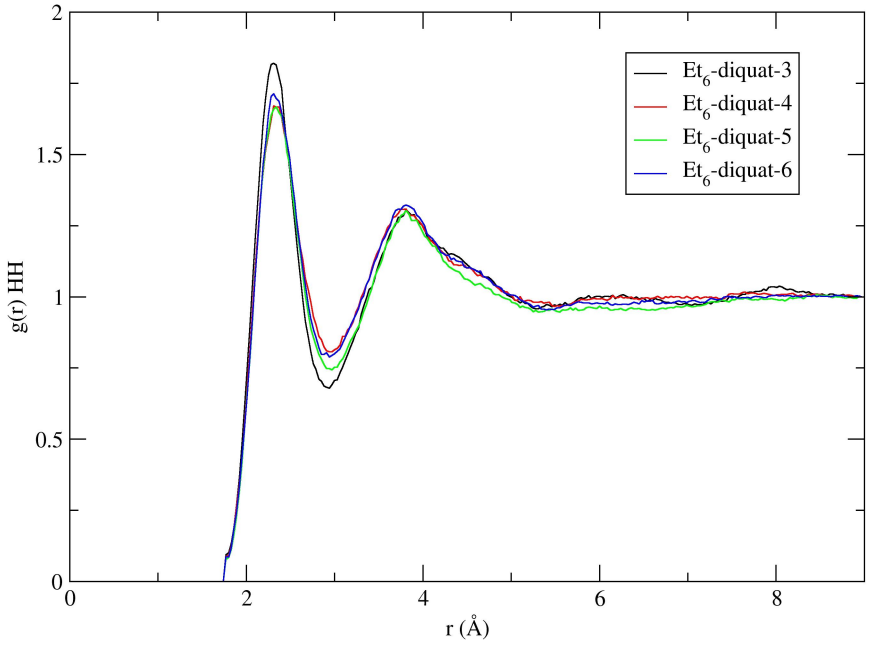

Figure 6.25: The H-H radial distribution function for Et_6-diquat-n with $n = 3 - 6$.

Et_6-diquat-3 than any other template at 12.32.

The first peak in the O-O RDF shifts slightly from 2.73 Å in Et_6-diquat-3 to 2.79 Å for Et_6-diquat-6 suggesting the hydration layer is further away from the organic. As with the H-H RDF the ratio of the peak for Et_6-diquat-3 is much larger than the other templates at 6.06 with Et_6-diquat-5 next highest at 4.29. The O-H RDF is similar to the O-O RDF with once again Et_6-diquat-3 having the highest peak ratio at 12.32 suggesting that this template promotes hydrogen bonding within the water. Et_6-diquat-5 is again second but we see very little shift in the peak position.

If we consider the coordination numbers, it is interesting to note that the highest degree of hydrogen bonding is found in the water surrounding Et_6-diquat-5, which is known to direct a number of frameworks. As with the methyl series, the shortest chain length ($n = 3$), has the lowest coordination number of O-H. This could be a factor of charge density, as this decrease was also observed when studying TMA/TEA [263]. Similarly, at long chain length, flexibility of the template may play a role in disrupting this network, implying there is an optimum chain length-/charge density. The O-O coordination number increases as the chain length is made longer also suggesting that charge causes disruption to the water network, breaking the tetrahedral structure.

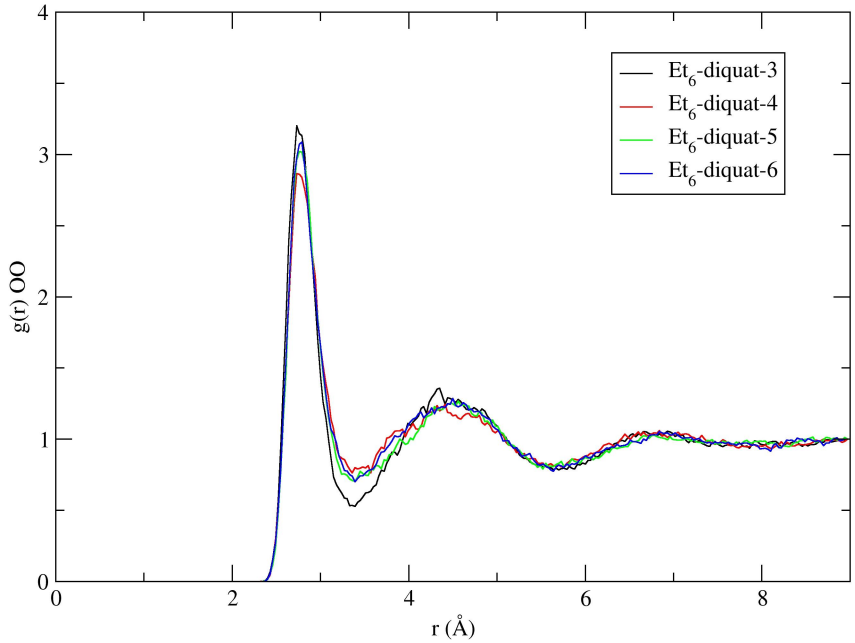

Figure 6.26: The O-O radial distribution function for Et_6-diquat-n with $n = 3 - 6$.

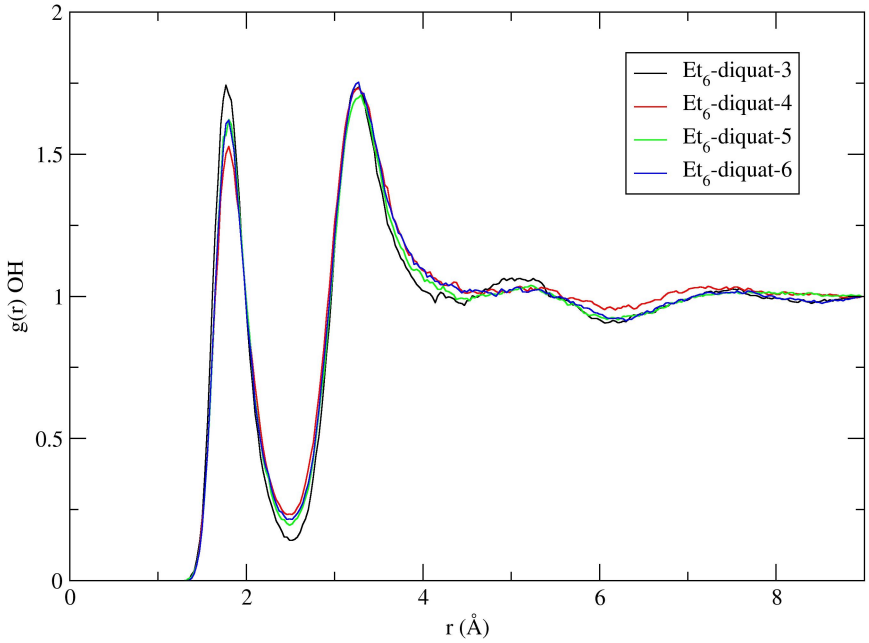

Figure 6.27: The O-H radial distribution function for Et_6-diquat-n with $n = 3 - 6$.

6.5.5.2 Ring Analysis

The second series studied was the ethyl diquaternary ammonium cation series with chain lengths of three to six. These templates can be seen in Figure 6.23. First looking at the whole hydration layer we can see there is far more variation in structure than was seen for the methyl compounds. The five ring is now more dominant, which correlates with previous work where it was determined that more hydrophobic surfaces promote five ring formation [263]. However, in contrast, six rings appear to be very unfavourable whilst four rings increase in number as the chain length is made longer.

Looking at the hydration layer around the end groups we do not see a similarity between the rings formed around Et_6-diquat-3 and those around TEA as was seen in Me_6-diquat-3/TMA. An interesting feature is the difference between Et_6-diquat-4 and the other diquats where the distribution of rings is quite different. There are almost half as many five rings in the hydration layer around the head groups of Et_6-diquat-4 as there are around Et_6-diquat-3. There is also a dramatic increase in the number of four rings for the chain length of four, and comparatively few six rings. For the Et_6-diquat-5 and Et_6-diquat-6 the five ring is again most stable.

However, the number of rings in the hydration layer around the chain look remarkably similar to that of the methyl series. Once again for the shortest chain the overall number of rings is low with four rings being most prevalent. There are about a quarter as many five rings and almost no six rings. Again we consider this to be the result of the hydration layer in this section being too small to support ring formation. As was seen for the methyl series there is an increase in the numbers of all rings formed with increasing chain length. However, the number of four rings appears to plateau whereas the number of five and six rings increases relatively linearly.

As with the methyl series, the average lifetime of the various rings are remarkably similar. For the whole solvation layer four rings are the most long lived, followed by five then six. This is the case for all chain lengths, but we again see the average lifetime increase with chain length. Around the head groups the same trend is maintained until Et_6-diquat-5 where five rings become most stable. However, unlike the Me_6-diquat-6 series this is not the case for Et_6-diquat-6. There is once again a general upward trend in average lifetimes. Finally around the the chain we see a decrease in the lifetime of four rings. Five and six rings seem to peak in the middle before dropping off again for Et_6-diquat-6: although we have not considered longer chains.

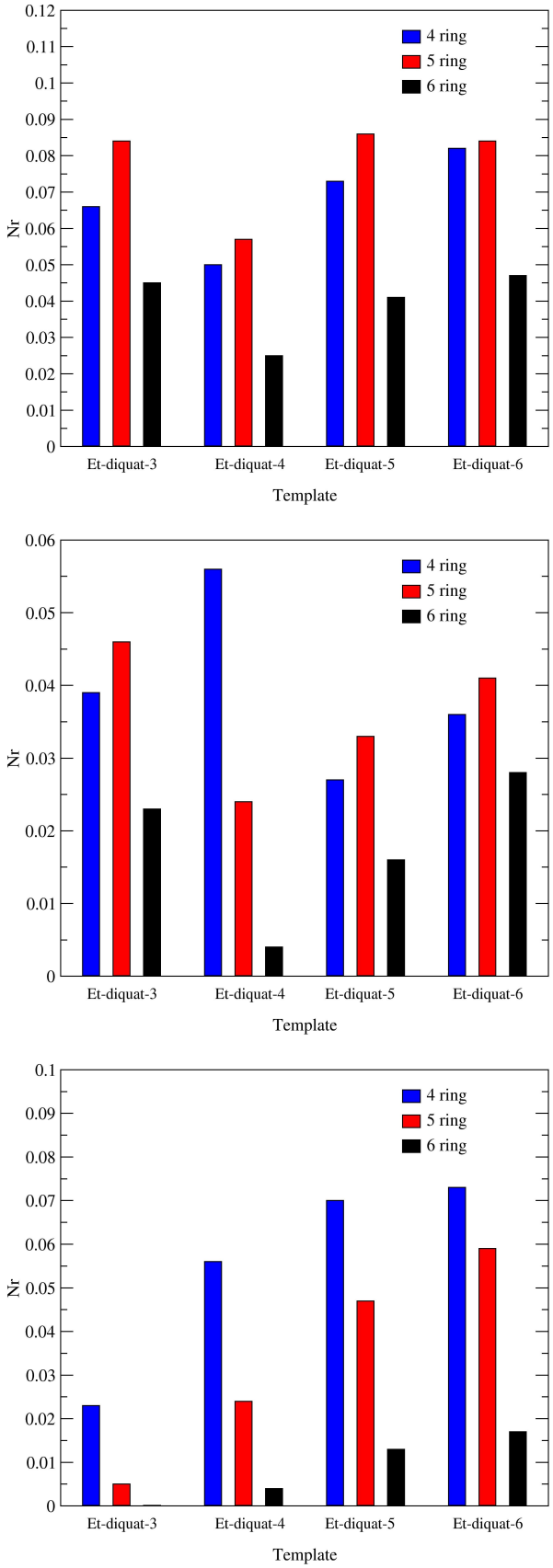

Figure 6.28: Average number of rings in the whole hydration layer (top), around the end nitrogen groups (middle) and around the chain (bottom) for Et_6-diquat series.

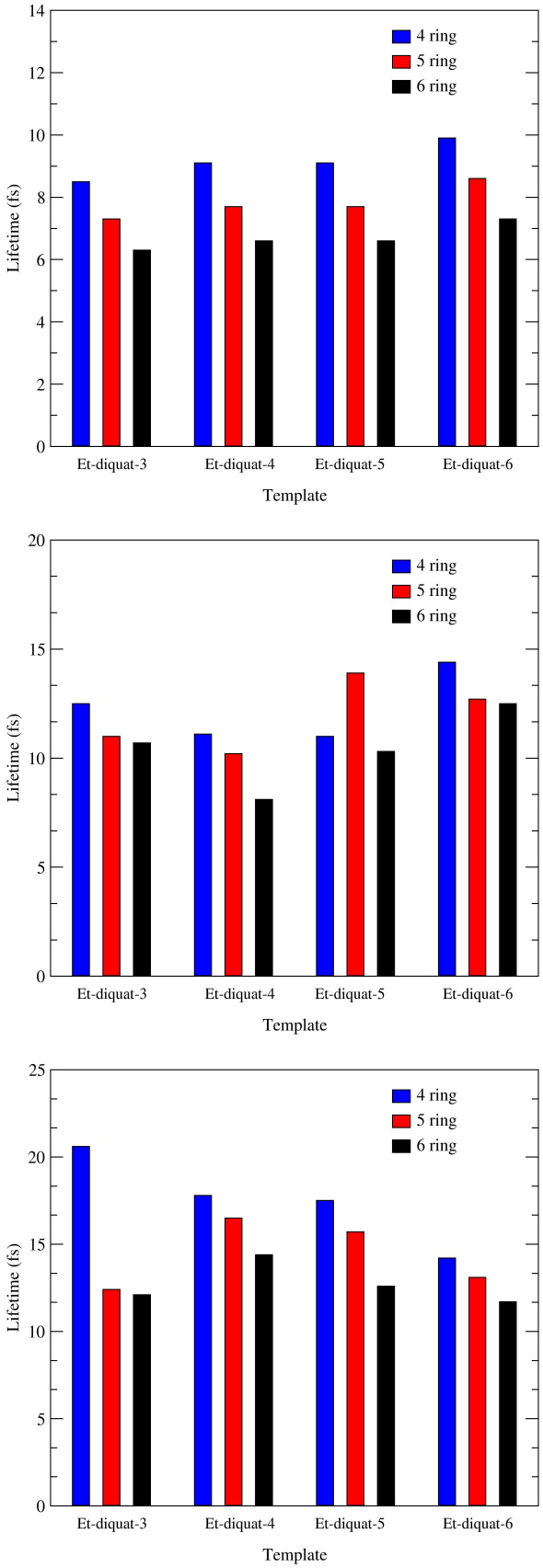

Figure 6.29: Average lifetime of rings in the whole hydration layer (top), around the end nitrogen groups (middle) and around the chain (bottom) for Et_6-diquat series.

6.5.6 Discussion

The simulations carried out on the TPA/TBA system yielded interesting results, whereby the lifetime of the rings in the hydration layer are dramatically reduced compared to pure water. However, as was seen in TMA/TEA, the numbers of both five and six rings has increased over pure water, with the most significant increases in five rings. If we consider the RDFs, we note that these templates disrupt the water structure as we see decreases in all the coordination numbers compared to pure water. The calculations on the cyclic amines also provided insight into how cyclic templates affect the water structure with pyrrolidinium far exceeding piperidinium in terms of altering the structure of the water. The O-H coordination number increases compared to bulk water and this increase is mirrored in the greater number of rings present in the hydration layer. Interestingly, the lifetime of these rings is almost identical suggesting that it may be charge which promotes longer lifetimes.

If we compare the results from the RDFs to the ring and lifetime statistics we see a distinct correlation. In the case of the methyl series, the RDF show that Me_6-diquat-5 has the most ordered water around it closely followed by Me_6-diquat-6. In the ring lifetime statistics these diquat templates show the longest lifetimes. In the ethyl series Et_6-diquat-3 shows the strongest ordering in the RDFs, but the correlation with lifetime is not as clear as for the methyl series. The lifetimes are generally quite similar, and there is a correlation with the ring statistics, where the four and five rings are most frequent. There is possibly a clearer link between the RDFs of Et_6-diquat-4 which shows weakest water ordering, where the lowest ring counts are found, and the ring and lifetime statistics, which are again short. Although the errors in the coordination numbers obtained form the RDFs are high, there appears to be a link between charge density and disruption of the hydrogen bond network in the water, as well as movement away from the tetrahedral configuration. However, it is also possible that this is a factor of hydrophobicity as longer chain length rather than charge density as in this case they are intrinsically linked. What we can say though is there is an optimum point where $n = 5$.

It was hoped that the structures formed in the water in the hydration layers of these templates could be linked to the zeolite structures they eventually form. To highlight the features that will be discussed, Figure 6.30 shows the first hydration layer around Et_6-diquat-5 within this hydration layer Figure 6.31 shows some of the different ring sizes which are present and a double five ring structure around the chain which is similar to that found in ZSM-57. We begin by considering the frequency that a particular ring occurs by summing the numbers of each type of ring (up to six) which form the composite building units. Table 6.8 contains the

Framework	4-rings	5-rings	6-rings
NON	2	32	16
MRE	2	8	30
MTW	2	16	24
FER	0	40	2
EUO	4	40	22
MWW	48	96	74
MTT	0	10	10

Table 6.8: Ring counts for zeolites made by Me_6-diquat-n with $n = 3-7$ taken from the IZA website [4].

frequencies for zeolites formed using methyl diquaternary ammonium series studied here. Although a number of different frameworks are made using these templates, it is interesting to note that when using Me_6-diquat-5 a very diverse range of framework topologies is made. The absolute values for the numbers of each ring type is not significant, but if we compare the relative numbers we can see that all have a large portion of five rings. If we now consider which template is "best" at directing the formation of five rings in water we can see that this peaks at Me_6-diquat-5 where relative to the others there is a larger proportion (around the head group) of five rings compared to the others.

Doing a similar analysis for the zeolites made by the ethyl diquaternary ammonium series, we can see similar trends where there are large proportions of five rings. However, within this series there are exceptions. Analcime (ANA), SSZ-16 (AFX) and P1 (GIS) all have zero five rings. However, if we look back to the ring statistics we can see that Et_6-diquat-4 (the template which forms Analcime) has an unusually large number of four rings present in the hydration layer. Both SSZ-16 and P1 are made using Et_6-diquat-5 but only when the MOH/SiO_2 (where M is Na^+ in the case of P1 and K^+ in the case of SSZ-16) ratio is increased. This suggests that here the main structure director may be the inorganic cation or as was suggested by Paik *et al.* , the inorganic cations influence the conformation of the template [41]. It is interesting to note here that Et_6-diquat-5 is the only template which can be used to form ZSM-57, and it is this template which appears to be the optimum for supporting five ring formation.

Another interesting feature of the analysis is the general increase in lifetime of the rings as we increased the chain length, with the exception of the rings around the chain of the ethyl compounds. This, coupled with the similarity in the ring statistics suggests that the structure around the chain is stable, and it is the head groups which disrupt the structure around the chain. In the case of the methyl

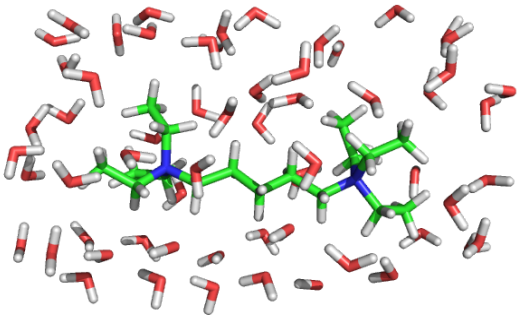

Figure 6.30: Picture of the first hydration layer around Et_6-diquat-5.

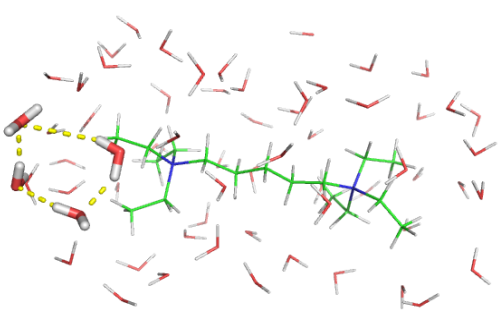

(i) Four ring

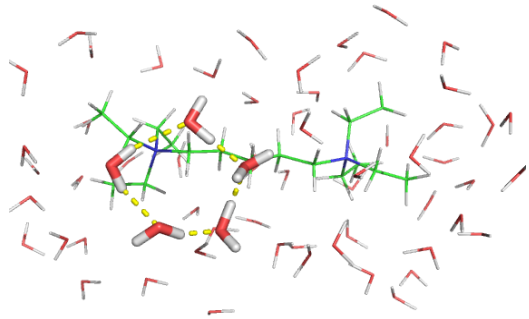

(ii) Five ring

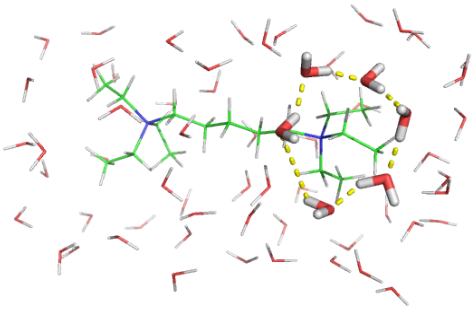

(iii) Six ring

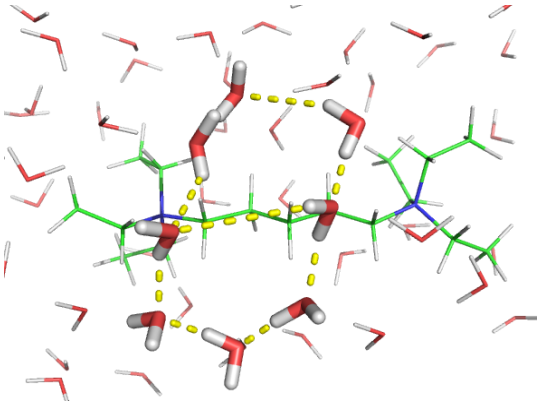

(iv) Double five ring

(v) MTT unit from ZSM-57

Figure 6.31: Pictures showing the various ring sizes formed around the template and an image showing two linked five rings around the chain which is similar to the ring structure found in ZSM-57.

Framework	4-rings	5-rings	6-rings
ANA	6	0	4
MOR	2	24	0
MFI	2	40	18
GIS	6	0	0
MFS	4	26	4
SZR	12	16	8
AFX	36	0	8

Table 6.9: Ring counts for zeolites made by Et_6-diquat-n with $n = 3-6$ taken from the IZA website [4].

series, the head groups are relatively small and so the influence is reduced and as such the lifetime of the rings increases. However, in the case of the ethyl series the more flexible ethyl groups can exert a greater influence on the chain and so we see the decrease in lifetimes. Attempts were made to explore the relationship between chain flexibility and lifetimes by plotting the nitrogen-nitrogen separation vs ring count over time. However, the relatively short production run meant the chain did not flex much. Combining this with noisy results meant no link was found.

6.6 PMF Calculation of Silica Approaching TMA

6.6.1 Introduction

In Chapter 2 the role of the template was introduced and the formation of a zeolite was hypothesised to proceed by the template first ordering the water in the hydration layer into a clathrate like structure which is followed by substitution of water for silica. In order to investigate the energetic barriers to this substitution, potential of mean force (PMF) calculations were carried out on a silica monomer approaching TMA. If large energetic barriers exist to this process then we might expect that the silica would be unable to break the hydration layer around the template.

6.6.2 Computational Details

PMF calculations were carried out using constrained molecular dynamics simulations in DLPOLY4 [260]. Images were created with TMA and silica monomer separations of 7 Å, 9 Å, 11 Å and 13 Å. These simulation cells were then filled with water which totalled 2,028 water molecules before running each cell under NPT for 200 ps. The final cell parameters were then averaged and these used for the following NVT simulations. Starting from the previously optimised images constrained MD

simulations were carried out with the separation being held fixed. Here separation is the distance between the centre of mass of two species which are 'connected' in the PMF simulation. In the case of the system studied here this will be the N-Si distance. The temperature was maintained at 350 K using a Nosé-Hoover thermostat with a relaxation constant of 0.5 fs. The simulation was carried out for 800 ps with a time step of 0.0002 ps. The separation of TMA and silica monomer was then adjusted by 0.1 Å and the simulation run again to give 100 images over a range of 5 Å to 15 Å. Given that to generate 800 ps of data takes approximately 40 hours on 16 cores, these calculations are extremely computationally expensive.

6.6.3 Results

Figure 6.32 is the approach profile of the TMA moving towards a silicate monomer. It is interesting to note that there are small barriers once we get to within approximately 13 Å of the monomer. There is a gentle rise in the free energy as we 'drag' the two species together. There are two distinct peaks at 8.2 Å where the species are separated by two hydration layers, i.e. one each, and at 6.2 Å where the species are separated by one hydration layer. The barrier to remove this final hydration layer is slightly higher at approximately 2.9 kJ mol^{-1}.

Figure 6.33 contains snapshots taken from the dynamics at 8.2 Å, 7.5 Å, 6.2Å and 5.0 Å. Here we can clearly see that at 8.2 Å there are two layers of water between the monomer and TMA. At 7.5 Å this has been reduced to one which is then compressed as we move to a separation of 6.2 Å, and finally removed completely at 5.1 Å. At a separation of 5 Å the TMA and monomer are just touching, and so after this we would expect to see a steep increase in the free energy as the molecules are forced together. To further illustrate this point, typical distances from shared hydration layer to the respective solvent molecules were taken. In the case of a separation of 6.2Å we find that the average distance to the silicon atom in the monomer is 3.98 Å, and 3.95 Åto the nitrogen in TMA. At a separation of 7.5 Å the average distance to silicon is again 3.98 Å but the distance to TMA has increased to 4.8 Å. This backs up the conclusion that the water layer is compressed at a separation of 6.2 Å.

6.6.4 Discussion

From Figure 6.32 we can see there are two distinct energetic barriers for a monomer to enter the first hydration layer of the TMA. It appears that both TMA and the monomer have one hydration layer which must be broken, with the removal of the final layer requiring approximately 2.9 kJ mol^{-1}. This is of course relatively

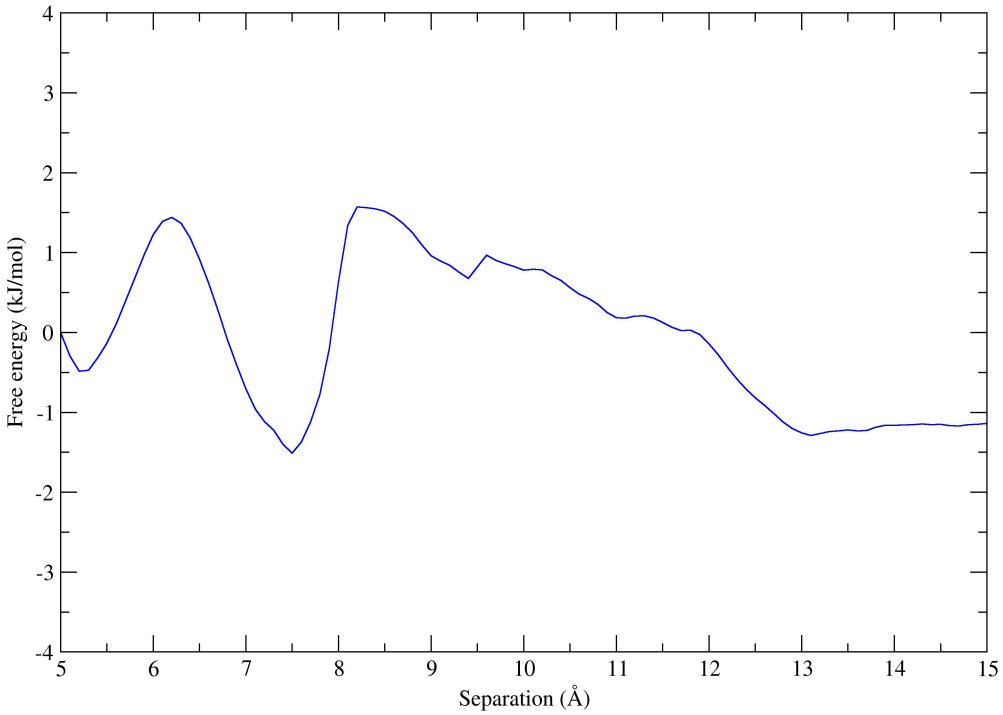

Figure 6.32: Approach profile for TMA moving toward a silica monomer calculated using a Potential of Mean Force calculation.

small, and under zeolite synthesis conditions we can expect this to proceed without hindrance. This lends credibility to the hypothesis that zeolites form by exchange of water for silica. However, this result alone does not give information on how the silica is structurally affecting the hydration layer, and this should be the focus of future calculations.

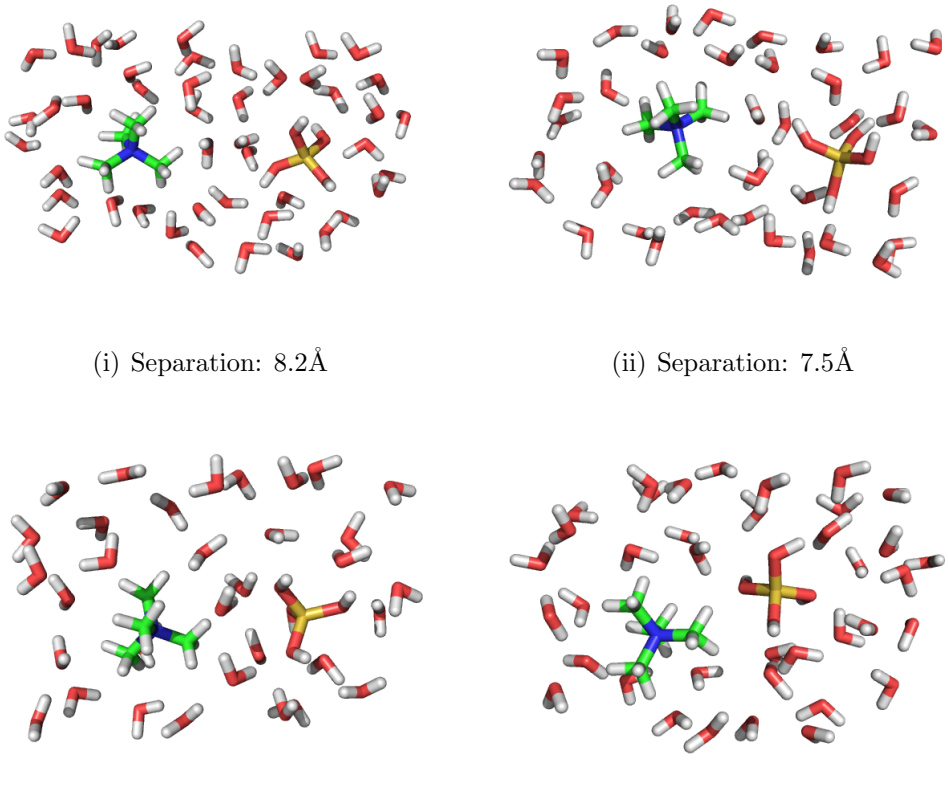

(i) Separation: 8.2Å

(ii) Separation: 7.5Å

(iii) Separation: 6.2Å

(iv) Separation: 5.1Å

Figure 6.33: Snapshots from the potential of mean force calculations at separation of: 8.2 Å (i), 7.5 Å (ii), 6.2 Å (iii) and 5.1 Å (iv). Note how at 8.2 Å there are two layers of water, which as we reduce the separation gets compressed and finally removed at 5.1 Å.

6.7 Conclusions

In this chapter we have studied how some organic molecules which are commonly used in zeolite synthesis affect the ring structures in their hydration layers. We have seen that small organic rings increase the number of four, five and six rings with the five member ring pyrrolidinium stabilising rings better than the six member ring piperidinium. Similarly, TPA and TBA have been shown to affect the water structure in ways similar to their smaller counterparts, TMA and TEA. An unusual result which arose from this work was the low lifetimes observed for TPA and TBA, which could be a result of either hydrophobicity or template flexibility. Considering the study by Szyja *et al.* [283] where they observed TPA stabilising five rings and TBA six rings, we observe the opposite trend. However, we have not included silica in these simulations which could completely change the ring statistics. In the simulations by Szyja *et al.* they just study preformed silicate oligomers and we can imagine that these units will interact differently with the template than a solution of water.

It was hoped that the ring statistics of the diquaternary ammonium templates studied here could be linked to the zeolites which they form. Although no clear link was found, these results do point to certain structures having a stronger ability to stabilise rings. Previous studies searched for zeolite "motifs" within the hydration layer and this proved extremely successful, highlighting the presence of the sodalite motif around TMA. The intention was to carry out a similar search in this work but the issue was which motif to search for. The zeolites here are formed of far more complex building units and a far larger variety and therefore a search was not attempted. Although, this kind of analysis was not carried out, it appears that the ability for the template to stabilise five rings is critical. When we have $n = 5$, there is an increase in the frequency of five rings, which may be linked to this templates ability to direct a wider variety of zeolites. The coordination number obtained from the RDFs also confirm this with the O-H coordination numbers peaking around $n = 5$.

An issue with this work is the templates are very concentrated. If we consider the experimental conditions used by Lee *et al.* [291] the water to template ratio is 1200:1 compared to around 100:1 for this work. This is a limitation in the method and future work should aim to use molecular mechanics methods. This will allow larger systems to be studied, and remove any template to water concentration issues. This of course produces its own problems where care must be taken to ensure the potentials used replicate well the structure of bulk water. It would also be desirable for further work to include silica monomers and eventually alumina as well.

CHAPTER 7

Conclusions

The initial aims of this thesis were to improve our understanding of the role of the template in zeolite synthesis, on both the topology and morphology. Knowledge of this, along with the effects of other species in the synthesis will allow zeolites to be designed and synthesised with a desirable set of properties. In order to do this, the problem has been broken down and analysed from both 'top down' and 'bottom up' approaches. The top down approach studies the influence of a template on the final zeolite structure in order to understand how and why a template leads to a particular framework, and how it affects the final crystal morphology. The bottom up approach studies the role of the template in the early stages of the synthesis to understand how it affects the initial gel.

In Chapter 4 the ZEBEDDE code has been further developed to give it more chemical knowledge. The ring making algorithm was modified to enable rings of any size to be formed in the growing molecule. Other major developments include the automation of the building and docking processes to enable ZEBEDDE to be run on supercomputers, but also to allow screening of molecules in much the same way as synthetic high throughput techniques, with minimal interaction for the user. Using the modified ZEBEDDE code, templates were designed for the zeolite Boggsite. The two templates meet many of the requirements set out by Gies and Marler [80], but synthetic testing is still required. At ExxonMobil Research and Engineering an extensive study on the zeolite MCM-68 was carried out to understand why three newly discovered templates are able to synthesise the zeolite which had for a decade been limited to only one template. A series of templates were docked into MCM-68,

along with a number of other zeolite frameworks commonly observed in synthesis. Based purely on van der Waals interactions with the framework, it was clear that the original template fitted extremely well, and has stronger interaction energies within MCM-68 than in all other frameworks tested. This was also the case for the hydrogenated version and the two newly discovered templates. These results validate the condition proposed by Gies and Marler that "the molecule should form as many van der Waals contacts as possible" [80]. The work here also validated the hypothesis that simpler templates should work and this was experimentally realised during the computational work.

In Chapter 5 the effects of template on the crystal morphology of zeolite L and AlPO-11 were investigated. The aim of the study on zeolite L was to alter the crystal morphology such that it had a lower aspect ratio, length/width. A series of crown ether and common template molecules were selected and docked into zeolite L. By analysing the interaction energies for each molecule, 21-crown-7 and 18-crown-6 were selected as possible structure modifiers. When these molecules were added to the synthesis, the zeolite L morphology was changed, but more detailed examination suggests that this modification occurs due to repositioning of the potassium into the channel. This provides support for the growing cancrinite columns in the normally frustrated *a*-direction. By understanding the growth of zeolite L, and with an understanding gained from the modelling results, of the likely location of the template within the final crystal it has been possible to influence the crystal growth. In a similar fashion, the role of large amine surfactants on the growth of AlPO-11 has been rationalised by an understanding of the location in which it most likely adsorbs on the surface.

In Chapter 6 the influence of the template on the structure of the water surrounding it was studied. The templates studied were TPA, TBA, pyrrolidinium, piperdinium and two series of diquaternary cations Me_6-diquat-n with $n = 3 - 7$ and Me_6-diquat-n with $n = 3 - 6$. The two quaternary cations, TPA and TBA were studied to build on previous work and also with hopes of linking to another study on the stabilising effects of TPA and TBA on silicate ring units in MFI and MEL. The results obtained suggest that TPA favours four rings, and TBA five. This is opposite to the results obtained by Szyja [283]. Although we are studying slightly different units (water as opposed to silicate) an agreement here would have provided a solid link between ring structures stabilised by templates in both the prenucleation stage, and in larger building units. The ring structures around small organic rings were also analysed and it is interesting to see that these templates generally have fewer rings around them, but the rings that are present are much longer lived than

the TAAs. Finally two series of diquaternary ammonium compounds were analysed, and compared back to the zeolite which they form. The main driving force appears to be the ability for it to form five rings, as in both cases the molecules with chain lengths of five most strongly promoted this. There also appears to be a complex interaction between the flexibility of hydrophobic chain and the head groups which come into balance at this chain length.

7.1 Future Work

Although improvements have been made to the building routines in ZEBEDDE, further modifications would be desirable. The templates generated, although chemically accurate, often have branched alkyl chains, or heavily substituted ring systems meaning in reality that they would be difficult to synthesise. By comparing these units to readily available organic molecules possibly via a space filling method, these chemically complicated units could be replaced with simpler structures. This would further automate the process and remove the most time consuming part of the calculation which was the manual inspection of the generated templates.

The zeolite L study showed that it is possible to predict the role of a template *a priori* by examining the location of the template in the final framework. Similarly, examining the location of long chain amine templates on the AlPO-11 structure gave clear reasons behind the observed crystal morphology. Computational methods can clearly play an important role in understanding how templates influence crystal morphology. However, overall what is lacking is detailed experimental evidence for the role of the templates. Of course this is not trivial to obtain, but it is essential in completing our understanding of the templates role during the growth of a zeolite.

The work on the structuring of water has yielded interesting results. There does appear to be a link between the numbers of rings present in the hydration layer and zeolite formed. However, a computational limit has been reached with respect to the size of system we are able to study. Future work should focus on comparing the results obtained here with simulations run using molecular mechanics. This will allow larger and more complex systems to be studied. It would also be desirable to include silicate monomers in the calculations to understand what effect these have on the water ring structures, moving eventually to a simulation cell with a composition comparable to a synthetic system. If a link between the structure of the water, and the eventual zeolite formed can be found, then combining this with the template design could allow complete design of a zeolite synthesis.

APPENDIX A

Interatomic Potential Parameters

The potentials used in this thesis are described here. For the zeolite the potentials of Sanders, Catlow and Leslie [188] were used, and the potentials for aluminophosphates are those of Gale and Henson [242]. The intramolecular potentials used to control the geometry of the organics are those of Oie *et al.* [261] with the intermolecular interactions being described by Kiselev [262]. The silanol potentials used here are those of Butler[263].

The atom types used here are, O_f for an oxygen in the bulk framework, OH for an oxygen in a silanol, O_w is an oxygen in water. H is hydrogen in silanol, H_w is hydrogen in water, H_o is a hydrogen attached to carbon and H_n is hydrogen connected to a nitrogen. C1 is a carbon attached to one "heavy" (non hydrogen) element, and C2 is carbon attached to two heavy elements. Unless suffixed with the word "shell", the interaction takes places between the cores. Potential cut-offs are described in the relevant computational section within each chapter of this thesis.

atom 1	atom 2	A (eVÅ^{1}2)	B (eVÅ^6)
H_o	O_f (shell)	1556.4	5.5717
C1	O_f (shell)	11000	17.654
N	O_f (shell)	8829.6998	19.8978
Hn	O_f (shell)	1556.4	5.5717
C2	O_f (shell)	11000	17.654
H_o	OH (shell)	1556.4	5.5717
C1	OH (shell)	11000	17.654
N	OH (shell)	8829.6998	19.8978
H_n	OH (shell)	1556.4	5.5717
C2	OH (shell)	11000	17.654

Table A.1: Values Lennard-Jones 12-6 potential parameters.

atom 1	atom 2	A (eV)	B (Å)	C(eVÅ^6)
Si (core)	O_f (shell)	1283.9073	0.3205	10.6616
Si (core)	OH (shell)	1283.9073	0.3205	5.3308
Si (core)	O_w (shell)	1283.9073	0.3205	10.6616
O_f (shell	O_w (shell)	22764.000	0.1490	15.4600
O_f (shell)	O_f (shell)	22764.000	0.1490	27.88
OH (shell)	OH (shell)	22764.300	0.1490	6.9700
Al	O_f (shell)	1460.3	0.2991	0.0
P	O_f (shell)	877.34	0.3594	0.0
H_o	C1	211.371328	0.279173	3.67259
H_o	N	880.208000	0.275482	11.0568
C1	C1	670.601424	0.320821	26.8355
C1	N	1356.04064	0.302114	29.7233
H_o	H_o	282.507744	0.266667	3.727659
H_o	C2	211.371328	0.279173	3.67259
C2	C2	670.601424	0.320821	26.8355
C2	N	1356.04064	0.302114	29.7233
H_n	H_n	282.507744	0.266667	3.727659
H_n	N	880.208000	0.275482	11.0568
H_n	C2	211.371328	0.279173	3.67259
H_n	C1	211.371328	0.279173	3.67259

Table A.2: Values for the Buckingham potentials.

atom	k_2 (eV)
O_f	74.9204
OH	74.9204
O_w	209.449602

Table A.3: Values for the core-shell springs.

atom 1	atom 2	atom 3	k (eV rad^{-2})	θ_0
H_f (shell)	Si	O_f (shell)	5.496300	109.4666667
OH (shell)	Si	O_f (shell)	5.496300	109.4666667
OH (shell)	Si	OH (shell)	5.496300	109.4666667
H_f (shell)	Al	O_f (shell)	2.097240	109.4666667

Table A.4: Three body terms. Note: Atom 2 is the central atom.

Atom	Charge
O_f	0.860
O_f (shell)	-2.860
O_w	1.25
O_w (shell)	2.05
OH	0.90
OH (shell)	-2.30
H	0.40
H_w	0.40
Si	4.00
Al	3.00
P	5.00

Table A.5: Charges for zeolite framework and water.

Atom	Charge
C1	-0.200
N	-0.440
H_o	0.180

Table A.6: Charges for TMA.

Atom	Charge
C1	-0.180
C2	-0.120
N	-0.920
H_o	0.060
H_n	0.360

Table A.7: Charges for hexadecylamine.

atom 1	atom 2	E_0	r_0	k (eV)
O_w	H_w	6.203713	0.92367	2.22003
OH (shell)	H	7.05250	0.92580	3.17490

Table A.8: Interatomic Morse potentials.

atom 1	atom 2	atom 3	atom 4	k (eV)
C1	N1	C1	H_o	0.0175
H_o	C2	C2	H_o	0.053
H_o	C1	C2	H_o	0.053
C2	C2	C2	N	0.035
C2	C2	C2	C1	0.032
H_o	C2	C2	C2	0.053

Table A.9: Torsional potentials.

atom 1	atom 2	k (eV)	l_0 (Å)
C1	H_o	28.71	1.095
N	H_o	18.81	1.0105
C1	N	28.75	1.495
C1	C1	27.46	1.52
C1	C2	27.46	1.52

Table A.10: Harmonic bond parameters.

atom 1	atom 2	atom 3	k (eV)	θ_0 (°)
H_n	N	H_n	5.00	110.0
H_n	N	C2	2.50	109.5
H_o	C2	H_o	2.06	109.2
H_o	C2	C2	2.50	109.0
C2	C2	C2	3.56	110.4
C2	N	C2	6.87	109.0
H_o	C1	H_o	2.06	109.2
H_w	O_w (shell)	H_w	4.19978	108.693195

Table A.11: Harmonic angle parameters.

atom 1	atom 2	Subtraction
O_w (shell)	H_w	50%
H_w	H_w	50%

Table A.12: Intramolecular coulombic subtraction.

APPENDIX B

ZEBEDDE Code

The modified ZEBEDDE routines which were discussed in Chapter 4 are given here.

B.1 Ring Maker

This section contains the modified ring counting code. The routines selects the first atom in the growing organic molecule checking if it is able to bond to another atom, i.e. it has free hydrogens. If this check returns true (it does have free hydrogens) it will then loop over all the atoms in the molecule searching for a second atom which is able to bond. Once a pair is found it then checks that the pair fall within the user defined ring cutoff, and calculates the order (also user definable). If all these conditions are satisfied the pair are stored in the array **near_neighs**. Once all the atoms have been tested, one pair is selected at random from the list and the bond created.

```
/************************************************************/
/**** Loop over all atoms to find atoms which are within *****/
/**** the cutoff and are able to form a ring             *****/
/************************************************************/
have_made_ring = FALSE;

for (atom1=0; atom1 < *p_num_atoms; atom1++)
    {
    allowed_bond1 = FALSE;
    p_atom1= p_molecule+atom1;

    if (atom_has_hyds(p_molecule, atom1)
       && p_atom1->num_neigh > 0) allowed_bond1 = TRUE;

       for (atom2=atom1+1; atom2 <= *p_num_atoms; atom2++)
           {
           p_atom2= p_molecule+atom2;
           can_bond = FALSE;
           allowed_bond2 = FALSE;

           if (atom_has_hyds(p_molecule, atom2)
              && p_atom2->num_neigh > 0) allowed_bond2 = TRUE;

              r2=atom_separation_squared(p_atom1, p_atom2, pbc);
              r=sqrt(r2);

              can_bond = !forbid_bond(p_atom1->elem,
                                 p_atom2->elem,
                                 p_forbidden_bond);

              order= neighbour_order(p_molecule, *p_num_atoms, atom1, atom2);

              if (r2 <= ring_ctf_2 && can_bond && allowed_bond1
                 && allowed_bond2 && order >=4) //store that pair of atoms
                 {
                 printf("DB>> Atom 1: %i, atom 2: %i\n",atom1,atom2);
                 near_neighs[i][0]=atom1;
                 near_neighs[j][1]=atom2;
                 i++;
                 j++;
                 num_pairs++;
                 }
           }
    }
\\Check that we have pairs, if not return.
```

```
if (num_pairs == 0)
   {
   printf("No pairs of atoms available to make rings. Returning\n");
   return FALSE;
   }
\\If we have a pairs, select one at random.
rand_no = get_random_int(0, num_pairs);

printf("The Random number is %i\n",rand_no);

i=0;
j=0;

for (this_pair=0;this_pair < num_pairs; this_pair++)
    {
    atom1 = near_neighs[i][0];
    atom2 = near_neighs[j][1];

    if (this_pair == rand_no)
       {
       printf("Pair to bind will be %i %i \n", atom1,atom2);
       break;
       }

    else
       {
       printf("Not this pair %i %i \n", atom1, atom2);
       }
       i++;
       j++;
    }
```

The code which actually alters the neighbours list is unchanged from the original version.

APPENDIX C

Boggsite Organics

C.1 Organic Molecules

This chapter lists two dimensional stick drawings of the templates generated to direct the synthesis of Boggsite in Section 4.3.

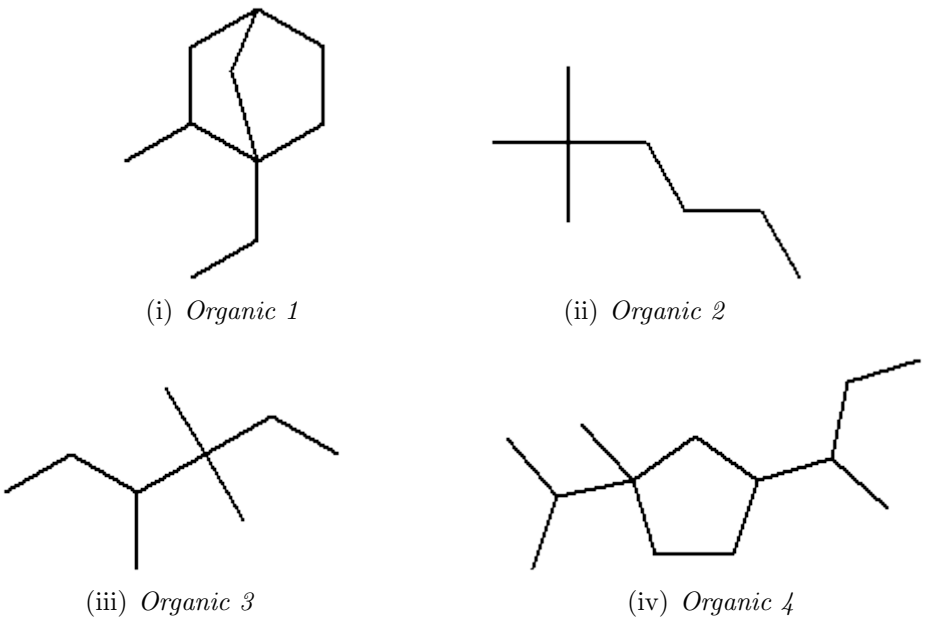

(i) *Organic 1*

(ii) *Organic 2*

(iii) *Organic 3*

(iv) *Organic 4*

Figure C.1: *Organic 1* to *Organic 4*

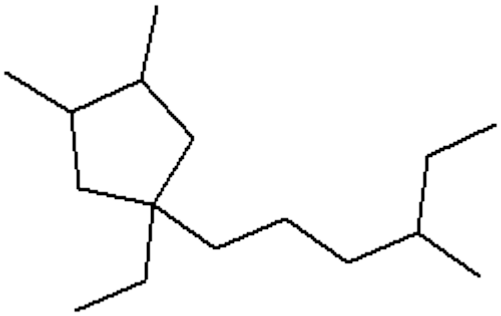

(v) *Organic 5*

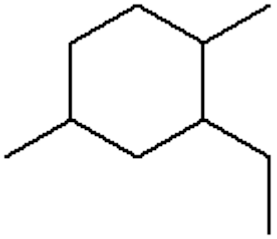

(vi) *Organic 6*

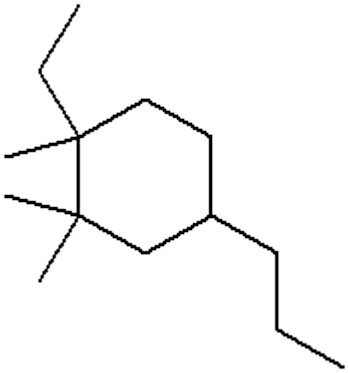

(vii) *Organic 7*

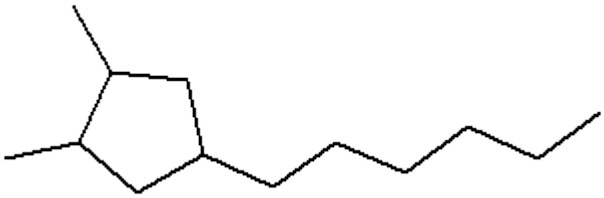

(viii) *Organic 8*

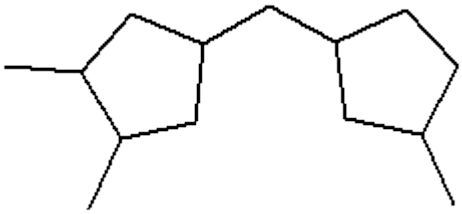

(ix) *Organic 9*

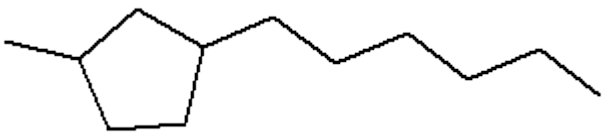

(x) *Organic 10*

Figure C.1: *Organic 5* to *Organic 10*

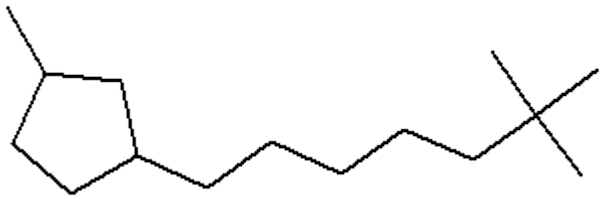

(xi) *Organic 11*

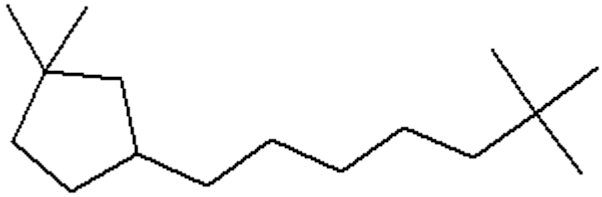

(xii) *Organic 12*

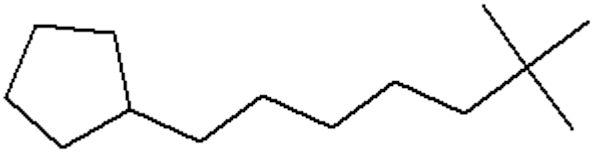

(xiii) *Organic 13*

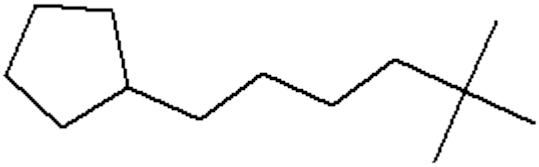

(xiv) *Organic 14*

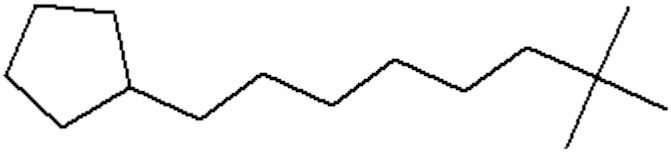

(xv) *Organic 15*

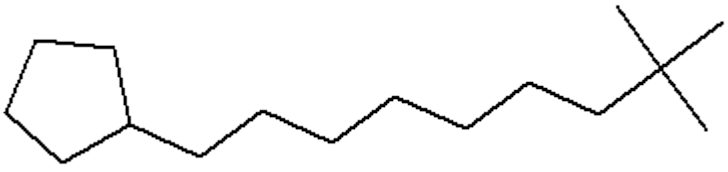

(xvi) *Organic 16*

Figure C.1: *Organic 11* to *Organic 16*

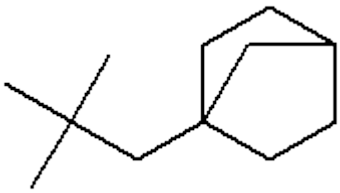

(xvii) *Organic 17*

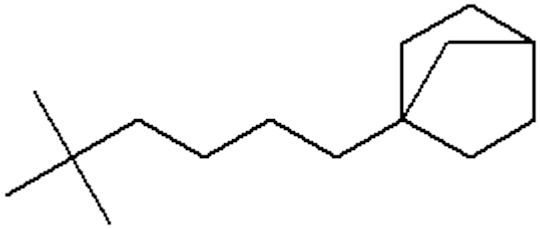

(xviii) *Organic 18*

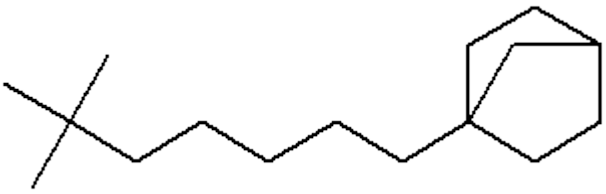

(xix) *Organic 19*

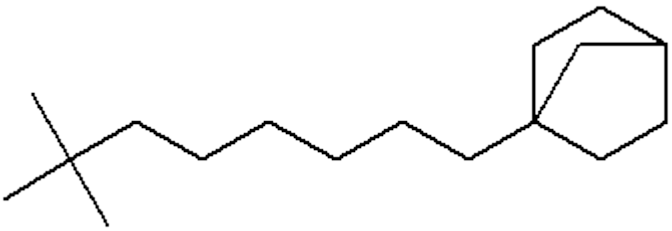

(xx) *Organic 20*

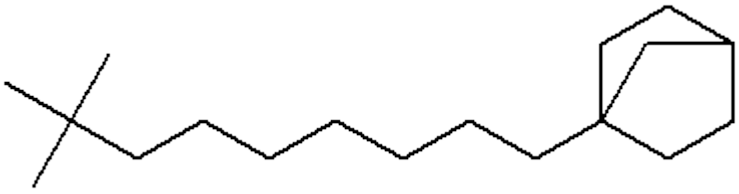

(xxi) *Organic 21*

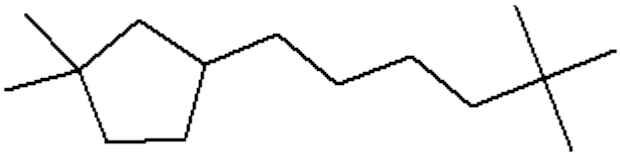

(xxii) *Organic 22*

Figure C.1: *Organic 17* to *Organic 22*

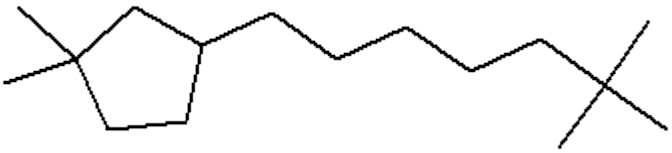

(xxiii) *Organic 23*

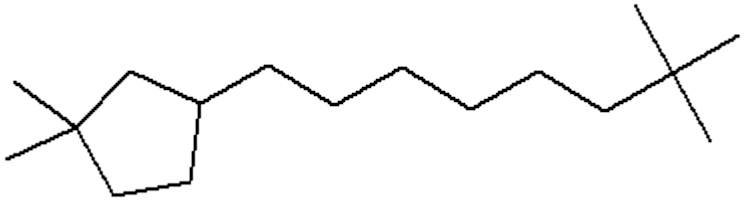

(xxiv) *Organic 24*

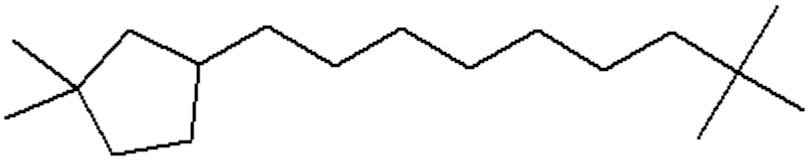

(xxv) *Organic 25*

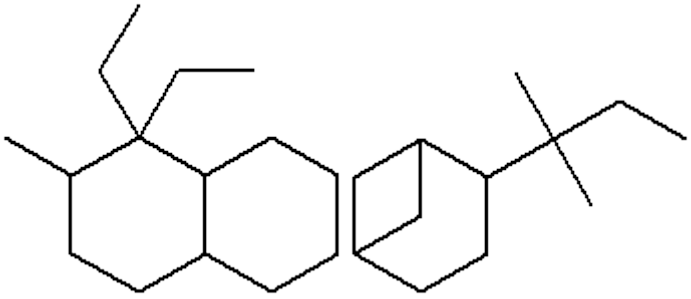

(xxvi) *Organic 26* (xxvii) *Organic 27*

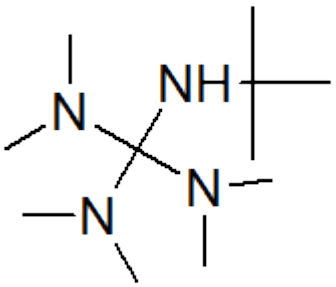

(xxviii) *Organic 28* with carbon instead of phosphorus

Figure C.1: *Organic 23* to *Organic 28*

APPENDIX D

Ring Searching Program

The ring searching program has been written in C++ and can be compiled and run on any Unix based machine which has a suitable C++ compiler. The program is easily compiled using the included makefile with minor alterations to direct to the C++ compiler. It is recommended that the code is compiled with the 'O2' optimisation flag as this greatly improves performance. The program requires an input file in order to run. This file contains the relevant information about the system being studied. These options are summarised below:

- **System parameters** Requires three integers on the first line. These are <number of MD steps>, <number of atoms>, <number of solute atoms>.
- **Cell Dimensions** Requires three real numbers corresponding to the cell x, y and z dimensions.
- **Trajectory file** The name of the trajectory file.
- **RDF** Select TRUE or FALSE depending on whether a RDF is desired.
- **Sphere** Select TRUE or FALSE depending on whether the solute can be approximated to a sphere. This causes the hydration layer to be calculated based on the centre of gravity of the solute.

The trajectory file should be in XYZ format as is output by the CP2K program. The solute coordinates must be the first at the start of each frame. The water molecules are then automatically sorted. It may be necessary to alter the value

of SOLUTE_RADIUS in the file "header.h" to a value suitable for the solute in question. To execute the program simply type "./analysis <input_filename>". The code with then start to analyse the supplied trajectory file. The results will be output into the current working directory. Many of the files are for debugging purposes only and so just the relevant files are listed here.

- **rings.csv**
  This file contains the total number of rings of size 3-6 in the hydration later around the solute. Along with this is the average number of oxygen atoms in the hydration layer. This can be imported into a spreadsheet for further analysis.

- **hemi_rings.csv**
  This file contains the number of rings of size 3-6 in the hydration layer around the head groups of a diquaternary ammonium cation.

- **cylinder.csv**
  This file contains the number of rings of size 3-6 in the hydration layer around the chain section of a diquaternary ammonium cation.

- **lifetime<n>.out**
  Lifetimes of ring size n where n=3-6.

- **rdf_XX**
  Where XX is HH, OO, or OH. These files contain the radial distribution functions, if requested.

Bibliography

[1] van Bekkum, H.; Flanigen, E. M.; Jacobs, P. A.; Jansen, J. C. *Introduction to Zeolite Science and Practice*; Elsevier, 2001.

[2] Cundy, C. S.; Cox, P. A. *Chemical Reviews* **2003**, *103*, 663–701.

[3] Serrano, D.; van Grieken, R. *J. of Mater. Chem.* **2001**, *11*, 2391–2407.

[4] `http://www.iza-structure.org/databases/`.

[5] Reed, T. B.; Breck, D. W. *J. Am. Chem. Soc.* **1956**, *78*, 5972–5977.

[6] Kerr, G. T. *Inorg. Chem.* **1966**, *5*, 1539.

[7] Corma, A.; Rey, F.; Ruis, J.; Sabater, M. J.; Valencia, S. *Nature* **2004**, *431*, 287–290.

[8] Sun, J.; Bonneau, C.; Cantin, A.; Corma, A.; Diaz-Cabanas, M. J.; Moliner, M.; Zhang, D.; Li, M.; Zou, X. *Nature* **2009**, *458*, 1154.

[9] Rohrig, C.; Gies, H.; Marler, B. *Zeolites* **1994**, *14*, 498–503.

[10] Barrer, R. M. *Hydrothermal Chemistry of Zeolites*; Academic Press, 1982.

[11] Ju, R.; Pang, W.; Yu, J.; Huo, Q.; Chen, J. *Chemistry of Zeolites and Related Porous Materials : Synthesis and Structure*; Wiley : Singapore, 2007.

[12] Olson, D. H.; Kokotailo, G. T.; Lawton, S. L.; Meier, W. M. *J. Phys. Chem.* **1981**, *85*, 2238–2243.

[13] Mater, S.; Hatch., L. *Chemistry of Petrochemical Processes: Second Edition.*; Butterworth-Heinemann, 2001.

[14] Chang, C. D.; Chu, C. T. W.; Socha, R. F. *J. Catal.* **1984**, *86*, 289–296.

[15] Chu, C. T. W.; Chang, C. D. *J. Catal.* **1984**, *86*, 297–300.

[16] Ratnasamy, P.; Babu, G. P.; Chanwadkar, A. J.; Kulikarni, S. B. *Zeolites* **1986**, *6*, 98–100.

[17] Xu, X.; Wang, J.; Long, Y. *Sensors* **2006**, *6*, 1751–1764.

[18] Barrer, R. M. *J. Chem. Soc.* **1948**, 127.

[19] de Sainte Claire Deville, H. *C. R., Acad. Sci.* **1862**, 324–327.

[20] Kerr, G. T. *Science* **1963**, *140*, 1412.

[21] Breck, D. W.; Eversole, W. G.; Milton, R. M.; Reed, T. B.; Thomas, T. L. *J. Am. Chem. Soc.* **1956**, *78*, 5963–5971.

[22] Bergerhoff, G. *Angew. Chem.-Int. Edit.* **1958**, *70*, 402.

[23] Barrer, R. M.; Denny, P. J. *J. Chem. Soc.* **1961**, 971.

[24] Barrer, R. M.; Baynham, J. W.; Bultitude, F. W.; Meier, W. M. *J. Chem. Soc.* **1959**, 195.

[25] Cundy, C. S.; Cox, P. A. *Micro. Meso. Mater.* **2005**, *82*, 1–78.

[26] Aiello, R.; Barrer, R. M. *J. Chem. Soc.* **1970**, 1470–&.

[27] Baerlocher, C.; Meier, W. M. *Helv. Chim. Acta* **1970**, *53*, 1285–&.

[28] Lok, B. M.; Cannan, T. R.; Messina, C. A. *Zeolites* **1983**, *3*, 282–291.

[29] Meier, W. M. *Zeolites* **1984**, *4*, 402.

[30] Argauer, R. J.; Landolt, G. R.; 1972; US Patent 3702886.

[31] Kokotailo, G. T.; Lawton, S. L.; Olson, D. H.; Meier, W. M. **1978**, *272*, 437–438.

[32] Olson, D. H.; Kokotailo, G. T.; Lawton, S. L.; Meier, W. M. **1981**, *85*, 2238–2243.

[33] Wadlinger, R. L.; Kerr, G. T.; Rosinski, E. J.; *Catalytic composition of a crystalline zeolite*; 1967; US Patent 3308069. `http://www.freepatentsonline.com/3308069.html`.

[34] Fyfe, C. A.; Gies, H.; Kokotailo, G. T.; Pasztor, C.; Strobl, H.; Cox, D. E. *J. Am. Chem. Soc.* **1989**, *111*, 2470–2474.

[35] Flanigen, E. M.; Bennett, J. M.; Grose, R. W.; Cohen, J. P.; Patton, R. L.; KIRCHNER, R.; SMITH, J. *Nature* **1978**, *271*, 512–516.

[36] Bibby, D. M.; Milestone, N. B.; Aldridge, L. P. *Nature* **1979**, *280*, 664–665.

[37] Dodwell, G. W.; Denkewicz, R. P.; Sand, L. B. *Zeolites* **1985**, *5*, 153–157.

[38] Shannon, M. D.; Casci, J. L.; Cox, P. A.; Andrews, S. J. *Nature* **1991**, *353*, 417–420.

[39] Lee, S. H.; Shin, C. H.; Yang, D. K.; Ahn, S. D.; Nam, I. S.; Hong, S. B. *Microporous Mesoporous Mat.* **2004**, *68*, 97–104.

[40] Lee, S. H.; Shin, C. H.; Choi, G. J.; Park, T. J.; Nam, I. S.; Han, B.; Hong, S. B. *Microporous Mesoporous Mat.* **2003**, *60*, 237–249.

[41] Paik, W. C.; Shin, C. H.; Lee, J. M.; Ahn, B. J.; Hong, S. B. *J. Phys. Chem. B* **2001**, *105*, 9994–10000.

[42] Boxhoorn, G.; van Santen, R. A.; van Erp, W. A.; Hays, G. R.; Huis, R.; Clague, D. *J. Chem. Soc.-Chem. Commun.* **1982**, 264–265.

[43] Čejka, J.; Corma, A.; Zones, S. *Zeolites and Catalysis: Synthesis, Reactions and Applications*; John Wiley & Sons, 2010.

[44] Davis, M. E.; Saldarriaga, C.; Montes, C.; Garces, J.; Crowder, C. *Nature* **1988**, *331*, 698–699.

[45] Dessau, R. M.; Schlenker, J. L.; Higgins, J. B. *Zeolites* **1990**, *10*, 522–524.

[46] Lobo, R. F.; Tsapatsis, M.; Freyhardt, C. C.; Khodabandeh, S.; Wagner, P.; Chen, C. Y.; Balkus, K. J.; Zones, S. I.; Davis, M. E. *J. Am. Chem. Soc.* **1997**, *119*, 8474–8484.

[47] Freyhardt, C. C.; Tsapatsis, M.; Lobo, R. F.; Balkus, K. J.; Davis, M. E. *Nature* **1996**, *381*, 295–298.

[48] Wagner, P.; Yoshikawa, M.; Lovallo, M.; Tsuji, K.; Taspatsis, M.; Davis, M. E. *Chem. Commun.* **1997**, 2179–2180.

[49] Burton, A.; Elomari, S.; Chen, C. Y.; Medrud, R. C.; Chan, I. Y.; Bull, L. M.; Kibby, C.; Harris, T. V.; Zones, S. I.; Vittoratos, E. S. *Chem.-Eur. J.* **2003**, *9*, 5737–5748.

[50] Cheetham, A. K.; Fjellvå g, H.; Gier, T. E.; Kongshaug, K.; Lillerud, K.; Stucky, G. *Stud. Surf. Sci. Catal.* **2001**, *135*, 158–162.

[51] Strohmaier, K. G.; Vaughan, D. E. W. *J. Am. Chem. Soc.* **2003**, *125*, 16035–16039.

[52] Corma, A.; Diaz-Cabanas, M. J.; Rey, F.; Nicolooulas, S.; Boulahya, K. *Chem. Commun.* **2004**, 1356–1357.

[53] Corma, A.; Diaz-Cabanas, M. J.; Luis Jorda, J.; Martinez, C.; Moliner, M. *Nature* **2006**, *443*, 842–845.

[54] Corma, A.; Diaz-Cabanas, M. J.; Jiang, J.; Afeworki, M.; Dorset, D. L.; Soled, S. L.; Strohmaier, K. G. *Proc. Natl. Acad. Sci. U. S. A.* **2010**, *107*, 13997–14002.

[55] Dorset, D. L.; Kennedy, G. J.; Strohmaier, K. G.; Diaz-Cabanas, M. J.; Rey, F.; Corma, A. *J. Am. Chem. Soc.* **2006**, *128*, 8862–8867.

[56] Dorset, D. L.; Strohmaier, K. G.; Kliewer, C. E.; Corma, A.; Diaz-Cabanas, M. J.; Rey, F.; Gilmore, C. J. *Chem. Mat.* **2008**, *20*, 5325–5331.

[57] Corma, A.; Diaz-Cabanas, M. J.; Jorda, J. L.; Rey, F.; Sastre, G.; Strohmaier, K. G. *J. Am. Chem. Soc.* **2008**, *130*, 16482–16483.

[58] Simancas, R.; Dari, D.; Velamazan, N.; Navarro, M. T.; Cantin, A.; Jorda, J. L.; Sastre, G.; Corma, A.; Rey, F. *Science* **2010**, *330*, 1219–1222.

[59] Wright, P. A.; Morris, R. E.; Wheatley, P. S. *Dalton Trans.* **2007**, 5359–5368.

[60] Delprato, F.; Delmotte, L.; Guth, J. L.; Huve, L. *Zeolites* **1990**, *10*, 546–552.

[61] Wu, C. N.; Chao, K. J. *J. Chem. Soc.-Faraday Trans.* **1995**, *91*, 167–173.

[62] Chatelain, T.; Patarin, J.; Fousson, E.; Soulard, M.; Guth, J. L.; Schulz, P. *Microporous Mater.* **1995**, *4*, 231–238.

[63] Chatelain, T.; Patarin, J.; Farre, R.; Petigny, O.; Schulz, P. *Zeolites* **1996**, *17*, 328–333.

[64] Shantz, D. F.; Burton, A.; Lobo, R. F. *Microporous Mesoporous Mat.* **1999**, *31*, 61–73.

[65] Patinec, V.; Wright, P. A.; Lightfoot, P.; Aitken, R. A.; Cox, P. A. *J. Chem. Soc.-Dalton Trans.* **1999**, 3909–3911.

[66] Wright, P. A.; Maple, M. J.; Slawin, A. M. Z.; Patinec, V.; Aitken, R. A.; Welsh, S.; Cox, P. A. *J. Chem. Soc.-Dalton Trans.* **2000**, 1243–1248.

[67] Shiralkar, V.; Clearfield, A. *Zeolites* **1989**, *9*, 363 – 370.

[68] Grose, R. W.; Flanigen, E. M.; *Novel zeolite compositions and processes for preparing and using same*; 1981; US Patent 4257885. `http://www.freepatentsonline.com/4257885.html`.

[69] Song, J. W.; Dai, L.; Ji, Y. Y.; Xiao, F. S. *Chem. Mat.* **2006**, *18*, 2775–2777.

[70] Warrender, S. J.; Wright, P. A.; Zhou, W. Z.; Lightfoot, P.; Camblor, M. A.; Shin, C. H.; Kim, D. J.; Hong, S. B. *Chem. Mat.* **2005**, *17*, 1272.

[71] Wu, Z.; Song, J.; Ji, Y.; Ren, L.; Xiao, F. S. *Chem. Mat.* **2008**, *20*, 357–359.

[72] Zhang, L.; Yang, C.; Meng, X.; Xie, B.; Wang, L.; Ren, L.; Ma, S.; Xiao, F. S. *Chem. Mat.* **2010**, *22*, 3099–3107.

[73] Yokoi, T.; Yoshioka, M.; Ima, H.; Tatsumi, T. *Angew. Chem.-Int. Edit.* **2009**, *48*, 9884–9887.

[74] Iyoki, K.; Kamimura, Y.; Itabashi, K.; Shimojima, A.; Okubo, T. *Chem. Lett.* **2010**, *39*, 730–731.

[75] Kamimura, Y.; Tanahashi, S.; Itabashi, K.; Sugawara, A.; Wakihara, T.; Shimojima, A.; Okubo, T. *J. Phys. Chem. C* **2011**, *115*, 744–750.

[76] Zhang, H.; Guo, Q.; Ren, L.; Yang, C.; Zhu, L.; Meng, X.; Li, C.; Xiao, F. S. *J. Mater. Chem.* **2011**, *21*, 9494–9497.

[77] Kamimura, Y.; Itabashi, K.; Shimojima, A.; Okubo, T. In *BZA Conference Abstracts 2011*.

[78] Zones, S. I.; Nakagawa, Y.; Lee, G. S.; Chen, C. Y.; Yuen, L. T. **1998**, *21*, 199–211.

[79] Wright, P. A. *Microporous Framework Solids*; RSC Publishing, 2008.

[80] Gies, H.; Marler, B. *Zeolites* **1992**, *12*, 42–49.

[81] Price, G. D.; Pluth, J. J.; Smith, J. V.; Araki, T.; Bennett, J. M. *Nature* **1981**, *292*, 818–819.

[82] Price, G. D.; Pluth, J. J.; Smith, J. V.; Bennett, J. M.; Patton, R. L. *J. Am. Chem. Soc.* **1982**, *104*, 5971–5977.

[83] Parker, L. M.; Bibby, D. M.; Patterson, J. E. *Zeolites* **1984**, *4*, 168–174.

[84] van Koningsveld, H.; van Bekkum, H.; Jansen, J. C. *Acta Crystallographica Section B* **1987**, *43*, 127–132.

[85] den Ouden, C. J. J.; Datema, K. P.; Visser, F.; Mackay, M.; Post, M. F. M. *Zeolites* **1991**, *11*, 418–428.

[86] Schmitt, K. D.; Kennedy, G. J. *Zeolites* **1994**, *14*, 635–642.

[87] Choi, M.; Na, K.; Kim, J.; Sakamoto, Y.; Terasaki, O.; Ryoo, R. *Nature* **2009**, *461*, 246.

[88] Flanigen, E. M.; Patton, R. L.; *Silica polymorph and process for preparing same*; 1978; US Patent 4073865. `http://www.freepatentsonline.com/4073865.html`.

[89] Camblor, M. A.; Corma, A.; Valencia, S. *J. Mater. Chem.* **1998**, *8*, 2137–2145.

[90] Caullet, P.; Paillaud, J. L.; Simon-Masseron, A.; Soulard, M.; Patarin, J. *C. R. Chim.* **2005**, *8*, 245–266.

[91] George, A. R.; Catlow, C. R. A. *Zeolites* **1997**, *18*, 67–70.

[92] Jon, H.; Oumi, Y.; Itabashi, K.; Sano, T. *J. Cryst. Growth* **2007**, *307*, 177–184.

[93] Li, H. L.; Yaghi, O. M. *J. Am. Chem. Soc.* **1998**, *120*, 10569–10570.

[94] Conradsson, T.; Zou, X. D.; Dadachov, M. S. *Inorg. Chem.* **2000**, *39*, 1716–1720.

[95] Blasco, T.; Corma, A.; Diaz-Cabanas, M. J.; Rey, F.; Vidal-Moya, J. A.; Zicovich-Wilson, C. M. *J. Phys. Chem. B* **2002**, *106*, 2634–2642.

[96] Zwijnenburg, M. A.; Bromley, S. T.; Jansen, J. C.; Maschmeyer, T. *Microporous Mesoporous Mat.* **2004**, *73*, 171–174.

[97] Corma, A.; Diaz-Cabanas, M. J.; Fornes, V. *Angew. Chem.-Int. Edit.* **2000**, *39*, 2346–2349.

[98] Jiang, J.; Yu, J.; Corma, A. *Angew. Chem.-Int. Edit.* **2010**, *49*, 3120–3145.

[99] Breck, D. W. *Zeolite molecular sieves: structure, chemistry, and use*; Wiley, New York, 1974.

[100] Earl, D. J.; Deem, M. W. *Ind. Eng. Chem. Res.* **2006**, *45*, 5449–5454.

[101] Deem, M. W.; Pophale, R.; Cheeseman, P. A.; Earl, D. J. *J. Phys. Chem. C* **2009**, *113*, 21353–21360.

[102] Friedrichs, O. D.; Dress, A. W. M.; Huson, D. H.; Klinowski, J.; Mackay, A. L. *Nature* **1999**, *400*, 644–647.

[103] Foster, M.; Friedrichs, O.; Bell, R.; Paz, F.; Klinowski, J. *Angew. Chem.-Int. Edit.* **2003**, *42*, 3896–3899.

[104] Foster, M. D.; Simperler, A.; Bell, R. G.; Friedrichs, O. D.; Paz, F. A. A.; Klinowski, J. *Nat. Mater.* **2004**, *3*, 234–238.

[105] Majda, D.; Paz, F. A. A.; Friedrichs, O. D.; Foster, M. D.; Simperler, A.; Bell, R. G.; Klinowski, J. *J. Phys. Chem. C* **2008**, *112*, 1040–1047.

[106] `http://www.hypotheticalzeolites.net/`.

[107] Treacy, M. M. J.; Randall, K. H.; Rao, S.; Perry, J. A.; Chadi, D. J. *Z. Kristall.* **1997**, *212*, 768–791.

[108] Treacy, M. M. J.; Rivin, I.; Balkovsky, E.; Randall, K. H.; Foster, M. D. *Micro. Meso. Mater.* **2004**, *74*, 121 – 132.

[109] Kapko, V.; Dawson, C.; Treacy, M. M. J.; Thorpe, M. F. *Phys. Chem. Chem. Phys.* **2010**, *12*, 8531–8541.

[110] Li, Y.; Yu, J. H.; Liu, D. H.; Yan, W. F.; Xu, R. R.; Xu, Y. *Chem. Mat.* **2003**, *15*, 2780–2785.

[111] Kerr, G. T. *J. Phys. Chem.* **1966**, *70*, 1047.

[112] Kerr, G. T. *Zeolites* **1989**, *9*, 451.

[113] Harris, R. K.; Knight, C. T. G.; Hull, W. E. *J. Am. Chem. Soc.* **1981**, *103*, 1577–1578.

[114] Kinrade, S. D.; Knight, C. T. G.; Pole, D. L.; Syvitski, R. T. *Inorg. Chem.* **1998**, *37*, 4272–4277.

[115] Kinrade, S. D.; Del Nin, J. W.; Schach, A. S.; Sloan, T. A.; Wilson, K. L.; Knight, C. T. G. *Science* **1999**, *285*, 1542–1545.

[116] Knight, C. T. G.; Wang, J. P.; Kinrade, S. D. *Phys. Chem. Chem. Phys.* **2006**, *8*, 3099–3103.

[117] Knight, C. T. G.; Balec, R. J.; Kinrade, S. D. *Angew. Chem.-Int. Edit.* **2007**, *46*, 8148–8152.

[118] Kirschhock, C. E. A.; Ravishankar, R.; Jacobs, P. A.; Martens, J. A. *J. Phys. Chem. B* **1999**, *103*, 11021–11027.

[119] Bussian, P.; Sobott, F.; Brutschy, B.; Schrader, W.; Schüth, F. *Angew. Chem.-Int. Edit.* **2000**, *39*, 3901.

[120] Pelster, S. A.; Schrader, W.; Schüth, F. *J. Am. Chem. Soc.* **2006**, *128*, 4310–4317.

[121] Pelster, S. A.; Kalamajka, R.; Schrader, W.; Schüth, F. *Angew. Chem.-Int. Edit.* **2007**, *46*, 2299–2302.

[122] Pelster, S. A.; Weimann, B.; Schaack, B. B.; Schrader, W.; Schüth, F. *Angew. Chem.-Int. Edit.* **2007**, *46*, 6674–6677.

[123] Pelster, S. A.; Schüth, F.; Schrader, W. *Anal. Chem.* **2007**, *79*, 6005–6012.

[124] Schaack, B. B.; Schrader, W.; Schüth, F. *Angew. Chem.-Int. Edit.* **2008**, *47*, 9092–9095.

[125] Schaack, B. B.; Schrader, W.; Corma, A.; Schüth, F. *Chem. Mat.* **2009**, *21*, 4448–4453.

[126] Schaack, B. B.; Schrader, W.; Schüth, F. *Chem.-Eur. J.* **2009**, *15*, 5920–5925.

[127] Schaack, B. B.; Schrader, W.; Schüth, F. *J. Phys. Chem. B* **2009**, *113*, 11240–11246.

[128] Corma, A.; Diaz-Cabanas, M.; Martinez-Triguero, J.; Rey, F.; Rius, J. *Nature* **2002**, *418*, 514–517.

[129] Taulelle, F. *Curr. Opin. Solid State Mat. Sci.* **2001**, *5*, 397–405.

[130] Taulelle, F.; Pruski, M.; Amoureux, J. P.; Lang, D.; Bailly, A.; Huguenard, C.; Haouas, M.; Gerardin, C.; Loiseau, T.; Ferey, G. *J. Am. Chem. Soc.* **1999**, *121*, 12148–12153.

[131] de Moor, P.-P. E. A.; Beelen, T. P. M.; Komanschek, B. U.; Diat, O.; van Santen, R. A. *J. Phys. Chem. B* **1997**, *101*, 11077–11086.

[132] Chang, C. D.; Bell, A. T. *Catal. Lett.* **1991**, *8*, 305–316.

[133] Flanigen, E. M.; Breck, D. W.; Abstracts of Papers, 137th National Meeting of the ACS; American Chemical Society; p 82.

[134] Burkett, S. L.; Davis, M. E. *J. Phys. Chem.* **1994**, *98*, 4647–4653.

[135] Jacobs, P. A.; Beyer, H. K.; Valyon, J. *Zeolites* **1981**, *1*, 161–168.

[136] Flanigan, E. M.; Khatami, H.; Szymansk, H. A. *Advances in chemistry series* **1971**, 201.

[137] Kragten, D. D.; Fedeyko, J. M.; Sawant, K. R.; Rimer, J. D.; Vlachos, D. G.; Lobo, R. F.; Tsapatsis, M. *J. Phys. Chem. B* **2003**, *107*, 10006–10016.

[138] Mohamed, R. M.; Aly, H. M.; El-Shahat, M. F.; Ibrahim, I. A. *Microporous Mesoporous Mat.* **2005**, *79*, 7–12.

[139] Catlow, C. R. A.; Bromley, S. T.; Hamad, S.; Mora-Fonz, M. J.; Sokol, A. A.; Woodley, S. M. *Phys. Chem. Chem. Phys.* **2010**, *12*, 786–811.

[140] Feuston, B. P.; Garofalini, S. H. *J. Phys. Chem.* **1990**, *94*, 5351–5356.

[141] Hill, J. R.; Sauer, J. *J. Phys. Chem.* **1994**, *98*, 1238–1244.

[142] Trinh, T. T.; Jansen, A. P. J.; van Santen, R. A. *J. Phys. Chem. B* **2006**, *110*, 23099–23106.

[143] Xiao, Y. T.; Lasaga, A. C. *Geochim. Cosmochim. Acta* **1996**, *60*, 2283–2295.

[144] Trinh, T. T.; Jansen, A. P. J.; van Santen, R. A.; Meijer, E. J. *Phys. Chem. Chem. Phys.* **2009**, *11*, 5092–5099.

[145] Car, R.; Parrinello, M. *Phys. Rev. Lett.* **1985**, *55*, 2471–2474.

[146] Mora-Fonz, M. J.; Catlow, C. R. A.; Lewis, D. W. *Angew. Chem.-Int. Edit.* **2005**, *44*, 3082–3086.

[147] Mora-Fonz, M. J.; Catlow, C. R. A.; Lewis, D. W. *J. Phys. Chem. C* **2007**, *111*, 18155–18158.

[148] Schaffer, C. L.; Thomson, K. T. *J. Phys. Chem. C* **2008**, *112*, 12653–12662.

[149] Agger, J. R.; Hanif, N.; Anderson, M. W. *Angew. Chem.-Int. Edit.* **2001**, *40*, 4065.

[150] Binnig, G.; Quate, C. F.; Gerber, C. *Phys. Rev. Lett.* **1986**, *56*, 930–933.

[151] Kacirek, H. and Lechert, H *J. Phys. Chem.* **1975**, *79*, 1589–1593.

[152] Kacirek, H.; Lechert, H. *J. Phys. Chem.* **1976**, *80*, 1291–1296.

[153] Gould, S. A. C.; Drake, B.; Prater, C. B.; Weisenhorn, A. L.; Manne, S.; Kelderman, G. L.; Butt, H. J.; Hansma, H.; Hansma, P. K.; Magonov, S.; Cantow, H. J. *Ultramicroscopy* **1990**, *33*, 93–98.

[154] Weisenhorn, A. L.; MacDougall, J. E.; Gould, S. A. C.; Cox, S. D.; Wise, W. S.; Massie, J.; Maivald, P.; Elings, V. B.; Stucky, G. D.; Hansma, P. K. *Science* **1990**, *247*, 1330–1333.

[155] Gratz, A. J.; Manne, S.; Hansma, P. K. *Science* **1991**, *251*, 1343–1346.

[156] Anderson, M.; Agger, J.; Thornton, J.; Forsyth, N. *Angew. Chem.-Int. Edit. Engl.* **1996**, *35*, 1210–1213.

[157] Agger, J. R.; Pervaiz, N.; Cheetham, A. K.; Anderson, M. W. *J. Am. Chem. Soc.* **1998**, *120*, 10754–10759.

[158] Yamamoto, S.; Sugiyama, S.; Matsuoka, O.; Kohmura, K.; Honda, T.; Banno, Y.; Nozoye, H. *J. Phys. Chem.* **1996**, *100*, 18474–18482.

[159] Vaughan, D. E. W. *Stud. Surf. Sci. Catal.* **1991**, *65*, 275–286.

[160] Terasaki, O.; Ohsuna, T.; Alfedsson, V.; Bovin, J. O.; Watanabe, D.; Carr, S. W.; Anderson, M. W. *Chem. Mat.* **1993**, *5*, 452–458.

[161] Alfredsson, V.; Ohsuna, T.; Terasaki, O.; Bovin, J. O. *Angew. Chem.-Int. Edit. Engl.* **1993**, *32*, 1210–1213.

[162] Meza, L. I.; Anderson, M. W.; Agger, J. R. *Chem. Commun.* **2007**, 2473–2475.

[163] Anderson, M. W.; Ohsuna, T.; Sakamoto, Y.; Liu, Z.; Carlsson, A.; Terasaki, O. *Chem. Commun.* **2004**, 907–916.

[164] Che, S. N.; Lund, K.; Tatsumi, T.; Iijima, S.; Joo, S. H.; Ryoo, R.; Terasaki, O. *Angew. Chem.-Int. Edit.* **2003**, *42*, 2182–2185.

[165] Cubillas, P.; Stevens, S. M.; Blake, N.; Umemura, A.; Chong, C. B.; Terasaki, O.; Anderson, M. W. *J. Phys. Chem. C* **2011**, *115*, 12567–12574.

[166] Charnell, J. F. *J. Cryst. Growth* **1971**, *8*, 291–&.

[167] Di Renzo, F. *Catal. Today* **1998**, *41*, 37–40.

[168] Romannikov, V. N.; Mastikhin, V. M.; Hocevar, S.; Drzaj, B. **1983**, *3*, 311–320.

[169] Cundy, C. S.; Lowe, B. M.; Sinclair, D. M. *J. Cryst. Growth* **1990**, *100*, 189–202.

[170] de Vos Burchart, E.; Jansen, J. C.; van de Graaf, B.; van Bekkum, H. *Zeolites* **1993**, *13*, 216–221.

[171] Bonilla, G.; Diaz, I.; Tsapatsis, M.; Jeong, H. K.; Lee, Y.; Vlachos, D. G. *Chem. Mat.* **2004**, *16*, 5697–5705.

[172] Chen, X.; Yan, W.; Cao, X.; Yu, J.; Xu, R. *Micro. Meso. Mater.* **2009**, *119*, 217–222.

[173] Warzywoda, J.; Thompson, R. W. *Zeolites* **1991**, *11*, 577–582.

[174] Camblor, M. A.; Perez-Pariente, J. *Zeolites* **1991**, *11*, 202–210.

[175] Drews, T. O.; Tsapatsis, M. *Curr. Opin. Colloid Interface Sci.* **2005**, *10*, 233–238.

[176] Loades, S. D.; Carr, S. W.; Gay, D. H.; Rohl, A. L. *J. Chem. Soc.-Chem. Commun.* **1994**, 1369–1370.

[177] Baram, P. S.; Parker, S. C. *Philos. Mag. B-Phys. Condens. Matter Stat. Mech. Electron. Opt. Magn. Prop.* **1996**, *73*, 49–58.

[178] Slater, B.; Titiloye, J. O.; Higgins, F. M.; Parker, S. C. *Curr. Opin. Solid State Mat. Sci.* **2001**, *5*, 417–424.

[179] Slater, B.; Catlow, C. R. A.; Liu, Z.; Ohsuna, T.; Terasaki, O.; Camblor, M. A. *Angew. Chem.-Int. Edit.* **2002**, *41*, 1235.

[180] Meza, L. I.; Anderson, M. W.; Slater, B.; Agger, J. R. *Phys. Chem. Chem. Phys.* **2008**, *10*, 5066–5076.

[181] Chiu, M. E.; Slater, B.; Gale, J. D. *Angew. Chem.-Int. Edit.* **2005**, *44*, 1213–1217.

[182] Agger, J. R.; Shoaee, M.; Mistry, M.; Slater, B. *J. Cryst. Growth* **2006**, *294*, 78–82.

[183] `http://www.hector.ac.uk/`.

[184] Leach, A. R. *Molecular Modelling: Principles and Applications*; Pearson Education, 2001.

[185] Born, M.; Oppenheimer, R. *Annal. der Phys.* **1927**, 457.

[186] Ewald, P. *Annal. der Phys.* **1921**, 253–287.

[187] Dick, B. G.; Overhauser, A. W. *Phys. Rev.* **1958**, *112*, 90–103.

[188] Sanders, M. J.; Leslie, M.; Catlow, C. R. A. *J. Chem. Soc.-Chem. Commun.* **1984**, 1271–1273.

[189] `http://www.phy.cmich.edu/people/petkov/isaacs/phys/pbc.html`.

[190] van Duin, A. C. T.; Dasgupta, S.; Lorant, F.; Goddard, W. A. *J. Phys. Chem. A* **2001**, *105*, 9396–9409.

[191] Schrodinger, E. *Annal. der Phys.* **1926**, *384*, 489–527.

[192] Hohenberg, P.; Kohn, W. *Phys. Rev. B* **1964**, *136*, B864.

[193] Kohn, W.; Sham, L. J. *Phys. Rev.* **1965**, *140*, 1133–&.

[194] Martin, R. M. *Electronic Structure: Basic Theory and Methods*; Cambridge University Press, 2004.

[195] Filippi, C.; Umrigar, C. J.; Taut, M. *J. Chem. Phys.* **1994**, *100*, 1290–1296.

[196] Becke, A. D. *Phys. Rev. A* **1988**, *38*, 3098–3100.

[197] Lee, C. T.; Yang, W. T.; Parr, R. G. *Phys. Rev. B* **1988**, *37*, 785–789.

[198] Meyer, B. *NIC Series* **2006**, 71–83.

[199] Verlet, L. *Phys. Rev.* **1967**, *159*, 98–103.

[200] Swope, W. C.; Anderson, H. C.; Berens, P. H.; Wilson, K. R. *J. Chem. Phys.* **1982**, *76*, 637–649.

[201] Woodcock, L. V. *Chem. Phys. Lett.* **1971**, *10*, 257–261.

[202] Berendsen, H. J. C.; Postma, J. P. M.; VanGunsteren, W. F.; Dinola, A.; Haak, J. R. *J. Chem. Phys.* **1984**, *81*, 3684–3690.

[203] Nosé, S. *J. Chem. Phys.* **1984**, *81*, 511–519.

[204] Nosé, S. *Mol. Phys.* **1984**, *52*, 255–268.

[205] Hoover, W. G. *Phys. Rev. A* **1985**, *31*, 1695–1697.

[206] Andersen, H. C. *J. Chem. Phys.* **1980**, *72*, 2384–2393.

[207] Kirkwood, J. G. *J. Chem. Phys.* **1935**, *3*, 300–313.

[208] Roux, B. *Comput. Phys. Commun.* **1995**, *91*, 275–282.

[209] Metropolis, N.; Rosenbluth, A. W.; Rosenbluth, M. N.; Teller, A. H.; Teller, E. *J. Chem. Phys.* **1953**, *21*, 1087–1092.

[210] Born, M. *Zeitschrift für Physik* **1940**, *1*.

[211] Onsager, L. *J. Am. Chem. Soc.* **1936**, *58*.

[212] Klamt, A. *J. Phys. Chem.* **1995**, *99*, 2224–2235.

[213] Lewis, D. W.; Willock, D. J.; Catlow, C. R. A.; Thomas, J. M.; Hutchings, G. J. *Nature* **1996**, *382*, 604–606.

[214] Gale, J. D.; Rohl, A. L. *Mol. Simul.* **2003**, *29*, 291–341.

[215] Accelrys; 2006; Materials Studio Release Notes, Release 4.1, Accelrys Software, Inc.: San Diego.

[216] Willock, D. J.; Lewis, D. W.; Catlow, C. R. A.; Hutchings, G. J.; Thomas, J. M. *J. Mol. Catal. A* **1997**, *119*, 415 – 424.

[217] `http://research.cs.wisc.edu/condor/`.

[218] Pluth, J. J.; Smith, J. V. *Am. Miner.* **1990**, *75*, 501–507.

[219] Howard, D. G.; Tschernich, R. W.; Smith, J. V.; Klein, G. L. *Am. Miner.* **1990**, *75*, 1200–1204.

[220] Galli, E.; Quartieri, S.; Vezzalini, G.; Alberti, A. *Eur. J. Mineral.* **1995**, *7*, 1029–1032.

[221] Simancas, R.; Dari, D.; Velamazan, N.; Navarro, M. T.; Cantin, A.; Jorda, J. L.; Sastre, G.; Corma, A.; Rey, F. *Science* **2010**, *330*, 1219–1222.

[222] Sun, H.; Mumby, S. J.; Maple, J. R.; Hagler, A. T. *J. Am. Chem. Soc* **1994**, *116*, 2978.

[223] Lewis, D. W.; Freeman, C. M.; Catlow, C. R. A. *J. Phys. Chem.* **1995**, *99*, 11194–11202.

[224] Calabro, D. C.; Cheng, J. C.; Jr, R. A. C.; Kresge, C. T.; andd M. A. Steckel, S. S. D.; Stern, D. L.; Weston, S. C.; 2000; US Patent 6049018.

[225] Dorset, D. L.; Weston, S. C.; Dhingra, S. S. *J. Phys. Chem. B* **2006**, *110*, 2045–2050.

[226] Johnson, I. D.; Stevens, H. B., L. M. Vroman; Weston, S. C.; *WO 2007/075383*; 2007.

[227] Weston, S. C.; Strohmaier, K. G.; Vroman, H. B.; Vartuli, J. C. *Proceedings of the 16th International Zeolite Conference* **2010**; Discovery of a new structure-directing agent for the aluminosilicate zeolite MCM-68 (MSE).

[228] Ernst, S.; Elangovan, S. P.; Gerstner, M.; Hartmann, M.; Hecht, T.; Sauerbeck, S.; Studies in Surface Science and Catalysis, Vol. 154; pp 2861–2868.

[229] Shibata, T.; Suzuki, S.; Kawagoe, H.; Komura, K.; Kubota, Y.; Sugi, Y.; Kim, J.-H.; Seo, G. *Microporous Mesoporous Mat.* **2008**, *116*, 216–226.

[230] Strohmaier, K. G.; Weston, S. C.; Vartuli, J. C.; Ippoliti, J. T.; *US Patent 8025863*; 2011.

[231] Weston, S.; Strohmaier, K.; Vroman, H.; *Patent filed*; 2011.

[232] Weston, S. C. **2011**; Private communication.

[233] Dent, L. S.; Smith, J. V. *Nature* **1958**, *181*, 1794–1796.

[234] Diaz-Cabanas, M. J.; Barrett, P. A.; Camblor, M. A. *Chem. Commun.* **1998**, 1881–1882.

[235] Ito, M.; Shimoyama, Y.; Saito, Y.; Tsurita, Y.; Otake, M. *Acta Crystallogr.* **1985**, *41*, 1698–1700.

[236] Harding, M. M.; Kariuki, B. M. *Acta Crystallogr.* **1994**, *50*, 852–854.

[237] Tusar, N. N.; Kaucic, V.; Geremia, S.; Vlaic, G. *Zeolites* **1995**, *15*, 708–713.

[238] Bennett, J. M.; Cohen, J. P.; Flanigen, E. M.; Pluth, J. J.; Smith, J. V. **1983**, *218*, 109–118.

[239] O'Brien, M. G.; Beale, A. M.; Catlow, C. R. A.; Weckhuysen, B. M. *J. Am. Chem. Soc.* **2006**, *128*, 11744–11745.

[240] Brand, H. V.; Curtiss, L. A.; Iton, L. E.; Trouw, F. R.; Brun, T. O. *J. Phys. Chem.* **1994**, *98*, 1293–1301.

[241] Beale, A. M.; O'Brien, M. G.; Kasunic, M.; Golobic, A.; Sanchez-Sanchez, M.; Lobo, A. J. W.; Lewis, D. W.; Wragg, D. S.; Nikitenko, S.; Bras, W.; Weckhuysen, B. M. *J. Phys. Chem. C* **2011**, *115*, 6331–6340.

[242] Gale, J. D.; Henson, N. J. *J. Chem. Soc.-Faraday Trans.* **1994**, *90*, 3175–3179.

[243] Lewis, D. W.; Catlow, C. R. A.; Thomas, J. M. *Chemistry of Materials* **1996**, *8*, 1112–1118.

[244] Sankar, G.; Wyles, J. K.; Catlow, C. R. A. *Topics in Catalysis* **2003**, *24*, 173–184; 10.1023/B:TOCA.0000003088.21277.f5.

[245] Davis, M. E.; Lobo, R. F. *Chem. Mat.* **1992**, *4*, 756–768.

[246] Brent, R.; Lobo, A. J. W.; Lewis, D. W.; Anderson, M. W. *J. Phys. Chem. C* **2010**, *114*, 18240–18246.

[247] Barrer, R. M.; Villiger, H. *Z. Kristallogr.* **1969**, *128*, 352–&.

[248] Breck, D.; Acara, N.; 1965; US Patent 3216789.

[249] Verduijn, J. P.; 1991.

[250] Larlus, O.; Valtchev, V. P. *Chem. Mat.* **2004**, *16*, 3381–3389.

[251] Lee, Y. J.; Lee, J. S.; Yoon, K. B. *Microporous Mesoporous Mat.* **2005**, *80*, 237–246.

[252] Brent, R.; Anderson, M. W. *Angew. Chem.-Int. Edit.* **2008**, *47*, 5327–5330.

[253] Fleming, S.; Rohl, A. *Z. Kristall.* **2005**, *220*, 580–584.

[254] Schröder, K. P.; Sauer, J.; Leslie, M.; Catlow, C. R. A.; Thomas, J. M. *Chem. Phys. Lett.* **1992**, *188*, 320–325.

[255] Bennett, J. M.; Jr, J. W. R.; Pluth, J. J.; Smith, J. V. *Zeolites* **1987**, *7*, 160 – 162.

[256] Richardson, J. W., Jnr; Pluth, J. J.; Smith, J. V. *Acta Crystallogr.* **1988**, *44*, 367–373.

[257] Flanigan, E. M.; M., L. B.; Patton, R. L.; Wilson, S. T. *Pure Appl. Chem.* **1986**, *58*, 1351–1358.

[258] Meriaudeau, P.; Tuan, V. A.; Hung, L. N.; Szabo, G. **1997**, *19*, 449–451.

[259] Strohmaier, K. G.; Vaughan, D. E. W.; 2001; US 6,238,550.

[260] Todorov, I. T.; Smith, W.; Trachenko, K.; Dove, M. . T. *J. Mater. Chem.* **2006**, *16*, 1911–1918.

[261] Oie, T.; Maggiora, G. M.; Christoffersen, R. E.; Duchamp, D. J. *Int. J. Quantum Chem.* **1981**, 1–47.

[262] Kiselev, A. V.; Lopatkin, A. A.; Shulga, A. A. *Zeolites* **1985**, *5*, 261–267.

[263] Butler, K. T.; Ph.D. thesis; University College London; 2009.

[264] de Leeuw, N. H.; Parker, S. C. *Phys. Rev. B* **1998**, *58*, 13901–13908.

[265] Gomez, A. G.; de Silveira, G.; Doan, H.; Cheng, C. H. *Chem. Commun.* **2011**, *47*, 5876–5878.

[266] Mootz, D.; Seidel, R. *J. Incl. Phenom. Mol. Recogn. Chem.* **1990**, *8*, 139–157.

[267] Wiebcke, M.; Emmer, J.; Felsche, J. *J. Chem. Soc.-Chem. Commun.* **1993**, 1604–1606.

[268] Marcus, Y. *Chem. Rev.* **2009**, *109*, 1346–1370.

[269] Marcus, Y. *J. Solut. Chem.* **1996**, *25*, 455–469.

[270] Bennetto, H. P.; Caldin, E. F. *J. Chem. Soc. A* **1971**, 2198–2207.

[271] Marcus, Y. *J. Solut. Chem.* **1992**, *21*, 1217–1230; 10.1007/BF00667218.

[272] Soper, A. K. *Chem. Phys.* **2000**, *258*, 121–137.

[273] Wernet, P.; Nordlund, D.; Bergmann, U.; Cavalleri, M.; Odelius, M.; Ogasawara, H.; Naslund, L. A.; Hirsch, T. K.; Ojamae, L.; Glatzel, P.; Pettersson, L. G. M.; Nilsson, A. *Science* **2004**, *304*, 995–999.

[274] Bergmann, U.; Di Cicco, A.; Wernet, P.; Principi, E.; Glatzel, P.; Nilsson, A. **2007**, *127*, 174504.

[275] Smith, J. D.; Cappa, C. D.; Wilson, K. R.; Messer, B. M.; Cohen, R. C.; Saykally, R. J. *Science* **2004**, *306*, 851–853.

[276] Smith, J. D.; Cappa, C. D.; Messer, B. M.; Drisdell, W. S.; Cohen, R. C.; Saykally, R. J. *J. Phys. Chem. B* **2006**, *110*, 20038–20045.

[277] Turner, J.; Soper, A. K.; Finney, J. L. *Mol. Phys.* **1990**, *70*, 679–700.

[278] Bradl, S.; Lang, E. W. *J. Phys. Chem.* **1993**, *97*, 10463–10471.

[279] Kumar, R.; Schmidt, J. R.; Skinner, J. L. *J. Chem. Phys.* **2007**, *126*.

[280] Xenides, D.; Randolf, B. R.; Rode, B. M. *J. Mol. Liq.* **2006**, *123*, 61–67.

[281] Madan, B.; Sharp, K. *Biophys. Chem.* **1999**, *78*, 33–41.

[282] Verstraelen, T.; Szyja, B. M.; Lesthaeghe, D.; Declerck, R.; Van Speybroeck, V.; Waroquier, M.; Jansen, A. P. J.; Aerts, A.; Follens, L. R. A.; Martens, J. A.; Kirschhock, C. E. A.; van Santen, R. A. *Top. Catal.* **2009**, *52*, 1261–1271.

[283] Szyja, B.; Vassilev, P.; Trinh, T.; van Santen, R.; Hensen, E. *Micro. Meso. Mater.* **2011**, *146*, 82 – 87.

[284] Kirschhock, C. E. A.; Buschmann, V.; Kremer, S.; Ravishankar, R.; Houssin, C. J. Y.; Mojet, B. L.; van Santen, R. A.; Grobet, P. J.; Jacobs, P. A.; Martens, J. A. *Angew. Chem.-Int. Edit.* **2001**, *40*, 2637–2640.

[285] Turner, J.; Soper, A. K. *J. Chem. Phys.* **1994**, *101*, 6116–6125.

[286] VandeVondele, J.; Krack, M.; Mohamed, F.; Parrinello, M.; Chassaing, T.; Hutter, J. *Comput. Phys. Commun.* **2005**, *167*, 103–128.

[287] Goedecker, S.; Teter, M.; Hutter, J. *Phys. Rev. B* **1996**, 1703.

[288] Hartwigsen, C.; Goedecker, S.; Hutter, J. *Phys. Rev. B* **1998**, 3641.

[289] Krack, M. *Theor. Chem. Acc.* **2005**, *114*, 145–152.

[290] Laasonen, K.; Sprik, M.; Parrinello, M.; Car, R. **1993**, *99*, 9080–9089.

[291] Lee, S. H.; Shin, C. H.; Yang, D. K.; Ahn, S. D.; Nam, I. S.; Hong, S. B. *Microporous Mesoporous Mat.* **2004**, *68*, 97–104.

[292] Soper, A. K. *J. Chem. Phys.* **1994**, *101*, 6888–6901.